UNIVERSIDAD COMPLUTENSE DE MADRID

FACULTAD DE CIENCIAS FÍSICAS

TESIS DOCTORAL

Comportamiento termomecánico del Manto de Hielo Laurentino: desde avances analíticos hasta una metodología de modelación

———————

Thermomechanical behaviour of the Laurentide Ice Sheet: from analytical advances to a modelling approach

MEMORIA PARA OPTAR AL GRADO DE DOCTOR

PRESENTADA POR

Daniel Moreno Parada

DIRIGIDA POR

Dr. Alexander Robinson
Dr. Jorge Alvarez Solas

Universidad Complutense de Madrid
Facultad de Ciencias Físicas

Tesis doctoral

Comportamiento termomecánico del Manto de Hielo Laurentino: desde avances analíticos hasta una metodología de modelación

Thermomechanical behaviour of the Laurentide Ice Sheet: from analytical advances to a modelling approach

Memoria para optar al grado de Doctor.

presentada por

Daniel Moreno Parada

Directores

Dr. Alexander Robinson

Dr. Jorge Alvarez Solas

This thesis has been supported by the Spanish Ministry of Science and Innovation (project IceAge, grant no. PID2019-110714RA-100) and the Ramón y Cajal programme of the Spanish Ministry of Science and Innovation and the Spanish Ministry of Universities (grant no. RYC-2016-20587). This research has also been funded by the European Union Horizon 2020 research and innovation programme (grant no. 820970). All model simulations analysed in this thesis were performed in Brigit, the High-Performance computing cluster of the International Campus of Excellence of Moncloa, funded by MECD (Ministerio de Eucación, Cultura y Deporte) and MICINN (Ministerio de Ciencias, Innovación y Universidades).

A Lucía, Natalia y Alfonso

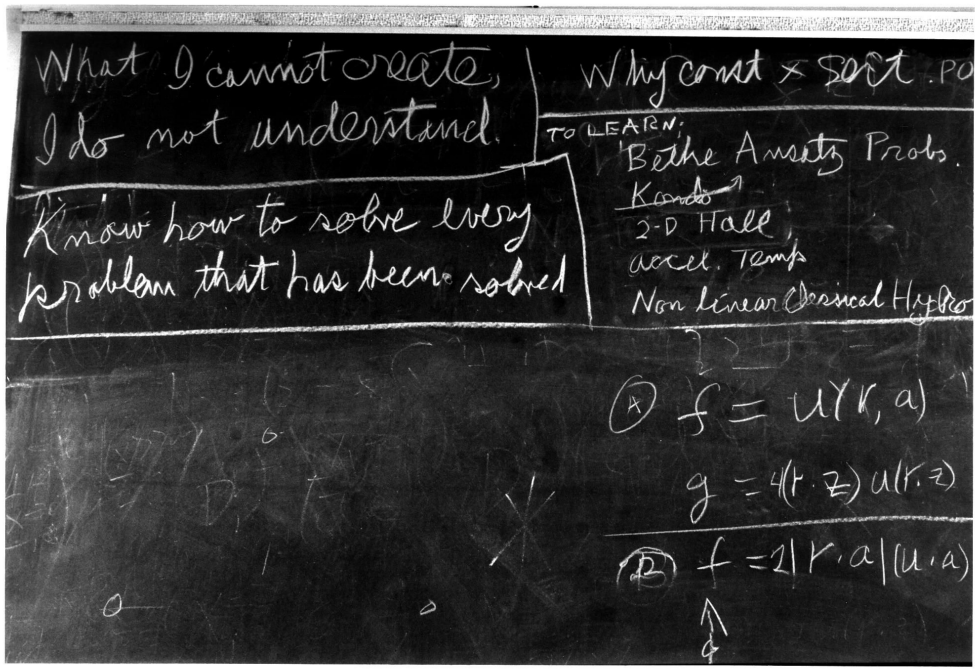

Richard Feynman's blackboard at time of his death. From *California Institute of Technology* (Caltech Images Collection, 1.10-29, 1988)

What I cannot create, I do not understand.

Richard Feynman's blackboard at time of his death.

Contents

Agradecimientos

Me pregunto qué habrá sido de aquel chico que, una calurosa mañana de junio y pocos minutos después de haber defendido su TFM, firmaba su primer contrato como investigador. ¿Es el mismo que hoy escribe estas palabras o ya sólo existe en la memoria de algunos? Sea como fuere, estoy seguro de que las preguntas de su tribunal serán algo menos rebuscadas.

Hoy me veo frente al papel en blanco con muchas personas a las que agradecer y pocas ideas de cómo hacerlo. Aún así, tengo la esperanza de que, todo aquel que lea estas líneas, se lleve un pedazo de mi.

Quiero empezar dando las gracias a Marisa. Tus clases de modelización en el máster me cautivaron y avivaron mi curiosidad por entender el esqueleto de todos esos modelos de los que tanto hablamos. Eres una docente ejemplar y tu forma de exponer y explicar ha dejado una huella imborrable en mi. A Jorge; no tuve la suerte de asistir a tus clases, pero me has enseñado uno de los aspectos más complejos de aprender: saber preguntar. Eso que todos los científicos deben dominar y que, con frecuencia, pasamos por alto. Alex; tu organización y capacidad de trabajo son envidiables, sin duda irán conmigo allá donde vaya. Espero poder mantener ese ímpetu por seguir avanzando. Fidel; a pesar de no ser mi director sobre el papel, me has transmitido sin dificultad alguna tu sed insaciable por aprender.

Tengo la suerte de no haber aprendido sólo de mis directores, sino de todos mis compañeros de trabajo. Felix ("¡mi niño!"), de no llevarnos muy bien en el master a ser inseparables en el despacho. Ha sido un placer discutir en la pizarra todas nuestras ideas y compartir esos viajes a Viena juntos. Con esa picardía que te caracteriza, eres un orador magnífico y un divulgador envidiable. Espero seguir aprendiendo de ti. Jan, mi gran políglota amante

de las matemáticas y el piano. Eres de las pocas personas con las que es un placer hablar de cualquier tema. Gracias por tener un corazón tan grande. Te espera un camino lleno de éxitos en aquello que te propongas y repleto de personas que te aprecian (aunque te empeñes en programar en Julia y no en C++). Sergio; el aventurero del despacho. Admiro tu resiliencia y disciplina. Has hecho de ellas tu virtud, sólo puedo animarte a que siga siendo así. Lucía (Palma); tu ingenio y tu dialéctica te van abrir muchas puertas y, entre ellas, las de este mundo científico, no me cabe duda alguna. Antonio, el despacho necesitaba a alguien con ese humor y tus juegos de palabras. Espero que los alumnos puedan seguir disfrutando de un profesor tan dedicado como tú; eres un ejemplo para todos los docentes. Álvaro; nuestro escalador profesional, dudo que algún día dejes de inspirarme con tu creatividad. Elena; gracias por ser la única persona capaz de superar mi humor absurdo. Espero algún día poder aprender a combinar tu tranquilidad con tu capacidad resolutiva. Cris (V), ¡nuestra estrella del pop! Tus ganas de hacer música son contagiosas, espero que continues siempre marcando el compás de este despacho. Nago, por todas esas veces que me has dicho lo poco que trabajo aunque en el fondo disfrutes como la que más de nuestra cháchara. Sé que vas a lograr grandes cosas aunque quizás aún no te lo creas; el tiempo me dará la razón. Lucía (Tropa), nuestra ávida lectora. Creo que son muchos los investigadores deberían aprender de tu humildad, gracias por ponernos los pies en la tierra. Poc; nuestro jugador de pádel por excelencia, ha sido un placer compartir esas EGUs juntos. Siempre dispuesto a echar una mano, eres el compañero de trabajo que todos desearían tener. Alex; el mejor repostero que ha pisado este despacho, gracias por tus frikadas y los datos más aleatorios que puede manejar un ser humano. A Javi, trombonista y amante de la historia. Gracias por acogerme y ayudarme como lo hiciste cuando entré en el despacho. Siento que el patrón se repite con la misma bondad, pero ahora abriéndome las puertas de tu casa en Bruselas. Te deseo todo lo mejor en tu nueva etapa en Berlín, te lo mereces. No quiero olvidarme del resto de mi gente en la facultad por llenar de risas este viaje: Juan, Pablo, Victor y Sofía. Mucho ánimo en esta etapa.

A mis amigos. Dani, por todas esas conversaciones en el pasillo de casa sobre cómo optimizar código y ejecutar en paralelo. Inés, por transmitirnos todo tu amor con tu exquisito gusto en la cocina. Espero que sigas exprimiendo ese talento que tienes para la pintura. David, por todas aquellas tardes

en la Plaza de Cervantes hablando de álgebra y de nuestros dilemas de la vida. No dejes de alegrar las casas rurales con tus juegos increíbles. Rodri, nunca olvidaré aquella tarde de verano en plena pandemia cuando te bajaste un cuaderno y un boli para entender mejor a qué me dedicaba. Espero haber podido transmitirte que la belleza de tu poesía también se encuentra en los números. Mawy; por escuchar mis penas, mis alegrías y mis excentricidades. Gracias por avivar las bromas interminables que perseguirán siempre a este grupo. A todos mis compañeros del Club de Atletismo Ajalkala. A Toni, Frami, Sotoca, Miky, Samu y Farelo por poder desahogarme con vosotros. A mi compi de piso; Yaiza, por preguntarme sobre todos los artículos que iba publicando y hacerme la comida cuando casi pierdo un pie entrenando. También a mi gran amigo Pedro ("The Man"), la distancia no ha conseguido romper aquello que forjó nuestro erasmus en Łódź. Estoy seguro de que nos veremos pronto en Oporto. A Iñaki; por mantener viva esa ilusión que todos los niños tienen y, por desgracia, muy pocos adultos conservan. Gracias por transmitir tu amor por la música en todos y cada uno de los ensayos que hemos compartido.

Llego ahora a la parte más difícil de expresar con palabras. Gracias, Lorena. Por todo. Por escuchar mis batallitas en medio de clase, por las innumerables gráficas que te he mostrado, por todas las revisiones de artículos que has escuchado, por venir a recogerme al aeropuerto, por lidiar con mis miles de preguntas y por mostrar tu apoyo incondicional en las decisiones más duras. En definitiva, por ser mi fiel compañera en este viaje. He tenido el placer de compartir escenario contigo estos años de la mano de la Orquesta Ciudad de Alcalá. Jamás pensé que ocuparía uno de aquellos asientos cuando disfrutaba desde mi butaca viéndoos tocar. Gracias por abrirme las puertas de una de las experiencias más bonitas que he vivido. Te has convertido en una pieza fundamental de esa ecuación que escapa al raciocinio. Sólo puedo darte las gracias por confiar en mí cuando yo no lo hacía.

Vienen etapas nuevas, quizá no mejores ni peores, sólo distintas. Sería iluso creer que no hay incertidumbre e incluso miedo, pero estoy seguro (con "certeza absoluta" dirían algunos) de que merecerá la pena. Has logrado absolutamente todo lo que te has propuesto con tu determinación y tu empeño, espero que me brindes el placer de estar ahí para celebrar todo lo que aún está por venir.

Por último, quiero darle las gracias a mi familia. A mi madre, por aguantar aquellas "preguntitas imposibles de responder" desde que aprendí a hablar y por tranquilizarme cuando olvidaba el nombre de una especie de dinosaurio cuando era sólo un niño. Me has enseñado a ser organizado, paciente y saber relativizar. A mi hermana; por aguantarme, tener siempre una sonrisa en la cara y traer esa felicidad a casa desde que naciste. Gracias por enseñarme, con tu ejemplo, que la humildad es una de las mejores virtudes. Quiero dar unas gracias especiales a mi padre, Alfonso. Hemos llegado a ser incluso compañeros de equipo federados en la liga de ajedrez. Imposible olvidar esas mañanas de domingo desayunando en el coche mientras conducías a nuestro destino como equipo visitante. Quiero que sepas que hoy soy el científico que soy gracias a ti. Desde que clasificábamos anfibios juntos con aquel libro, pasando por tus sutiles explicaciones del concepto de derivada sin que yo fuese consciente, hasta la importancia de saber hablar en público. Aún recuerdo cuando leíamos el libro de Carl Sagan donde aprendí qué era el Big Bang o el nombre del número más grande: el "Googol". Convertiste el aprender en un juego que me cautivó desde que tengo uso de razón y del que nunca podré dejar de jugar. Me habéis guiado con pericia, dejándome cometer esos errores que otorgan lecciones a veces amargas, pero necesarias e inolvidables. Hoy sólo puedo daros las gracias porque, sin vosotros, esto nunca habría sido posible.

List of acronyms

AIS	Antarctic Ice Sheet
AMOC	Atlantic Meridional Overturning Circulation
BP	Before Present
DIVA	Depth-Integrated Viscosity Approximation
D-O	Dansgaard-Oeschger
EIS	Eurasian Ice Sheet
ELRA	Elastic Litosphere-Relaxing Asthenosphere
FIS	Fennonscadian Ice Sheet
GCM	Global Circulation Model
GIA	Glacial Isostatic Adjustment
HE	Heinrich Event
IRD	Ice Rafted Debris
LGM	Last Glacial Maximum
LIS	Laurentide Ice Sheet
PD	Present Day
PDD	Positive Degree-Day
RMSD	Root Mean Square Deviation
SIA	Shallow Ice Approximation
SLE	Sea Level Equivalent
SSA	Shallow Shelf Approximation

List of parameters

A_0	Arrhenius Law constant ($1.257\ 10^{-5}\,\mathrm{yr}^{-1}\,\mathrm{Pa}^{-3}$ for $\mathrm{T} \leq 263.15$ K; $6.042\ 10^{-6}\,\mathrm{yr}^{-1}\,\mathrm{Pa}^{-3}$ for $\mathrm{T} > 263.15$ K)
b	Base of the ice sheet (m)
B_{ref}	Reference submarine melting rate, assumed at the present-day ($\mathrm{m\,yr}^{-1}$))
B	Basal melt (B_{gl}, at the grounding line; B_{sh}, below the ice shelf; $\mathrm{m\,yr}^{-1}$)
Br	Brinkman number
c	Heat capacity of ice (146.3 + 7.253 T[K]) J $\mathrm{kg}^{-1}\,\mathrm{K}^{-1}$)
g	Gravitational acceleration ($9.81\ \mathrm{m\,s}^{-2}$)
H	Ice thickness (m)
M	Surface mass balance ($\mathrm{m\,yr}^{-1}$)
n	Flow law stress exponent
N_{eff}	Effective pressure between ice and water pressure (Pa)
p	Pressure (Pa)
P_{ann}	Annual precipitation ($\mathrm{m\,a}^{-1}$)
Pe	Peclét number
Q	Activation energy (60 kJ mol^{-1} for $\mathrm{T} \leq 263.15$ K; 139 kJ mol^{-1} for $\mathrm{T} > 263.15\ K$)
R	Universal gas constant ($8.314\ J\ \mathrm{mol}^{-1}\ \mathrm{K}^{-1}$)
S	Ice surface elevation (m)
T	Temperature (K)
T_{f}	Temperature at the freezing point (K)
T_{atm}	Atmospheric temperature (K)
T_{ocn}	Oceanic temperature (K)
t	Time (yr)

U	Depth-averaged horizontal ice velocity (=(U,V))
$\mathbf{v}$	Ice velocity (=(u, v, w))
α	Orbital climatic index
β	Millennial climatic index
ΔT_{atm}	Atmospheric temperature anomaly
ΔT_{ocn}	Oceanic temperature anomaly ($\Delta T_{\mathrm{ocn}}^{\mathrm{mil}}$, interstadial-stadial anomaly; $\Delta T_{\mathrm{ocn}}^{\mathrm{orb}}$, glacial-interglacial anomaly)
β	Dimensionless surface insulation
γ	Dimensionless combined contribution of geothermal heat flow and basal frictional heat
ϵ_{ij}	Strain rate
η	Ice viscosity
κ	Ice-ocean heat-flux coefficient (oceanic sensitivity; ($\mathrm{m\,a^{-1}\,K^{-1}}$))
κ_i	Heat conductivity of ice (9.828 exp(-0.0057 T[K]) $\mathrm{W\,m^{-1}\,K^{-1}}$)
Λ	Normalised horizontal advection
ρ	Density of the ice (910 kg $\mathrm{m^{-3}}$)
ρ_w	Density of seawater (1028 kg $\mathrm{m^{-3}}$)
$\boldsymbol{\sigma}$	Cauchy stress tensor
τ_{ij}	Deviatoric stress
τ_{b}	Basal drag term
τ_{d}	Driving stress

Summary

Introduction

The Laurentide Ice Sheet (LIS) was the largest of the former Northern Hemisphere ice sheets during the Last Glacial Maximum (LGM, 21,000 years before present). Nevertheless, there are large uncertainties regarding the behaviour of the LIS and its main features such as maximum elevation, total volume and extent among others. Moreover, North Atlantic sediment cores contain quasi-periodic layers with extremely high percentages of lithic fragments during glacial periods. Our current explanation for the presence of such layers considers that the sediments were captured by the ice, transported from the Northern Hemisphere ice sheets and eventually unloaded onto the seafloor when the enclosing ice melted. The ultimate physical explanation underlying any oscillatory mechanism that causes the Heinrich Events (HEs) is still under debate.

Aim of this thesis

The goal of this thesis is to perform a comprehensive study on the thermomechanical behaviour and the plausibility of internal physically-based oscillations of the Laurentide Ice Sheet. To this end, the present study combines a variety of approaches. First, it employs analytical tools to derive an analytical time-dependent description of ice temperatures. Then, the necessary coupling with other fundamental components of the ice sheet behaviour is

included by developing the ice-sheet model Nix v1.0. Lastly, the third and fourth studies aim at simulating the LIS under LGM conditions for a realistic setup using the three-dimensional ice-sheet model Yelmo.

Results

The first study analytically solves the 1D time-dependent advective-diffusive heat problem including additional terms due to strain heating and depth-integrated horizontal advection. A Robin-type top boundary condition considers potential non-equilibrium temperature states across the ice-air interface. The solution is expressed in terms of confluent hypergeometric functions following a separation of variables approach. Non-dimensionalisation reduces the parameter space to four numbers that fully determine the shape of the solution at equilibrium: surface insulation, effective geothermal heat flow, the Peclét number and the Brinkman number. The initial temperature distribution exponentially converges to the stationary solution. Transient decay timescales are only dependent on the Peclét number and the surface insulation, so that higher advection rates and lower insulating values imply shorter equilibration timescales, respectively. Lastly, we present a suite of benchmark experiments to test numerical solvers against analytical solutions. Four experiments of gradually increasing complexity capture the main physical processes for heat propagation.

The second study develops the ice-sheet model Nix v1.0, a 2D thermomechanical model written in C/C++ that simultaneously solves for the momentum balance equations, mass conservation and temperature evolution. Nix's velocity solver includes a hierarchy of Stokes approximations: Blatter-Pattyn, depth-integrated higher order, shallow-shelf and shallow-ice. The grounding-line position is explicitly solved by a moving coordinate system that avoids further interpolations. Here we show results for a number of benchmark tests from standard intercomparison projects and assess grounding-line migration with an overdeepened bed geometry. Lastly, we further exploit the thermomechanical coupling by designing a suite of experiments where the forcing is a physical variable. Namely, we use atmospheric temperatures and oceanic temperature anomalies to assess model hysteresis behaviour with active thermodynamics. Notably, the classical hysteresis loop is narrowed for both forcing

scenarios (i.e., atmospheric and oceanic) if the ice sheet is thermomechanically active as a result of the internal feedback among ice temperature, stress balance and viscosity.

The third study evaluates the role played by different basal friction formulations when reconstructing the LIS. To this end, Yelmo ice-sheet model is used to simulate the LIS under LGM boundary conditions for a number of basal friction formulations of varying complexity. Their consequences on the Laurentide ice streams, configuration, extent and volume are explicitly quantified. Total volume and ice extent generally reach a constant equilibrium value that falls close to prior LIS reconstructions. Simulations exhibit high sensitivity to the dependency of the basal shear stress on the sliding velocity. In particular, a regularized-Coulomb friction formulation appears to be the best choice in terms of ice volume and ice-stream realism. Pronounced differences are found when the basal friction stress is thermomechanically coupled: the base remains colder and the LIS volume is lower than in the purely mechanical friction scenario counterpart. Thermomechanical coupling is fundamental for producing rapid ice streaming, yet it leads to a similar ice distribution overall.

Lastly, the fourth study performs a comprehensive study on the plausibility of internal physically-based oscillations of the Laurentide Ice Sheet. Experiments show an oscillatory equilibrium state of the ice stream located along Hudson Strait whose period is consistent with hypothesized discharges from the LIS observed in ocean sediment cores. More precisely, the ice stream transitions between two modes of ice flow: rapid sliding over a saturated till and slow creeping ice over a fully drained till. The period and amplitude of the oscillation are highly dependent on the hydrology parametrization and the physical properties of the till. Notably, this phenomenon does not appear to be model-resolution dependent, thus discounting a numerical cause of the oscillatory behaviour. It must be stressed that only minor changes on the LIS and Hudson Bay ice volume are found throughout this study as a consequence of the ice stream temporal variability.

Main conclusions

To conclude, the thermal behaviour of the ice is a fundamental piece to understand both the past and future of large ice masses. Yet it is poorly understood. The inherent coupling with other key elements such as glacial hydrology and ice dynamics shapes the complexity of this problem. Basal friction appears to be a crucial component, of which little we know particularly in past ice-sheet reconstructions with evidence of periodic ice stream activation. This work demonstrates the unveiled potential of a time-dependent analytical description of the ice temperatures. Low dimensional models, though far from an exhaustive description of reality, present themselves as an extremely convenient tool to understand the basic physical mechanisms that are otherwise hidden by the complexity of highly sophisticated models. By means of a balanced combination of novel theoretical advances and modelling efforts, this thesis has cast light upon the thermomechanical behaviour of the LIS and the overall stability of terminating glaciers.

Resumen

Introducción

El Manto de Hielo Laurentino (LIS) fue el mayor de los antiguos mantos de hielo del hemisferio norte durante el Último Máximo Glacial (LGM, 21.000 años antes del presente). No obstante, existen grandes incertidumbres sobre el comportamiento del LIS y sus principales características. Además, los testigos de sedimentos del Atlántico Norte contienen capas cuasiperiódicas con porcentajes extremadamente altos de fragmentos líticos durante los periodos glaciares. Nuestra explicación actual de la presencia de tales capas considera que los sedimentos fueron capturados por el hielo durante el deslizamiento de éste, transportados desde los mantos de hielo del hemisferio norte y finalmente descargados en el fondo marino cuando se derritió el hielo que los contenía. Sin embargo, la explicación física definitiva subyacente a cualquier mecanismo oscilatorio que cause estos eventos sigue siendo objeto de debate.

Objetivo de la tesis

El objetivo de esta tesis es realizar un estudio exhaustivo sobre el comportamiento termomecánico y la plausibilidad de las oscilaciones internas de base física del Manto de Hielo Laurentino. Para ello, el presente estudio combina diversos enfoques. En primer lugar, emplea herramientas analíticas para derivar una descripción analítica con dependencia temporal de las temperaturas del hielo. A continuación, se incluye el acoplamiento necesario con

otros componentes fundamentales del comportamiento de un manto de hielo mediante el desarrollo del modelo Nix v1.0. Por último, los estudios tercero y cuarto pretenden simular el LIS durante el LGM para una configuración realista utilizando el modelo tridimensional de manto de hielo Yelmo.

Resultados

El primer estudio resuelve analíticamente la ecuación de calor advectivo-difusivo 1D dependiente del tiempo, incluyendo el calentamiento por deformación y a la advección horizontal integrada en profundidad. La solución se expresa en términos de funciones hipergeométricas confluentes siguiendo un método de separación de variables. La adimensionalización reduce el espacio de parámetros a cuatro números que determinan completamente la forma de la solución en equilibrio: el aislamiento de la superficie, el flujo de calor geotérmico efectivo, el número de Peclét y el número de Brinkman. La distribución inicial de la temperatura converge exponencialmente a la solución estacionaria. Las escalas de tiempo de decaimiento transitorio sólo dependen del número de Peclét y del aislamiento superficial, de modo que mayores tasas de advección y menores valores de aislamiento implican escalas de tiempo de equilibrio más cortas, respectivamente.

El segundo estudio desarrolla el modelo de manto de hielo Nix v1.0. Nix es un modelo termomecánico 2D escrito en C/C++ que resuelve simultáneamente las ecuaciones de equilibrio de momento, conservación de la masa y evolución de la temperatura. Los resultados de esta tesis muestran que la histéresis en geometrías con un máximo local es similar para forzamientos atmosféricos y oceánicos. En particular, el bucle de histéresis clásico se ensancha para ambos escenarios de forzamiento si la viscosidad del hielo termomecánicamente activa.

El tercer estudio evalúa el papel desempeñado por diferentes formulaciones de fricción basal a la hora de reconstruir el LIS. Para ello, se utiliza el modelo de capa de hielo Yelmo para simular el LIS en condiciones límite LGM para una serie de formulaciones de fricción basal de complejidad variable. Se cuantifican explícitamente sus consecuencias sobre las corrientes de hielo de Laurentide, su configuración, extensión y volumen. El volumen total y la extensión del hielo alcanzan en general un valor de equilibrio constante que se

aproxima a las reconstrucciones anteriores del LIS. Las simulaciones muestran una gran sensibilidad a la dependencia del esfuerzo cortante basal de la velocidad de deslizamiento. En particular, una formulación de fricción de Coulomb regularizada parece ser la mejor opción en términos de volumen de hielo y realismo de la corriente de hielo. Se encuentran diferencias pronunciadas cuando el esfuerzo de fricción basal está acoplado termomecánicamente: la base permanece más fría y el volumen del LIS es menor que en la contrapartida del escenario de fricción puramente mecánica. El acoplamiento termomecánico es fundamental para producir una rápida corriente de hielo, pero conduce a una distribución general del hielo similar.

Por último, el cuarto estudio realiza un estudio exhaustivo sobre la plausibilidad de las oscilaciones internas de base física de la capa de hielo de Laurentide. Los experimentos muestran un estado de equilibrio oscilatorio de la corriente de hielo situada a lo largo del estrecho de Hudson cuyo periodo coincide con las hipotéticas descargas del LIS observadas en los núcleos de sedimentos oceánicos. Más concretamente, la corriente de hielo oscila entre dos modos de flujo de hielo: deslizamiento rápido sobre un suelo saturado y deslizamiento lento sobre un suelo completamente drenado. El periodo y la amplitud de la oscilación dependen en gran medida de la parametrización hidrológica y de las propiedades físicas del suelo. En particular, este fenómeno no parece depender de la resolución del modelo, lo que descarta una causa numérica del comportamiento oscilatorio. Cabe destacar que a lo largo de este estudio sólo se observan pequeños cambios en el LIS y en el volumen de hielo de la bahía de Hudson como consecuencia de la variabilidad temporal de la corriente de hielo.

Conclusiones generales

En conclusión, el comportamiento termomecánico del hielo es un aspecto fundamental para comprender tanto el pasado como el futuro de las grandes masas de hielo. Sin embargo, es poco conocido. El acoplamiento con otros elementos clave, como la hidrología glaciar y la dinámica del hielo, configura la complejidad de este problema. La fricción basal parece ser un componente crucial, del que se tienen escasos conocimientos, sobre todo en las reconstrucciones de capas de hielo del pasado con evidencias de activación periódica de

"ríos de hielo". Este trabajo desvela el potencial de una descripción analítica y explícitamente dependiente del tiempo de las temperaturas. Finalmente, el presente estudio demuestra cómo los modelos de baja dimensión proporcionan una herramienta extremadamente apropiada para comprender los mecanismos físicos básicos. Mediante una combinación equilibrada de avances analíticos y esfuerzos de modelización, esta tesis ha arrojado luz sobre el comportamiento termomecánico del LIS y la estabilidad marina general de los glaciares y ríos de hielo que finalizan en contacto con el océano.

Chapter 1
Introduction

This chapter introduces the Laurentide Ice Sheet (LIS) and discusses its role as the main contributor to sea level rise during the Last Glacial Maximum (LGM). First, a general review of the LIS is made, where the most prominent reconstructions available in the literature are compared in terms of methodology and results (Section 1.1). Then, Heinrich Events and their connection to the LIS is elaborated (Section 1.2), focusing both on proposed physical hypotheses, reconstructions and experimental measurements. Special focus is given to the long debate on the potential thermomechanical instabilities of the LIS and their overall impact on the LIS dynamics. Section 1.3 expands on the temperature behaviour within ice sheets from a theoretical perspective, including a thorough review of the approaches previously taken to analytically solve the associated heat problem and the usefulness of theoretical advances for numerical modelling. Section 1.4 stresses the importance of ice-sheet models and describes specifically their state of the art applied to grounding-line migration of marine-terminating glaciers. The subject of grounding-line stability has been long studied both from analytical and numerical approaches, where understanding the mechanisms governing ice-stream temporal variability remains as a major obstacle. Recent technical improvements, as well as limitations, and current major challenges are briefly described. Finally, the main motivations of this thesis are laid out (Section 1.5) and the overall structure of the work is outlined (Section 1.6).

1.1 The Laurentide Ice Sheet (LIS)

The Laurentide Ice Sheet (LIS; note that we use the term Laurentide Ice Sheet in the broadest sense including the Cordilleran and Innuitian ice sheets) was the largest of the former Northern Hemisphere ice sheets during the Last Glacial Maximum (LGM, ca. 21,000 years before present, 21 kyr ago) as shown in Fig. 1.1. The LIS is thought to have advanced to its maximum extent as early as 29–27 kyr ago, well before the LGM, and remained near that limit until 17 kyr ago (Dyke et al., 2002; Tarasov et al., 2012). Consequently, the LIS was the main contributor to sea-level change during the last glacial period, with an estimated sea-level equivalent (SLE) of about 70 metres (28×10^6 km^3) with respect to present (Peltier, 2004; Tarasov et al., 2012).

Great effort has been made to reconstruct the LIS at the LGM throughout the last five decades. Several approaches are found in the literature. The first numerical methods relied on simplified ice physics, a prescribed ice accumulation rate and ice surface temperature and the assumption that the ice sheet was in a steady state (e.g., Paterson, 1972; Sugden, 1977; Hughes et al., 1980). This assumption was later relaxed by Mahaffy (1976) and Jenssen (1977), though the former was applied to the Barnes Ice Cap (Canada) and not to the late glacial history of the entire LIS. A completely independent approach was taken by Clark (1980) based on an inversion study of sea-level data where none of the previous assumptions are applied. Compared to previous methods of reconstructing the LIS, the inversion approach only shares the ice extent with prior studies, which is, in general, well known. This further allowed for independent tests on the reliability of such assumptions by juxtaposing ice-sheet reconstructions.

Reconstructions of the size and distribution of the LIS based on forward ice-sheet modelling at the LGM have long dealt with the implications of a heterogeneous bedrock geology on the ice-sheet flow dynamics (e.g., Calov et al., 2002; Tarasov and Peltier, 2004). The central core of the LIS rests on the hard bedrock of the Canadian shield, whereas nearly the entire region of Hudson Bay and Hudson Strait consist of Paleozoic carbonates, which are easily eroded into a soft, slippery base (Lawley et al., 2024). In view of this configuration, two approaches were classically taken. First, a simplification of the bedrock complexity was made by ignoring this deformable bed, thus resulting in a single-domed reconstruction centred over Hudson Bay (Den-

ton, 1981). The second approach considered lubricated basal conditions by reducing the maximum basal shear stress in this region. Unlike the previous results, the reconstructions presented a multi-domed ice sheet with a thinner ice sheet and a less steep slope over Hudson Bay (Boulton et al., 1985; Fisher et al., 1985). This multi-domed configuration is also found in recent reconstructions (Tarasov et al., 2012; Gowan et al., 2021).

As a result of fundamental uncertainties underlying ice-sheet modelling of the LIS, its maximum elevation, extent and total volume differ largely among studies (Stokes, 2017). In particular, the total volume carries the greatest uncertainty. Originally, Ramsay (1931) estimated a total LIS volume of 45.45×10^6 km^3, with a 15.75×10^6 km^2 extent and a maximum elevation of 2.9 km (here, and subsequently, above present-day sea level). More than three decades later, Paterson (1972) provided a significantly lower volume estimation of 26.5×10^6 km^3 with 11.6×10^6 km^2 ice covered area and 2.7 km maximum ice thickness. The lowest overall volume estimate was given by Peltier (1994) (ICE-4G) with 19.0×10^6 km^3, whereas more recent studies yield 28×10^6 km^3 (Tarasov et al., 2012) and 35×10^6 km^3 (including the Cordilleran Ice Sheet, Gregoire et al., 2012).

Already noted by Clark (1980), the LIS may have never attained a steady state, and it was possibly a rather dynamic system with rapid variations of its southern margin as well as a variable Hudson Bay ice thickness. Nevertheless, the representation of these ice streams in numerical ice-sheet models remains challenging. As a result, we lack a deeper comprehension of the role of ice streams which leads to larger model output uncertainties.

The reconstruction of paleo ice streams is typically based on two methods. The first one rests on the assumption that the subglacial imprint of streaming and non-streaming areas is distinct (e.g., Kleman et al., 1997; Stokes and Clark, 1999) and consists of gathering enough evidence from landforms and sediments so as to reconstruct the ice dynamics that produced them (e.g., Winsborrow et al., 2004; Ottesen et al., 2005). The second one is, again, based on forward ice-sheet modelling using numerical models capable of simulating ice streaming (e.g., Boulton and Hagdorn, 2006). This capability is usually provided by thermomechanical feedbacks in topographic troughs and parametrizations of ice-bed coupling strength over soft sediments (Marshall et al., 1996a).

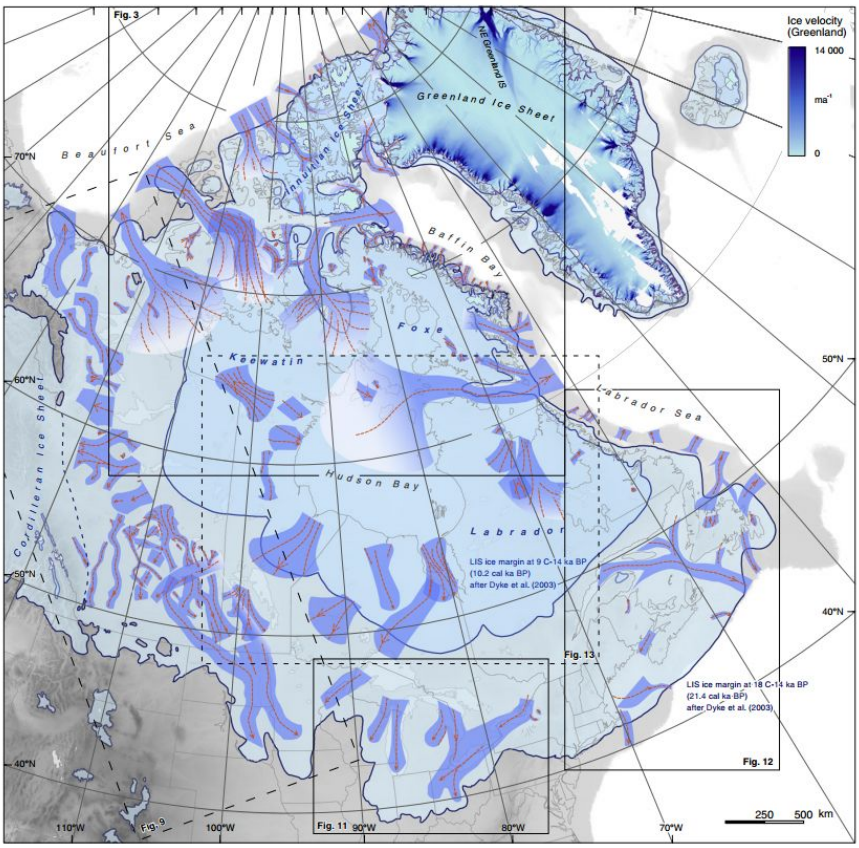

Fig. 1.1: Laurentide Ice Sheet extent for the Last Glacial Maximum from (Margold et al., 2015) and at 10.2 kyr BP, from Dyke et al. (2003). Ice streams of the Laurentide Ice Sheet drawn after Margold et al. (2014). Present-day glaciation is shown in light turquoise with a thin purple line denoting ice margins. The Greenland Ice Sheet contains ice flow velocities from Joughin (2015). Data coverage is incomplete and missing data is shown in white.

1.2 Connection to Heinrich Events (HE)

It is well known that North Atlantic sediment cores contain quasi-periodic layers with extremely high amounts of lithic fragments generally regarded to fall within six short time intervals during the last glacial period (Heinrich, 1988; Hemming, 2004). Our current explanation for the presence of such layers considers that Hudson Bay sediments were captured by the ice (Meyer et al., 2019), discharged from Hudson Strait ice stream as icebergs into the

North Atlantic, and eventually unloaded onto the seafloor when the enclosing ice melted. In other words, Heinrich layers are ice-rafted debris (IRD). The active ice-stream period and the resultant IRD layers are known as Heinrich Events (HEs).

The ultimate physical explanation underlying any oscillatory mechanism that causes the HEs, however, is still under debate. In fact, whether the cause is even unique still remains as an open question (Roberts et al., 2016). There are three key observations that must be explained by any theory that attempts to provide an answer: a roughly 7-kyr periodicity (Hemming, 2004), the presence of IRD layers in sediment cores taken from the North Atlantic (formed on short timescales), and the spatial source of such debris as traced from geological evidence. In fact, such evidence narrowed the spatial uncertainty to Hudson Strait (e.g., Naafs et al., 2013) and the sediments are thought to be transported due to oceanic circulation, thus turning a periodic surge from Hudson Strait into a necessary condition.

MacAyeal (1993a) proposed a mechanism by which Hudson Bay would periodically switch from a quiescent to a surging state (controlling the flux of ice through Hudson Strait ice stream) and further tested his theoretical prediction with a simple model (MacAyeal, 1993b). Later, Payne (1995a) and Marshall and Clarke (1997) also noted internal instabilities as self-sufficient mechanisms to trigger a periodic collapse of the Laurentide Ice Sheet (LIS). In fact, the LIS ice-mass loss is intimately related to a variable Hudson Bay ice thickness through rapidly-flowing ice streams that account for most of the ice-sheet discharge (Stokes and Tarasov, 2010).

The so-called "binge-purge" mechanism proposed by MacAyeal (1993a) consists of two phases (see Fig. 1.2). First, a growth ("binge") phase occurs when the ice sheet rests on frozen sediments forming a rigid bed, preventing sliding and increasing thickness due to accumulation. This yields an insulating effect over the base since temperature oscillations at the surface are strongly attenuated and phase shifted with increasing depth below the surface, thus enhancing basal melt. Second, during the purge, the thawing of unconsolidated basal sediments over Hudson Strait (solely due to the geothermal heat flow) serves as a lubricant that allows for sliding. Consequently, rapid streaming is enhanced and the LIS volume quickly adjusts to this sudden decrease in the basal friction by iceberg calving into the Labrador Sea. Further studies of notably higher complexity regarding ice dynamics and geometry have also

investigated the "binge-purge" mechanism (Calov et al., 2002; Roberts et al., 2014, 2016). These studies exhibit varying complexity, though they share a stress balance given by the SIA and a prescribed sliding from a purely geometrically controlled basal drag that is not physically adequate, additionally affecting the thermal conditions at the ice base.

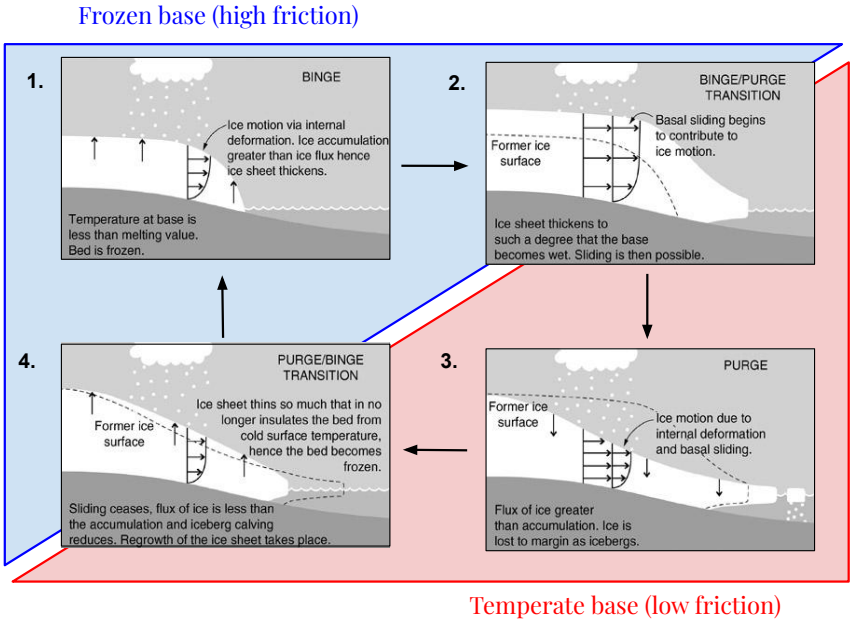

Fig. 1.2: Binge-purge oscillator proposed by MacAyeal (1993a) (adapted from Siegert, 2009). First, a growth ("binge") phase occurs when the ice sheet rests on frozen sediments forming a rigid bed, preventing sliding and increasing thickness due to accumulation (1). This yields an insulating effect over the base since temperature oscillations at the surface are strongly attenuated and phase shifted with increasing depth below the surface, thus enhancing basal melt (2). Then, during the "purge", the thawing of unconsolidated basal sediments over Hudson Strait serves as a lubricant that allows for sliding and enhances iceberg calving (3). Lastly, at the end of the purge stage, heat is lost as the insulating effect is reduced and colder ice is advected downstream, eventually refreezing the base (4).

An alternative to internal oscillations of the LIS to explain HEs is an externally-driven response of the LIS (Hulbe, 1997; Hulbe et al., 2004; Moros

et al., 2002; Hulbe et al., 2004; Alvarez-Solas et al., 2013; Bassis et al., 2017). MacAyeal (1993a), Marshall and Clarke (1997) and Payne (1995a) proposed internal instabilities as self-sufficient mechanisms to trigger a periodic collapse of the Laurentide Ice Sheet (LIS), whereas evidence for a discharging ice-dammed lake in Hudson Bay (Johnson and Lauritzen, 1995) and a collapse of an ice shelf in Davis Strait (Hulbe, 1997; Hulbe et al., 2004) supports the latter.

Meyer et al. (2019) noted that the atmosphere seems meagre to provide a driving force for such events even though there is a remarkable accordance between HEs periodicity and relatively cold temperatures in the Northern Hemisphere (yet not clearly connected with Daansgaard-Oescher events). Originally, iceberg discharges during HEs were thought to cause an AMOC collapse as suggested by low salinity and low δ^{13}C records (Alley et al., 1999), thus leading to stadial conditions. In other words, freshwater fluxes were commonly interpreted as the cause of shift into cold conditions (i.e., stadial). By contrast, a later study showed a systematic lag whereby the arrival of IRD appears to be 200 $\pm$ 110 years after an abrupt cooling event (van Kreveld et al., 2000). This led to the hypothesis that iceberg discharges may be the consequence of stadial conditions rather than the cause. More recently, this hypothesis has been supported by a systematic delay between the pronounced surface cooling and the arrival of IRD at a site southwest of Iceland over the past four glacial cycles (Barker et al., 2015). In view of this result, the authors describe the abrupt transitions to stadial conditions as a nonlinear response to a more gradual cooling across the North Atlantic, but not as the response of the iceberg discharges.

On the other hand, changes in the Atlantic Ocean overturning circulation do correlate with the timing of HEs (Alvarez-Solas et al., 2010, 2011, 2013) and may yield periodic discharges by isostatic adjustment (Bassis et al., 2017) or by ice-shelf break-up (Hulbe et al., 2004; Marcott et al., 2011). The former is in fact relevant at millennial timescales given that the ice-sheet retreat continues until the bedrock rise isolates the oceanic forcing. In addition, the buttressing effect yielded by the ice shelves must be considered since it inhibits the surging of coastal grounded ice streams (Alvarez-Solas et al., 2010). In reality, the frequency in the oceanic forcing differs from that of the surging events. No discharge takes place unless the ice shelf falls below a threshold extent (even if the basal melting reaches its maximum several

times). Therefore, the ice sheet continues growing until the ice shelf is unable to provide enough buttressing at the grounding line. Hence, the onset of an event is determined by a sudden acceleration of the grounding line due to a drastic decrease in the exerted buttressing force.

Despite the fact that evidence clearly supports an external forcing as the driver of HEs, the question as to whether an ice sheet can show internal oscillations has gathered substantial attention in the last decades. Interestingly, Feldmann and Levermann (2017) found that, in agreement with the existence of a critical minimum ice thickness (Schubert and Yuen, 1982), an oscillatory equilibrium can be maintained for a medium-sized thickness ice sheet. Strictly speaking, when the ice thickness sustained by the basal conditions is lower than the equilibrium value reached during the buildup, an abrupt surge event takes place. Moreover, their results showed that complex boundary conditions (spatially varying surface temperature and accumulation as employed by Pelt and Oerlemans, 2012) are not necessary to obtain cyclic surging.

Long debate has been held on thermomechanical instabilities, yet the physics that would lead to large-scale oscillatory phenomena are far from being understood. Conceptually, a strong case can be made for oscillatory phenomena arising based on the physics. However, a major issue with ice-internal mechanisms is the role played by parametrizations and discretization as well as the way basal hydrology is captured in these models. Although surges are present even in simple models, it is difficult to determine whether these oscillations are just the result of numerical approximations (Bueler and Brown, 2009; Roberts et al., 2016). For example, the extent of simulated ice streaming is strongly dependent on resolution for shallow-ice models and any specific implementation of the discrete model may lead to non-physical streaming. Moreover, the question itself of whether thermomechanical instabilities can arise in reality is still debatable, given that certain studies using higher complexity models do not show internal oscillations (e.g., Alvarez-Solas et al., 2011; Moreno-Parada et al., 2023a).

The physical realism of internal oscillations (as opposed to a purely numerical issue) was considered by Calov et al. (2010) in an idealised experimental setup with a set of nine different ice-sheet models. One of them was a hybrid ice-sheet model, while the remaining eight models were based on the SIA only. Oscillations with periodicities between 5-17 kyr were found for a

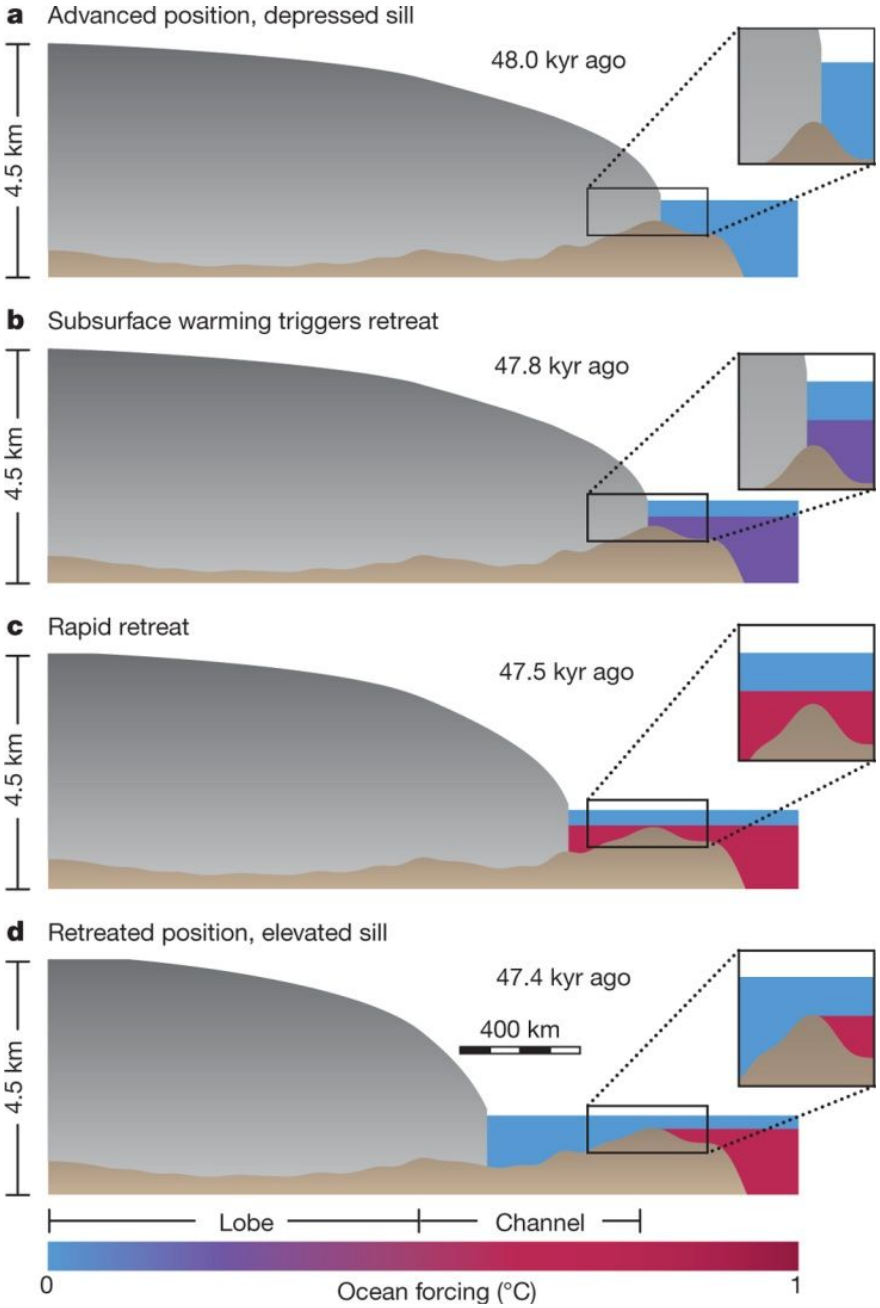

Fig. 1.3: Stages of the proposed Heinrich event mechanism (from Bassis et al., 2017). First, from an extended position (a), subsurface warming triggers the ice sheet retreat (b), further intensified by the new terminus position in deeper water (c). The ice-sheet thickness reduction yields an isostatic adjustment that uplifts the bedrock, thus isolating the grounding line from warm subsurface water and eventually allowing for ice-sheet advance (d).

broad range of parameters in all models, including the hybrid model. Low surface temperatures, low accumulation rates and high sliding velocities over sediment were found to favour oscillatory surges. In the case of the hybrid model, the recurrence time of the oscillations was above 10 kyr.

Cyclic behaviour has also been reported more recently using a state-of-the-art hybrid model by Pelt and Oerlemans (2012) and Feldmann and Levermann (2017). The latter established a competing internal feedback mechanism regarding two different timescales. A negative feedback loop among ice thickness, basal friction and till water takes place on the slow timescale (buildup), whereas a positive loop is found between the basal friction, till water and the ice velocity on the fast timescale (surge) as shown in Fig. 1.4. Lastly, the associated large-scale ice discharge during the surge leads to stabilisation due to a diminishing ice thickness. Nevertheless, important limitations are found in these studies, such as a strongly idealised domain and bed geometry.

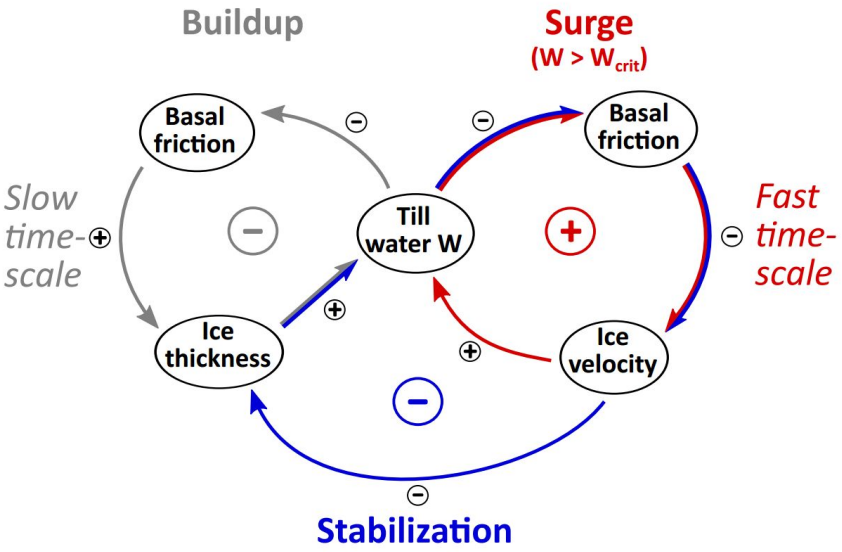

Fig. 1.4: Schematic visualization of the main internal feedback mechanism that dictate the binge-purge cycle (Feldmann and Levermann, 2017). Each colour correspond to a subsequent phase forming a full surge cycle. The sign indicates whther a positive perturbationin variable A leads to an increase (+) or decrease (−) in variable B.

More recently, Ziemen et al. (2019) also showed instabilities in simulations using a comprehensive, fully coupled ice sheet-climate model. The ice dynamics considers a linear friction parametrization that does not account for cavitation effects (Joughin et al., 2019). Instead, an empirically demonstrated (Tulaczyk et al., 2000a) regularised coulomb behaviour fairly reproduces reality irrespective of the till strength (Joughin et al., 2019). Thus, the plausibility of internal LIS instabilities in a hybrid model has not been investigated in depth, except in the aforementioned studies by Calov et al. (2010) and Alvarez-Solas et al. (2013), and these yielded conflicting results.

Finally, as noted by Bueler and Brown (2009), to achieve physical authenticity sliding must account for both the till strength and basal water content. Additionally, Brocq et al. (2009) showed an intimate connection between water depth and sliding speed, displaying the relevance of basal water during the onset of HEs. In early studies, the thermodynamic switch mechanism that allows for oscillatory behaviour often depended on the temperature alone. Indeed, the assumption that the ice starts to slide when the pressure melting point is reached irrespective of the amount of water is likely incorrect, as noted by Roberts et al. (2016). Yet it is unclear how hydrology affects dynamics in such a way as to allow for oscillations within a broader range of parameters. In fact, Roberts et al. (2016) solved for the SIA alone and then, sliding is included with a tunable parameter that modulates the transition between creeping and sliding as a smooth function of the water depth (similarly to the purely geometrically controlled basal drag in (Calov et al., 2010)). Even though oscillations are found for a broad range of values, their results warrant reassessment using a model that neither requires this parameter nor solely employs a linear friction law.

Several approaches have been considered to simulate the presence of liquid water underneath an ice sheet, i.e. the representation of subglacial hydrology. Two common features are found among them: a conserved mass of water and a hydraulic potential that determines the water flow. Any variation of further complexity is fundamentally based on these two elements. For instance, regarding hydraulic mobility, liquid water can be considered to be stored in a porous till (Tulaczyk et al., 2000a) or transported in a macro-porous englacial system (Bartholomaus et al., 2011). Remarkably, considering the basal water content even for the simplest conceivable spatial ice stream model (a single

lumped element) is sufficient to find two major modes of ice stream behaviour Robel et al. (2013). Namely, steady-streaming and binge-punge variability.

Multiple combinations of the aforementioned morphologies are considered in the literature (Flowers and Clarke, 2002; Hewitt, 2013; Hoffman and Price, 2014; van der Wel et al., 2013; Werder et al., 2013; de Fleurian et al., 2016) where attainable observations and the uncertain model parameters determine the completeness of the modelled processes. Notably, Bueler and van Pelt (2015) developed an extension of the "undrained" plastic model of Tulaczyk et al. (2000b) by accounting for an additional distributed system of linked subglacial cavities that ensures mass conservation.

If the link between ice dynamics and basal hydrology is then considered by following the effective pressure formulation of Bueler and van Pelt (2015), three explicit additional degrees of freedom naturally arise: till compressibility, the minimum allowed effective pressure and maximum basal water content. It is thus clear that the representation of the consolidation state noted by Tulaczyk et al. (2000a) is crucial, since the till saturation is highly sensitive to compressibility. Then, an appropriate parameter choice appears to be essential to simulating sliding with physical authenticity. Even so, there is an important gap in our understanding as to how a potential internal oscillatory phenomenon in the ice sheet is altered by the physical properties of the till.

1.3 Temperature in large ice masses

The former discussion stresses the fact that the study of ice thermodynamics is of crucial importance for understanding the behaviour of glaciers, ice sheets and ice shelves, as their evolution is strongly dependent on the physical properties of the ice. Even more importantly, thermomechanical instabilities arise from the assumption that there exists a transition from a quiescent to a surging state dictated by the thermal state of the ice base. The periodic switch between these stages form the relaxation oscillator proposed by MacAyeal (1993a).

Ice thermodynamics is the result of a complex interplay between advection, diffusion and various heat sources. Only an accurate representation of these processes will allow for a robust description of ice flow, mass balance and

overall stability. In this context, the development of analytical solutions for ice thermodynamics can provide a deeper comprehension of the fundamental physics of ice, as they are intuitively interpretable, reveal hidden symmetries and further serve as a verification tool of numerical models.

Robin (1955) and Lliboutry (1963) first laid the groundwork for understanding ice-column thermodynamics in the presence of vertical advection and diffusion by providing analytical solutions for stationary scenarios. These seminal works offered valuable insights into the steady-state behaviour of ice columns subject to advective-diffusive processes. Nevertheless, they did not consider the time-dependent evolution of ice temperatures. Hence, their applicability was limited to situations involving steady-state ice flow and fixed environmental conditions.

In a broader context, the 1D advective-diffusive equation has been thoroughly studied in a wide range of fields, particularly in dispersion problems. In early studies, the basic approach was to reduce the advection-diffusion equation to a purely diffusive problem by eliminating the advective terms. This was achieved via a moving coordinate system (e.g., Ogata and Banks, 1961; Harleman and Rumer, 1963; Bear, 1975; Guvanasen and Volker, 1983; Aral and Liao, 1996; Marshall et al., 1996b) or through the introduction of another dependent variable (e.g., Banks and Ali, 1964; Ogata, 1970; Lai and Jurinak, 1971; Marino, 1974; Al-Niami and Rushton, 1977). To solve the equations, quite diverse mathematical methods are employed, such as the Laplace transformation (McLachlan, 2014), the Hankel transform (Debnath and Bhatta, 2014), the Aris moment method (Merks et al., 2002), Green's function (Evans, 2010) or superposition approaches (Lie and Scheffers, 1893) among others. More recent studies (e.g., Selvadurai, 2004) provide time-dependent analytical solutions for which Darcy flow is applicable, yet they lack an appropriate set of boundary conditions given the infinite length of the domain.

Steady-state ice temperature distribution studies also provide analytical solutions in bounded spatial domains, but fall short if the transient nature of the solution is to be captured. This is the case of the studies on the shear heating margins of West Antarctic ice streams (e.g., Perol and Rice, 2011, 2015) for which a steady but more refined one-dimensional thermal model was produced, first introduced by Zotikov (1986). Meyer and Minchew (2018) later solved a similar advective-diffusive problem under stationary conditions

accounting for a constant strain-heating rate and further neglecting lateral (horizontal) advection after a scaling analysis. These one-dimensional studies imposed a stationary nature of the temperature distribution, thus assuming an idealised equilibrated energy state.

Despite these simplifications, heat transfer is well-known to be a three-dimensional process with a higher level of complexity that encompasses several mechanisms such as horizontal and vertical advection, the potential presence of liquid water within the ice, a varying ice thickness, internal heat deformation and frictional heat production among others (e.g., Greve and Blatter, 2009; Cuffey and Paterson, 2010). Full numerical models are therefore also essential if a simultaneous consideration of such mechanisms needs to be achieved (Winkelmann et al., 2011; Pattyn, 2017).

However, numerical models require caution as their accuracy and consistency must be previously assessed. Intercomparison projects are thus fundamental since they can provide consensus in a series of benchmark experiments that further serve as a reference solution for validation. In this context, analytical descriptions are extremely useful as they provide a control irrespective of the resolution or discretisation schemes. For instance, Huybrechts and Payne (1996) already noted the lack of analytical temperature solutions for such cases. Previously obtained solutions relied on strong assumptions regarding the particular vertical velocity profile (linear profile, Robin 1955; quadratic, Raymond 1983) and therefore an independent analytical description of the temperatures was not available.

More recently, Rezvanbehbahani et al. (2019) proposed an improved temperature solution that considers a power-law vertical velocity profile derived from the Shallow Ice Approximation. The authors showed the importance of the strain heating term and demonstrated that including it as an additional basal heat source yields good results for the interior regions of an ice sheet. Nevertheless, horizontal advection is absent in their analytical solutions and a further comparison with numerical solutions reveals that their analytical results are only applicable to slowly moving regions (mostly below 20 m/yr). As with prior studies, steady-state conditions are also assumed and thus no information about the time evolution of ice temperatures can be obtained.

Traditional approaches both from numerical and analytical perspectives assume the simplest heat-flux boundary condition at the ice surface: the imposition of the air temperature at the uppermost ice layer. Knowing that

glacial ice forms through snow densification, this imposition appears to be an oversimplification, given that thermal conductivity increases with density (e.g., Sturm et al., 2002; Calonne et al., 2011, 2019). Therefore, in view of the surface fraction of the Greenland and Antarctic Ice Sheets covered by a firn layer (90% and ∼100%, respectively, Medley et al., 2022; Noël et al., 2022), a more sophisticated description of the energy balance between the ice and the atmosphere may be beneficial. Already noted by Carslaw and Jaeger (1988), prescribing a fixed temperature is in fact a limit case of a broader set of boundary conditions known as 'linear heat transfer' or 'Newton's law of cooling' that accounts for a more realistic heat flux across the interface given by the temperature difference between the two media.

Ice temperatures are not only critical to understand the dynamics and an ice body's evolution in time, but also in ice-sheet initialisation of numerical models. Poorly known parameter fields such as the ice temperature are estimated minimising the mismatch between observations and model output variables. Traditional approaches compute a steady-state temperature field, incorrectly assuming that the ice is at thermal equilibrium (e.g., Morlighem et al., 2010, 2011; Pralong and Gudmundsson, 2011; Perego et al., 2014). This issue can be mitigated via transient optimisation approaches that incorporate available data that accounts for the transient nature of observations and the model dynamics (e.g., Goldberg et al., 2015), though this method is significantly more expensive. Nonetheless, time integration with transient optimisation that includes all relevant model processes is not feasible for high-resolution, large-scale ice sheet models. As a result, a time-dependent description of ice temperatures would strongly reduce the computational demands in modelling exercises.

A literature review thus exhibits the need for a time-dependent analytical description, in spite of the inevitable compromise of designing a model that is both mathematically solvable and accurate. It is thus of utmost importance to carefully navigate this trade-off, deciding the appropriate level of analytical tractability and physical realism based on the specific goals of the study. Attaining the right balance allows for meaningful insights, while avoiding excessive computational demands or oversimplification that may hinder accurate representation and understanding of the real-world system.

1.4 Numerical modelling of ice sheets

Models are used to predict and understand the underlying mechanisms of complex processes. They simulate, through mathematical formulations, simplified representations of reality. Because the Earth System encompasses land, ocean, atmosphere, biosphere and ice sheets, it is complicated to account for all the involved natural processes and it is necessary to use such tools. Whereas the first scientific Earth models used rather simple parameterisations, technical improvements, as well as a more profound understanding of the fundamental physics and gradually increasing computational power, have greatly advanced the state of the art.

Ice-sheet models are no exception, but they were developed later than other climatic models. However, ice-sheet models are necessary building blocks to study and understand the past, present and future evolution of ice sheets to climatic changes. Initially, ice models were conceptual two-dimensional flow models used for dating ice cores (i.e., Dansgaard and Johnsen, 1969). Nowadays, there is a large variety of sophisticated ice-sheet models which account for three-dimensional representations, thermo-mechanical coupling and increased spatial resolution among other technical advances (i.e. Gagliardini and Zwinger 2008; Lipscomb et al. 2019; Winkelmann et al. 2011; Cornford et al. 2013; Pattyn 2017; Quiquet et al. 2018).

In the context of this thesis, numerical ice-sheet models will be particularly employed to comprehend the thermomechanical coupling effect on the grounding line migration and the overall stability of an ice sheet. Information about the real world is in fact not only obtained from spatially explicit models and simpler 2D models also facilitate the investigation of the relevance of specific processes. It is often hard to discern the particular physical mechanism underlying certain behaviours for highly sophisticated 3D models, as the strong coupling among elements becomes an obstacle to isolate hypothesised causes. For this reason, 2D models are an extremely convenient tool to investigate the physical behaviour of ice sheets both from a theoretical (e.g., Weertman, 1974; Hindmarsh, 1993a; Chugunov and Wilchinsky, 1996; Hindmarsh, 1996; Schoof, 2005, 2006b, 2007a,b, 2011) and a modelling perspective.

It is illustrative to show the practical use of such a 2D setup as it provides insight into the behaviour of realistic ice sheets. Hindmarsh and le Meur

(2001) assessed the dynamic processes involved in the retreat of marine ice sheets, with a particular interest in the WAIS the Last Glacial Maximum. Haseloff and Sergienko (2018) later considered the effect of buttressing on grounding-line dynamics, thus corroborating the findings of existing numerical studies that the stability of confined marine ice sheets is influenced by ice-shelf properties. Other 2D ice-sheet models additionally employ real bedrock geometry sections. This is the case of Pattyn et al. (2006), who studied the role of transition zones in marine ice-sheet dynamics, and Jamieson et al. (2012), where ice-stream stability was investigated on a reverse bed slope. The realism of the 2D setup can even account for glacial isostatic adjustment. To illustrate this, Payne (1995b) studied limit cycles in the basal thermal regime of ice sheets considering a constant diffusivity of the asthenosphere. More recently, Bassis et al. (2017) investigated how Heinrich events are triggered by ocean forcing and modulated by isostatic adjustment. Even though ice shelves are not explicitly resolved in 2D models, the potential role of buttressing can also be considered via a parametrisation (e.g., Dupont and Alley, 2005; Schoof, 2007a; Jamieson et al., 2012; Robel et al., 2014, 2019).

An accurate numerical description of the grounding line is thus fundamental for the reliability of such projections. A number of attempts have been made in the past to simulate grounding-line migration within marine ice-sheet models. Weertman (1974) and Thomas and Bentley (1978) proposed that no stable steady states of the grounding line could be found on inland-sloping or retrograde beds. Hindmarsh (1993b) later introduced the possibility of neutral equilibrium under the premise that the equilibirium position is continuous and hence there exists an infinite number of equilibrium configurations. More recently, Vieli and Payne (2005) assessed the influence of numerical details and discretization on the dynamics of the grounding line, concluding that a reliable method of treating grounding-line migration within numerical ice-sheet models was unknown. Later studies confirmed the possibility of numerical artefacts (Pattyn et al., 2006; Hindmarsh, 2006; Schoof, 2006a,b, 2011), in agreement with the early works of Weertman (1974) and Thomas and Bentley (1978). Even so, Vieli and Payne (2005) and Pattyn et al. (2006) hypothesised the possibility of "neutral equilibrium", first introduced by Hindmarsh (1993b). The analytical approach of Schoof (2007a) based on assymptotic expansions eventually concluded that these results were numerical artefact appearing for certain parameter regimes. Only in the ab-

sence of basal sliding has the possibility of non-unique steady states been raised (Nowicki and Wingham, 2008).

Amidst the lack of a reliable model of grounding-line migration, the first Marine Ice Sheet Intercomparison Project (MISMIP, Pattyn et al., 2012) shed light on the agreement of modelling efforts to describe the grounding-line motion and assessed the appropriateness of numerical schemes. The authors proposed a set of benchmark experiments on an idealised two dimensional bed geometry, concluding that moving grid models are the most reliable choice from a numerical perspective as the grounding line is part of the solution and no interpolations are required. The comparison between numerical models and exact semi-analytical solutions was possible since MacAyeal and Barcilon (1988) had notably showed that a two-dimensional free-floating shelf has no effect on the dynamics of the grounded ice upstream of it (later underlined by Schoof, 2007a). Hence, a boundary condition can be directly imposed at the grounding line that is solely dependent on the ice thickness therein, irrespective of the particular shape or the dynamics of the shelf. A correct description of a 2D marine ice sheet thus relies on an appropriate formulation of the grounded ice dynamics, specially near the terminus position where ice streaming is generally found.

Additional numerical efforts showed the possibility of stable grounding-lines on reversed-bed slopes solutions if two horizontal dimensions are instead considered (Gudmundsson et al., 2012). More recently, Haseloff and Sergienko (2018) analytical advances of the ice flux at the grounding line elucidated the dependency on both local bed properties and non-local ice shelf properties. As a result, the stability of confined marine ice sheets is influenced by ice-shelf properties and the MISI hypothesis may not apply to buttressed marine ice sheets. Other potential stabilizing mechanisms on reversed bed slopes have been also explored, such as gravity and deformation-induced sea-level changes (e.g., Gomez et al., 2010, 2012).

For a comparison with the semi-analytical solutions of Schoof (2007a), ice streaming (i.e., fast flowing ice due to basal sliding) becomes a necessary condition given that the boundary layer theory assumes rapid sliding near the grounding line. Ice streams are in fact a distinct feature of ice sheets with no counterpart in other geophysical thin-film flows. These regions of rapidly flowing ice exhibit velocities even three orders of magnitude faster than the usual glacial ice, yet they only account for a small fraction of the total ice-

sheet area (e.g., less than 5% of the Antarctic ice sheet; Bamber et al., 2000). Even so, it is important to represent them correctly to evaluate ice outflow discharge, ice-sheet sensitivity and overall stability.

The rapid flow of ice streams fails to be explained by vertical shearing of ice. In other words, friction at the bed is typically smaller than the driving stress predicted by a lubrication approximation (Whillans and van der Veen, 1997; Joughin et al., 2004). Rather, high ice-stream velocities are caused by the deformation of meltwater-saturated, weak subglacial till (Alley et al., 1986; Blankenship et al., 1986; Engelhardt et al., 1990), thus consistent with geophysical studies showing that basal sliding is fundamentally a sort of Coulomb slip connected with the mechanical failure of plastic till (e.g., Tulaczyk, 1999).

Schoof (2006b) later extended the work to depth-integrated viscous flows used in three-dimensional ice-sheet models. Namely, a variational formulation of the two-dimensional Shallow Shelf Approximation (SSA) equations is given without assumptions on the extension of the sliding domain. In fact, as noted by the author, sliding regions must be determined as part of the solution and are consequently not known *a priori*. Notably, a solvability condition was also derived (as in Schoof, 2006b) to guarantee the existence of physical solutions. Strictly speaking, if the till is too weak so that the total momentum of applied forces is greater than the maximum momentum of frictional force about a given point, then no solutions are expected to exist.

A variational formulation entails strong consequences both from a physical and a mathematical point of view. Particularly, it eludes explicit manipulation of the unknown sliding domain extension, additionally provides a numerical method for solving the ice flow problem and it ensures well-posedness of the SSA non-linear elliptic equations since they can be derived from a convex and bounded below functional (Schoof, 2006b). However, the time-evolving system of the SSA stress balance coupled to the advection equation is not yet known to be mathematically well posed (Bueler and Brown, 2009).

More recently, Goldberg (2011) derived a higher-order stress approximation using variational methods with similar accuracy to the Blatter-Pattyn momentum equations (Blatter, 1995; Pattyn, 2003), though differences are particularly notable for resolutions below 20 km. The velocity solver was first adapted for multimillenial 3D ice-sheet models CISM (Lipscomb et al., 2019), where this depth-integrated velocity approximation was referred to as DIVA.

Nevertheless, the DIVA solver had been previously used in continental scale models by Arthern et al. (2015) and Arthern and Williams (2017). The numerical stability of this solver was systematically studied by Robinson et al. (2022), who show that the DIVA solver outperformed the remaining solvers in terms of both model performance and the representation of the ice-flow physics itself.

The appropriate stress balance treatment is merely one of the challenges of ice streaming and grounding-line stability. Understanding the mechanisms governing its temporal variability also remains as a major obstacle, particularly at the aim of developing models of ice-sheet dynamics (Robel et al., 2013). Given the broad range of ice-flow speeds observed in real ice sheets (e.g., Shepherd and Wingham, 2007; Truffer and Fahnestock, 2007; Vaughan and Arthern, 2007), numerical simulations of these rapidly flowing bands are a well-known difficulty, partially due to the fact that fast grounded ice flow is a combination of sliding over a hard/soft bed and shear deformation of the basal. Moreover, ice high-quality spatially distributed observations of near-base conditions are rare and constraining models becomes challenging (Bueler and Brown, 2009). Various modelling approaches have been considered to correctly describe the large complexity of ice-stream dynamics. Tulaczyk et al. (2000a) found that subglacial hydrology yields multiple modes of ice stream flow in a highly reduced model. Parameterizations of observed small-scale phenomena (e.g., drainage networks) were later considered by coupling a flow-band model and a simple hydrological model (Bougamont et al., 2003; Bougamont and Tulaczyk, 2003). Another flow-band model was employed by van der Wel et al. (2013), additionally introducing a dynamic drainage model.

1.5 Motivation

The physical basis for the oscillatory mechanism causing HEs is still a subject of debate. Certainly, whether there is a singular cause still remains as an open question (Roberts et al., 2016). There are three key observations that must be explained by any theory that attempts to provide an answer: a roughly 7-kyr periodicity (Hemming, 2004), the presence of IRD layers in sediment

cores taken from the North Atlantic (formed on short timescales) and the spatial source of such debris as traced from geological evidence.

Suggested hypotheses behind the cause of HEs can be classified according to the nature of the driving mechanism that triggers such events: internal or external. This thesis focuses on the former, first proposed by MacAyeal (1993a) where Hudson Bay would periodically switch from a quiescent to a surging state. This switch simply occurs due to the transition between a high-friction state in frozen basal conditions (binge) and a low-friction state if the base is thawed (purge). The so-called "binge-purge"1 mechanism thus depends on the thermal state of the base, which is inevitably coupled with the overlying ice. Therefore, an accurate description of ice temperatures and basal friction is necessary to understand this thermomechanical instability hypothesis (i.e., the "binge-purge" oscillator) as a potential cause of HEs (MacAyeal, 1993a; Payne, 1995b).

The following scientific questions will be addressed:

Can we obtain a time-dependent analytical description of the ice-sheet temperature?

There is a clear gap in our theoretical understanding of how ice temperatures evolve in time, a fundamental piece to correctly describe potential thermomechanical instabilities. Given the extremely high mathematical complexity of the problem, a limited number of analytical solutions for the associated heat problem are available in the literature.

Robin (1955) and Lliboutry (1963) first laid the groundwork for understanding ice-column thermodynamics in the presence of vertical advection by providing analytical solutions for the stationary cases. Nevertheless, these solutions relied on strong assumptions regarding the particular vertical velocity profile: linear (Robin, 1955) and quadratic (Raymond, 1983). Hence, their applicability was limited to situations involving steady-state ice flow and idealised vertical velocity conditions. Similarly, studies on the shear heating margins of West Antarctic ice streams (e.g., Perol and Rice, 2011, 2015) for which a steady but more refined one-dimensional thermal model was produced, first introduced by Zotikov (1986). Meyer and Minchew (2018) later solved a similar advective-diffusive problem under stationary conditions

accounting for a constant strain-heating rate and further neglecting lateral (horizontal) advection after a scaling analysis. These one-dimensional studies imposed a stationary nature of the temperature distribution, thus assuming an idealised equilibrated energy state.

Despite all the effort in previous works, there is still a gap in the understanding of the analytical nature of time-dependent ice temperatures. As a result, there are no available benchmark experiments to test numerical solvers extensively employed in ice-sheet models. The current study presents an analytical formulation of the transient ice temperature equation and provides useful insight in two ways. First, allowing for a simplified way of deriving physical insight into the physics of heat transfer in ice (as demonstrated by an equilibrium timescales analysis) and secondly, by providing a way of benchmarking numerical solvers for heat transfer.

How does thermomechanical coupling affect the grounding line migration and the overall stability of an ice sheet?

Despite the extensive research on the topic, important questions regarding the particular effect of thermodynamics remain unanswered. Specifically, whether marine ice sheets have discrete steady surface profiles if ice temperatures can freely evolve in time and further the potential implications on the hysteresis behaviour in overdeepened bed geometries. In ice streaming regions, ice flow occurs mostly along one main direction, thus becoming the preferred axis across which lateral variations are negligible. It is a common approach to reduce the number of horizontal dimensions to the main flow direction so as to minimise computing time. Nonetheless, the thermal state of the ice and the potential oceanic forcing are still fundamental pieces to understanding the future evolution of ice sheets that have not been considered in low-dimensional models.

This work aims to close these gaps by building Nix: a 2D thermomechanically-coupled ice-sheet model. From a hierarchy of approximations to the full Stokes problem, combined with an explicit computation of the time-dependent heat

problem, is necessary to assess the role of the thermal coupling in the grounding line position and the general stability of an ice sheet.

What are the implications of different basal friction formulations to simulate the LIS?

Despite the comprehensive work carried out in the last decades, none of the past studies addressed the repercussions of different basal friction formulations when simulating the LIS during the LGM nor their explicit implications in ice extent, volume and ice-stream representation. In fact, recent studies have also shown significant consequences of this uncertainty for the Antarctic Ice Sheet (e.g., Blasco et al., 2021). In addition, some authors (e.g., MacAyeal, 1993a) have also proposed a mechanism by which Hudson Bay would periodically switch from a quiescent to a surging state (controlling the flux of ice through Hudson Strait ice stream) and further tested his theoretical prediction with a simple model (MacAyeal, 1993b). Notably, the LIS mass loss is intimately related to a variable Hudson Bay ice thickness through rapidly-flowing ice streams that account for most of the ice sheet discharge (Stokes and Tarasov, 2010). Nevertheless, the representation of these ice streams into numerical ice-sheet models remains challenging. As a result, we lack a deeper comprehension of the role of ice streams which leads to larger model output uncertainties.

This thesis considers distinct physical scenarios of varying dynamic complexity regarding basal friction that are necessary to systematically assess the simulated LIS under LGM boundary conditions, thus improving our understanding of both paleo and present day ice sheets.

Could the LIS have exhibited internal oscillations?

LIS internal ice instabilities provide a potential explanation for HEs irrespective of the external forcing. The "binge-purge" mechanism was originally proposed by MacAyeal (1993a) and consists of two phases. First, a growth ("binge") phase occurs when the ice sheet rests on frozen sediments forming

a rigid bed, preventing sliding and increasing thickness due to accumulation. Second, during the purge, the thawing of unconsolidated basal sediments over Hudson Strait (solely due to the geothermal heat flow) serves as a lubricant that allows for rapid sliding. As a result, ice streaming is enhanced and the LIS volume rapidly adjusts to this sudden decrease in the basal friction by iceberg calving into the Labrador Sea.

Nonetheless, the ultimate physical explanation underlying any oscillatory mechanism that causes the HEs is still under debate. In fact, whether the cause is unique still remains as an open question (Roberts et al., 2016). It is thus necessary to explore the very nature of the mechanism from different perspectives: analytical, idealised numerical and performing full reconstructions with realistic geometries and boundary conditions.

1.6 Overview

This thesis aims to study the physical mechanisms behind internal ice instabilities. The problem will be tackled from three different approaches. First, a time-dependent analytical solution of the heat problem will be obtained (Chapter 2). Time scales and decay times will be derived, along with explicit formulas both for stationary and transient temperature solutions. Non-dimensionalisation of the problem will allow for a succinct description of the main parameters that control the temperature profiles and the relaxation times. These solutions will serve as a suite of benchmark experiments to test numerical solvers upon discretisation over unevenly-spaced coordinate systems, consistent with state-of-the-art ice sheet models. In the next approach, the ice sheet model Nix is described: a two-dimensional thermo-mechanically coupled ice sheet model built as part of this thesis (Chapter 3). This allows for an explicit description of the grounding line position without further interpolations (unlike 3D ice sheet models), whilst keeping a higher-order Stokes flow approximation combined with a fully coupled temperature solver. Next, for studying the LIS response under LGM conditions to different basal conditions, the three-dimensional thermo-mechanical ice sheet model Yelmo will be described in Chapter 4. Lastly, Chapter 5 builds on the results of LIS reconstructions using Yelmo ice-sheet model. It includes extensive testing of calibration parameters, as well as a comprehensive study of the basal drag-

ging and hydrology parameterisations used in the code. Chapter 6 discusses the broader context of the main scientific results presented in this thesis and finally Chapter 7 summarises the main conclusions.

Scientific publications related to this thesis:

Analytical solutions for the advective-diffusive ice column in the presence of strain heating

Moreno-Parada, D., Robinson, A., Montoya, M., and Alvarez-Solas, J.: Analytical solutions for the advective-diffusive ice column in the presence of strain heating, *The Cryosphere Discuss.* [preprint], DOI 10.5194/tc-2022-97, in review, 2022.

This work is reported in Section 2. The main goal is to describe the time-dependent behaviour of the ice temperatures by analytically solving the 1D time-dependent advective-diffusive heat problem including a source term due to strain heating and a Rob across the ice-air interface. The solution is expressed in terms of confluent hypergeometric functions following a separation of variables approach. Non-dimensionalisation reduces the parameter space to four numbers that fully determine the shape of the solution at equilibrium: surface insulation, effective geothermal heat flow, the Peclét number and the Brinkman number. The initial temperature distribution exponentially converges to the stationary solution. Transient decay timescales are only dependent on the Peclét number and the surface insulation, so that higher advection rates and lower insulating values imply shorter equilibration timescales, respectively. On the contrary, equilibrium temperature profiles are mostly independent of the surface insulation parameter. We have extended our study to a broader range of vertical velocities by using a general power-law dependence on depth, unlike prior studies limited to linear and quadratic velocity profiles. Lastly, we present a suite of benchmark experiments to test numerical solvers. Four experiments of gradually increasing complexity capture the main physical processes for heat propagation. Analytical solutions are then compared to their numerical counterparts, upon discretisation over unevenly-spaced coordinate systems. We find that a symmetric scheme for the

advective term and a three-point asymmetric scheme for the basal boundary condition best match our analytical solutions. A further convergence study shows that $n \geq 15$ vertical points are sufficient to accurately reproduce the temperature profile. The solutions presented herein are general and fully applicable to any problem with an equivalent set of boundary conditions and any given initial temperature distribution.

Description and validation of the ice sheet model Nix v1.0

Moreno-Parada, D., Robinson, A., Montoya, M., and Alvarez-Solas, J.: Description and validation of the ice sheet model Nix v1.0, *EGUsphere* [preprint], https://doi.org/10.5194/egusphere-2023-2690, 2023.

This work is reported in Chapter 3. The aim of the section is to provide a physical description of the ice-sheet model Nix v1.0, an open-source project intended for collaborative development. Nix is a 2D thermomechanical model written in C/C++ that simultaneously solves for the momentum balance equations, mass conservation and temperature evolution. Nix's velocity solver includes a hierarchy of Stokes approximations: Blatter-Pattyn, depth-integrated higher order and shallow-shelf. The grounding-line position is explicitly solved by a moving coordinate system that avoids further interpolations. The model can be easily forced with any external boundary conditions. Nix has been verified for standard test problems. Here we show results for a number of benchmark tests from the Marine Ice Sheet Intercomparison Project (MISMIP) and assess grounding-line migration with an overdeepened bed geometry. Lastly, we further exploit the thermomechanical coupling by designing a suite of experiments where the forcing is a physical variable, unlike previously idealised forcing scenarios where ice temperatures are implicitly fixed via an ice rate factor. Namely, we use atmospheric temperatures and oceanic temperature anomalies to assess model hysteresis behaviour with active thermodynamics. Our results show that hysteresis in an overdeepened bed geometry is similar for atmospheric and oceanic forcings. We find that not only the particular sub-shelf melting parametrisation determines the temperature anomaly at which the ice sheet retreats, but also the particular value of calibrated heat exchange velocities. Notably, the classical hysteresis loop is widened for both forcing scenarios (i.e., atmospheric and oceanic) if the

ice sheet is thermomechanically active as a result of the internal feedback among ice temperature, stress balance and viscosity. In summary, Nix combines rapid computational capabilities with a Blatter-Pattyn stress balance fully coupled to a thermomechanical solver, not only validating against established benchmarks but also offering a powerful tool for advancing our insight into ice dynamics and grounding-line stability.

Simulating the Laurentide Ice Sheet of the Last Glacial Maximum

Moreno-Parada, D., Alvarez-Solas, J., Blasco, J., Montoya, M., and Robinson, A.: Simulating the Laurentide Ice Sheet of the Last Glacial Maximum, *The Cryosphere*, **17**, 121-133, DOI 10.5194/tc-17-2139-2023.

The main results of this work are described in Section 4. The goal is to reconstruct the Laurentide Ice Sheet (LIS) during the Last Glacial Maximum (LGM, ca. 21,000 years before present, 21 kyr ago). Uncertainties underlying its modelling have led to notable differences in fundamental features such as its maximum elevation, extent and total volume. As a result, the uncertainty in ice dynamics and thus in ice extent, volume and ice-stream stability remains large. We herein use a higher-order three-dimensional ice-sheet model to simulate the LIS under LGM boundary conditions for a number of basal friction formulations of varying complexity. Their consequences on the Laurentide ice streams, configuration, extent and volume are explicitly quantified. Total volume and ice extent generally reach a constant equilibrium value that falls close to prior LIS reconstructions. Simulations exhibit high sensitivity to the dependency of the basal shear stress on the sliding velocity. In particular, a regularized-Coulomb friction formulation appears to be the best choice in terms of ice volume and ice-stream realism. Pronounced differences are found when the basal friction stress is thermomechanically coupled: the base remains colder and the LIS volume is lower than in the purely mechanical friction scenario counterpart. Thermomechanical coupling is fundamental for producing rapid ice streaming, yet it leads to a similar ice distribution overall.

Chapter 2
Analytical solutions for the advective-diffusive ice column in the presence of strain heating*

Ice temperatures are essential to comprehend the current state of the cryosphere and make accurate and reliable predictions of their future evolution. More precisely, in the context of ice stream periodic surges, an appropriate description of thermomechanical instabilities require a deep understanding of the temperature changes in time. Nevertheless, most analytical descriptions of the associated heat problem assume thermal equilibrium for simplicity. Robin (1955) and Lliboutry (1963) first laid the groundwork for understanding ice-column thermodynamics in the presence of vertical advection. Further studies on the shear heating margins of West Antarctic ice streams (e.g., Perol and Rice, 2011, 2015) include a more refined one-dimensional thermal model first introduced by Zotikov (1986). A similar problem was also solved by Meyer and Minchew (2018) under stationary conditions given the complexity of the problem.

Full numerical models overcome all this simplifications, albeit the inevitably error introduced in discretisation schemes and the demand of large computational resources (Winkelmann et al., 2011; Pattyn, 2017). Moreover, numerical solutions require caution as their accuracy and consistency must be previously assessed. In this context, analytical descriptions are extremely useful as they provide a control irrespective of the resolution and the particular stencil. Huybrechts and Payne (1996) already noted the lack of analytical temperature solutions, necessary in benchmark experiments and

* The main contents of this chapter are published in:
Moreno, D., Robinson, A., Montoya, M., and Alvarez-Solas, J.: On the periodicity of free oscillations for a finite ice column, *The Cryosphere Discuss.* [preprint], 2022, DOI 10.5194/tc-2022-97 https://doi.org/10.5194/tc-2022-97,inreview.

Intercomparison projects. Lastly, ice-sheet intilisation also benefits from a time-depedent temperature description. Traditional approaches compute a steady-state temperature field, incorrectly assuming that the ice is at thermal equilibrium (e.g., Morlighem et al., 2010, 2011; Pralong and Gudmundsson, 2011; Perego et al., 2014). Even though transient optimisation methods are now available (e.g., Goldberg et al., 2015), time integration is computationally prohibited for high-resolution, large-scale ice sheet models. The need for a time-dependent temperature description is evident in multiple aspects: advances in the theoretical understanding, validation of numerical models, benchmarks for intercomparison projects and ice-sheet initialisation.

The chapter is structured as follows: first a physical description of the processes involving heat propagation in a one-dimensional column are laid (Section 2.1); then the analytical solution is outlined (Section 2.2). In Section 2.3, the equilibirium solutions are presented for different scenarios and advective regimes. Next, in Section 2.4, the time-dependent nature of the solution is described and a time scale analysis is further elaborated directly from the eigenvalues of the problem. Then, Section 2.5 elaborates on a suite of benchmark experiments to test numerical solver on irregular grids. Section 2.6 discusses all results herein presented. Finally, the main conclusions of this work are summarized (Section 2.7).

2.1 Advective-diffusive ice column

This thesis considers a one-dimensional ice column with diffusive heat transport, vertical advection, strain heat and depth-integrated horizontal advection. Our domain is defined as the interval $z \in [0, L] \equiv \mathcal{L}$ and we further impose a Robin-type boundary condition at the top of the column, $z = L$ (Fig. 2.1). The aim of this section is to provide a rigorous mathematical formulation of the physical mechanisms involved in the heat problem necessary to obtain an exact solution of the ice temperature $\theta(z, t)$.

In the simplest physical scenario, the ice surface temperature is set to the air temperature value $\theta(L, t) = T_{\text{air}}$. However, surface temperatures are in fact the result of the energy balance between the ice and the atmosphere. To address this limitation, we refine the surface boundary condition by allowing for a potential deviation from the air temperature, accounting for the

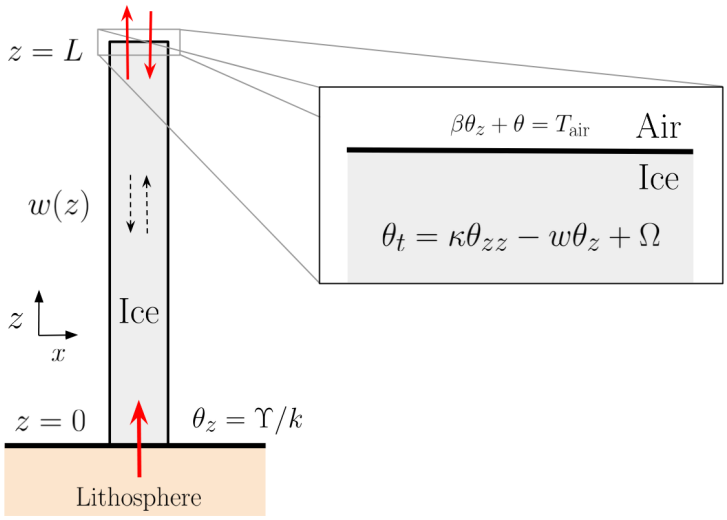

Fig. 2.1: Schematic view of the one-dimensional ice column with vertical advection $w(z)$ and inhomogeneous term Ω (here, we independently consider both strain heating and depth-integrated horizontal advection). Temperature evolution is dictated by the heat equation and an appropriate set of initial and boundary conditions. Subscripts denote partial differentiation. At the top, both the ice temperature and the vertical gradient can vary in time, thus allowing for non-equilibrium thermal states across the ice-air interface. At the base, the vertical gradient is fixed to the value given by the combined contribution of geothermal heat flow and potential basal frictional heat $\theta_z = -\Upsilon/k$. Note that our formulation is one-dimensional so that the x-axis is solely introduced for visualization.

thermal insulating effect in the uppermost region of the ice column. This insulation effect is a direct consequence of the reduction in ice density towards the surface (e.g., Stevens et al., 2020) and, as a result, the reduced ice thermal conductivity (Sturm et al., 2002; Calonne et al., 2011, 2019). This surface energy balance falls within the so-called linear heat-transfer boundary conditions or 'Newton's law of Cooling' (Carslaw and Jaeger, 1988, Chapter § 1.9). Briefly, Newton's law of cooling states that the heat flux across the interface is proportional to the temperature difference between the surface and the surrounding medium. It is applicable to a large variety of conditions such as a body cooling by forced convection (i.e., a fluid forced rapidly past the surface of a solid) or a a thin surface layer of a poor conductor (such as a low density firn or snow layer above the glacial ice). Moreover, Newton's

law of cooling captures the two simpler boundary conditions as limit cases: (1) prescribed surface temperature and (2) no heat flux across an interface.

This refinement enables a more accurate representation of the surface heat transfer dynamics and contributes to a comprehensive understanding of the energy balance within the ice column. In this description, both the surface ice temperature $\theta(L,t)$ and its vertical gradient $\theta_z(L,t)$ can vary in time:

$$\beta\theta_z + \theta = T_{\text{air}}, \qquad z = L,\ t > 0, \tag{2.1}$$

where italic subscripts denote partial differentiation and β is a parameter with length dimensions that modulates the permissible deviation between ice and air temperatures, often referred to as the surface thermal resistance (per unit area). We physically interpret β as the thermal insulation of the ice-air interface. In other words, β is a length-scale over which the ice column feels the air temperature. A zero value corresponds to an ideal conductor $\theta(L,t) = T_{\text{air}}$, whereas $\beta \to \infty$ represents a perfect thermal insulator characterized by a null heat exchange across the interface. In the limit case $\beta = 0$, the interface ice-air is always at thermal equilibrium (i.e., $\theta = T_{\text{air}}$). For $\beta \neq 0$, we allow for a heat exchange across the ice surface driven by the temperature difference between the two media. The thermal equilibrium is only reached if the ice surface and the atmosphere temperatures are identical. In such conditions, the heat flux across the interface is null and the vertical gradient at the top the ice column vanishes regardless of the value of β.

Considering diffusive heat transport, vertical advection, and a potential heat source, the ice temperature $\theta(z,t)$ satisfies an initial value problem given by the heat equation:

$$\begin{cases} \theta_t = \kappa\theta_{zz} - w\theta_z + \Omega, & z \in \mathcal{L},\ t > 0, \\ \theta = \theta_0(z), & z \in \mathcal{L},\ t = 0, \\ \theta_z = -\Upsilon/k, & z = 0,\ t > 0, \\ \beta\theta_z + \theta = T_{\text{air}}, & z = L,\ t > 0, \end{cases} \tag{2.2}$$

where the heat source Ω is an inhomogeneous term that captures strain heat and horizontal advection, $\Upsilon = G + Q$ is the combined contribution of geothermal heat flow G and potential basal frictional heat Q, k is the ice conductivity and κ is the ice diffusivity, both assumed to be constant. We further consider a z-dependent vertical velocity component given by $w(z)$.

In order to solve this problem, we must first provide the particular form of the vertical velocity term. As in Clarke et al. (1977) and Zotikov (1986), we first assume a linear variation of $w(z)$ with depth:

$$w(z) = w_0 \frac{z}{L}, \tag{2.3}$$

where w_0 is the vertical velocity at the ice surface $z = L$.

Standard values for w_0 usually read from -0.1 to -0.3 m/yr (Glovinetto and Zwally, 2000; Spikes et al., 2004). Positive values of w_0 imply an upward movement of ice and are physically plausible, though quite rare. Dahl-Jensen (1989) calculated steady temperature distributions (Fig. 5 therein) and found that profiles near the terminus position resemble those predicted for an ablation zone ($w_0 > 0$). Solutions herein presented are applicable to both positive and negative values of w_0, though we will focus on the downward movement of ice (i.e., $w_0 < 0$). The linear dependency is widely used in the literature (e.g., Joughin et al., 2002, 2004; Suckale et al., 2014). Nonetheless, we will also explore a more general power-law relationship that better describes vertical velocities modeled by Glen's flow law (see Appendix A.3).

The inhomogeneous term Ω can encompass a number of heat sources and sinks. Here we focus on strain heating $\mathcal{S}$ and horizontal advection $\mathcal{H}$, so that $\Omega = \mathcal{S} + \mathcal{H}$. In general, the strain heating term can be expressed as $\mathcal{S} = \sigma_{ij}\dot{\epsilon}_{ij}$, where σ_{ij} is the Cauchy stress tensor and $\dot{\epsilon}_{ij}$ is the strain rate tensor (expressed in index notation). Upon application of Glen's law, the rate of strain heating is solely a function of the second invariant of the strain rate tensor:

$$\mathcal{S} = \sigma_{ij}\dot{\epsilon}_{ij} = 2A^{-1/n}\ \dot{\epsilon_e}^{(n+1)/n}, \tag{2.4}$$

where $\dot{\epsilon_e} = (\dot{\epsilon}_{ij}\dot{\epsilon}_{ij}/2)^{1/2}$ is the second invariant of the strain rate tensor and summation is implied over repeated indexes (Einstein notation). This formulation does not impose any conditions on the strain rate regime (i.e., the dominant components) and only assumes $\dot{\epsilon}$ to be constant in depth. This requirement ensures the analytical tractability of the solution while including a potential strain contribution throughout the ice column.

The horizontal advection term $\mathcal{H}$ can imply a heat source or a sink, depending on the sign of the horizontal temperature gradient along a particular direction. We herein consider such a contribution by defining a depth-averaged lateral advection term (Meyer and Minchew, 2018):

$$\mathcal{H} = \frac{1}{L}\int_0^L (\mathbf{u}\cdot\hat{\mathbf{n}})\,\theta_{\hat{\mathbf{n}}}\,dz, \tag{2.5}$$

where $\mathbf{u}$ is the horizontal velocity vector, $\hat{\mathbf{n}}$ is the normal vector along an arbitrary direction contained in the horizontal plane and $\theta_{\hat{\mathbf{n}}} = \partial\theta/\partial\hat{\mathbf{n}}$ denotes the directional derivative along $\hat{\mathbf{n}}$.

This assumptions allow us to include a potential strain heat source $\mathcal{S}$ and a horizontal advection of heat term $\mathcal{H}$ while keeping the analytical tractability of Eq. 2.2. The limitations of these simplifications are discussed in Section 2.6.

2.2 Analytical solution

We next outline our analytical approach. We first non-dimensionalise our problem and exploit the linearity of the differential operator by further decomposing the solution as a sum of stationary and transient components to deal with the inhomogeneity. Lastly, we apply separation of variables to obtain a solution of the time-dependent problem and impose the corresponding initial and boundary conditions. Derivation details are elaborated in Appendix A.1.

It is natural to non-dimensionalise our problem by defining the following variables:

$$\xi = \frac{z}{L},\ \tau = \frac{\kappa}{L^2}t,\ \theta = \frac{T}{T_{\text{air}}},\ \tilde{w} = \frac{L}{\kappa}w,\ \tilde{\beta} = \frac{\beta}{L},\ \tilde{\Omega} = \frac{L^2}{\kappa T_{\text{air}}}\Omega \tag{2.6}$$

over the domain $\tilde{\mathcal{L}} = [0,1]$. Tildes are hereinafter dropped to lighten the notation.

Hence, we can express our Problem 2.2 as:

$$\begin{cases} \theta_\tau = \theta_{\xi\xi} - \text{Pe}\ \xi\theta_\xi + \Omega, & \xi \in \mathcal{L},\ \tau > 0, \\ \theta = \theta_0(\xi), & \xi \in \mathcal{L},\ \tau = 0, \\ \theta_\xi = \gamma, & \xi = 0,\ \tau > 0, \\ \beta\theta_\xi + \theta = 1, & \xi = 1,\ \tau > 0, \end{cases} \tag{2.7}$$

Table 2.1: Non-dimensional definitions and characteristic ranges. Summation is implied over repeated indices. Pe and Br are the Peclét and Brinkman numbers, respectively. Λ is the normalised horizontal advection, β is the surface insulation parameter and γ is the dimensionless combined contribution of geothermal heat flow and basal frictional heat. Physical magnitudes employed to obtain these ranges are give in Table 2.2.

Symbol	**Definition**	**Characteristic range**
Pe	$\frac{L}{\kappa} w_0$	$0.0 - 30.0$
Br	$\frac{L^2}{\kappa T_{\text{air}}} \sigma_{ij} \dot{\epsilon}_{ij}$	$0.0 - 5.0$
Λ	$\frac{L^2}{\kappa T_{\text{air}}} \int_0^1 (\mathbf{u} \cdot \hat{\mathbf{n}})\, \theta_{\hat{\mathbf{n}}}\ d\xi$	$0.0 - 10.0$
γ	$-\frac{T_{\text{air}}}{kL} \Upsilon$	$0.1 - 5.0$
β	$\frac{\beta}{L}$	$0.0 - 1.0$

where $\gamma = -T_{\text{air}}\Upsilon/(kL)$, $w = \text{Pe}\ \xi$ and $\theta_0(\xi)$ are the non-dimensional geothermal heat flow, vertical velocity and initial profile respectively. The vertical velocity is thereby conveniently expressed in terms of the Peclét number $\text{Pe} = w_0 L/\kappa$ (i.e., the ratio of advective to diffusive heat transport). The non-dimensional strain heat source term $\mathcal{S}$ can be identified with the Brinkman number Br, which represents the ratio of deformation heating to thermal conduction (see Table 2.1). The non-dimensional number γ is the combined contribution of geothermal heat flow and potential basal frictional heat, normalised by the vertical temperature gradient that would exists for a column thickness L and temperature T_{air}. It provides the relative strength of the basal inflow of heat compared to the ice-column extent and the air temperature.

The dimensionless problem clearly shows that five numbers completely determine the shape of the stationary solution: γ, β, Pe, Λ and Br. Their particular impact on the temperature distributions is discussed below.

Given that Eq. 2.7 is inhomogeneous, we will decompose the solution as a sum of a transient $\mu(\xi, \tau)$ and a stationary $\vartheta(\xi)$ components, so that $\theta(\xi, \tau) = \mu(\xi, \tau) + \vartheta(\xi)$. As a result, the transient and stationary problems are subject to homogeneous and inhomogeneous boundary conditions, respectively:

Table 2.2: Physical parameters values employed to determine the non-dimensional range shown in Table 2.1.

Parameter	Definition	Explored range	Units
L	Ice thickness	1 - 3	km
T_{air}	Air temperature	223.15 - 263.15	K
κ	Thermal diffusivity	$1.4 \cdot 10^{-6}$	$\text{m}^2\ \text{s}^{-1}$
k	Thermal conductivity	2.0	$\text{W m}^{-1}\ \text{K}^{-1}$
β	Surface insulation	0 - 1	km
G	Geothermal heat flow	0.01 - 0.05	W m^{-2}
Q	Frictional heat	0 - 0.5	W m^{-2}
u	Horizontal velocity	0 - 300	m yr^{-1}
$\theta_{\hat{\boldsymbol{n}}}$	Horizontal temperature gradient	0 - 1	K km^{-1}
$\dot{\epsilon}_e$	Effective strain rate	10^{-4} - 10^{-2}	yr^{-1}
A	Ice rate factor	10^{-25} - 10^{-24}	$\text{Pa}^{-3}\text{s}^{-1}$

$$\begin{cases} \mu_\tau = \mu_{\xi\xi} - w\mu_\xi, & \xi \in \mathcal{L},\ \tau > 0, \\ \mu = \mu_0, & \xi \in \mathcal{L},\ \tau = 0, \\ \mu_\xi = 0, & \xi = 0,\ \tau > 0, \\ \beta\mu_\xi + \mu = 0, & \xi = 1,\ \tau > 0, \end{cases} \tag{2.8}$$

and

$$\begin{cases} \Omega = \vartheta_{\xi\xi} - w\vartheta_\xi, & \xi \in \mathcal{L}, \\ \vartheta_\xi = \gamma, & \xi = 0, \\ \beta\vartheta_\xi + \vartheta = 1, & \xi = 1, \end{cases} \tag{2.9}$$

where $\mu_0 = \theta_0(\xi) - \vartheta(\xi)$ is the initial profile of the transitory solution.

The solution to the stationary component (Eq. 2.9) already differs from previous analytical works as Robin (1955) and Lliboutry (1963). First, they considered a homogeneous version of the problem (i.e., $\Omega = 0$) so that potential strain heating or horizontal advective contributions are neglected. Moreover, they simplified the top boundary condition since they imposed a prescribed constant temperature value at $\xi = 1$ (see also Clarke et al., 1977). However, our refinements still allow for analytically tractability and thus the stationary solution is (see Appendix A.2 for derivation details):

$$\vartheta(\xi) = \Omega\frac{\xi^2}{2}\ {}_2F_2\left(1, 1; \frac{3}{2}, 2; -\zeta\right) + A\ \text{erf}\left[a\xi\right] + B \tag{2.10}$$

where ${}_2F_2(a_1, a_2; b_1, b_2, x)$ is the generalised hypergeometric function, $\zeta = (a\xi)^2$, $a = (w_0/2)^{1/2}$, $A = -\gamma\,(\pi/(4a))^{1/2}$ and $B = 1 - A\left(2a\pi^{-1}\beta e^{-a^2} + \mathrm{erf}\,[a]\right)$. Note that if the inhomogeneous term is zero (i.e., $\Omega = 0$), the stationary temperature profile reduces to the well-known error function previously obtained by Robin (1955) and Lliboutry (1963). Even so, the temperature distribution would still differ as the boundary condition considered herein reflects a potential surface thermal insulation unlike prior studies.

We now take a step further and allow for time evolution by solving Eq. 2.8 and building our solution as the sum of both contributions. Namely, the general solution of the transient problem $\mu(\xi, \tau)$ is (see Appendix A.1 for derivation details):

$$\mu(\xi, \tau) = \sum_{n=0}^{\infty} \left[A_n \Phi\left(\alpha_n; \delta; \zeta\right) + B_n \Psi(\alpha_n; \delta; \zeta)\right] e^{-\lambda_n \tau} \tag{2.11}$$

where $\Phi\left(\alpha; \delta; \zeta\right)$ and $\Psi\left(\alpha; \delta; \zeta\right)$ are the Kummer (Kummer, 1836) and Tricomi confluent hypergeometric functions respectively (also known as confluent hypergeometric functions of the first and second kind). $\alpha_n = -\lambda_n / \left(2w_0\right)$ and $\delta = 1/2$. As the solution must be bounded at the origin, we set $B_n = 0$.

The full solution $\theta(\xi, \tau) = \vartheta(\xi) + \mu(\xi, \tau)$ thus reads:

$$\theta(\xi, \tau) = \Omega \frac{\xi^2}{2}\, {}_2F_2\left(1, 1; \frac{3}{2}, 2; -\zeta\right) + A\,\mathrm{erf}\,[a\xi] + B + \sum_{n=0}^{\infty} A_n \Phi\left(\alpha_n; \delta; \zeta\right) e^{-\lambda_n \tau} \tag{2.12}$$

where the coefficients A_n are obtained from the initial temperature profile (Eq. A.13 in Appendix A.1).

2.3 Stationary solutions

Before displaying the results of the full time-dependent problem, it is worth describing the temperature solutions at equilibrium.

Figure 2.2 shows our steady-state solutions as vertical profiles for a subset of the permutations of the non-dimensional numbers Pe, Br, γ, Λ and β. It is illustrative to compare the shape of our temperature solutions with Clarke et al. (1977) (Fig. 1 therein). We must stress that a one-to-one comparison is not readily possible since they imposed a simpler top boundary condition in

which the ice surface temperature is fixed to a given value, though the exact same solutions can be simply obtained by setting $\beta = 0$ in our case (see Eq. 2.1).

The non-dimensionalization of our analytical model provides simplicity and further reduces the parameter dimensionality of the solutions to solely five numbers, each corresponding to one column in Fig. 2.2. The Peclét number produces significant changes in the equilibrium solutions, as colder ice is advected from the uppermost part of the column, consequently cooling down the profile with increasing Pe values (Fig. 2.2a), in contrast to the well-known linear profile resulting for the purely diffusive case (i.e., $\mathrm{Pe} \to 0$). The combined contribution of geothermal heat flow and friction heat dissipation γ also yields large temperature amplitudes within the explored range. Nevertheless, the impact is clearly limited to the lower half of the column, thus leaving the upper regions nearly unperturbed as shown in Fig. 2.2c. Likewise, for the surface insulation parameter β in the presence of downwards advection ($\mathrm{Pe} = 7$), the entire temperature profile is left unchanged despite varying values of β (Fig. 2.2b). This can be understood as the heat exchange at the ice-air interface is not relevant for strong downward transport of colder ice, which is a far more effective heat transport compared to dissipation. Unlike γ, the strain heat dissipation Br influences the upper region of the ice temperature as its contribution is distributed throughout the column (Fig. 2.2d), rather than being a basal heat source. Even so, the impact is most notable near the base given that the temperature therein can freely evolve so long as the geothermal heat flow condition is met (Eq. 2.2). Similarly, the vertically-averaged lateral heat advection Λ also affects upper regions of the column (Fig. 2.2e). Here we have chosen positive Λ values, implying advection of colder ice. As a result, for sufficiently large values of Λ, the temperature within the column can be lower than at the surface, reaching a local minimum therein and gradually increasing as the base is approached. For negative values of Λ, we would find temperature profiles as those obtained in Fig. 2.2d.

2.4 Full solutions

We now present the results of the full problem presented in Eq. 2.2 by including the time-dependent solution. This transient nature depends on the

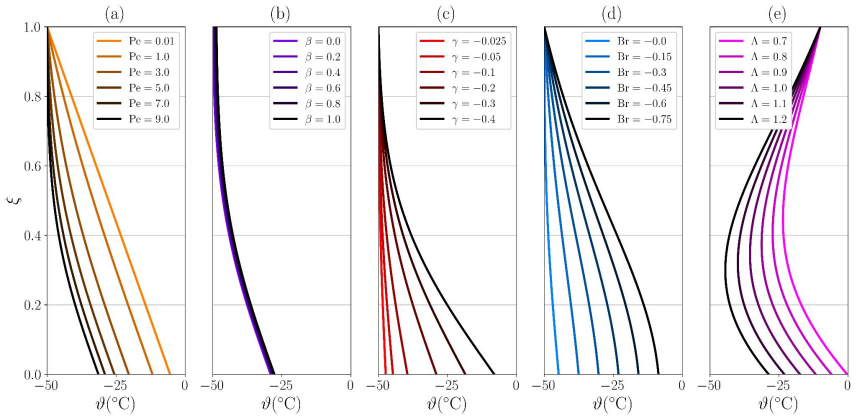

Fig. 2.2: Stationary temperature profiles $\vartheta(\xi)$. Solutions are fully determined by five non-dimensional numbers: Pe, β, γ, Br and Λ, corresponding to each panel respectively. Default values are: Pe $= 5$, $\beta = 0$, $\gamma = -0.2$, Br $= 0$ and $\Lambda = 0$, except for panel (e), where $\gamma = -0.4$.

initial state of the system, although it exponentially converges to the steady state as the transient component vanishes under the assumption of constant boundary conditions. We overcome the arbitrariness on the initial temperature profile by directly calculating the eigenvalues of the problem and their corresponding decay times as an estimation of the time scale of our system in different physical scenarios.

To illustrate the full solutions, we show the explicit time evolution from an initial profile as it approaches the corresponding stationary solution (Fig 2.3). In this instance, we employ constant initial temperature profiles for simplicity, $\theta_0(\xi) = 0.5$ and $\theta_0(\xi) = 2.5$ in panels Fig 2.3a and b, respectively. With these particular choices, we ensure that the initial temperature profile is below and above the stationary solution for two strong advective scenarios: vertical and lateral. Fig. 2.3a shows how temperature both at the ice surface and most notably at the base start to increase for $\tau > 0$, while at the central region of the column remains constant until heat propagates along the column. It is worth noting how the surface temperature gradually relaxes to the equilibrium profile since instead of imposing the air temperature, a more realistic heat exchange at the ice-air interface is considered via $\beta = 0.5$. On the contrary, Fig. 2.3b shows an instantaneous change at the surface by an oversimplified top boundary condition if $\beta = 0$ (i.e., a perfectly conductive

ice-air interface). As a result, the cold air temperature rapidly propagates into the uppermost region of the ice column rapidly, whereas the geothermal heat flow contribution requires a longer time to propagate from the base. On the contrary, the lower part of the domain increases its temperature notwithstanding the sudden decrease of the upper region. As the column evolves in time, the rate of change gradually diminishes and it approaches zero as the transient solution asymptotically reaches the temperature profile given by the stationary temperature profile $\vartheta(\xi) = \lim_{\tau\to\infty} \theta(\xi, \tau)$.

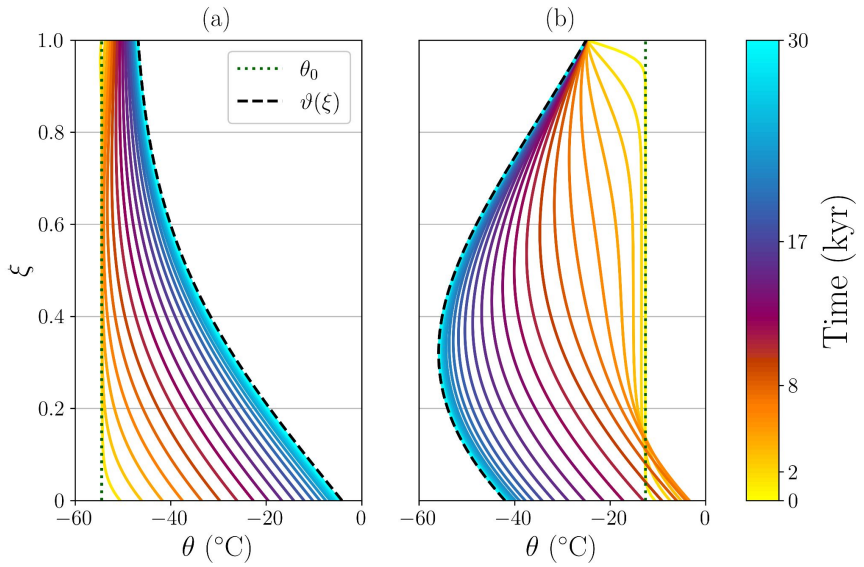

Fig. 2.3: Time-dependent solution $\theta(\xi, t)$ given an initial temperature profile $\theta_0(\xi)$ (vertical dotted line). Dimensionless values: (a) $\beta = 0.5$, $\Lambda = 0$ and (b) $\beta = 0.0$, $\Lambda = 1.0$. Default values: Pe $= 5.0$, $\gamma = -0.35$, Br $= 0$. Black dashed lines represent the stationary solution $\vartheta(\xi)$. To ease visualization, the time variable is quadratically spaced as indicated in the colourbar.

To examine closely the transient nature of the solutions, we present the temperature evolution of a given initial profile for a certain range of the non-dimensional parameters (Fig. 2.4). This gives us information about the time-dependent effects of each parameter, unlike Fig. 2.2 that was restricted to equilibrium states. Addtionally, the continuous representation (i.e., colourbar in Fig. 2.4), as opposed to the discrete number of vertical profiles in Fig. 2.3 facilitates comparison among particular parameter choices.

The particular parameter values were selected so that we obtain four physically distinct scenarios: (a) high geothermal heat flow under a large advection regime, (b) high strain heat dissipation in a low vertical advection regime, (c) strong lateral advection of colder ice under surface insulating conditions and (d) weak geothermal heat flow under a low vertical advection regime. This setup allows us to separately determine the role played by each mechanism during the transient regime of the solution.

Figure 2.4a shows that the thermal equilibration begins by an increase of the basal temperature that gradually propagates upwards until it is balanced by the downward advection ice from the colder surface. A similar transient behaviour is found if strain heat dissipation is additionally considered (Fig. 2.4b). Even though the geothermal heat flow is significantly smaller in this scenario, the heat travels further upwards as a result of a low vertical advection regime (Pe = 2) combined with a source of strain heat throughout the column (Br = 6). If we instead consider a scenario where heat is removed by lateral advection of colder ice $\Lambda = 6$ (Fig. 2.4c), we note two different timescales: the geothermal heat flow first warms the ice base, then the lateral removal of heat takes over with a consequent reduction of temperature in the entire column. Lastly, a low basal inflow of heat combined with a weak vertical advective regime (Fig. 2.4d) yields the smallest temperature gradients within the column.

We can also predict the behaviour of the transitory component directly from the eigenvalues of the problem. By calculating the inverse of the eigenvalues λ_n^{-1}, we obtain a magnitude that can be expressed with time dimensions and represents the decay time of each Fourier mode (Fig. 2.5a). Physically, this is the time required for the transient component to be reduced a factor e^{-1} at any point and it further allows us to estimate the equilibration time from an arbitrary initial state. As we would expect, higher order modes have a shorter life time. Notably, the eigenvalue equation solely depends on Pe and the surface insulation parameter β (Eq. A.8, Appendix A.1). This implies that the time to reach equilibrium exclusively depends on these two numbers. The remaining dimensionless parameter values yield the exact same equilibration time, despite playing a role in the particular form of the solution. In other words, the five dimensionless numbers shape the temperature profile, but only the vertical advection and the surface insulation parameter influence the exponential decay of the transitory component and therefore,

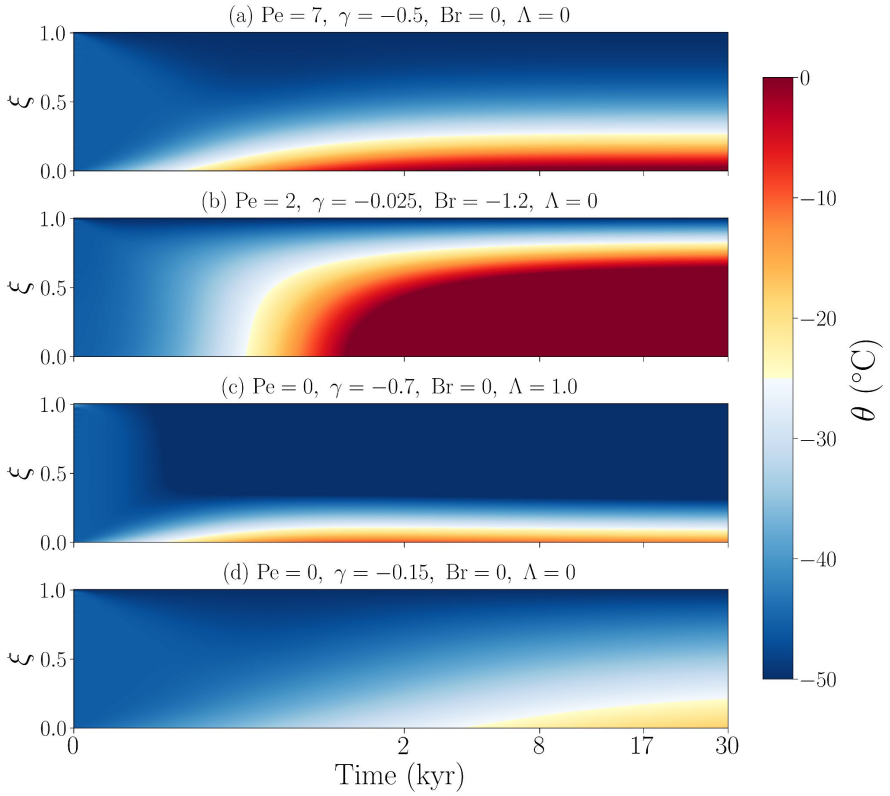

Fig. 2.4: Time-dependent solution $\theta(\xi, \tau)$ given an initial temperature profile. For simplicity, here the initial temperature profile is $\theta_0(\xi) = -40^{\text{o}}\text{C}$ at all depths and in all cases.

the timescale to reach equilibrium from an arbitrary initial state (Fig. 2.5b). Particularly, scenarios with a high advective regime yield shorter equilibration times (Fig. 2.5b) $\sim$ 2-10 kyr, unlike highly insulating scenarios at the surface, characterized by long decay times ($\sim$ 25-40 kyr).

2.5 Benchmarks for numerical solvers

The analytical solutions obtained herein are valuable tools for testing numerical solvers. We thus propose a suite of benchmark experiments with

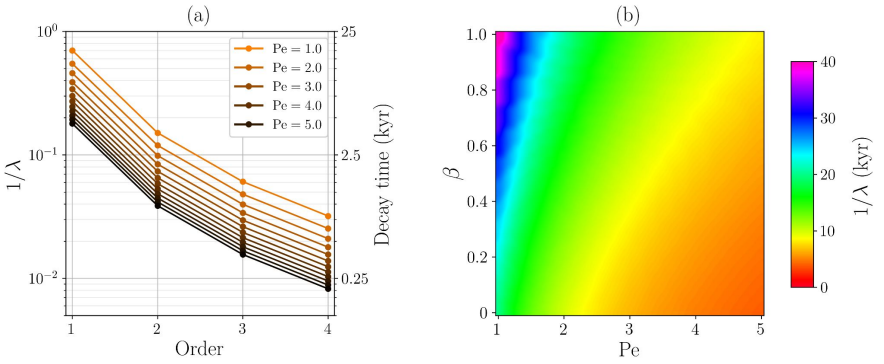

Fig. 2.5: Decay time and corresponding eigenvalues. (a) First four eigenvalues for the set of β values shown in Fig. 2.2b. (b) Decay time (kyr) of the first eigenvalue as a function of Pe and β.

gradually increasing complexity to test the representation of each physical process involved in ice temperature evolution (see Table 2.3).

Table 2.3: Benchmark experiments for numerical solvers and main physical processes considered for heat propagation. The experiments are named in increasing complexity order.

Experiment name	Physical processes			
	Diffusion	Vertical adv.	Strain heating	Horizontal adv.
Exp-1	Yes	No	No	No
Exp-2	Yes	Yes	No	No
Exp-3	Yes	Yes	Yes	No
Exp-4	Yes	Yes	Yes	Yes

First, the well-known purely diffusive case (Exp-1) is simply considered. Then, vertical advection is additionally included (Exp-2). Lastly, strain heating (Exp-3) and the vertically-averaged horizontal advection (Exp-4) are considered. Given the analytical nature of our solutions, spatial and temporal resolutions can be set arbitrarily high as there are neither convergence nor stability constraints. This allows for a comparison against spatial and temporal resolutions found in numerical solvers. It must be stressed that the initial

temperature profile and all other parameters can be set by the user to test the solution at any desired scenario. These are simply proposed benchmarks, but the solutions developed here can be used for any type of benchmark test that is desired and fits the limitations of the equations.

A numerical model is further developed for testing by performing a finite differences discretisation of Eq. 2.7 and the basal boundary condition over a sigma coordinate system, where grid points are unevenly-spaced. This uniform grid can follow either a quadratic or an exponential relation, set by the user. This yields higher resolutions near the base for a fixed number of points, thus minimising the computational costs. Several discretisation schemes are employed with varying orders of convergence, summarised in Table 2.4. Numerical solutions are then compared at equilibrium with their analytical counterpart (Fig. 2.6).

Table 2.4: Finite-difference approximations employed in the numerical study (Fig. 2.6) for unevenly-spaced grids ζ_i, as detailed in Appendix A.4. Distance between two adjacent points is defined as $h_i = \zeta_{i+1} - \zeta_i$. Note that vertical velocities are negative (downwards movement of ice) and the advection stencils are consequently adjusted. Discretization coefficients for the S-5p scheme are given in Appendix A.4.

Quantity	**Continous**	**Discrete approx.**	**Stencil name**	**Order**
Diffusion	$\theta_{\xi\xi}$	$\frac{2[h_{i-1}\theta_{i+1} - (h_i + h_{i-1})\theta_i + h_i\theta_{i-1}]}{h_i h_{i-1}(h_i + h_{i-1})}$	Three-point symmetric (S-3p)	$\mathcal{O}(\varepsilon^2)$
		$c_{i+2}\theta_{i+2} + c_{i+1}\theta_{i+1} + c_i\theta_i + c_{i-1}\theta_{i-1} + c_{i-2}\theta_{i-2}$	Five-point symmetric (S-5p)	$\mathcal{O}(\varepsilon^4)$
Vert. advection	$w\theta_\xi$	$-w_i \frac{\theta_{i+1} - \theta_i}{h_i}$	Two-point forward (F-2p)	$\mathcal{O}(\varepsilon^1)$
		$-w_i \frac{\theta_{i+1} - \theta_{i-1}}{h_i + h_{i-1}}$	Two-point symmetric (S-2p)	$\mathcal{O}(\varepsilon^2)$
		$-w_i \left[\frac{2h_{i-1} + h_i}{h_{i-1}(h_{i-1} + h_i)}\theta_i - \frac{h_{i-1} + h_i}{h_{i-1}h_i}\theta_{i+1} + \frac{h_{i-1}}{h_i(h_{i-1} + h_i)}\theta_{i+2} \right]$	Three-point forward (F-3p)	$\mathcal{O}(\varepsilon^2)$
Basal BC	$\theta_\xi = \gamma$	$\frac{\theta_1 - \theta_0}{h_0}$	Two-point forward (F-2p)	$\mathcal{O}(\varepsilon^1)$
		$\frac{2h_0 + h_1}{h_0(h_0 + h_1)}\theta_0 - \frac{h_0 + h_1}{h_0 h_1}\theta_1 + \frac{h_0}{h_1(h_0 + h_1)}\theta_2$	Three-point forward (F-3p)	$\mathcal{O}(\varepsilon^2)$

As could be expected, Figure 2.6 illustrates that spatial discretisation becomes a fundamental piece to obtain an accurate temperature solution, particularly at the base of the ice. The purely diffusive scenario (Exp-1, Fig. 2.6a) shows the smallest (negligible) errors for all discretisation schemes given its mathematical simplicity. If vertical advection is further introduced (Exp-2, Fig. 2.6), the particular choice by which the temperature first derivative θ_ξ is discretised becomes important, as temperature gradients can be transported via non-zero vertical velocities. Forward stencils slightly overestimates (F-2p) and underestimates (F-3p) the solution as shown in Fig. 2.6b. On the contrary, symmetric stencils S-2p provides a numerical solution significantly closer to the analytical profile, particularly near the base. The next benchmark experiment (Exp-3, Fig. 2.6c), where the inhomogenous term captures a source of heat throughout the column due to strain deformation, presents a similar behaviour, where the F-3p stencil undersetimates the solution. Again, the symmetric scheme outperforms the asymmetric ones. Lastly, the inhomogeneous term is introduced, physically capturing a vertically-averaged source or sink of heat as a consequence of the advected ice in the horizontal dimension. This work thus considered a negative contribution that physically describes a downstream advection of colder ice (Exp-4, Fig. 2.6d). Numerical solutions overestimate the analytical solution for the assymetric discretisation schemes (i.e., F-2p and F-3p), unlike the two-point symmetric scheme (S-2p). It is worth noting that the closest result to the analytical solution is obtained using S-2p for the advective term and F-3p for boundary condition discretisation. In the remaining experiments, the particular scheme employed in the basal boundary condition does not modify the solution.

For all experiments tested, results are identical irrespective of the particular discretisation of the diffusion term (Table 2.4), so that both a three-point and a five-point symmetric stencils yield the same stationary temperature profiles. Overall, all finite differences stencils herein presented successfully converge (Fig. 2.6e) for all benchmark experiments, yielding the smallest residual error for the purely diffusive scenario (Exp-1).

Additionally, a resolution convergence test is performed for the best discretisation choice (Table 2.4): a F-3p for the diffusive term, a S-2p for vertical advection and a F-3p basal boundary condition. In order to quantify the residual error as a function of the spatial resolution for each benchmark experiment (Fig. 2.7), the ℓ^2-norm of the difference between the numerical and

the analytical solutions $\varepsilon = ||\vartheta_{\text{num}} - \vartheta^-||_{\ell^2}$, defined as $||\boldsymbol{x}||_{\ell^2} = \left(\sum_i x_i^2\right)^{1/2}$ is computed. The larger deviations from the analytical solutions are found for the lower half of the ice column and are strongly dependent on the vertical resolution. Results show that a coarse resolution tends to overestimate the equilibrium temperature for all benchmark experiments. The residual error between the analytical and numerical solution exponentially decays, reaching values of $\varepsilon < 10^{-2}$ for $n > 15$.

2.6 Discussion

The adoption of dimensionless variables results in enhanced generality and mathematical convenience, albeit at the expense of veiling the practical significance to real glaciers and ice sheets. Data for characteristic values have been consequently tabulated to ease interpretation (Table 2.1), thus showing that the explored range encompasses realistic values found in ice caps.

First, results are compared with previously obtained solution for a simpler case (e.g., Clarke et al., 1977). Identical profiles can be obtained by setting the ice surface temperature to a fixed value given by the air temperature, i.e., imposing $\beta = 0$ in Eq. 2.2 (Figs. 2.2c and 2.2f). Prominently, note that a non-zero β value is fundamental in the transitory regime (Fig. 2.11), though it leads to negligible changes at equilibrium (Fig. 2.2).

The transient behaviour of the solution is intricate given the freedom to choose an arbritary initial state. This issue can be overcome by direct inspection of the eigenvalues of the problem. An estimation of the decay time of the analytical solution shows that the advection and the surface insulation are the only parameters that determine the timescale to reach thermal equilibrium. This approach has some limitations, some of which are now discussed. The decay time dependency is subjected to the mathematical form of our problem (Eq. 2.2). If an analytical solution could be obtained with an additional explicit horizontal advection term (rather than a vertically-averaged contribution), then the eigenvalues, and consequently the decay times, would also depend on Λ. A second limitation concerns the boundary conditions. This solution required time-independent conditions and therefore the decay time estimations do not hold if, for instance, the surface temperature changes over time. Even so, the approach developed here provides estimates of relaxation

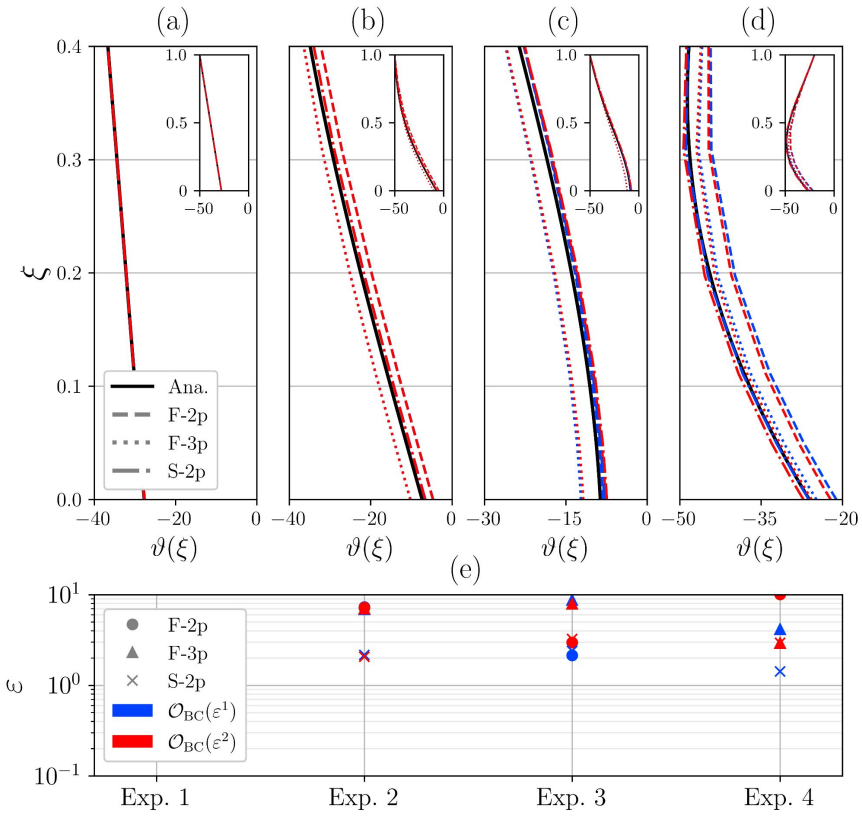

Fig. 2.6: Numerical steady-state solutions (red, blue) for all discretisations shown in Table 2.4 compared with the analytical solution (solid black). Colour code represents the two asymmetric discretisation schemes for the basal boundary condition: F-2p (blue) and F-3p (red). Marker and line styles denote the discretisation stencil of the vertical advective term. The number of vertical points $n = 10$ is fixed for all cases. Numerical solutions are identical upon spatial discretisation of the difussive term at orders $\mathcal{O}(\varepsilon^2)$ and $\mathcal{O}(\varepsilon^4)$ (see Table 2.4). The purely diffusive case (Exp. 1) yields negligible errors $\varepsilon < 10^{-5}$.

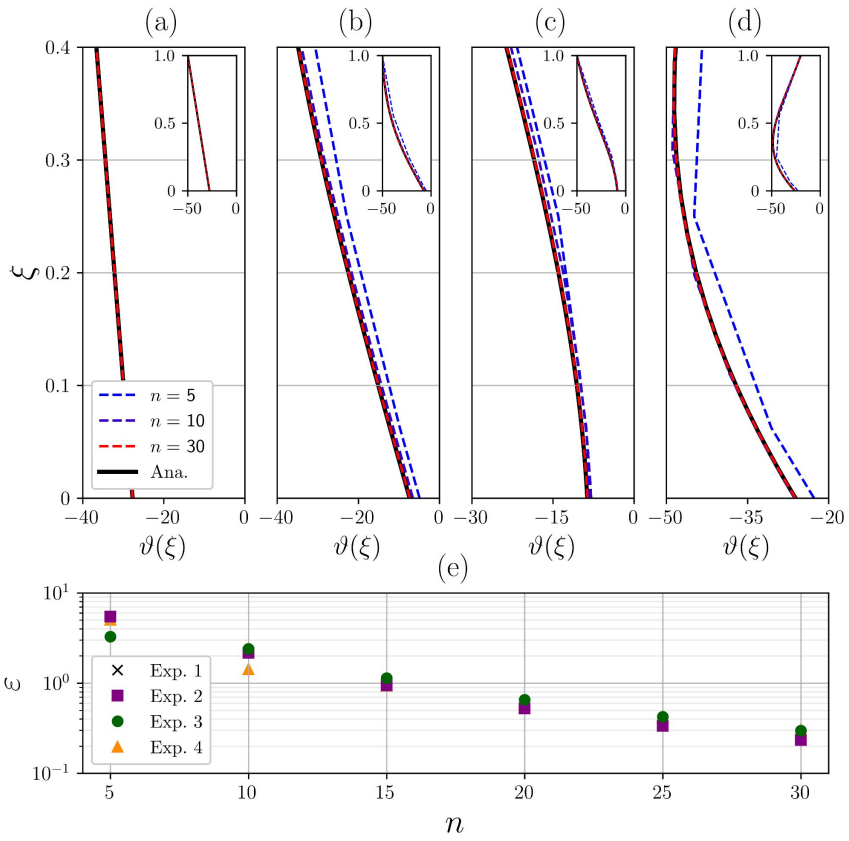

Fig. 2.7: Convergence study of benchmark experiments. Steady-state analytical solutions shown in black solid line. (a) Exp-1, (b) Exp-2, (c) Exp-3 and (d) Exp-4, (e) Residual error defined as $\varepsilon = ||\vartheta_{\text{num}} - \vartheta||_{\ell^2}$. For all experiments, $\gamma = 2$ and $\beta = 0$.

times under different physical conditions and gives an explicit expression for the time-dependent temperature profile from any arbitrary initial state.

The tractability of the analytical solution does not allow for further complexity and hence additional numerical methods would be necessary if such a physical description is desired. Nonetheless, a constant horizontal advection term Λ was also introduced as part of the inhomogeneous term Ω, for which the sign of the horizontal temperature gradients must be chosen a priori. Even though horizontal variability of temperature distributions can vary greatly, this effect is considered by assuming a constant term (throughout

the ice column) entering the heat equation, thus not reflecting much of the non-local features of the thermal structure of the ice sheets.

It must be stressed that our analytical solutions are not limited to regions with negligible horizontal velocities, since the true constraining quantity is the vertical gradient of the horizontal velocity u_z. Hence, rapidly sliding regions with a small vertical gradient of the horizontal velocity are also suitably described by our solutions, for that $u_z \simeq 0$ implies that the temperature profile is merely transported along the flow direction, while compressing the temperature gradient as the ice stream thins (Robel et al., 2013). One can argue that the additional source of heat due to frictional dissipation should be now also considered. Nonetheless, in terms of the temperature distribution, this effect is equivalent to an increased geothermal heat flux, as it is purely restricted to the column base and therefore already encompassed in Eq. 2.7.

The strain rate regime pose further limitations on the applicability of the solution. Particularly, regions where vertical shear dominates and the strain heat dissipation is concentrated near the base, a vertically-averaged contribution appears to be inaccurate. Nevertheless, as already noted by Rezvanbehbahani et al. (2019), this effect is instead well captured by an increase in the inflow of heat from the base (i.e., equivalent to a larger geothermal or frictional heat term) under conditions where most of the vertical shear is concentrated in the basal layers (Fowler, 1992).

It is worth noting that phase changes are not herein considered, so that temperature evolution is strictly confined to values below the pressure-melting point. Unlike a numerical solver, where temperature is manually limited, these solutions must be taken with caution as the problem herein addressed describes a frozen ice column. Results are still compatible with a potential heat contribution due to basal frictional heat Eq. 2.2, even though fast sliding regions are often related with temperate basal conditions. Nevertheless, an additional heat contribution would imply an increased vertical temperature gradient even if the column base eventually reached the pressure-melting point.

Knowing that ice forms by snow densification through time (Stevens et al., 2020), layers of progressively increasing ice density descending from the surface are found. Likewise, snow thermal conductivity increases with density (e.g., Sturm et al., 1997, 2002; Calonne et al., 2011, 2019), resulting in a poorer heat conductor as the snow-air interface is approached. As already

noted by Carslaw and Jaeger (1988), if the flux across a surface is proportional to the temperature difference between the surface and the surrounding medium, the appropriate boundary condition takes the form of Eq. 2.1, rather than the oversimplified version $\theta(L,t) = T_{\text{air}}$. Here it is explicitly described the ice column with a constant thermal conductivity to keep analytical tractability, but this works aims at describing the fact that the thermal conducivity of glacial ice $k(\rho)$ is reduced towards the surface. Following Carslaw and Jaeger (1988), a general "Newton's Law" also captures the traditional approach (i.e., imposing a particular ice surface temperature given by the air temperature) as a limit case if $\beta \to 0$.

Our suite of benchmark experiments allows us to test numerical solvers and assess reliability for different discretisation schemes and resolutions. The basal boundary condition is sensitive to the particular discretisation scheme, as the geothermal flux is the main source of heat in the ice column and is considered via a Neumann boundary condition. The simplest two-point stencil does not correctly represent the equilibrium temperatures, yielding larger deviations at the base (Fig. 2.6). Higher order discretisations are necessary to obtain a more reliable temperature distribution. In our benchmark experiments, significant improvement is found between $\mathcal{O}(\varepsilon^1)$ and $\mathcal{O}(\varepsilon^2)$ schemes for the basal boundary condition (Fig. 2.6), particularly for scenarios with large strain heating values or strong horizontal heat advection. Results for the different vertical advection schemes show that forward stencils (both F-2p and F-3p) deviate further from the analytical solution when compared to a symmetric scheme. Despite the fact that symmetric advective schemes might show some instabilities, no numerical issues have been found in the present study. On the contrary, such schemes appear to outperform the asymmetric counterparts for all benchmark experiments.

Resolution plays a fundamental role to obtain a reliable temperature profile. A sigma coordinate system with quadratic spacing accurately ($\varepsilon < 10^{-2}$) reproduces the analytical solution for $n \geq 15$ grid points provided our best numerical scheme choice. Additional calculations performed for an exponential grid spacing (not shown) reveal consistent results with the quadratic dependency (Figs. 2.6 and 2.7). This shows robustness of our numerical schemes, from which the symmetric advective stencil (S-2p) and the three-point basal boundary conditions (F-3p) again outperform the remaining choices.

2.7 Conclusions

The analytical solution to the 1D time-dependent advective-diffusive heat problem including additional terms due to strain rate deformation and depth-integrated horizontal advection has been determined. A Robin-type top boundary condition further considers potential non-equilibrium temperature states across the ice-air interface. The solution was expressed in terms of confluent hypergeometric functions following a separation of variables approach. Non-dimensionalisation reduced the parameter space to five numbers that fully determine the shape of the solution at equilibrium. The arbitrariness on the initial temperature profile has been further overcome by directly calculating the eigenvalues of the problem and their corresponding decay times as an estimation of the time scale of our system in different physical scenarios. The transient component exponentially converges to the stationary solution with a decay time that solely depends on vertical advection and surface insulation.

The sign of vertical advection is of utmost importance as it determines the direction along which temperature gradients are transported. The present study focuses on the downward advective scenario, given the implausibility of an upward advection of ice. At equilibrium, basal temperatures are particularly sensitive to four physical quantities: vertical advection, geothermal heat flow, strain heat and lateral advection. On the contrary, the surface insulation yields negligible changes in the stationary solution. This is true even for highly insulating conditions at the ice surface, so long as colder ice is transported more efficiently than heat travels upwards due to diffusion.

The transient regime shows a strongly distinct behaviour. The arbitrariness of the initial state is overcome by a direct inspection of the eigenvalues of the problem. A magnitude that represents the decay time of each Fourier mode is obtained, thus providing information about the equilibration time of the system. The decay time of the transient component is found to be solely dependent on two magnitudes: advection (Pe) and surface insulation (β). The remaining dimensionless parameters shape the temperature solution, though they have no influence in the timescale to reach equilibrium. Strong advective regimes (Pe ~ 5) yield $\sim$ 2-10 kyr decay times under null and strong surface insulation conditions, $\beta = 0$ and $\beta = 1$ respectively. On the contrary, weak advective regimes are characterised by longer timescales $\sim$ 20-40 kyr, also depending on the particular insulating scenario.

Our suite of benchmark experiments are convenient for assessing accuracy and reliability of numerical schemes. This thesis employes unevenly-spaced grid discretisations to obtain higher resolution near the base whilst minimising the total number of grid points, thus reducing computational costs. A symmetric discretisation of the advective term combined with a three-point basal boundary condition yields the best agreement compared to analytical solutions. In terms of convergence and grid resolution, $n \geq 15$ is found to be the lower limit to obtain accurate temperature profiles. These results are robust both for a quadratic and an exponential grid spacing.

Lastly, it must be stressed that our analytical solutions are general and can be applied to any initial boundary value problem that fulfils the conditions herein described. They can provide temperature distributions for any 1D problem at arbitrarily high spatial and temporal resolutions, that considers the combined effects of diffusion, advection and strain heating without any additional numerical implementation. Furthermore, they present a reliable benchmark test for any numerical thermomechanical solver to quantify accuracy losses and necessary spatial and temporal resolutions.

Chapter 3
Description and validation of ice-sheet model Nix v1.0*

The previous chapter analytically described the time-dependent behaviour of the ice temperatures over a one-dimensional column and provided with a suite of benchmark experiments to test numerical solvers. Advection of heat (both vertically and horizontally) and frictional dissipation appear to be fundamental components that shall not be overlooked. Nevertheless, the particular shape of the vertical velocity profile must be imposed a priori to obtain a solution. More importantly, horizontal advection cannot be explicitly resolved and a parametrised contribution shall be only considered. Furthermore, the low dimensionality constrain to obtain analytical results does not allow for higher complexity. Thus, the highly coupled nature of a real ice sheet necessitates an explicit description that can be only accounted with a numerical model.

The capability of ice sheet models to reproduce grounding line migration was thoroughly studied since Weertman (1974) and Thomas and Bentley (1978) proposed that no stable steady states of the grounding line could be found on inland-sloping or retrograde beds. The first Marine Ice Sheet Intercomparison Project (MISMIP, Pattyn et al., 2012) shed light on the agreement of modelling efforts to describe the grounding line motion and assessed the appropriateness of numerical schemes. The authors proposed a set of benchmark experiments on an idealised two dimensional bed geometry that serves as an extremely convenient evaluation for ice sheet models to re-

* The main contents of this chapter are published in:
Moreno-Parada, D., Robinson, A., Montoya, M., and Alvarez-Solas, J.: Description and validation of the ice sheet model Nix v1.0, *EGUsphere* [preprint], https://doi.org/10.5194/egusphere-2023-2690, 2023.

produce grounding line migration. Nonetheless, there are important questions regarding the particular effect of thermodynamics that remain unanswered. Specifically, whether marine ice sheets have discrete steady surface profiles if ice temperatures can freely evolve in time and the potential implications on the hysteresis behaviour in overdeepened bed geometries.

The following chapter thus presents a comprehensive description of the ice-sheet model Nix v1.0: a 2D thermomechanical model that simultaneously solves for the momentum balance equations, mass conservation and temperature evolution. The chapter is structured as follows: first a Nx ice sheet model v1.0 is introduced and described (Sections 3.1, 3.2 and 3.3); then the experimental setup is described (Section 3.4). In Section 3.5.1, Nix model is validated against established benchmarks from MISMIP. Next, in Section 3.5.2, novel experiments coupling ice dynamics with thermomechanics are carried out using physical variables as a forcing: atmospheric temperatures and oceanic temperature anomalies. Section 3.6 discusses all results herein presented. Finally, the main conclusions of this work are summarized (Section 3.7).

3.1 Model design

Nix is an open source software available under the Creative Commons Attribution 4.0 International license. The model has been derived from scratch with a clear Application Programming Interface (API). It is written in C/C++ for efficiency and extremely fast computing (see Appendix B) and is readily available to run in any High Performance Computing Cluster. There are two key dependencies: NetCDF (Rew and Davis, 1990; Brown et al., 1993) and Eigen (Guennebauda et al., 2010) libraries. The former handles tasks for convenient community-standard input/output capability, whereas the latter serves to define vectors, matrices and further necessary computations (Fig. 3.1). Nix users can optionally select parallel computing (supported by Eigen library) simply by enabling OpenMP on the employed compiler, particularly convenient for high resolutions in the Blatter-Pattyn approximation, where large sparse matrices must be inverted. Moreover, it is also possible to use Eigen's matrices, vectors, and arrays for fixed size within CUDA kernels (Nickolls et al., 2008).

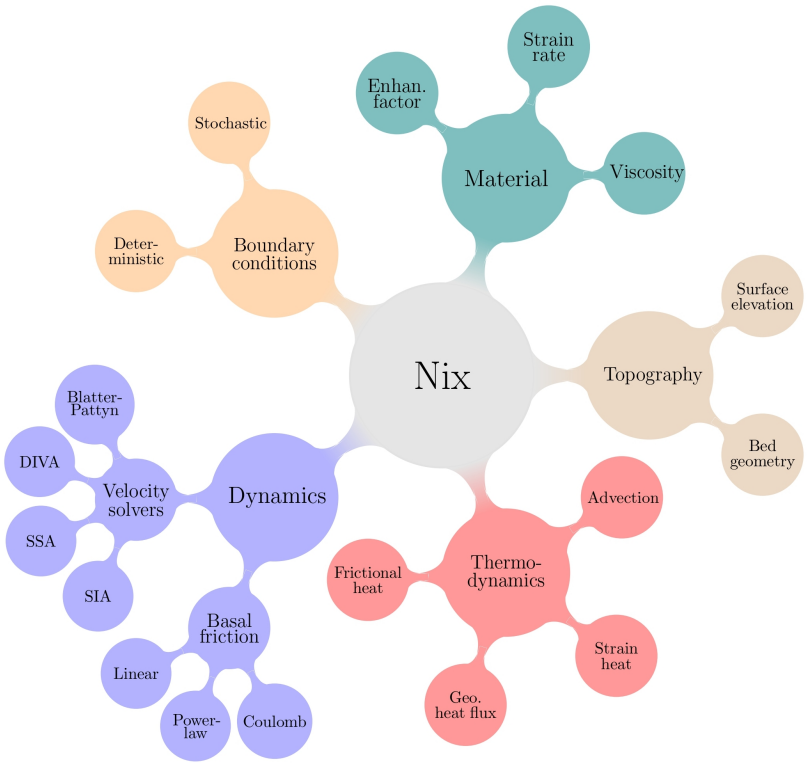

Fig. 3.1: Overview of Nix modular structure. Each colour represents a C++ class: dynamics, material, topography, thermodynamics and boundary conditions. The Python wrapper is an optional user friendly option and the code can be compiled without any additional depedencies at any standard High Performance Computing Cluster.

Nix's design offers a friendly Python wrapper module that handles directory management and compilation, though it can be compiled and run independently. The exact version used to produce the results of this work is archived at a persistent Zenodo repository (Moreno-Parada et al., 2023b) while the latest version can be accessed on GitHub at: https://github.com/d-morenop/nix.

3.2 Model physics

In this section, the fundamental equations of the model are described. Generally speaking, an ice slab of two spatial dimensions (i.e., horizontal and vertical) is considered by coupling a particular choice of stress balance, the advection equation and the associated heat problem.

Our system evolves thermodynamically in time through three main processes concerning heat propagation: vertical diffusion, horizontal and vertical advection and internal deformation of the ice. Viscosity is thus dependent on both the strain rate and the temperature. With respect to dynamics, basal friction can be parametrised by three distinct formulations (linear, power-law and Regularized-Coulomb). Additionally, basal friction captures the thermal state of the base by a two-valued friction coefficient encapsulating frozen and thawed bedrocks.

3.2.1 The Blatter-Pattyn approximation

Ice sheets and glaciers are generally described as an incompressible fluid with a low Reynolds number flow. Conservation of momentum is ensured through the Stokes equations, a quasi-static stress description where intertial and advective terms are neglected due to the slow movement of the ice.

The typical ice-sheet geometry allows to further simplify the Stokes flow equations by defining an aspect ratio ε. Given the characteristic length scales for the horizontal and vertical dimensions, $\varepsilon \ll 1$ (e.g., Greve and Blatter, 2009). Simply by keeping terms of order $\mathcal{O}(\varepsilon)$ in the Stokes equations, the Blatter-Pattyn model (Blatter, 1995; Pattyn, 2003) arises with a hydrostatic approximation error of $\mathcal{O}\left(\varepsilon^2\right)$ (Dukowicz et al., 2010; Schoof and Hindmarsh, 2010). This first-order approximation forms an elliptic coercive problem, significantly easier to solve than the intricate saddle-point problem of the full Stokes system.

For the purpose of this work, we shall consider two spatial dimensions: horizontal x and vertical z, respectively. This considerably reduces the computational time and allows for extremely high spatial resolutions ($\Delta x \sim 0.5$ km), whilst explicitly accounting for the vertical gradients in ice viscosity and velocity. The 2D version of the Blatter-Pattyn model can be written as:

$$\frac{\partial}{\partial x}\left(4\eta\frac{\partial u}{\partial x}\right)+\frac{\partial}{\partial z}\left(\eta\frac{\partial u}{\partial z}\right)=\rho g\frac{\partial h}{\partial x}, \tag{3.1}$$

where ρ is the ice density, g is the gravitational acceleration, $\eta(x,z)$ is the effective viscosity, $h(x)$ is the surface elevation and $u(x,z)$ is the ice velocity.

The problem is subjected to a set of boundary conditions. Nix considers potential friction at the base of the ice, and a free surface on the upper boundary (Veen and Whillans, 1989). In terms of velocity gradients, the free surface condition can be expressed as (Pattyn, 2003):

$$\frac{\partial u}{\partial z}=4\frac{\partial u}{\partial x}\frac{\partial h}{\partial x}, \tag{3.2}$$

and the basal drag is defined as the sum of all resistive forces:

$$\frac{\partial u}{\partial z}=4\frac{\partial u}{\partial x}\frac{\partial b}{\partial x}+\frac{\tau(u)}{2\eta}, \tag{3.3}$$

for the base ($z=b$) in the presence of potential drag $\tau(u)$ (see Section 3.2.4 for a thorough description on basal friction). A stress-free base can be obtained simply by setting $\tau=0$ in Eq. 3.3.

We further assume an ice divide at one end of the domain ($x=0$), where $\partial u/\partial x=0$, and hydrostatic equilibrium at the ice-ocean boundary ($x=L$), where the water pressure balances the longitudinal stress gradient. The full problem thus takes the following succinct form (subscripts hereinafter denotes partial differentiation):

$$\begin{cases} \left(4\eta u_x\right)_x+\left(\eta u_z\right)_z=\rho g h_x, & x\in\mathcal{I},\ z\in\mathcal{L},\\ u_z=4u_x h_x, & x\in\mathcal{I},\ z\in\partial\mathcal{L}^+,\\ 2\eta u_z=8\eta u_x b_x+\tau, & x\in\mathcal{I},\ z\in\partial\mathcal{L}^-,\\ u_x=0, & x=0,\ z\in\mathcal{L},\\ 8\eta u_x=\rho g H^2-\rho_w g z^2, & x=L,\ z\in\mathcal{L}, \end{cases} \tag{3.4}$$

where ρ_w is the water density, H is the ice thickness evaluated at the grounding line $x=L$ and the $\partial\mathcal{L}^{\pm}$ symbols denote the upper and lower vertical boundaries, respectively.

3.2.2 The Depth Integrated Viscosity Approximation

The mathematical problem underlying the Depth Integrated Viscosity Approximation (DIVA) stress balance is briefly described in Cartesian coordinates (Goldberg, 2011; Lipscomb et al., 2019).

As for the Blatter-Pattyn model, only one horizontal dimension shall be considered, leaving unaltered the nature of DIVA/SSA equations. This allows us to consider our model as a longitudinal section of a three-dimensional ice stream:

$$\frac{\partial}{\partial x}\left(4\bar{\eta}H\frac{\partial u}{\partial x}\right)+\tau(u)=\rho g H\frac{\partial h}{\partial x}. \tag{3.5}$$

Since the stress balance is also a second-order partial differential equation on the velocity, two boundary conditions are again needed. Analogously to the Blatter-Pattyn approximation, an ice divide is assumed at one end. At the other end of the domain, the problem is subjected to a dynamic boundary condition that accounts for the balance between cryostatic and hydrostatic pressures. Thus, the DIVA/SSA boundary problem can be expressed in the following compact form:

$$\begin{cases} \left(4\bar{\eta}Hu_x\right)_x+\tau(u)=\rho g H h_x, & x\in\mathcal{I},\\ u=0, & x=0,\\ 8\bar{\eta}u_x=\rho g H^2-\rho_w g D^2, & x=L, \end{cases} \tag{3.6}$$

where D is the distance from the sea surface to the bottom of the ice.

Equation 3.5 is an elliptic non-linear differential equation. In the purely SSA form (neither velocity nor viscosity dependency on z, i.e., $u=\bar{u}$ and $\eta=\bar{\eta}$), it constitutes the simplest form of longitudinal stress balance derivable from the Stokes model (Bueler and Brown, 2009). Solving for the velocity $u(x)$ is then possible by integrating Eq. 3.6 if the functions $H(x)$, $\bar{\eta}(x)$, $h(x)$ and $\tau(u)$ are known. This work implements an implicit algorithm so as to numerically integrate the one-dimensional DIVA/SSA equation (see integrating scheme description in Appendix B.3).

3.2.3 The advection coupling

Given that all models herein presented provide a quasi-static description of the ice flow, the stress balance does not determine the temporal evolution of the system, but rather it represents an equilibrium state for a particular ice thickness $H(x)$ and viscosity $\eta(x, z)$ configuration. The temporal evolution is generally considered by coupling the stress balance to the advection equation:

$$H_t + (\bar{u}H)_x = S(x), \tag{3.7}$$

where $S(x)$ is the surface mass balance. Given that Eq. 3.7 is first order, only one boundary condition is needed $H(x = 0, t)$ and the consequent initial condition $H(x, t = 0)$.

Equations 3.6 and 3.7 are now coupled to study the evolution of the ice thickness $H(x, t)$ governed by the advection equation, where the velocity field $u(x, z)$ satisfies the stress balance imposed by a particular choice of the Stokes approximation. Namely, our problem takes the following mathematical form:

$$\begin{cases} H_t + (\bar{u}H)_x = S(x), & x \in \mathcal{I},\ t > 0 \\ (4\eta u_x)_x + (\eta u_z)_z = \rho g h_x, & x \in \mathcal{I},\ z \in \mathcal{L}, \\ H = H_0, & x \in \mathcal{I},\ t = 0. \\ h_x = 0, & x = 0,\ t > 0. \\ u = 0, & x = 0,\ t > 0. \\ 8\eta u_x = \rho g H^2 - \rho_w g z^2, & x = L,\ z \in \mathcal{L},\ t > 0. \end{cases} \tag{3.8}$$

From a purely physical perspective, Eq. 3.8 describes a fluid membrane of variable thickness driven by its own weight that evolves in time due to advection.

3.2.4 Basal friction

Basal shear stress can be generally expressed as a function of the sliding velocity u_b and the effective pressure N, i.e., $\tau_b = f(u_b, N)$. The physical properties of the material over which the ice may potentially slide can correspond either to a hard bedrock flow (e.g., Weertman, 1957) or to a Coulomb-plastic

rheology (e.g., Tulaczyk et al., 1998). Moreover, the influence of the sliding velocity on τ_b is often represented by a power friction law, although a regularization term u_0 accounting for local properties of the bed has been shown to outperform such a power law in both pressurized ice experiments (Zoet and Iverson, 2020) and observations (Minchew et al., 2018; Stearns and van der Veen, 2018; Joughin et al., 2019)

As a result, Nix can calculate the basal shear stress (i.e., basal drag) via two independent formulations: a pseudo-plastic power law (Schoof, 2010; Aschwanden et al., 2013) and the regularized-Coulomb law (Schoof, 2005; Joughin et al., 2019). The former reads:

$$\boldsymbol{\tau}_b = -c_b \left(\frac{|\boldsymbol{u}_b|}{u_0} \right)^q \frac{\boldsymbol{u}_b}{|\boldsymbol{u}_b|}, \tag{3.9}$$

where $u_0 = 100$ m/yr and c_b is a spatially-variable friction coefficient defined below. Two particular cases of the pseudo-plastic law based upon the choice of the exponent q deserve special attention. Namely, the linear law ($q = 1$; e.g., Quiquet et al., 2018) and the purely plastic law ($q = 0$).

On the other hand, the regularized-Coulomb formula is given by:

$$\boldsymbol{\tau}_b = -c_b \left(\frac{|\boldsymbol{u}_b|}{|\boldsymbol{u}_b| + u_0} \right)^q \frac{\boldsymbol{u}_b}{|\boldsymbol{u}_b|}, \tag{3.10}$$

behaving as a power law for small sliding velocities (i.e., $u_b < u_0$) whilst always yielding a bounded friction value for arbitrarily high velocities (i.e., $u_b \gg u_0$). Following Zoet and Iverson (2020), this thesis sets $q = 1/5$ and $u_0 = 100$ m/yr by default to ensure a reasonable transition to the steady-state shear stress supported by the till bed. The same study empirically established that q remains unaffected by variations in the detailed bed surface geometry.

The basal drag coefficient β is usually defined as:

$$\beta = c_b(x) N, \tag{3.11}$$

where $N = \rho g H$ is the overburden pressure exerted by the ice column and $c_b(x)$ is a coefficient that reflects the bedrock characteristics.

Nevertheless, for simplicity and consistency with prior benchmark experiments as MISMIP (Pattyn et al., 2012), the model also allows to represent basal friction as:

$$\tau_b = Cu^q, \tag{3.12}$$

with the chosen value of $C = 7.624 \times 10^6$ Pa m$^{-1/3}$ s$^{1/3}$ and $q = 1/3$, a sliding velocity of about 35 m yr^{-1} yields a basal shear stress of 80 kPa.

3.2.5 Thermodynamics

The ice temperature in the flow line depends on the two spatial dimensions x and z (horizontal and vertical, respectively) along with time (i.e., $\theta = \theta(x, z, t)$). Heat transfer is further considered to occur due to vertical diffusion, both horizontal and vertical advection and internal heat deformation. Energy conservation is ensured in a classical approach by a balance equation that neglects neglecting horizontal diffusion (Greve and Blatter, 2009):

$$\begin{cases} \rho c \theta_t = k\theta_{zz} - \rho c \left(u\theta_x + w\theta_z \right) + \Phi, & x \in \mathcal{I},\ z \in \mathcal{L},\ t > 0, \\ \theta = \theta_0, & x \in \mathcal{I},\ z \in \mathcal{L},\ t = 0, \\ \theta_z = -G/k, & x \in \mathcal{I},\ z = \partial\mathcal{L}^-,\ t > 0, \\ \theta = \theta_L, & x \in \mathcal{I},\ z = \partial\mathcal{L}^+,\ t > 0, \end{cases} \tag{3.13}$$

where k is the ice conductivity, c is the specific heat capacity, $\Phi = 4\eta\dot{\varepsilon}^2$ denotes the internal strain heating, G is the geothermal heat flow, θ_0 is the initial temperature profile and θ_L surface ice temperature. The $\partial\mathcal{L}^\pm$ symbols denote the upper and lower vertical boundaries, respectively.

The energy balance is discretised using an upwind scheme with a forward Euler step and centred differences for the spatial derivatives (see Appendix A4 for a detailed description).

3.2.6 Viscosity

Glen's flow law (Glen 1955; Nye, 1957) is considered to relate the shear stress, the ice temperature and the pressure of isotropic polycrystaline ice. Formation of anistropic fabric is considered via a flow enhancement factor.

As shown in Section 3.1, the Blatter-Pattyn stress balance equations define the effective viscosity as:

$$\eta = \frac{B}{2} \left(\dot{\varepsilon}^2 + \dot{\varepsilon}_0^2 \right)^{\frac{1-n}{2n}}, \tag{3.14}$$

where B is the ice hardness, $n = 3$ is the exponent in Glen's flow law, $\dot{\varepsilon}^2$ is the effective strain rate and $\dot{\varepsilon}_0^2$ is a regularization factor to elude potential singularities when velocity gradients are zero. Notably, for a 2D model with explicit thermodynamics, the viscosity expression further simplifies the expression of B and $\dot{\varepsilon}^2$:

$$B = A(\theta)^{-1/n}, \tag{3.15}$$

$$\dot{\varepsilon}^2 = \left(\frac{\partial u}{\partial x} \right)^2 + \frac{1}{4} \left(\frac{\partial u}{\partial z} \right)^2, \tag{3.16}$$

where $n = 3$ is the Glen-flow exponent. $A(\theta)$ is the rate factor and follows an Arrhenius law:

$$A(\theta) = A_0 E e^{-Q/R\theta}, \tag{3.17}$$

A_0 and Q are the temperature-dependent rate factor coefficient and activation energy, respectively (Greve and Blatter, 2009). E_f is the so-called enhancement factor, commonly used to approximate the effect of anisotropic flow. It is possible to specify different values of the enhancement factor for different flow regimes (shear or stream). Typical values of the enhancement factor for the shearing and streaming regimes are $E_{\text{shr}} = 3.0$ and $E_{\text{strm}} = 0.7$ (Ma et al., 2010), respectively. Here, a default value of $E = 1.0$ is used in both cases.

For the vertically-integrated stress balance models (i.e., DIVA and SSA), Eqs. 3.14 and 3.15 are slightly modified by computing the vertically averaged quantities $\bar{\eta}$ and $\bar{B}$ following the generic formula $\bar{f} = \frac{1}{H} \int_b^h f dz$.

3.2.7 Grounding line

Nix aims at simulating the flow of a sliding ice sheet. Since the longitudinal stress at the grounding line $x = L$ is simply a function of the ice thickness therein $H(x = L)$ for a 2D ice sheet (Schoof, 2007a), the behaviour of grounded ice and the location of the grounding-line itself are completely independent of the floating part.

Neither the potential distinct shapes of the ice shelf (e.g., due to sub-shelf melting) nor the calving affect the dynamics of grounded ice. Thus, the flotation condition and the stress condition (Eq. 3.8) can be considered as boundary conditions at the grounding line. These two conditions are in fact sufficient to study the ice thickness evolution and the grounding-line migration.

Following Hindmarsh (1996), an explicit expression for the grounding-line migration rate $\dot{L}$ can be readily obtained from a total differentiation of the flotation condition:

$$\dot{L} \equiv \frac{dL}{dt} = \frac{\varrho D_t + (\bar{u}H)_x - S}{H_x - \varrho D_x}, \tag{3.18}$$

where D is the water depth at the grounding line and $\varrho = \rho_w/\rho$ is the water-to-ice density ratio, respectively.

More recent studies suggest that the maximum terminus thickness is bounded by the yield strength of ice τ_c (Bassis and Walker, 2012; Bassis and Jacobs, 2013). Hence, a maximum ice thickness at the terminus occurs when the stress exceeds the depth integrated strength of ice:

$$H^{\max} = \frac{\tau_c}{\rho g} + \sqrt{\left(\frac{\tau_c}{\rho g}\right)^2 + \varrho D^2}, \tag{3.19}$$

thus constraining the terminus thickness such that $H(x = L, t) \leq H^{\max}$.

This approach eludes semi-empirical parametrizations of the calving (as in Schoof, 2007) and further provides a lower bound on the rate of grounding line advance (Bassis et al, 2017). Combining the continuity equation and the material derivative of $H^{\max}$ (Eq. 3.19), an expression for the rate of advance/retreat of the terminus can be readily obtained:

$$\frac{dL}{dt} \geq \frac{H_t}{H_x^{\max} - H_x}, \tag{3.20}$$

at $x = L$. Negative sign indicates retreat.

Inequality Eq. 3.20 is analogous to the grounding-line migration derived for a marine ice sheet by Schoof (2007a; 2007b). Particularly, if $H^{\max}$ is given by the flotation condition, Eq. 3.20 exactly reproduces the grounding line position derived by Schoof (2007b) (Bassis et al., 2017).

3.2.8 Sub-shelf melting parametrization

Oceanic melting beneath ice shelves is the main driver of the current mass loss of the Antarctic ice sheet (Favier et al., 2014; Joughin et al., 2014). For this reason, Nix considers various melting parameterisations, such as simple scaling with far-field thermal driving (e.g., Favier et al., 2019).

We adhere to local yet physically-based parametrizations based on ocean circulation models (Grosfeld et al., 1997). Namely, the linear dependency can be expressed as:

$$M = \gamma_T \varrho \frac{c_{\mathrm{po}}}{L_{\mathrm{i}}} \left(T - T_0\right), \tag{3.21}$$

where γ_T is the heat exchange velocity, T_0 is a reference temperature, c_{po} is the specific heat capacity of the ocean mixed layer and L_{i} is the latent heat of fusion of ice.

This linear formulation with a constant exchange velocity γ_T assumes a circulation in the ice-shelf cavity that is independent from the ocean temperature. This assumption is neither supported by modelling (Holland et al., 2008; Donat-Magnin et al., 2017) nor by observational studies (Jenkins et al., 2018) that suggest a larger circulation in response to a warmer ocean, subsequently increasing melt rates. One manner to account for this positive feedback is by considering a quadratic dependency (Holland et al., 2008):

$$M = \gamma_T \left(\varrho \frac{c_{\mathrm{po}}}{L_{\mathrm{i}}}\right)^2 \left(T - T_0\right)^2. \tag{3.22}$$

These two parametrizations have been employed in numerous studies (e.g., review in Asay-Davis et al., 2017; Favier et al., 2019). This melt rate is included as an additional term in the ice flux computation (Eq. 3.7 and 3.18). By default, Nix uses this quadratic parametrization.

3.2.9 Calving

The objective of Nix model is to simulate the dynamics of grounded ice and understand the implications of thermodynamic coupling on grounding line migration and the overall stability. Notably, grounded ice flow is completely decoupled from the shelf evolution in a two-dimensional ice sheet (Schoof,

2007a). In other words, changes in the shelf have no effect on the grounded ice so long as the following conditions are met: the existence of a freely-floating, finite and two-dimensional shelf.

As a result, the calving rate does not perturb the grounded ice flow, thus relaxing the necessity of prescribing a certain calving rate. This precisely becomes one of the limitations of the model: absence of buttressing. Such mechanism produces a reduction in grounding line stress, though solely half as sensitive as it is to ice thickness (Eq. 19 in Schoof, 2007a). Moreover, buttressing should not be parametrised via a corrector factor in the ice flux at the grounding line since it must be determined from the conservation of momentum in the shelf (e.g., Schoof, 2007a).

Nonetheless, in real marine-terminating ice sheets, flux anomalies could be driven by submarine melt, variable calving or a combination. Following Christian et al. (2022), Nix simply interprets these as flux anomalies at the grounding line determined by variable ocean conditions. Consquently, frontal ablation thus encompasses both processes as an ice flux perturbation at the terminus position and amounts to an additional outflow of ice beyond the local velocity given by the stress balance. Compared to the absence of frontal ablation (i.e., no calving or sub-shelf melt), the terminus retreats further and the surface slope therein becomes steeper to compensate for the additional outflow of ice.

3.3 Model numerics

3.3.1 Moving grid transformation

Nix uses a nonuniform moving spatial grid that explicitly solves the grounding-line position. By default, the grid points distribution yields higher resolution near the grounding line following a polynomial or an exponential law (details in Appendix A.4). Evenly-spaced grids are also possible by setting the polynomial order to one.

As already noted by Pattyn et al. (2012), moving grid models are presumably the best choice in 2D models from a numerical perspective, as the grounding line position $L(t)$ is part of the solution and no interpolations are further required. Given that neither the terminus position $L(t)$ (i.e., the

grounding line) nor the ice thickness $H(x,t)$ are fixed in time, Nix adopts a moving grid to trace their positions:

$$\sigma = \frac{x}{L(t)}, \quad \zeta = \frac{z - b(x)}{H(x,t)}, \quad \tau = t, \tag{3.23}$$

thus mapping the time-dependent intervals $0 \leq x \leq L(t)$ and $0 \leq z \leq H(x,t)$ into fixed ones $0 \leq \sigma \leq 1$ and $0 \leq \zeta \leq 1$. The variable τ is merely introduced to distinguish partial derivatives defined holding both σ and ζ constant (as opposed to hold x and z constant).

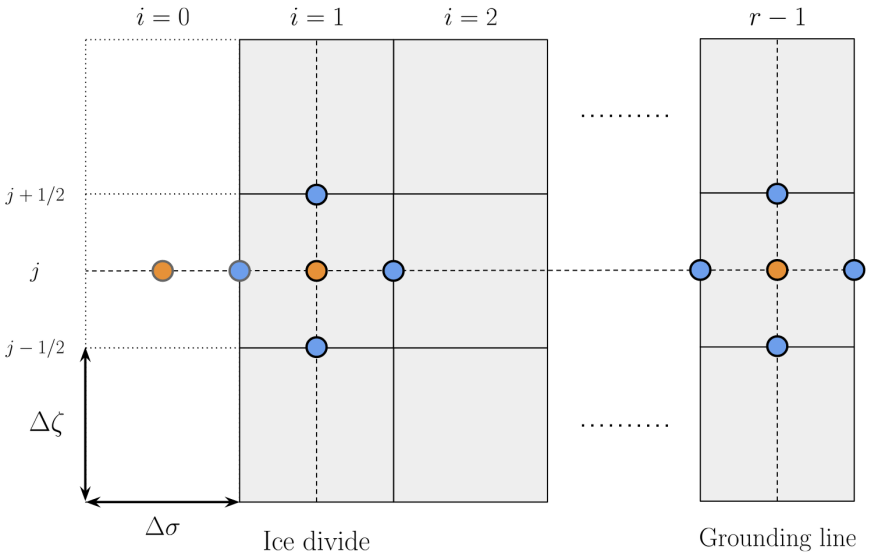

Fig. 3.2: Nix staggered grid definition follows an Arakawa-C scheme (Arakawa and Lamb, 1977). The number of grid points the the horizontal r and vertical p is fixed in time (see Appendix B.1). As Nix employs a moving grid, the position of the last horizontal point $(r - 1/2)$ explicitly tracks the grounding line $L(t)$. The grid spacing in the vertical $\Delta\zeta_j$ and horizontal $\Delta\sigma_i$ axis can be spatially dependent as Nix allows for nonuniform grids. Ghost points required to satisfy the boundary condition at the ice divide are noted in grey edge colour.

As a result, the corresponding derivatives contain additional terms (upong application of the Leibniz rule):

$$\frac{\partial}{\partial z} = \frac{1}{H}\frac{\partial}{\partial \zeta}, \tag{3.24}$$

$$\frac{\partial}{\partial x} = \frac{1}{L}\frac{\partial}{\partial \sigma} - \frac{1}{H}\left[(1-\zeta)\,\frac{\partial b}{\partial \sigma} + \zeta\frac{\partial H}{\partial \sigma}\right]\frac{\partial}{\partial \zeta}, \tag{3.25}$$

$$\frac{\partial}{\partial t} = \frac{\partial}{\partial \tau} - \frac{\sigma}{L}\frac{\partial L}{\partial \tau}\frac{\partial}{\partial \sigma} - \frac{\zeta}{H}\frac{\partial H}{\partial \tau}\frac{\partial}{\partial \zeta}. \tag{3.26}$$

For simplicity and analogously for the Blatter-Pattyn approximation, the advection equation coupled with the SSA/DIVA stress balance can be written in terms of the new variables. Thus, Eq. 3.8 reads:

$$\begin{cases} LH_\tau - \sigma\dot{L}H_\sigma + (uH)_\sigma = LS(\sigma,\tau), & \sigma \in \tilde{\mathcal{I}},\ \tau > 0 \\ (4\bar{\eta}Hu_\sigma)_\sigma + \tau L^2 = L^2\rho g h_\sigma & \sigma \in \tilde{\mathcal{I}}. \\ H = H_0, & \sigma \in \tilde{\mathcal{I}},\ \tau = 0. \\ H_\sigma = 0, & \sigma = 0,\ \tau > 0. \\ u = 0, & \sigma = 0, \\ 4\eta u_\sigma = \left(\rho g H^2 - \rho_w g D^2\right) L/2, & \sigma = 1, \end{cases} \tag{3.27}$$

where $\tilde{\mathcal{I}} \in [0,1]$ is the transformed interval and the subscripts denote partial differentiation.

Likewise, the third evolution equation that determines the behaviour of our system (i.e., the energy balance, Eq. 3.13) can be readily obtained in terms of our new variables:

$$\begin{cases} \rho c\left[L\theta_\tau - \sigma\dot{L}\theta_\sigma - \zeta L H_\tau \theta_\zeta/H\right] = \\ \qquad kL\theta_{\zeta\zeta}/H^2 - \rho c u\left[\theta_\sigma - (b_\sigma + \zeta H_\sigma)\theta_\zeta/H\right] + L\Phi, & \sigma \in \tilde{\mathcal{I}},\ \zeta \in \tilde{\mathcal{L}},\ \tau > 0, \\ \theta = \theta_0, & \sigma \in \tilde{\mathcal{I}},\ \zeta \in \tilde{\mathcal{L}},\ \tau = 0, \\ \theta_z = -G/k, & \sigma \in \tilde{\mathcal{I}},\ \zeta = \partial\tilde{\mathcal{L}}^-,\ \tau > 0, \\ \theta = \theta_L, & \sigma \in \tilde{\mathcal{I}},\ \zeta = \partial\tilde{\mathcal{L}}^+,\ \tau > 0, \end{cases} \tag{3.28}$$

where the transformed intervals are again denoted by $\tilde{\mathcal{I}}$ and $\tilde{\mathcal{L}}$ respectively.

3.3.2 Spatial integration

3.3.2.1 Implicit scheme and Picard iteration

The lateral boundary condition is in fact non-trivial to implement using an explicit scheme (e.g., a shooting-like method) since it depends on the first spatial derivative of the velocity at the terminus position $\sigma = 1$, which might lead to convergence issues. Nix thus includes an alternative velocity solver based on an implicit discretization shcheme of all stress balance models described in Section 3.3 (discretisation details in Appendix B).

To account for the potential non-linearity in the velocity as a consequence of the viscosity and basal friction $\tau(u)$, the implicit solver uses a initial guess τ_0 and η_0 and then enters a Picard iteration (see Theorem 2.2 in Teschl, 2012). A solution is hence obtained when the convergence criterion:

$$\frac{||u^n - u^{n-1}||}{||u^n||} < \phi_{\text{tol}} \tag{3.29}$$

is satisfied. The tolerance ϕ_{tol} can be set by the user but the default value is 10^{-6}.

For the Blatter-Pattyn approximation, a sparse matrix must be solved in each Picard iteration. To do so, a Biconjugate Gradient Stabilized method (commonly known as BiCGSTAB) is applied with an Incomplete preconditioner (ILUT). On the contrary, the DIVA/SSA approximation solely requires solving a tridiagonal matrix at in each Picard iteration step, where the ice viscosity is updated. A tridiagonal solver algorithm is implemented as a subroutine within Nix to avoid additional external dependencies (see Appendix B.1).

3.3.3 Time integration

Once the velocity field $u(x, z)$ is obtained for a given set of boundary conditions and a particular ice thickness initial distribution $H(\sigma, \tau_0)$, the time evolution of the latter is computed as a consequence of the advection imposed by $\bar{u}(x)$ and the surface mass balance $S(x, t)$ (Eq. 3.7). Thus, this coupled system formed by the momentum conservation and the continuity equation

(Eq. 3.27) is fully integrated in two steps: first, a spatial integration to obtain the velocity (where the ice viscosity is known); and then, a forward time integration to determine the new ice thickness. Lastly, the energy balance equation is integrated to compute the new temperature field.

Specifically, for a given initial ice-thickness distribution $H(x, t_0)$, the stress balance equation is spatially integrated, thus yielding the velocity $u(x, z)$. Then, the solution $u(x, z)$ (at t_0) and $H(x, t_0)$ allow us to integrate the continuity equation forward in time, consequently obtaining $H(x, t_0 + \Delta t)$. Additionally, this new ice thickness distribution yields $\theta(x, z, t_0 + \Delta t)$, thus constituting a self-consistent iterative method.

3.4 Methods and experimental set-up

Prior to any comprehensive description of the results, Nix capability of reproducing the benchmark tests of the Marine Ice Sheet Model Intercomparison Project (MISMIP Pattyn et al., 2012) is first tested. To this end, we will perform all three MISMIP experiments: relaxation to steady state on a downward-sloping bed (Exp. 1), reversal of parameter (Exp. 2) and hysteresis on an overdeepening bed (Exp. 3). The aim of Exp. 1 was to show that there should be a single stable equilibrium profile on a downward-sloping bed. A backwards parameter relaxation in Exp. 2 was intended to demonstrate that grounding-line positions should be identical during advance and retreat, as steady states are unique. Exp. 3 was designed to assess whether ice-sheet models exhibit hysteresis behaviour and has become a benchmark for testing the capability of numerical models to simulate grounding-line migration.

First, the exact same problem definition is adopted so as to perform a one-to-one comparison. Next, an ensemble of simulations is run to address the question of whether the hysteresis with respect to model parameters variations found in MISMIP Exp. 3 is still present even if the thermal state of the ice can evolve in time (as opposed to the idealised constant ice factor A set in Pattyn et al., 2012). Fixing A uniquely determines a constant ice temperature, since $A(T)$ is a bijective function of the temperature. This thesis therefore impose an atmospheric forcing (i.e., the ice surface boundary condition) that spans a wide range of realistic temperatures. As the geothermal heat flux provides a positive energy contribution, it is expected a different

thermal equilibrium profile for each imposed surface temperature. This yields a different viscosity field for each scenario, consequently leading to a different equilibrium velocity. As noted by Sergienko et al. (2013), the temperature profile is mostly determined by horizontal advection in streaming regions, thus bringing forward a strongly non-linear feedback worthy of attention.

Lastly, the system is forced via ocean temperature anomalies with respect to a reference value T_0, so that $\Delta T_{\text{oce}} = T_{\text{oce}} - T_0$, whilst holding constant the air temperature throughout the simulation. These temperature anomalies are then converted into sub-shelf melting at the grounding line (e.g., Favier et al., 2019) by computing any of the parametrizations described in Section 3.2.8. Even though the air temperature is held constant (i.e., the boundary condition of our heat problem), the thermal state of the ice may evolve as both the thickness and extent are perturbed by the changing sub-shelf melting at the grounding line. Our particular ocean forcing consist of steps of 0.5ºC evenly-spaced in time by 30 kyr to ensure equilibration, from $\Delta T_{\text{oce}} = 0$ to a maximum applied anomaly of 7ºC. Then, the forcing is reversed to recover the unperturbed state (i.e., zero anomaly).

It is worth noting that the basal friction remains identical to that in the MISMIP experiments both for the atmospheric and oceanic forcings. This means that no additional dependency of friction on temperature or hydrology is considered.

Table 3.1: Nix suite of experiments. The first row replicates MISMIP benchmark tests, whereas MISMIP-therm explores the hysteresis behaviour of a thermomechanically active ice sheet in two different forcing scenarios: amospheric and oceanic.

Experiment name	Forcing variable	Thermodynamics	Melting/calving at GL
MISMIP (Exp. 1, 2 and 3)	Ice rate factor A	No	No
MISMIP+therm (Exp. 3)	Air temperature T_{air}	Yes	No
	Ocean temperatures anom. ΔT_{oce}	No ($A = \text{const.}$)	Yes
		Yes ($A = f(T)$)	Yes

3.5 Results

3.5.1 MISMIP benchmark experiments

As a performance test for the Nix ice sheet model, simulations (Fig. 3.3) fairly reproduce the results shown by models that employ a stretched coordinate system as ours.

Figure 3.3b shows both the advancing and retreating phase in Pattyn et al. (2012) (Experiments 1 and 2, respectively), equilibrium grounding-line positions coincide and points thus overlap. Additionally, we find no stable equilibrium states for the downward-sloping bed of Exp. 3 (Fig. 3.3a and 3.3b), in agreement with the theoretical considerations by Weertman (1974) and Schoof (2007a). Namely, as we gradually decrease A (i.e., increasing ice viscosity), the grounding-line position advances across the downward sloping bed until the upward-sloping region is reached (Fig. 3.3c). The ice flux at the grounding line then continuous to increase as A decreases. Illustrated by Fig. 3.3d, when the ice flux is large enough so that there exists a stable solution beyond the unstable region (at the right-hand side of the bedrock peak in Fig. 3.3c), the grounding line traverses the upwards-sloping sector reaching a new stable solution.

Additionally, the three MISMIP experiments are repeated using the more sophisticated velocity solvers available in Nix: DIVA and Blatter-Pattyn. A direct inspection of Figs. 3.3b and 3.3d reveals that the solutions are nearly identical to the simpler SSA version, both for a downwards sloping and the overdeepending beds. The hysteresis is particularly well captured in all three Stokes approximations. Thus, the SSA solver is employed in the remainder of the current work to minimise computational costs unless otherwise stated.

3.5.2 MISMIP + thermodynamics

To exploit the fact that Nix is fully coupled with a thermodynamic solver, we further investigate the equilibrium states (Schoof, 2007a) when the system is forced via two different forcings: air temperatures T_{air} and ocean temperature anomalies ΔT_{oce}. Both describe more realistic conditions with slight variations. The former implies the same underlying perturbation mechanism

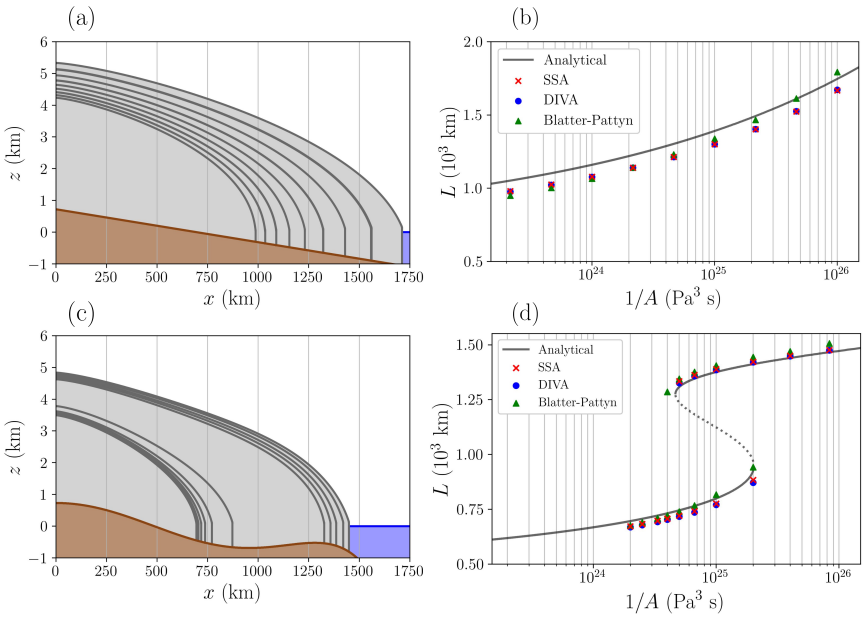

Fig. 3.3: Left column: ice sheet extent. Right column: grounding-line position as a function of the MISMIP forcing A for three independent Stokes approximations: SSA, DIVA and Blatter-Pattyn. Grey line represents the analytical solution at equilibrium from Schoof (2007a): solid line, stable branch; dashed line, unstable. Markers represent Nix results after the equilibration time given in Pattyn et al. (2012). Bed geometries correspond to Experiments 1 and 2 (first row) and Experiment 3 (second row), respectively.

(as for the idealised rate factor A forcing): temperature changes within the ice modify its viscosity so that the grounding line migrates to reach a new equilibrium position. Nevertheless, when forcing the system with ocean temperature anomalies ΔT_{oce} while keeping the air temperature constant, we perturb the system via an additional outflow term at the grounding line. By separately studying each mechanism, it can be determined whether a marine terminating ice sheet might undergo hysteresis under different forcings.

3.5.2.1 Air temperature T_{air} forcing

At the aim of building a thermomechanically active version of MISMIP experiments, the natural choice is to convert the idealised ice-rate factor forcing in

MISMIP into temperatures (via an Arrhenius law, Eq. 4.11) and then use it explicitly as a forcing of the new experimental setup. For a more sophisticated forcing, a vertical dependency of the temperature is further considered via a lapse rate. Default setup in Nix accounts for adiabatic conditions $\Gamma = -9.8$ $^{\mathrm{o}}$C/km, though any value can be imposed.

The particular atmospheric forcing is imposed at the sea level $T_{\mathrm{air}}(t)$ as shown in Fig. 3.4a. Starting from warm conditions $T_{\mathrm{air}} = 0^{\mathrm{o}}$C, it reaches a minimum value of -30^{o}C in gradual steps that last 40 kyr each to ensure thermal quasi-equilibrium. Nonetheless, lower temperatures are present near the ice divide as the surface extends far above the sea level, wherein the lapse rate correction becomes relevant. This experiment reflects the insulating effect of the ice sheet as the forcing eventually reaches the initial atmospheric temperature but the grounding line does not retreat (Fig. 3.4b and 3.4f). It is not possible to make a one-to-one comparison with (Schoof, 2007a), given the different physical description of the system. Nonetheless, it is illustrative to represent the grounding-line position as a function of the ice temperature therein evaluated at two different depths and the vertical mean (Fig. 3.4b). The near-base temperature closely matches the theoretical prediction by the boundary layer. Shallower layers appear shifted the right since the effect of the warmer surface becomes relevant.

In terms of the hysteresis behaviour, the jump over the retrograde region of the bed geometry occurs for near-base temperature of -30^{o}C, as predicted by the semi-analytical counterpart (see grey solid line, Fig. 3.4). Even so, when the forcing returns to the initial value, the grounding line does not retreat back to its original position and remains advanced (black square in Fig. 3.4b). On the contrary, for shallower ice layers, the warming branch extends far from the analytical results, thus showing larger bistability against atmospheric temperature changes. As for the near-base layer, when the initial forcing state is eventually reached, the ice sheet extends beyond the bedrock peak and does not retreat. This is also well captured in Fig. 3.5 by comparing panels 3.5b and 3.5f knowing that both are equilibrium states with identical forcing. These results strongly differ when using a downwards-sloping bed geometry, as shown in panels 3.5a, 3.5b 3.5e, where thermodynamics is also active but not hysteresis is present as the bedrock does not present retrograde regions.

Lastly, it is worth noting the temperature proximity to melting point particularly at right hand side of the base in all panels due to the combined contribution of geothermal heatflux and frictional heat dissipation, Fig. 3.5a, 3.5b, 3.5e and 3.5f favoured by a warmer atmospheric temperature. Unlike panels 3.5c and 3.5d, where the lower surface temperature perturbs the entire temperature profile, thus only partially cooling the ice sheet base. It must be stressed that near the grounding line, there is a reduction in the basal temperature as a result of a considerably thinner ice, thus providing less thermal insulation of the colder surface.

3.5.2.2 Ocean temperature anomalies ΔT_{oce} forcing

In this configuration, ocean temperature anomalies are applied with respect to a reference value T_0, so that $\Delta T_{\mathrm{oce}} = T - T_0$. These temperature anomalies are then converted into sub-shelf melting at the grounding line (e.g., Favier et al., 2019) by usingany of the parametrizations shown in Section 3.2.8.

First, this study performs two identical hysteresis experiments forced by ΔT_{oce} that solely differ on the thermodynamic treatment of the ice: an idealised fixed ice rate factor A (Fig 3.6, blue curve) and a more realistic active thermodynamic scenario with a constant boundary condition T_{air} (Fig 3.6, red curve). Results show that active thermodynamics considerably widens the width of the hysteresis loop. This behaviour resembles that obtained for the atmospheric-forced simulations (Fig. 3.4), where a larger extent of the cooling branch compared to the semi-analytical solutions is found (grey line, Fig. 3.4)..

In addition to the experiments carried out to assess the importance of thermodynamics on the hysteresis behaviour of a marine terminating ice sheet, a sensitivity study is performed to quantify the differences caused by parameter uncertainty (e.g., Favier et al., 2019), particularly on the heat exchange velocity γ.

Figure 3.7 illustrates the high sensitivity to that stems from the heat exchange velocity parameter γ. It is worth noting that the retreat is much more sensitive to the particular γ choice than the later advance as the anomalies approach zero. Namely, all intermediate values advance at $\Delta T_{\mathrm{oce}} = +1.5^{\mathrm{o}}\mathrm{C}$. On the contrary, the retreat occurs for a wider range of temperature anoma-

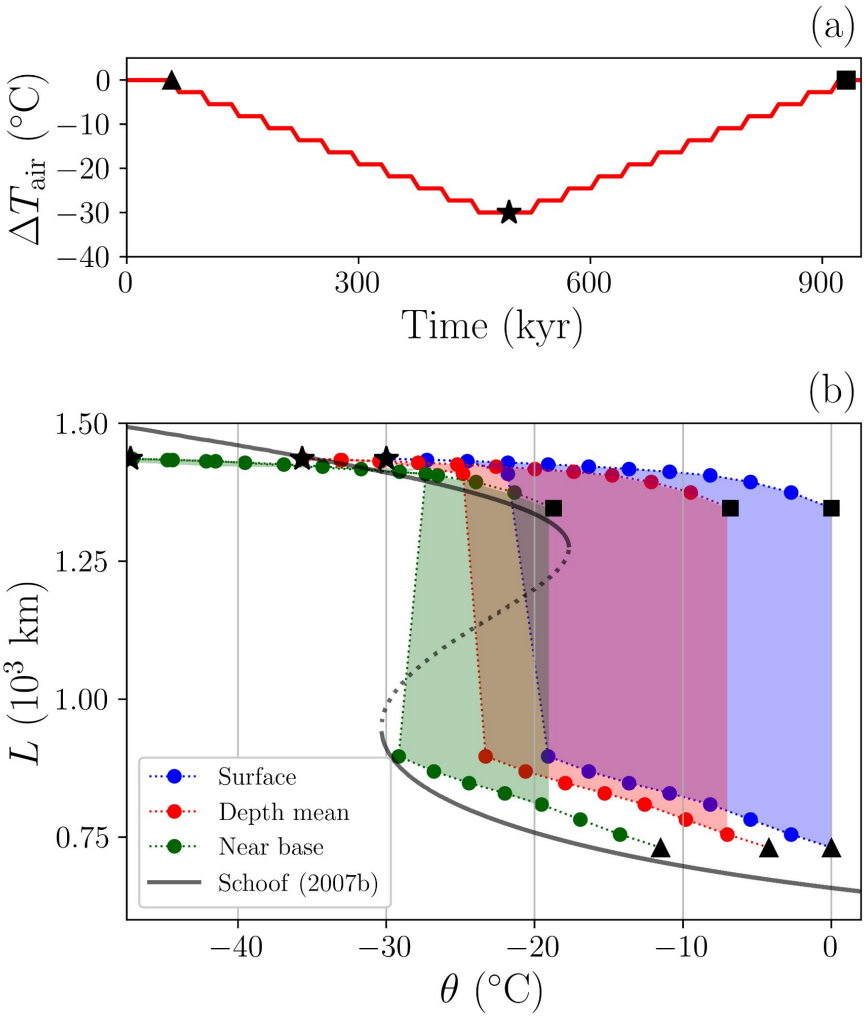

Fig. 3.4: Overdeepened bed experiment forced with atmospheric temperatures. (a) Forcing time series: atmospheric temperatures $T_{\text{air}}(t)$. Each black symbol represents three snapshots of particular interest: initial state (triangle, warmest conditions), coldest forcing conditions (star) and final state (square, same exact atmospheric conditions as the beginning). (b) Grounding line position as a function of the ice temperature evaluated at two different depths (near-base and surface) and vertical mean. Note that the initial and end states strongly differ in ice extent even though the atmospheric forcing is identical. The grey line represents analytical results in the absence of thermodynamics (i.e., imposed rate factor A), following Schoof (2007a).

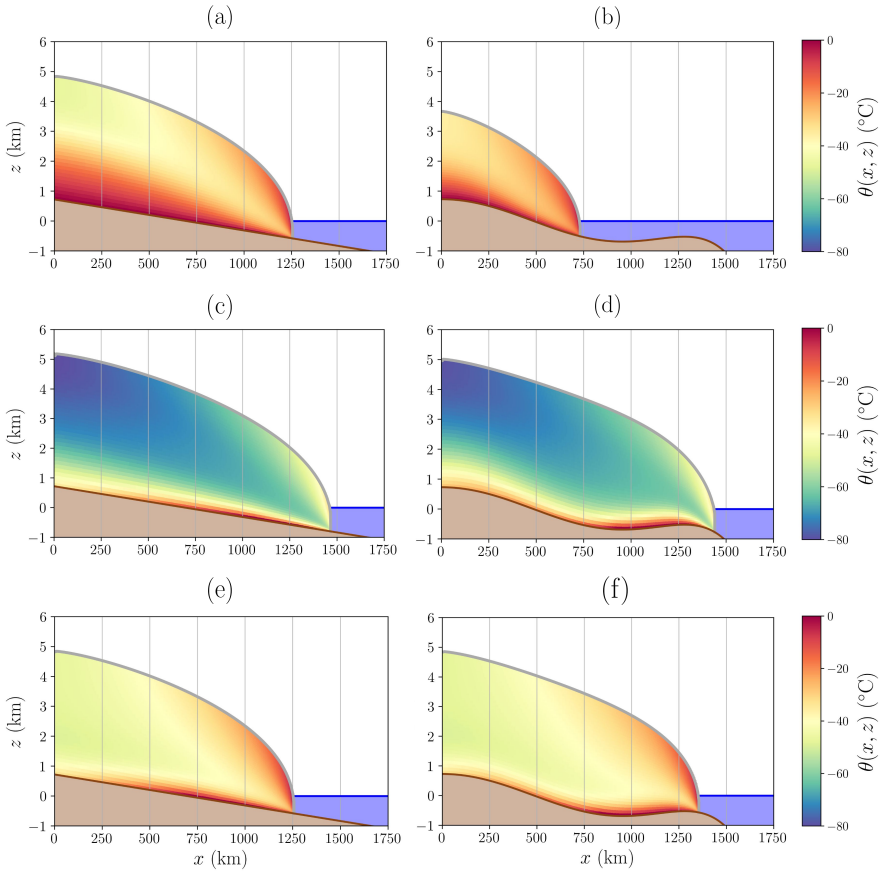

Fig. 3.5: Ice sheet extent and temperature distribution for the prograde (left column) and the overdeepened (right column) bed geometries. Each row represents a snapshot given by each symbol in Fig. 3.4 (triangle, star and square, respectively): initial warm state (first row), coldest atmospheric conditions (second row) and final atmospheric configuration (third row). Note that the overdeepening bed geometry yields a final ice sheet profile extended far beyond the initial state even though the boundary conditions are identical, thus exhibiting hysteresis. Colours indicate the ice temperature at the given time.

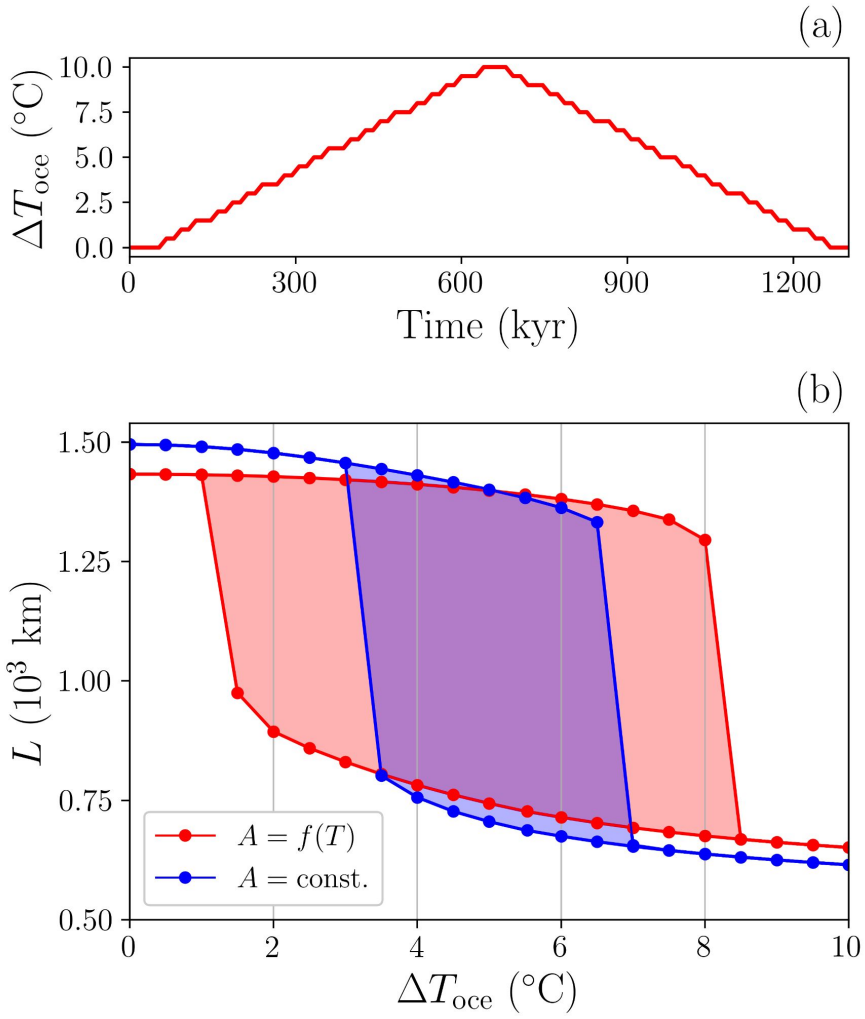

Fig. 3.6: (a) External forcing time series: ocean temperature anomalies $\Delta T_{\text{oce}}(t)$. Time duration of each step equals 30 kyr. (b) Hysteresis experiments for the overdeepened bed geometry forced via slowly-varying ocean temperature anomalies $\Delta T_{\text{oce}}(t)$. Blue: constant ice rate factor $A = 10^{-26}$ Pa^3s. Red: active thermodynamics $A = f(T)$ with fixed boundary condition $T_{\text{air}} = -40$ ºC. Each forcing step is ran for 30 kyr to ensure quasi-equilibrium (solid dots). A quadratic sub-shelf parametrisation is employed in both scenarios. Heat exchange velocity parameter $\gamma = 10^{-3}$ m/s.

lies from +4.5ºC to +6.5ºC for $\gamma = 2.1 \times 10^{-5}$ m/s and 1.3×10^{-5} m/s, respectively.

For a quadratic sub-shelf parametrisation (Eq. 3.22), the retreat takes place at $\Delta T_{\text{oce}} = +2.5$ºC for the highest heat exchange velocity calibrated in Favier et al. (2019), i.e., $\gamma = 100 \times 10^{-5}$ m/s. Even the lowest parameter value presented in the same work also presents a retreat if the ocean temperature anomalies reach $\Delta T_{\text{oce}} = +6.5$ºC. Multiple different values of γ advance back at nearly the same particular forcing value ΔT_{oce} 3.7, whereas the retreat happens at significantly different values. To illustrate this, it is illustrative to observe the hysteresis loops corresponding to $\gamma = 20 \times 10^{-5}$ m/s, 25×10^{-5} m/s, 35×10^{-5} m/s. They respectively retreat at $\Delta T_{\text{oce}} = +5.5$ºC, +5.0ºC and +4.5ºC, whereas the advance take place at precisely the same anomaly value $\Delta T_{\text{oce}} = +2.5$ºC.

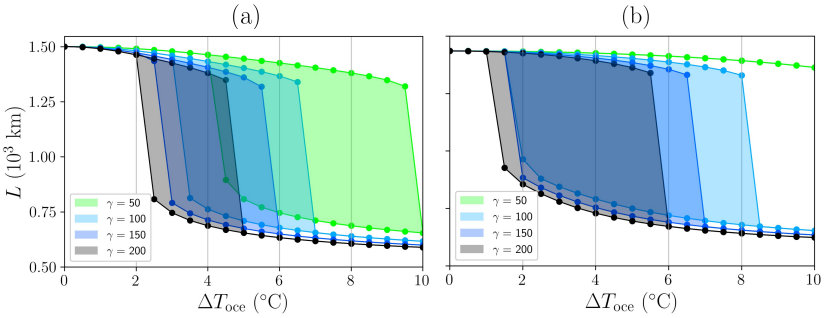

Fig. 3.7: Sensitivity tests. As in Fig. 3.6a, but for (a) Constant ice rate factor $A = 10^{-26}$ Pa^{3}s. (b) Active thermodynamics with fixed T_{air}. Values of the heat exchange velocity parameter γ are given in 10^{-5} m/s and fall within the spanned range in Favier et al. (2019).

3.6 Discussion

The results of MISMIP benchmark experiments are successful given the good agreement between our numerical solution and the semi-analytical work of Schoof (2007a) (Fig. 3.3). From a modeling perspective, our grounding-line position is slightly shifted upstream, like in other moving grid models shown in Pattyn et al. (2012). Nevertheless, a sensitivity test to spatial resolution

shows an asymptotic convergence towards the semi-analytical solution (Fig. B.1, Appendix B.9), thus providing robustness to our results. A further comparison among the Nix velocity solvers show an excellent agreement on the equilibrium solutions for both bed geometries herein studied: downward sloping and overdeepening.

For active thermodynamics and air temperature forcing, the corresponding temperature range spanned by MISMIP ice rate factor $A(T)$ does not yield a full advance/retreat of the ice sheet. This can be understood by the insulating effect of the ice sheet. The MISMIP idealised forcing with varying rate factor simultaneously modifies the ice viscosity over the entire domain, whereas the real temperatures given by an active thermomechanical solver will adjust to the new surface temperature (Fig. 3.4). This further means that the impact on the viscosity is weaker as there are other heat sources as the basal friction dissipation and the geothermal heat flow.

The stability of the system is accordingly perturbed, as shown in Fig. 3.6. Particularly, the bistability of the system is increased, in the sense that a larger range of perturbation values have two stable solutions. To illustrate this, for a rate factor $A = 10^{-26}$ Pa^{3}s, the oceanic anomaly perturbation ranges from $\Delta T_{\text{oce}} = +3$ to $+7^{\text{o}}$C, whereas for the thermomechanically active scenario, the bistability solution is found for a wider range from a $\Delta T_{\text{oce}} = +1.0$ to $+8.0^{\text{o}}$C. This can be understood as the result of a thermal adjustment that occurs when the temperature of the ice can evolve in time. As the forcing changes over time (i.e., the ocean temperature anomalies), the ice flux at the grounding line is modified and the inland ice thickness is perturbed accordingly. The new ice thickness distribution implies a slightly different temperature solution and the viscosity is consequently modified. Knowing that the viscosity field determines the velocity solution via the stress balance, we therefore find a clear feedback that allows for the ice sheet to adjust if thermodynamics are active.

It must be noted that this stability study employs a time duration in each forcing step of 30 kyr to elude transient responses (Fig.3.6b). This allows for the ice geometry to reach a steady-state as these experiments are intended to be quasi-equilibrium simulations (as MISMIP). If the time between steps was reduced, the hysteresis loop would then be a transitory response given that the ice temperature may not adjust to the new geometry. The added value of the thermomechanical coupling does not solely rely on the transi-

tory response (i.e., thermal inertia), but also on the perturbed stability of the quasi-equilibrium hysteresis loop. In other words, the thermomechanical coupling already determines the stable regions in a quasi-steady description and not only through the effects of thermal inertia. Our goal here is to first show this more fundamental behaviour. Further work is needed to assess the relevance of potential transient responses.

It is worth noting the fundamental role of vertical advection if the system is to be forced with air temperatures. The magnitude of vertical advection and its vertical dependency determine the temperature distribution within the ice (Moreno-Parada et al., 2022). This mechanism strongly determines the equilibrium profiles as it modifies the overall outflow of ice via the viscosity dependency on temperatures (i.e., Arrhenius law Eq. 4.11).

The calibrated values of γ_T (Favier et al., 2019) must be also discussed. The impact on the hysteresis behaviour is interesting as it does not imply a symmetric effect on the retreat/advance of the ice sheet (Fig. 3.7). Strictly speaking, the temperature anomaly necessary for the ice sheet to retreat is far more sensitive to the particular γ value than the anomaly necessary to advance. One potential explanation for this interesting behaviour rests on the very nature of the melting/calving parametrisation at the grounding line. Since M grows with ΔT_{oce} (Eq. 3.21 and 3.22), the difference among M values for a fixed γ increases with the temperature anomaly. Hence, knowing that the advance occurs when the ice flux value reaches a certain value at the grounding line, the temperature anomaly range covered by different γ that yields such a melting/calving values is smaller (as $\Delta T_{\text{oce}} \to 0$). Moreover, if thermodynamics is considered (Fig. 3.7b), the required calving at the grounding line to retreat is generally larger than that for a fixed rate factor (Fig. 3.7b). In fact, for sufficiently low values of γ, the thermomechanically active ice sheet never retreats. The thermal behaviour of the ice thus provides additional *inertia* in the sense that the ice sheet is less prone to change its current state, thus endowing the system with higher stability. This result is not exclusive of the oceanic forcing, as it also shown in Fig. 3.4, where the ice sheet does not collapse to a retreated position when the perturbation vanishes.

Lastly, results herein presented show that active thermodynamics perturbs the hysteresis loop and the overall stability of an ice sheet. The particular grid over which the equations are discretised do not alter this behaviour, for

that our results are not numerical artefacts of the chosen mesh. Therefore, we do not expect our results to change for a different grid discretisation. More precisely, we expect the same physical behaviour as long as the ice viscosity varies upon temperature changes, irrespective of the chosen grid. The exact grounding-line position may differ for a different grid, yet the physical mechanism underlying this mechanism remains unperturbed. It is thus expected that other models with distinct meshes will exhibit a similar mechanism to Nix simulations.

3.7 Conclusions

The thermomechanically-coupled 2D model Nix has been presented and thoroughly described. There are a number of novelties compared to other two-dimensional models: a stress balance given by the Blatter-Pattyn approximation, a fully coupled thermodynamics solver, explicit calculation of the grounding line by a stretched coordinate system, stochastic boundary conditions capability, adaptive time stepping and potential melting/calving at the grounding line. Nix allows the user to choose between explicit and implicit solvers for the main differential equations, while numerical stability is ensured by a staggered grid.

First, Nix's performance was tested by reproducing Experiments 1, 2 and 3 from MISMIP benchmarks (Pattyn et al., 2012). Results were further compared to semi-analytical solutions (Schoof, 2007a) yielding an excellent agreement for all Stokes approximation available in Nix: SSA, DIVA and Blatter-Pattyn. In general, our grounding line position slightly underestimates the boundary layer results in Schoof (2007a), likewise all moving-grid models participating in MISMIP. The well-known hysteresis behaviour in Experiment 3 is also captured.

The complexity of the system described was further increased by solving the associated heat problem. This allows us to investigate to which extent the hysteresis behavior under parameter variations is perturbed. In so doing, we designed two different suites of experiments regarding the variable forcing of the system: air temperatures T_{air} and ocean temperature anomalies ΔT_{oce}.

When forcing with air temperatures, the hysteresis loop width is widened and the system exhibits larger bistability as the dynamics are perturbed via

the ice viscosity dependency on temperature. In an idealised overdeepened bed geometry, it is necessary to reach an air temperature of -40^{o}C at the sea level (provided an adiabatic lapse rate dependency with height) for the grounding line to advance beyond the bedrock local maximum.

If the system is instead forced by ocean temperature anomalies (i.e., melting/calving at the grounding line), we find that the hysteresis behaviour also persists. Notably, the ocean temperature anomaly at which the ice sheet retreats depends on the particular heat exchange parameter. Our results show that the quadratic parametrisation retreats at $\Delta T_{\mathrm{oce}} = +8.0^{\mathrm{o}}$C of temperature anomaly. The system advances back to its unperturbed state at $\Delta T_{\mathrm{oce}} = +1.0^{\mathrm{o}}$C for the quadratic parametrisation.

Results for an oscillatory regime show that a thermomechanically coupled friction alone is not sufficient to produce a stable oscillatory regime. Additional experiments show that vertical advection of ice is found to be a necessary condition to obtain a periodically surging ice stream. For a vertically-integrated stress balance, as the SSA and DIVA, it is necessary to indendently compute the vertical veloctiy component that it is then considered in the thermodynamical solver. This can be understood by considering the counterbalance contribution of negative temperature gradients advected from the uppermost layers. As the ice velocities reach equilibrium, so does the heat production due to friction along most of the streaming region. If vertical advection of colder ice is sufficient to counterbalance this heat production, the base can eventually reduce its temperature and leave the surging stage, yielding a growth phase of the ice sheet. Otherwise, the frictional heat production ensures that the base remains at the pressure melting point at all times. Hence, the frequency, intensity and duration of these purges are determined by numerous factors, though mainly by the reduced friction coefficient, the surface mass balance and the vertical advection magnitude.

More generally, irrespective of the particular external forcing applied (i.e., oceanic or atmospheric), a thermodynamically active ice sheet shows a narrowing hysteresis loop as a result of the internal feedback among ice temperature, stress balance and viscosity.

Chapter 4
Yelmo ice-sheet model

Yelmo is a three-dimensional, higher-order thermomechanical ice-sheet model (Robinson et al., 2020). Important differences with respect to other models include its division into four independent blocks: topography, dynamics, material properties and thermodynamics. This division allows for a clear and clean way of defining variables. In addition, boundary conditions such as atmospheric or oceanic temperature fields, precipitation or sea-level variations are defined outside of Yelmo, greatly facilitating ice-sheet coupling to other models.

Here, the most fundamental equations and approximations used in Yelmo will be described. Many of these physical processes are already described in depth in Greve and Blatter (2009). Special focus will be given to the parameterisation used for the basal drag routine because of their important role within this thesis. Further details can be found in the Yelmo model description (Robinson et al., 2020).

4.1 Topography

Mass conservation is expressed via the continuity equation as:

$$\frac{\partial \rho}{\partial t} + \boldsymbol{\nabla} \cdot (\rho \mathbf{v}) = 0, \tag{4.1}$$

where ρ represents the ice density and $\mathbf{v}$ the ice velocity vector. Assuming that enough time has passed, so that ice has been pressed towards an incompressible state under its own weight, the mass conservation equation (Eq.

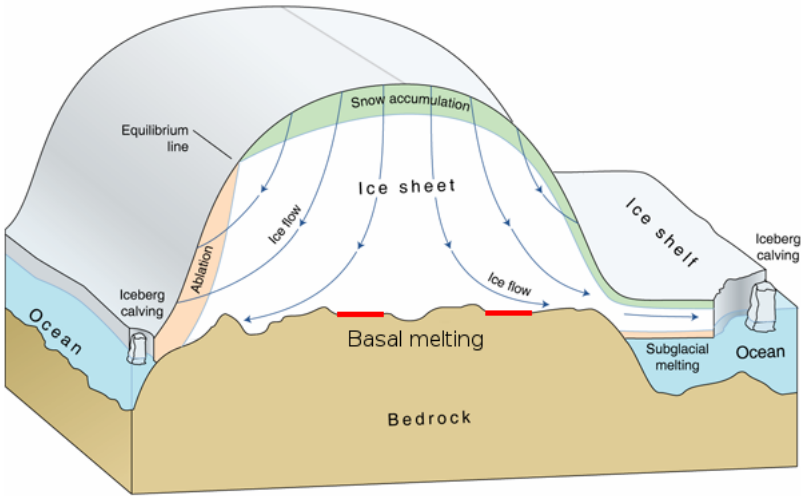

Fig. 4.1: Sketch of an ice sheet interacting with the climate system (from U.S. Geological Survey , USGS). At the surface, accumulation and ablation take place through interaction with atmosphere. At the ice base, the ice sheet interacts with the bedrock via geothermal heat flux exchange. Mass loss takes places at the ice front via calving and at the shelf base due to subglacial melting.

4.1) can be rewritten as:

$$\boldsymbol{\nabla} \cdot \mathbf{v} = \frac{\partial u}{\partial x} + \frac{\partial v}{\partial y} + \frac{\partial w}{\partial z} = 0, \tag{4.2}$$

where u, v and w represent the x,y and z components of the velocity vector $\mathbf{v}$ (being x and y the horizontal component, and z the vertical component). Integrating Eq. 4.2 vertically and considering boundary conditions, determined by mass gain and mass loss, gives:

$$\frac{\partial H}{\partial t} = a - b - c - \left(\frac{\partial (H \cdot \bar{u})}{\partial x} + \frac{\partial (H \cdot \bar{v})}{\partial y} \right). \tag{4.3}$$

This equation describes the mass conservation of the ice column. The ice thickness evolution ($\frac{\partial H}{\partial t}$) is obtained from the surface mass balance (a; difference of ice accumulation and ice ablation), the basal melting at the ice base (b; valid for grounded and floating ice), the advected ice flux ($\frac{\partial (H \cdot \bar{u})}{\partial x}$ and $\frac{\partial (H \cdot \bar{v})}{\partial y}$) and the calving rate ($c$), that applies at the ice front of ice shelves. In

this thesis, the method of Peyaud et al. (2007) and Lipscomb et al. (2019) is followed, where calving occurs if the ice thickness decreases below an imposed threshold (H_{ref}) and the upstream ice flux is not large enough to provide the necessary ice for maintaining the reference thickness on a characteristic calving time τ_c:

$$c = \frac{H_{ref} - H}{\tau_c}. \tag{4.4}$$

An ice sheet is in equilibrium if the ice loss from the dynamics is compensated by the total accumulation and melting from the boundary conditions and hence $\frac{\partial H}{\partial t} = 0$. Melting of floating ice-shelves depends on the oceanic heat-flux exchange, which in turn depends on oceanic temperatures and salinity. Melting of grounded ice occurs if the bed temperature is at the pressure melting point. Because the melting rates are imposed as boundary conditions, they will be discussed more extensively in Section 4.7.

4.2 Material

The material component of Yelmo computes the strain rate tensor and effective strain rate (amount of deformation as a consequence of stress), the rate factor, and the effective viscosity (fluidity of a material). Additionally, Yelmo offers the possibility of computing the ice age through an Eulerian tracer advection model (Robinson et al., 2020) . The material component is the link between thermodynamics and ice dynamics. The grid cells of ice can be imagined as a virtual ice box. The Cauchy stress tensor (or simply stress tensor) $\boldsymbol{\sigma}$ defines the state of stress of ice and is expressed as:

$$\boldsymbol{\sigma} = \begin{pmatrix} \sigma_{xx} & \sigma_{xy} & \sigma_{xz} \\ \sigma_{yx} & \sigma_{yy} & \sigma_{yz} \\ \sigma_{zx} & \sigma_{zy} & \sigma_{zz} \end{pmatrix} = \sigma_{ij}. \tag{4.5}$$

Note that the diagonal components (σ_{xx},σ_{yy},σ_{zz}) represent the normal stresses (i.e. perpendicular to the referred plane), whereas the other six components (σ_{xy}, σ_{xz}, σ_{yx}, σ_{yz}, σ_{zx}, σ_{zy}) are called shear stress (i.e. act parallel to the referred plane; Fig. 4.2a). This stress tensor can be split up into a deviatoric part (τ_{ij}), which tends to distort the ice box, and a hydrostatic stress component, which tends to change the size, and hence the volume. The

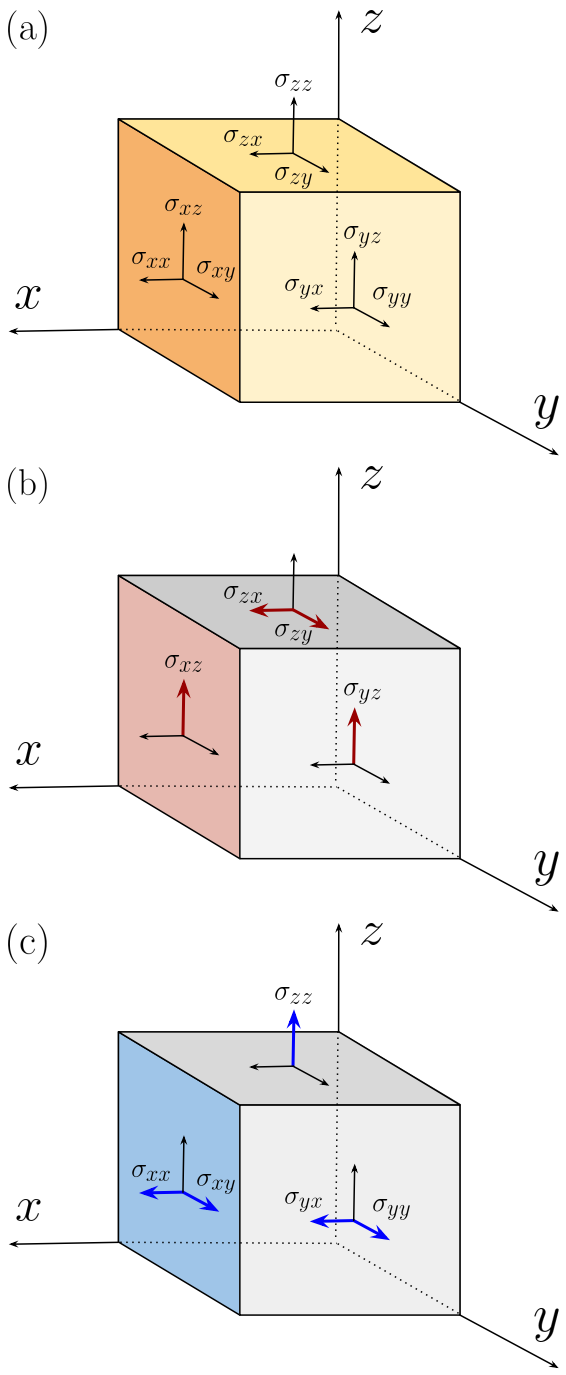

Fig. 4.2: Schematic representation of the stresses acting over a virtual ice box. (A) shows all the stress components as in a full Stokes problem. (B) represents the acting stresses for the SIA solution and (C) for the SSA solution.

hydrostatic stress components are commonly referred as pressure p:

$$\sigma_{ij} = \tau_{ij} - \frac{1}{3}\tau_{kk}\delta_{ij} = \tau_{ij} - p, \tag{4.6}$$

where Einstein's tensorial notation is followed. This deviatoric stresses can be split up into an effective viscosity component (η) and a strain rate tensor ($\dot{\epsilon}_{ij}$):

$$\tau_{ij} = 2\eta\dot{\epsilon}_{ij}, \tag{4.7}$$

where the strain rate tensor itself is:

$$\dot{\epsilon}_{ij} = \frac{1}{2}\left(\frac{\partial u_i}{\partial x_j} + \frac{\partial u_j}{\partial x_i}\right). \tag{4.8}$$

The second invariant of the stress deviatoric tensor defines the effective strain:

$$\dot{\epsilon} = \left(\frac{1}{2}\dot{\epsilon}_{ij}\dot{\epsilon}_{ij}\right)^{\frac{1}{2}}. \tag{4.9}$$

Using Glen's flow law (Glen, 1955), which relates creep and stress, the effective viscosity is calculated as:

$$\eta = \frac{1}{2}\left(\dot{\epsilon}^2\right)^{\frac{1-n}{2n}} A^{-\frac{1}{n}}, \tag{4.10}$$

where n is the Glen's flow law exponent, set to $n = 3$ within this thesis. A is the rate factor, which is computed as a function of ice temperature following the Arrhenius law:

$$A\left(T_i\right) = E_f A_0 \exp\left(-\frac{Q_a}{RT_i}\right), \tag{4.11}$$

where $R = 8.314$ [J mol^{-1} K^{-1}] is the universal gas constant. Q_a is the activation energy and A_0 the rate factor coefficient. E_f is the enhancement factor, which captures the impact of ice anisotropies on the ice flow. Because this effect is not captured by Glen's flow law, this variable is often set as a tuning parameter (Hooke, 2005; Ma et al., 2010; Pollard and DeConto, 2012a; Maris et al., 2014; Albrecht et al., 2020). Yelmo distinguishes between three flow regimes: shear, stream and shelf. Wherever there is floating ice, the shelf value is set. The enhancement factor for inland grounded ice is then the weighted average between the shear and stream enhancement factors, depending on the shear fraction of total deformation at a given location.

4.3 Dynamics

The dynamics of the ice sheet are deduced from the momentum conservation equation:

$$\rho \frac{d\mathbf{v}}{dt} = \boldsymbol{\nabla} \cdot \boldsymbol{\sigma} + \rho \mathbf{g}, \tag{4.12}$$

where $\mathbf{g}$ is the Earth's gravitational acceleration. At the involved timescales, the acceleration term of ice is considerably smaller than the ice deformation. Thus, neglecting $\frac{d\mathbf{v}}{dt}$, Eq. 4.12 can be rewritten as:

$$\boldsymbol{\nabla} \cdot \boldsymbol{\sigma} + \rho \mathbf{g} = 0, \tag{4.13}$$

which constitutes the steady-state (Stokes) equation. Expressed in Cartesian components, the quasi-static description of the convervation of momentum reads:

$$\frac{\partial \sigma_{xx}}{\partial x} + \frac{\partial \sigma_{xy}}{\partial y} + \frac{\partial \sigma_{xz}}{\partial z} = 0 \tag{4.14}$$

$$\frac{\partial \sigma_{yx}}{\partial x} + \frac{\partial \sigma_{yy}}{\partial y} + \frac{\partial \sigma_{yz}}{\partial z} = 0 \tag{4.15}$$

$$\frac{\partial \sigma_{zx}}{\partial x} + \frac{\partial \sigma_{zy}}{\partial y} + \frac{\partial \sigma_{zz}}{\partial z} = -\rho g. \tag{4.16}$$

Solving this system of equations is computationally very expensive, hence, for the sake of simplicity, several assumptions are made.

4.3.1 Hydrostatic approximation

This approximation relies on the assumption that the horizontal extent of the ice sheet (and more particularly Antarctica) is much greater than its height (Antarctica's horizontal extension reaches up to 4000 km, whereas its largest ice column is around 4 km thick). Hence the vertical shear stresses σ_{xz} and σ_{yz} are much smaller than σ_{zz} and can be neglected. Thus integrating over z in Eq. 4.16 gives:

$$\sigma_{zz} = \rho g \left(H - z \right), \tag{4.17}$$

which is the hydrostatic pressure. Substituting Eq. 4.17 into Eq. 4.14 and Eq. 4.15 (following Greve and Blatter (2009)):

$$2\frac{\partial \tau_{xx}}{\partial x} + \frac{\partial \tau_{yy}}{\partial x} + \frac{\partial \sigma_{xy}}{\partial y} + \frac{\partial \sigma_{xz}}{\partial z} = \rho g \frac{\partial z_s}{\partial x} \tag{4.18}$$

$$2\frac{\partial \tau_{yy}}{\partial y} + \frac{\partial \tau_{xx}}{\partial y} + \frac{\partial \sigma_{yy}}{\partial y} + \frac{\partial \sigma_{yz}}{\partial z} = \rho g \frac{\partial z_s}{\partial y}, \tag{4.19}$$

where z_s is the surface elevation. Inserting in these equations the deviatoric stress definition (Eq. 4.7) the hydrostatic approximation is obtained:

$$\begin{aligned} 4\frac{\partial}{\partial x}\left(\eta\frac{\partial u}{\partial x}\right) + 2\frac{\partial}{\partial x}\left(\eta\frac{\partial v}{\partial y}\right) + \frac{\partial}{\partial y}\left(\eta\left(\frac{\partial u}{\partial y} + \frac{\partial v}{\partial x}\right)\right) & \\ + \frac{\partial}{\partial z}\left(\eta\left(\frac{\partial u}{\partial z} + \frac{\partial w}{\partial x}\right)\right) &= \rho_i g \frac{\partial z_s}{\partial x} \end{aligned} \tag{4.20}$$

$$\begin{aligned} 4\frac{\partial}{\partial y}\left(\eta\frac{\partial v}{\partial y}\right) + 2\frac{\partial}{\partial y}\left(\eta\frac{\partial u}{\partial x}\right) + \frac{\partial}{\partial x}\left(\eta\left(\frac{\partial u}{\partial y} + \frac{\partial v}{\partial x}\right)\right) & \\ + \frac{\partial}{\partial z}\left(\eta\left(\frac{\partial v}{\partial z} + \frac{\partial w}{\partial y}\right)\right) &= \rho_i g \frac{\partial z_s}{\partial y}. \end{aligned} \tag{4.21}$$

4.3.2 Shallow Ice Approximation

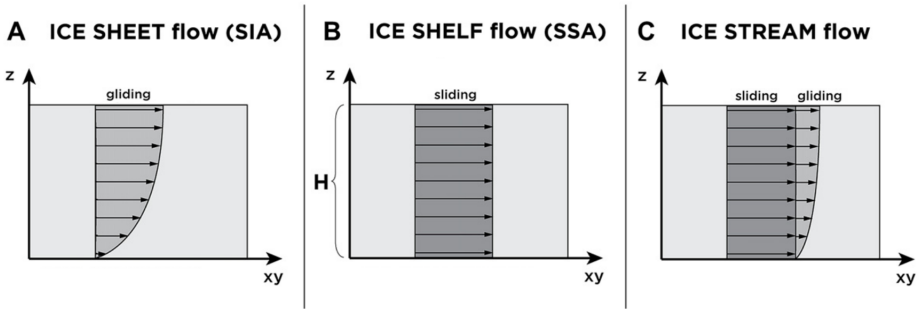

Fig. 4.3: Velocity profile of the SIA solution (A) and the SSA solution (B). In the SIA solution gliding processes prevail, the SSA solution is dominated by sliding. Yelmo computes all inland ice points as ice streams (C). Ice closer to the dome regions will have a small sliding velocity contribution, whereas it will increase towards the coast. Ice shelves velocities are solved only with the SSA solution (figure based on Kirchner et al., 2011).

Yelmo is a hybrid model which includes the Shallow Ice Approximation (SIA) and Shallow Shelf Approximation (SSA). In this thesis, it treats the horizontal velocities ($u(x,y,z)$ and $v(x,y,z)$) as a sum of the internal deformation computed by the SIA solution (denoted with a sub-index *sia*) and sliding at the base calculated by the SSA solution (denoted with a sub-index *ssa*), hence:

$$u = u_{sia} + u_{ssa} \tag{4.22}$$

$$v = v_{sia} + v_{ssa}. \tag{4.23}$$

The SIA solution (Hutter, 1983) is a further simplification from the hydrostatic approximation. It only considers deformation terms, hence $\tau_{xx} = \tau_{yy} = 0$, and assumes that the shear component in the z direction is dominant over the xy plane, thus $\sigma_{xy} = 0$. It thus describes slow flowing ice, dominated by the shearing regime (see Fig. 4.3a). With this Eq. 4.18 and Eq. 4.19 simplify to:

$$\frac{\sigma_{xz}}{\partial z} = \rho g \frac{\partial z_s}{\partial x} \tag{4.24}$$

$$\frac{\sigma_{yz}}{\partial z} = \rho g \frac{\partial z_s}{\partial y}. \tag{4.25}$$

If these equations are integrated taking into account that here no basal sliding is allowed within the SIA solution, as it is assumed that the SIA solution is frozen to bedrock ($u_{sia}(x,y,z_b) = v_{sia}(x,y,z_b) = 0$), and that the ice surface is stress-free ($\sigma_{xz}|_{z_s} = \sigma_{yz}|_{z_s} = 0$), then the zero-order depth-dependent SIA solutions are obtained:

$$u_{sia}(z) = -\left[2\left(\rho g\right)^n \left|\nabla z_s\right|^{n-1} \int_{z_b}^{z} A(z_s - z)^n\right] \frac{\partial z_s}{\partial x} \tag{4.26}$$

$$v_{sia}(z) = -\left[2\left(\rho g\right)^n \left|\nabla z_s\right|^{n-1} \int_{z_b}^{z} A(z_s - z)^n\right] \frac{\partial z_s}{\partial y}, \tag{4.27}$$

where n is the Glen exponent and A the material rate factor described in the Material module (Section 4.2; Eq. 4.11).

4.3.3 Shallow Shelf Approximation

The SSA solution (MacAyeal, 1989) is applied to fast flowing areas, characteristic of ice shelves and ice streams, dominated by the stretching regime (see Fig. 4.3b). It is a further approximation of the hydrostatic approximation, but now vertical components are neglected. Following Greve and Blatter (2009) the vertical shear stresses are simplified to:

$$\sigma_{xz} = \eta \frac{\partial w}{\partial x} \tag{4.28}$$

$$\sigma_{yz} = \eta \frac{\partial w}{\partial y}. \tag{4.29}$$

Inserting these equations into the hydrostatic approximation and integrating over depth, the SSA solution is obtained:

$$\frac{\partial}{\partial x}\left[\bar{\eta}_d\left(4\frac{\partial u_{ssa}}{\partial x} + 2\frac{\partial v_{ssa}}{\partial y}\right)\right] + \frac{\partial}{\partial y}\left[\bar{\eta}_d\left(\frac{\partial u_{ssa}}{\partial y} + \frac{\partial v_{ssa}}{\partial x}\right)\right] = \rho g H \frac{\partial z_s}{\partial x} - \tau_{b,x} \tag{4.30}$$

$$\frac{\partial}{\partial y}\left[\bar{\eta}_d\left(4\frac{\partial v_{ssa}}{\partial y} + 2\frac{\partial u_{ssa}}{\partial x}\right)\right] + \frac{\partial}{\partial x}\left[\bar{\eta}_d\left(\frac{\partial u_{ssa}}{\partial y} + \frac{\partial v_{ssa}}{\partial x}\right)\right] = \rho g H \frac{\partial z_s}{\partial y} - \tau_{b,y}. \tag{4.31}$$

Note that $\bar{\eta}_d$ is the depth-integrated ice viscosity described as:

$$\bar{\eta}_d = \frac{1}{2}\bar{B}\left(\dot{\varepsilon}_d^2 + \dot{\varepsilon}_0^2\right)^{\frac{1-n}{2n}}, \tag{4.32}$$

where

$$\bar{B} = \frac{1}{H}\int_{z_b}^{z_s} A^{-1/n} dz, \tag{4.33}$$

is the vertically averaged ice hardness. $\dot{\epsilon}_0$ is a regularization factor to avoid singularities and $\dot{\epsilon}_d$ the effective strain rate computed as a reduced form of the second invariant of the strain rate tensor without vertical shear terms, hence:

$$\dot{\epsilon}_d^2 = \left(\frac{\partial u_b}{\partial x}\right)^2 + \left(\frac{\partial v_b}{\partial y}\right)^2 + \frac{\partial u_b}{\partial x}\frac{\partial v_b}{\partial y} + \frac{1}{4}\left(\frac{\partial u_b}{\partial y} + \frac{\partial v_b}{\partial x}\right)^2. \tag{4.34}$$

$\boldsymbol{\tau_b}$ is the basal stress applied at the base to the SSA solution. For ice shelves its value is set to zero, while for grounded ice, Yelmo offers different treatments.

4.3.4 Basal friction

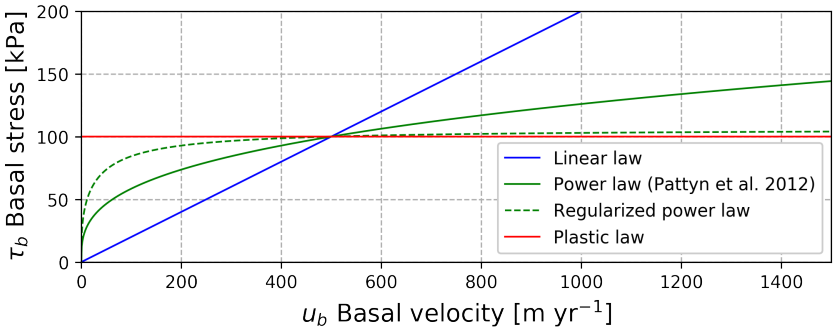

Fig. 4.4: Graphical illustration of the basal shear stress function ($\boldsymbol{\tau_b}$) for different friction laws (linear, Coulomb, regularized Coulomb and plastic). Friction coefficients have been tuned to obtain 100 kPa for a basal velocity of 500 m yr−1 (figure based on Joughin et al. (2019)).

Friction on a surface is based on Newton's third law, where the bedrock responds with an opposite reaction to the applied force. Hence, the simplest way to relate the basal stress $\boldsymbol{\tau_b}$ with the horizontal basal velocity vector $\mathbf{u_b}$ is with the so-called basal friction coefficient β

$$\boldsymbol{\tau_b} = -\beta \mathbf{u_b}. \tag{4.35}$$

Note that the horizontal basal velocity vector is expressed in [m yr^{-1}] and the basal stress in [Pa], thus β has units of [Pa yr m^{-1}] (e.g., MacAyeal et al., 1995; Cuffey and Paterson, 2010). This representation allows for an indirect inference of basal friction at the ice base through inversion methods based on surface velocities (e.g., Morlighem et al., 2013; Le clec'h et al., 2019). Nonetheless, these inversion methods show a particular configuration of PD conditions which is not necessarily valid for other time periods. The actual resistance relation $\boldsymbol{\tau_b}(\mathbf{u_b})$ depends on local properties, such as the presence of

sediments or basal water. Therefore, to account for bedrock characteristics, Yelmo splits the friction coefficient into a a bedrock coefficient c_b, which accounts for several bedrock properties, a threshold velocity u_0, which will be discussed later, and a velocity function $f(\mathbf{u_b})$:

$$\beta = \frac{c_b}{u_0} f(\mathbf{u_b}) . \tag{4.36}$$

Note that $f(\mathbf{u_b})$ is dimensionless, thus c_b has units of [Pa] and the threshold speed u_0 [m yr^{-1}]. The velocity function accounts for the sliding character of the ice sheet. Different frictions apply at the ice base depending on the velocity regime. For *hard beds* resistance will become stronger with increasing velocity as a consequence of null water presence or no sediments. On the contrary, at *weak/soft beds*, the glacial till might yield a certain drag irrespective of the particular sliding velocity and the presence of water can further enhance basal sliding. Yelmo accounts for these features through different basal friction laws.

Basal friction laws

The choice of the velocity function, $f(\mathbf{u_b})$, as described above, and thereby the friction law is relatively arbitrary and unconstrained in ice modelling, as no universal law has been defined. It is poorly constrained but plays a fundamental role within the dynamics of continental ice-sheets. Several observational studies are beginning to identify the most realistic friction-laws from satellite observations (e.g. Joughin et al. (2019)). Still it is not clear whether a unique friction law can be used for large ice-sheets and whether the same friction-law holds for cold and warm periods. Although Yelmo offers the possibility to couple with a hydrological model, in this thesis the presence of basal water is assumed through different friction representations. The presented friction laws are intended to cover the whole range of possibilities as well as the most common laws used in the literature.

Power law

Any power law can generally be expressed as $f(\mathbf{u_b}) = u_0^{1-q} |\mathbf{u_b}|^{q-1}$ (Robinson et al., 2020). This yields when substituted into Eq. 4.35 (Schoof, 2010; Aschwanden et al., 2013)

$$\boldsymbol{\tau_b} = -c_b \left(\frac{|\mathbf{u_b}|}{u_0} \right)^q \left(\frac{\mathbf{u_b}}{|\mathbf{u_b}|} \right), \tag{4.37}$$

where u_0 is the regularizing velocity term and $q \in [0, 1]$ is the non-dimensional pseudo-plastic exponent. From here, three of the most common friction laws used in ice-sheet models can be obtained: linear power-law, pseudo-plastic power law and a purely plastic law. If $q = 1$, then a linear power law is obtained:

$$\boldsymbol{\tau_b} = -c_b \frac{\mathbf{u_b}}{u_0}. \tag{4.38}$$

Due to its simplicity, this law is very popular in ice-sheet models (e.g. Alvarez-Solas et al., 2013; Quiquet et al., 2018). It is especially relevant for *hard beds* as the basal stress scales proportionally to basal velocity (blue curve; Fig 4.4). Hence, unless the presence of water or sediments is taken into account, higher velocities generate a larger bedrock friction. Because velocity increases towards the margins, this provides a very stable solution for ice sheets in fast flowing regions. However, as friction increases one could expect that frictional heat increases, resulting in more basal water production, which facilitates ice flow. This law hence does not include cavitation effects at the ice base which could limit the total friction.

At the other extreme, if q =0, then a purely plastic behaviour results from Eq. 4.37

$$\boldsymbol{\tau_b} = -c_b \frac{\mathbf{u_b}}{|\mathbf{u_b}|}. \tag{4.39}$$

This friction law applies the same basal stress independent of the flowing regime (red curve; Fig. 4.4). It represents a *weak bed* where the presence of basal water lubricates the ice flow and hence friction is independent of the basal velocity. This provides a more dynamic ice sheet than a linear law. This can have profound implications. For instance, a MISI mechanism will most likely occur earlier for a plastic law than for a linear law as fast velocities are not suppressed with a corresponding high friction. On the other hand, for a plastic law more friction is applied in slow regimes.

A typical value used in ice-sheet modeling for a middle case scenario is $q = \frac{1}{3}$, which will be defined hereafter as the pseudo-plastic power law

$$\boldsymbol{\tau_b} = -c_b \left(\frac{|\mathbf{u_b}|}{u_0} \right)^{\frac{1}{3}} \frac{\mathbf{u_b}}{|\mathbf{u_b}|}. \tag{4.40}$$

This solution also increases with increasing basal velocity but is not as pronounced as the linear case (green curve; Fig 4.4). This law intends to capture the phenomenon by which a high friction in fast flowing regimes releases more heat, melting the ice base, and enhances the ice flow. It resembles a *hard bed* better than a *weak bed* as it does not fully saturate and hence cavitation effects are not completely taken into account, but it clearly provides a lower friction than the linear case. A particular case is $u_0 = 1$ m yr^{-1} and $c_b = 3.165176\ 10^4$ Pa which are the friction parameters used in the MISMIP experiments (Pattyn et al., 2012).

Regularized-Coulomb law

The Regularized-Coulomb law is defined as $f(\mathbf{u_b}) = u_0 \left(|\mathbf{u_b}| + u_0\right)^{-q} |\mathbf{u_b}|^{q-1}$ and thus:

$$\boldsymbol{\tau_b} = -c_b \left(\frac{|\mathbf{u_b}|}{|\mathbf{u_b}| + u_0} \right)^{q} \frac{\mathbf{u_b}}{|\mathbf{u_b}|}. \tag{4.41}$$

This friction law allows for a power-law behaviour for low velocities (*hard bed* below u_0) and saturates afterwards if ice becomes too fast (*weak bed*), taking into account potential cavitation effects (green discontinuous line; Fig. 4.4). Recently, observations suggest that this solution may be the most adequate one for representing ice-sheet dynamics (Joughin et al., 2019). Because it combines low friction for both, slow and fast velocities, this solution provides the most dynamic ice sheet. This has profound implications for future sea-level projections. If the basal friction saturates beyond a threshold velocity, then the MISI instability for instance is more likely to occur than for a linear friction law and more inland ice will be discharged than for a plastic law.

4.3.5 Basal friction coefficient

The bedrock friction coefficient c_b is intended to provide information about bedrock characteristics such as basal temperature, the presence of basal sediments or the effective pressure for instance. The friction coefficient is split into a universal friction coefficient for the whole ice sheet (c_f), a topographic scaling parameter (λ) and the effective pressure (N_{eff})

$$c_b = c_f \lambda N_{eff}. \tag{4.42}$$

The effective pressure does not explicitly account for the presence of basal water and the potential intrusion through crevasses. It is instead parametrised following the Leguy et al. (2014) formulation

$$N_{eff}(p) = \rho_i g H \left(1 - \frac{H_f}{H}\right)^p, \tag{4.43}$$

where ρ_i stands for the ice density. H_f represents the floating portion of the grounded ice column. If ice is grounded above sea level, then it is set to zero, if it is grounded below sea level, the portion of floating ice depends on the bed depth and the sea-water density (ρ_w), thus:

$$H_f = max\left[0, -\frac{\rho_w}{\rho_i}\left(z_{sl} - z_b\right)\right], \tag{4.44}$$

where z_b denotes the bedrock elevation (positive/negative numbers above/below sea level) and z_{sl} the sea-level elevation. If the exponent p in Eq. 4.43 is set to zero, then the pressure exerted at the ice base is the weight of the ice column. If p =1 then full water pressure is applied at the marine zones. This means that the effective pressure is corrected subtracting the overburden pressure. Intermediate values allow for a partial connectivity to the ocean.

The scaling parameter $\lambda \in [0, 1]$ is used to scale the universal friction coefficient c_f depending on bedrock characteristics. A lower λ allows for faster basal sliding because of the existence of a temperate bedrock base (i.e. $T_b = T_{fp}$) or because of the presence of sediments, for instance. In this thesis either a constant value will be used for the whole domain, hence $\lambda = 1$ (Chapter 3), or either through a depth dependent parameterisation, which enhances ice flow in topographic lows (Chapters 4,5). For this last case λ is defined

through an exponential function dependent on bedrock elevation (z_b):

$$\lambda = \begin{cases} 1 & \text{if } z_b > z_1 \\ \max\left[\exp\left(\frac{z_b - z_1}{z_1 - z_0}\right), \lambda_{\min}\right] & \text{if } z_b < z_1. \end{cases} \tag{4.45}$$

Here z_0 and z_1 are internal parameters prescribed in the code, where $z_1 > z_0$. For a bedrock elevation above z_1 the scaling factor λ saturates to 1. This represents a bedrock depth where sliding is hampered (see Fig. 4.5). At z_0 the bedrock coefficient is always $1/e$ (the e-folding depth). Thus, if z_0 is set close to z_1 then the friction decreases more abruptly with decreasing depth than if these parameters are set more distanced. $\lambda_{\min}$ determines a threshold which allows for a faster or slower sliding. This parameterisation is intended to capture the nature of the fast sliding zones especially of the marine parts in Antarctica. It is ultimately based on the approach of Martin et al. (2011). They use a till friction angle which facilitates sliding as the bedrock decreases in the marine regions. They find that this formulation for the bedrock friction simulates more realistic PD states than a bedrock temperature approach, when a basal hydrology model is not present.

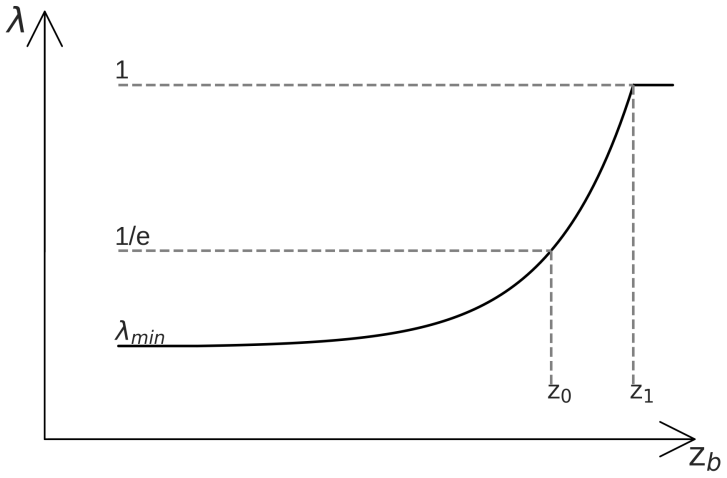

Fig. 4.5: Sketch of the scaling parameter λ for a depth dependent parameterisation.

4.4 Thermodynamics

Finally, the thermodynamics of the model are defined through energy conservation:

$$\rho_i c \left(\frac{\partial T}{\partial t} + \mathbf{v} \cdot \boldsymbol{\nabla} T \right) = \boldsymbol{\nabla}(k \boldsymbol{\nabla} T) + \Phi. \tag{4.46}$$

Here, c is the heat capacity of ice, T the ice temperature, k the heat conductivity of ice and Φ the internal deformation, also called strain heating. The ice temperature is necessary for solving the Arrhenius law as seen in Eq. 4.11 which determines the ice deformation through viscosity. Again, for solving the heat equation some assumptions are made for the sake of simplicity. First, the strain heating can be expressed as:

$$\Phi = 4\eta\dot{\epsilon}^2. \tag{4.47}$$

where $\dot{\epsilon}$ is the effective strain rate described in Eq. 4.8. Heat diffusion within the ice is considered purely vertical (only the ice column), as horizontal diffusion is considered negligible (Greve and Blatter, 2009). Thus, the energy conservation equation can be rewritten as

$$\frac{\partial T}{\partial t} = \frac{k}{\rho_i c} \frac{\partial^2 T}{\partial z^2} - u \frac{\partial T}{\partial x} - v \frac{\partial T}{\partial y} - w \frac{\partial T}{\partial z} + \frac{4\eta\dot{\epsilon}^2}{\rho_i c}. \tag{4.48}$$

Ice surface temperature

To solve the Equations 4.48, boundary conditions are necessary. These are set separately and are commented on in Section 4.7. Nonetheless it is worth mentioning, that at the ice surface, the ice temperature is limited to a maximum value of $T_0 = 273.15\text{K}$, the freezing-point temperature.

Grounded ice basal temperature

At the ice-bedrock interface Yelmo distinguishes between two cases: a frozen bedrock and a temperate bedrock. If the ice base is frozen ($T_i < T_{fp}$), then the boundary condition for the vertical gradient of temperature is prescribed as

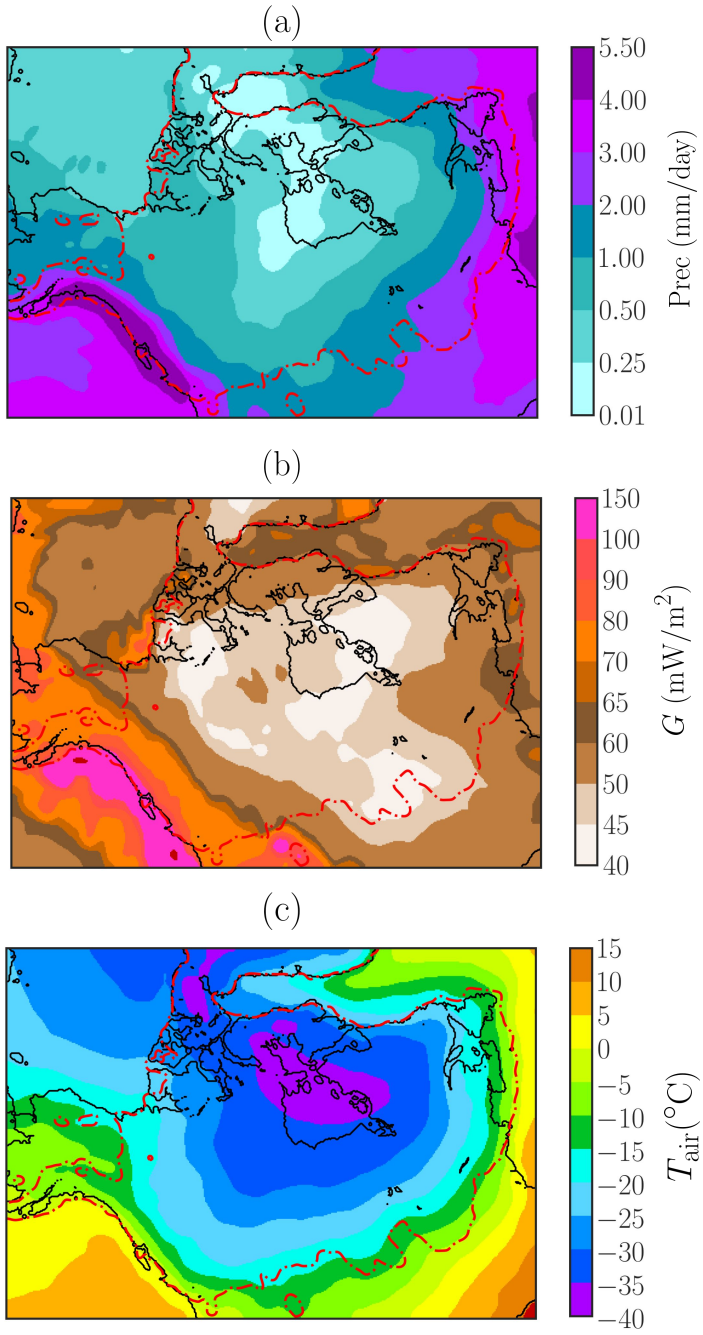

Fig. 4.6: Mean imposed climate fields: (a) Annual mean precipitation (mm/day), (b) Geothermal heat flow (mW/m^2) and (c) Annual mean surface temperature (ºC). LGM constant conditions define the external climatic forcing so that none of these boundary conditions exhibit temporal dependency. Red dashed line shows maximum reconstructed LIS extent (ICE-6G).

$$\left.\frac{\partial T}{\partial z}\right|_{z=z_b} = -\frac{Q_{geo}}{k}, \tag{4.49}$$

where Q_{geo} is the geothermal heat flux, which is set as a boundary condition. In this thesis is also a spatially-variable boundary condition and it is acquired from Shapiro and Ritzwoller (2004) (Fig. 4.6b). If the basal temperature is at the pressure melting point, then the bed is temperate and the melting rate (B) is diagnosed as (Cuffey and Paterson, 2010):

$$B = -\frac{1}{\rho L}\left(Q_b + k\left.\frac{\partial T}{\partial z}\right|_{z=z_b} + Q_{geo}\right). \tag{4.50}$$

Here L is the latent heat for fusion for ice and Q_b the basal heat production due to sliding friction. Melting of ice shelves is not computed through the thermodynamics module and is set as a boundary module (a detailed description can be found in Section 4.7).

4.5 Grounding-line diagnosis

The grounding-line is the limit between the marine grounded ice and the ocean or floating ice. Yelmo diagnoses the grounding-line through the overburden ice thickness, which is computed as

$$H_{grnd} = H_i - \frac{\rho_w}{\rho_i}\max\left(z_{sl} - z_b, 0\right), \tag{4.51}$$

where z_{sl} represents the sea level. Thus, if $H_{grnd} > 0$, then the ice is grounded and if $H_{grnd} < 0$ then the ice is floating (or an ocean grid point). The grounding line is diagnosed as the last grounded point before floating and is therefore considered fully grounded.

4.6 Basal hydrology

Yelmo considers a local evolution equation for basal water content H_{w} without horizontal advection. In this case, the non-local term of the time-

dependent diffusion equation is assumed to be negligible, yielding the following approximation:

$$\frac{\partial H_{\mathrm{w}}}{\partial t} = \frac{Q}{\rho_w L_i} - d_r, \tag{4.52}$$

Here, Q is the net heat flux, given by the sum of the frictional heating at the ice-bed interface, and the gradients in heat flow at the base of the ice column and at the bedrock surface (Eq. 3). d_r is the till drainage rate, set to $dr = 10^{-3}$ m/yr in the default case which means that its value is generally small compared to $Q/\rho_w L_i$. Negative values of $Q/\rho_w L_i$ are allowed, implying refreezing. The water layer thickness is bounded between zero and a maximum value of $H_{\mathrm{w,max}}$ (Bueler and Brown, 2009; Bueler and van Pelt, 2015):

$$0 \leq H_{\mathrm{w}} \leq H_{\mathrm{w,max}}, \tag{4.53}$$

By default, $H_{\mathrm{w,max}}$ is set to 2 m, but its influence is tested in sensitivity experiments. Moreover, $H_{\mathrm{w,max}}$ will be also estimated in Section 3.3 based on estimates of total IRD volume (Hemming, 2004).

It must be recalled that the till represents a mixture of fluid and rigid particles, thus resulting in a high complexity of deformation processes. The ability of soil to change its water content under different effective pressures (Wood, 1991) inevitably renders such complexity. Furthermore, the till compressibility depends on both the stress history and the current effective pressure of the sample under consideration (Tulaczyk et al., 2000a). Hence, two soil states can be distinguished: normally consolidated and overconsolidated. The former describes a till in which the current effective pressure is the highest to which the soil was subjected in the past, i.e., $N = N_{\mathrm{max}}$. The second state satisfies a less restrictive condition, $N < N_{\mathrm{max}}$.

As a result, the till compressibility C_t (referred to as C_ξ by Tulaczyk et al., 2000a) is best described by a logarithmic function that relates the void ratio $e = V_w/V_s$ to the effective pressure N (Scott, 1963; Hooke et al., 1997; Tulaczyk et al., 2000a) as follows:

$$e = e_0 - C_t \log_{10}\left(N/N_0\right), \tag{4.54}$$

The void ratio then quantifies the pore volume V_w relative to the volume of solid mineral V_s. The dimensionless parameter C_t and the void ratio e_0

at the reference effective pressure N_0 differ regarding the consolidation state of the till. The compressibility C_t actually depends on the effective stress history (i.e., the consolidation state of the till) hereafter indicated by C_c (consolidated) and C_s ('swelling'; i.e., overconsolidated), respectively. These values are estimated through laboratory geotechnical tests on till recovered underneath Ice Stream B, West Antarctica (Table 4.1, Tulaczyk et al., 2000a):

Table 4.1: Values of compressibility C_t and void ratio e_0 (Tulaczyk et al., 2000a) for the two soil states regarding stress history.

Parameter	**Normally consolidated**	**Overconsolidated**
e_0	0.78	0.53
C_t	0.15	0.014

The effective pressure formulation of Bueler and van Pelt (2015) is further employed to link the dynamics of the ice sheet base to the till water content H_w:

$$\tilde{N} = N_0 \left(\frac{\delta P_0}{N_0} \right)^s 10^{\frac{e_0}{C_t}(1-s)}, \tag{4.55}$$

where P_0 is the overburden pressure, $s = H_\mathrm{w}/H_{\mathrm{w,max}}$ is the till saturation and δ is the minimum overburden pressure fraction for a completely saturated till. In reality, the effective pressure N cannot exceed the overburden pressure P_0 for any sustained period, shaping P_0 into an upper limit:

$$N = \min \left\{ P_0, \tilde{N} \right\}. \tag{4.56}$$

Therefore, the effective pressure of the till is an exponential transition between these two extreme cases:

$$\begin{cases} s = 0 \rightarrow \text{no basal water} \rightarrow N = P_0 \\ s = 1 \rightarrow \text{saturated till} \rightarrow N = \delta P_0 \end{cases} \tag{4.57}$$

It is worth noting the additional link provided by this formulation through the values of e_0 and C_t besides the purely water content H_w. In terms of $N(H_\mathrm{w})$, for a fixed basal water content value H_w, the effective pressure depends on the consolidation state of the till.

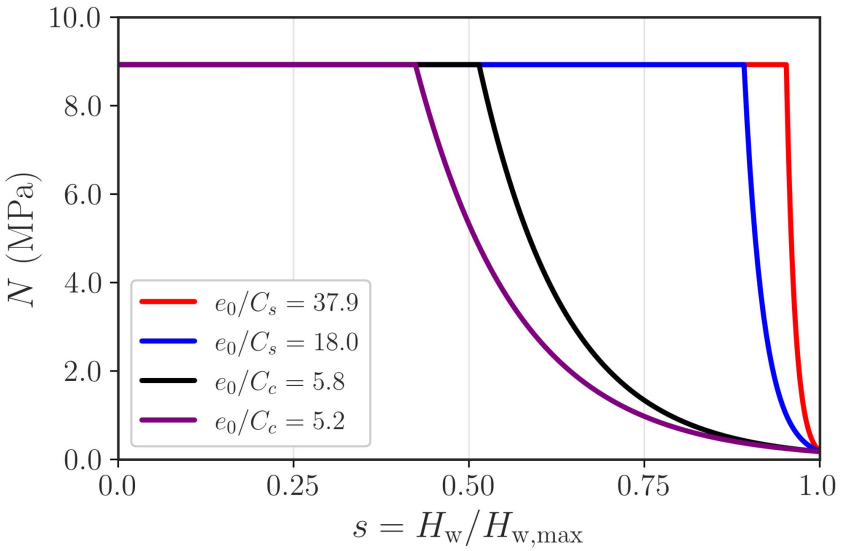

Fig. 4.7: Effective pressure N as a function of the basal water thickness (Eq. 4.55). Here, $H_{\mathrm{w,max}} = 2.0$ m, $P_0 = \rho_i g H_0$ and $H_0 = 1.0$ km. Overconsolidated C_s (red and blue lines) and normally consolidated C_c (black and purple lines) compressibility values taken from Tulaczyk et al. (2000a).

As a consequence, it is likely that the consolidation state of the soil cannot be ignored. The original formulation proposed by Bueler and van Pelt (2015) assumed a normally consolidated till (CSL, Fig 4.7). In other words, their till effective pressure must be the highest to which the soil was subjected in the past (i.e., $N = N_{\mathrm{max}}$). Nevertheless, as noted by Tulaczyk et al. (2000a), fluctuations of water pressure are sufficient to induce consolidation irrespective of ice thickness changes. This idea is supported by empirical measurements since basal water pressure records obtained beneath mountain glaciers show large pore pressure fluctuations (Blake, 1992; Hooke et al., 1997; Iverson et al., 1995). For this reason, the assumption of an overconsolidated state

$$N(t) < N_{\mathrm{max}}. \tag{4.58}$$

appears to be more reasonable since it is met most of the time as pore pressure fluctuates around a mean value (Tulaczyk et al., 2000a).

4.7 Boundary conditions

Yelmo includes a module which loads all the necessary fields that the model requires as boundary conditions. The required boundary conditions can be set manually or from other model outputs. This construction also allows for a potential coupling of the ice model with other Earth System models for instance. Here the most relevant boundary conditions in this work are discussed.

4.7.1 Surface mass balance

The surface mass balance is computed as the sum of the mass gain through accumulation and the mass loss via ablation. Accumulation is derived from the total snowfall from a mean climatic precipitation field. In this thesis, for PD boundary conditions, temperatures and precipitation are given from the regional climate model RACMO 2.3 (van Wessem et al., 2018) forced by the ERA-Interim reanalysis (Dee et al., 2011). Ablation is computed through the Positive-Degree Day Scheme (PDD; Reeh (1991)). This method is very po pular in ice models since it only requires surface temperatures as input. It calculates the number of days that temperatures are sufficiently high to melt ice from a normal statistical distribution around a mean, thus

$$PDD = \frac{1}{\sigma\sqrt{2\pi}} \int_{1\text{yr}} \int_{0}^{\infty} \exp\left(\frac{-(T - T_d)^2}{2\sigma^2}\right) dT dt. \tag{4.59}$$

Here, σ is the standard deviation, assuming that daily temperatures (T_d) follow a normal distribution ($\sigma = 5$ K). The temperature evolution during one year follows a cosine function scaled with the mean summer and mean annual temperature. There are more complex methods that account for an energy-balance through short-wave radiation for instance (Robinson et al., 2010). Nevertheless, the PDD scheme is commonly used in ice models in the Antarctic domain, because ablation at these latitudes is almost negligible and there is no need for more sophisticated methods (Winkelmann et al., 2011; Pollard and DeConto, 2012a; Pattyn, 2017).

4.7.2 Glacial Isostatic Adjustent (GIA)

Yelmo is coupled to a simple glacial-isostatic adjustment (GIA) model to account for bedrock changes. The GIA describes the evolution of the solid Earth through the growth or decay of large ice sheets. It has profound implications for the AIS as it can hamper (or enhance) ice advance and facilitate the intrusion of warm water onto the continental-shelf (Whitehouse et al., 2019). However, although the physical basis is now well established (Whitehouse, 2018), ice models use rather simple schemes for long timescale simulations. In this thesis, the Elastic Lithosphere-Relaxed Asthenosphere method is used (Meur and Huybrechts, 1996). This model assumes that due to the elasticity of the lithosphere a deposition of ice weight has to result in a non-local response caused by a lateral shift (Greve and Blatter, 2009). The asthenosphere below, on the other hand, relaxes to its equilibrium in a defined characteristic time which is set as a parameter (in this work, set to 3000 yr). However, it is worth mentioning that this method does not capture differences in the asthenosphere viscosity and rheological properties as in the WAIS for example, where bedrock responses may occur on a different timescale.

Chapter 5
Simulating the Laurentide ice sheet of the Last Glacial Maximum*

Among the Northern Hemisphere ice sheets, the LIS was the largest in terms of volume and extent. Given an estimated SLE during the LGM of about 70 metres (28×10^6 km^3) with respect to present (Peltier, 2004; Tarasov et al., 2012), it was the main contributor to sea-level change during the last glacial period. Even so, fundamental uncertainties underlying ice-sheet modelling of the LIS, its maximum elevation, extent and total volume differ largely among studies (Stokes, 2017).

Before diving into a comprehensive study of the potential thermomechanical instabilities in the LIS, the parameter sensitivity of Yelmo model, the ice stream representation and the role played by friction shall be addressed. In fact, the LIS mass loss is intimately related to a variable Hudson Bay ice thickness through rapidly-flowing ice streams that account for most of the ice sheet discharge (Stokes and Tarasov, 2010). However, the representation of these ice streams into numerical ice-sheet models remains challenging. As a result, we lack a deeper comprehension of the role of ice streams which leads to larger model output uncertainties.

The following chapter is structured as follows. First, a physical description of the methods and the experimental setup is presented (Sections 5.1 and 5.2). Then the results are laid in Section 5.3, further divided into two subsections where friction is a function of velocity alone (Section 5.3.1) and further coupled to the thermal state of the ice-sheet base (Section 5.3.2). Section 5.4

* The main contents of this chapter are published in:
Moreno-Parada, D., Alvarez-Solas, J., Blasco, J., Montoya, M., and Robinson, A.: Simulating the Laurentide Ice Sheet of the Last Glacial Maximum, *The Cryosphere*, **17**, 121-133, DOI 10.5194/tc-17-2139-2023., https://doi.org/10.5194/tc-17-2139-2023

discusses all the results herein presented. Lastly, the main conclusions of this work are summarized (Section 5.5).

5.1 Methods

Numerical experiments are conducted with the higher-order three-dimensional ice-sheet model Yelmo (Robinson et al., 2020, 2022). Here, its domain covers the entire LIS topography with a 16 km horizontal resolution. Namely, 21 unevenly-spaced vertical levels in sigma-coordinates are set, with higher resolution at the base of the ice sheet. Yelmo uses a higher-order stress approximation known as Depth Integrated Velocity Approximation (DIVA) to compute the horizontal velocity (Goldberg, 2011; Lipscomb et al., 2019). DIVA replaces the horizontal velocity gradients with their vertical averages in the effective strain rate, thus leading to a set of equations similar in accuracy to the Blatter-Pattyn approximation (Blatter, 1995; Pattyn, 2003). The internal ice temperature is determined by the advection-diffusion equation. Anisotropy of the ice is not explicitly modeled so an enhancement factor accounts for crystal orientation on the strain rate (Hooke, 2005; Ma et al., 2010; Pollard and DeConto, 2012a; Maris et al., 2014; Albrecht et al., 2020). For simplicity here, the enhancement factor of grounded ice is prescribed to 1.0, whereas floating ice requires a slightly lower value of 0.7 (e.g., Ma et al., 2010).

The total mass balance in Yelmo is governed by three terms: surface mass balance, calving and basal melting. Calving occurs when the ice-front thickness decreases below an imposed threshold (200 m in this study, Thomas, 1979; Tabone et al., 2019; Blasco et al., 2021) and the upstream ice flux is not large enough to advect the necessary ice to maintain such thickness (Peyaud et al., 2007; Colleoni et al., 2014). Importantly, basal melting of floating ice is a boundary condition whereas it is calculated internally for grounded ice.

5.2 Experimental setup

In order to investigate the effect of different friction formulations on the simulation of the LIS at the LGM, two sets of experiments were carried out. First, the effective pressure N is assumed to solely depend on the overburden pressure (Section 5.1) exerted by the ice column. In this simple scenario (purely mechanical friction), three different basal friction laws are considered with different dependencies of the basal shear stress on the sliding velocity: linear, power law (purely plastic) and regularized-Coulomb parametrizations. Second, for the most comprehensive basal friction parametrization law (i.e., regularized-Coulomb), thermomechanical coupling of the sliding is further allowed by introducing an additional dependency of N on the thermal state of the base via the water-dependent formulation.

Constant LGM conditions define the climatic boundary conditions. To this end, atmospheric temperature and precipitation are climatologies obtained from the mean of the output of the 11 General Circulation Models (GCMs) participating in the Paleoclimate Modelling Intercomparison Project Phase III (PMIP3) as part of the Coupled Model Intercomparison Project Phase 5 (CMIP5; Taylor et al., 2012) (Fig. 4.6a and 4.6c). The geothermal heat flow is also a spatially-variable boundary condition in our simulations and it is acquired from Shapiro and Ritzwoller (2004) (Fig. 4.6b).

Additionally, the initial bedrock elevation is taken from the RTopo2.0.1 present-day Earth topography dataset (Schaffer et al., 2016). The bedrock topography evolves under glacial isostatic adjustment (GIA) via the elastic lithosphere-relaxed asthenosphere (ELRA) method (Meur and Huybrechts, 1996) with a spatially-constant relaxation time of 3000 years.

Table 5.1: Parameter choice employed in our simulations and the sample range that was explored. The friction exponent q is taken from Zoet and Iverson (2020) for the regularized-Coulomb case.

	Linear	**Plastic**	**Coulomb**	**Explored range**
q	1	0	1/5	N/A
z_0 (m)	-100	-100	-100	$[-800, 200]$
u_0 (m/yr)	100	100	100	$[25, 250]$

Finally, a broad parameter range of z_0 values are sampled and then tuned so as to obtain an ice stream network that resembles previous mapping inventories (e.g., Fig. 2 in Margold et al., 2015). Hence, an ice stream is first defined as a set of grid points that satisfy $u_\mathrm{b}/u_\mathrm{def} > 10$. In other words, ice streams are here defined as regions of the ice sheet where the sliding contribution is, at least, one order of magnitude greater than ice deformation. It must be stressed that no particular LIS volume value was targeted but rather, the model is tuned based on the dynamics. The same z_0 value is then employed throughout the study (see Table 5.1). This approach provides good qualitative results and facilitates comparison among the model formulations used here.

Simulations throughout this study ran for 200 kyr to ensure a smooth equilibration from the initial state. An initial ice thickness of 1000 m is imposed over bedrock above sea level in North America above 50N to urge the spin up. The necessary length of the spin-up is quantified by a two-phase linear regression (Hinkley, 1969, 1971), i.e. a statistical test for detecting a change in behaviour of a variable time series (i.e., the so-called *changepoint*, details in Appendix C.1). Namely, a two-phase regression model is applied to the ice-sheet volume above flotation time series so as to determine the equilibration time (Fig. 5.1). The average equilibration time of all simulations herein presented reads $\bar{t}_\mathrm{eq} = 86.3$ kyr.

Thus, the first 100 kyr were assumed to represent model spin-up and are not considered in the analysis here. The remaining 50 kyr are shown in the figures below. All simulations were performed with a horizontal grid resolution of 16 km.

5.3 Results

Two main experiments were performed throughout this study accounting for each effective pressure formulation: purely mechanical friction (overburden) and thermomechanically coupled (i.e., a water-dependent parametrization), as described above. Each of this cases is described in the following sections.

In general, our simulations largely agree in extent with prior reconstructions (Stokes et al., 2016; Stokes, 2017). This result is not expected *a priori* since Yelmo ice-sheet model was not tuned to obtain a fully-developed ice

[b]0.7

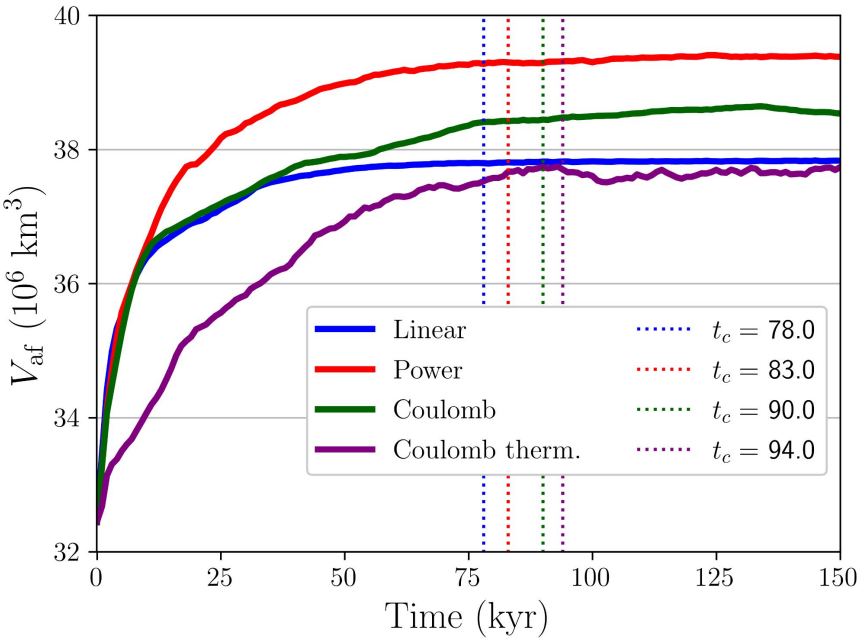

Fig. 5.1: Ice volume above flotation V_{af} for the main simulations. Vertical dashed lines represent the changepoint (i.e., the transition from transitory to stationary regime) for each time series as determined by the two-phase linear regression (details in Appendix C.1). For $t > t_c$, a constant equilibrium volume is reached in all cases.

stream network (e.g., Margold et al., 2014, 2015) but to match a certain volume and extent estimation (Section 5.2). It is worth noting that Margold et al. (2015) already stressed that that no inferences on the timing of ice stream operation at the LGM are possible because only a small number of the mapped ice streams have any chronological control. Rather, their mapped ice stream tracks represent a time-transgressive imprint of evolving ice stream trajectories, i.e. they can not have all operated at once. Nonetheless, some broad spatial patterns appear and this fact is further exploited to compare our simulations. Potential timing inconsistencies are thus inevitable, though the time-transgressive inventory remains as an appropriate reference for the simulated ice streams.

Further comparison with Margold et al.'s (2014) ice stream inventories was performed by re-projecting their data to the same coordinate system used in Yelmo LIS simulations. Namely, from a Lambert conformal conic projection (EPSG:3978) to polar stereographic.

As it shall be noted, the particular basal friction dependency on the sliding velocity leaves the ice extent and total volume nearly unchanged even though it strongly influences the ice stream configuration. On the contrary, the thermodynamical treatment of the ice-sheet base entails significant differences mainly in total volume.

5.3.1 Purely mechanical friction

The reconstruction of our simulated LIS under LGM conditions are first described for the three basal friction laws (linear, plastic and regularized-Coulomb) and no thermal coupling of the basal sliding. All simulations are numerically stable and reach constant equilibrium values within the first 100 kyr. Figure 5.2a shows important differences in the dynamic configuration of the ice sheet among the three cases.

In the linear case, ice streams appear to be widely distributed, far beyond the expected locations from prior reconstructions (e.g., Margold et al., 2015), thus differing from the purely plastic and regularized-Coulomb scenarios (Fig. 5.2b and c). As a result, horizontal velocities are generally high, even far from topographic troughs, allowing for strong lateral ice advection and both the ice thickness and the volume above flotation reach a minimum (Table 5.2). Rapid sliding also occurs near the margins where the continuity equations favours ice advection partially due to a large calving term. A more comprehensive dependency of the basal stress on the sliding velocity (e.g., a plastic or a regularized-Coulomb) shows that a fully-developed ice-stream network can be simulated even for a simple overburden formulation (Fig. 5.2b and c). Unlike the linear case, ice streams in the latter case are constrained spatially to lower troughs as a result of friction saturation at higher velocities (Joughin et al., 2019), allowing fast streams to develop mainly where soft sediments are assumed to enhance sliding (Eq. A.3).

In terms of the ice-thickness dome configuration, all reconstructions show a multi-domed configuration with two relative maxima: the eastern dome, cen-

tred over Hudson Bay and the western dome, over Lake Claire. Nevertheless, the minimum/maximum thicknesses are found for the linear and the power law scenarios respectively, whilst leaving the regularized-Coulomb case as an intermediate reconstruction. This is presumably caused by a further inland penetration of the Northwest ice streams in the regularized-Coulomb scenario compared to the purely plastic case. For the linear friction, higher velocities are generally found in the northwest and inner LIS. This translates into a larger amount of ice advected, consequently reducing the ice equilibrium thickness (mass balance equation).

The basal friction law has implications for the thermal state of the base even in the absence of thermomechanical coupling (Fig. 5.3). The LIS appears to be mostly temperate, except for the south-eastern region of the Canadian Shield. The spatial distribution of the basal temperature can be understood given that the ice sheet behaves as a thermal insulator. The nearly fully temperate base in the power law corresponds to the thickest LIS reconstruction. For the base to remain frozen two main requirements must be met: low sliding velocities (i.e., low frictional heat) and low geothermal heat flow (Fig. 5.3). The former is demonstrated in Fig. 5.2 for all three cases, whereas a strong correlation between frozen basal regions of the LIS and minimum geothermal heat flow values (Shapiro and Ritzwoller, 2004) supports the latter.

Figure 5.4 shows that the dynamic state of the ice sheet is highly sensitive to the particular function $\tau_b(u_b)$. It is noticeable that the regularized-Coulomb case appears to be an intermediate scenario between the linear and the purely plastic. However, there is a distinct common feature of the Coulomb and purely plastic cases: a linearly increasing lower boundary of τ_b for velocities $u_b > 200$ m/yr. This can be explained by the minimum value of the friction coefficient (to avoid spurious velocities). This value is a constant so that the basal shear stress becomes proportional to the sliding velocity, thus giving rise to a linear dependency. The behaviour is only visible for high velocities given the nature of minimum shear stress.

From an energy balance perspective, the dissipated frictional heat Q provides an idea of how the mechanical energy is distributed in the system (Fig. 5.5). Our simulations have attained a steady state so all the energy that enters our system must be dissipated. The ice mass moves as a consequence of its own weight, i.e. the potential energy transfers to kinetic energy via the surface elevation slope (driving stress). The equilibrium velocity field is

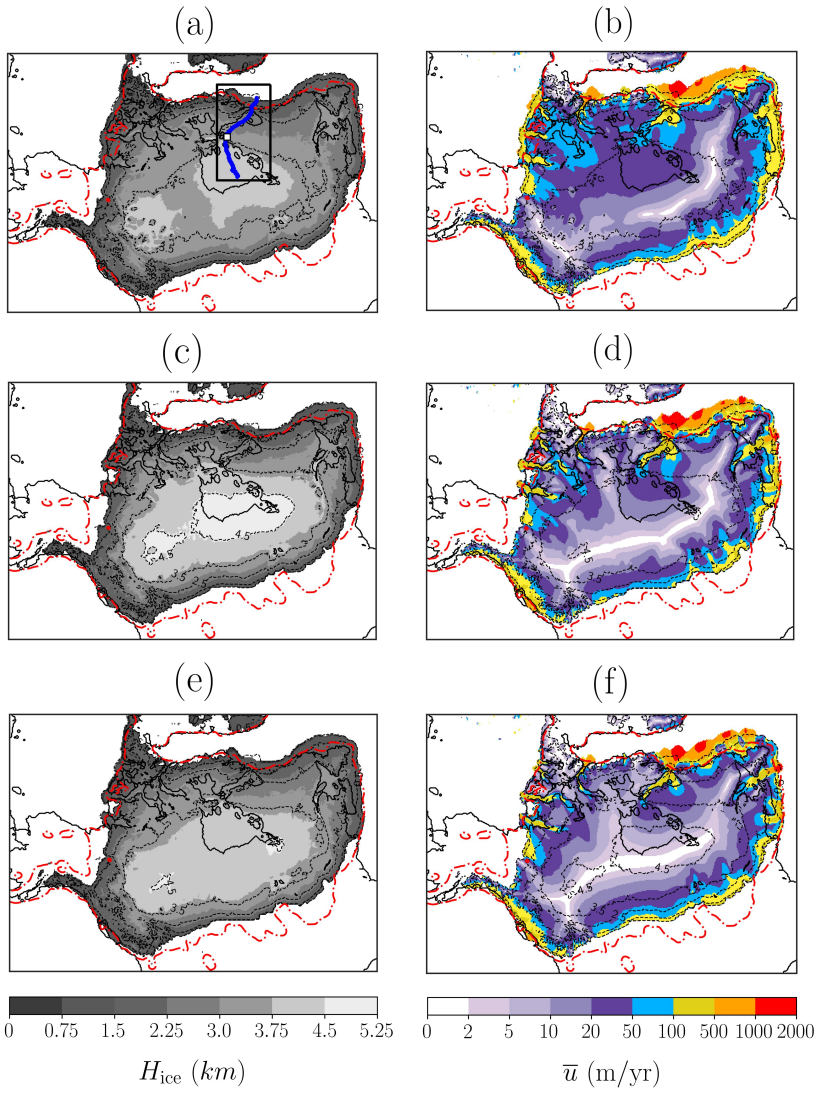

Fig. 5.2: First column, LIS ice thickness in kilometres; second, vertically averaged horizontal velocity. Each row corresponds to one friction law, from top to bottom: linear, purely plastic and regularized-Coulomb. Red dashed line shows maximum reconstructed LIS extent (ICE-6G). Black dashed line shows ice thickness contours in kilometres at values of 1.0, 2.5, 3.0, 3.5, 4.0 and 4.5 km. In panel (a), the black rectangle defines the Hudson Strait subdomain as referred to in the text. A blue solid line represents the Hudson ice stream section and a black solid contour denotes the present day coastline. Time series evaluated over a 9-grid-point square are centred in the white dot.

then maintained by the new ice accumulated on the domain. In the linear case, most of the kinetic energy is dissipated by thin ice with relatively large shear stresses. The purely plastic scenario yields a more distributed energy dissipation, where thick ice ($H > 3.0$ km) also has a significant contribution. As mentioned before, the Coulomb case appears as an intermediate physical description, thin ice dissipates more heat compared to the purely plastic scenario, yet large thicknesses have a significant frictional heat unlike in the linear case.

The basal stress distribution for different ice thicknesses (Fig. 5.4) may seem counterintuitive given that, for a fixed velocity, lower τ_b values are generally reached for thicker grid points. Yet this can be understood in terms of the bedrock characteristics as follows. Thick ice within the LIS is unable to reach high velocities unless it is restricted to low elevations (as c_b approaches its minimum). On the contrary, if low thicknesses are instead considered, the same velocities can be found for considerably higher c_b values (since $N = \rho g H$ is smaller). In other words, for a particular velocity, thinner ice yield higher basal stress due to the bedrock characteristics.

The different ice-sheet dynamics result in different configurations for the LIS (Table 5.2). In general, our simulations are consistent with our current knowledge of the LIS during the LGM, yet it is worth noting certain aspects of each parametrization. The fact that the linear law leads to the lowest values of ice volume (above flotation) and ice thickness can be explained by recalling Joughin et al. (2019). For low velocities (i.e., the centre of the LIS), the linear friction law (Fig. 5.3d) yields lower τ_b values than a plastic/Coulomb law (Fig. 5.3e and 5.3f). Such inland points consequently have higher velocities, thus advecting ice towards the margins and decreasing the equilibrium ice thickness. This entails a straightforward reduction in the effective pressure N. As a result, the basal friction coefficient reaches a minimum. In contrast, only minor differences in ice volume are found between the more comprehensive plastic law and regularized-Coulomb parametrizations.

Lastly, longitudinal sections of the Hudson Strait ice stream are presented for the linear, the purely plastic and the regularized-Coulomb friction laws (Fig. 5.6). The location of the points of the section was selected on the basis of a maximum velocity criterion so that the section lies in the centre of the ice stream and extends from Hudson Bay to the grounding line (Fig. 5.2a). As it would be expected, results with a linear friction law differ most. Particularly,

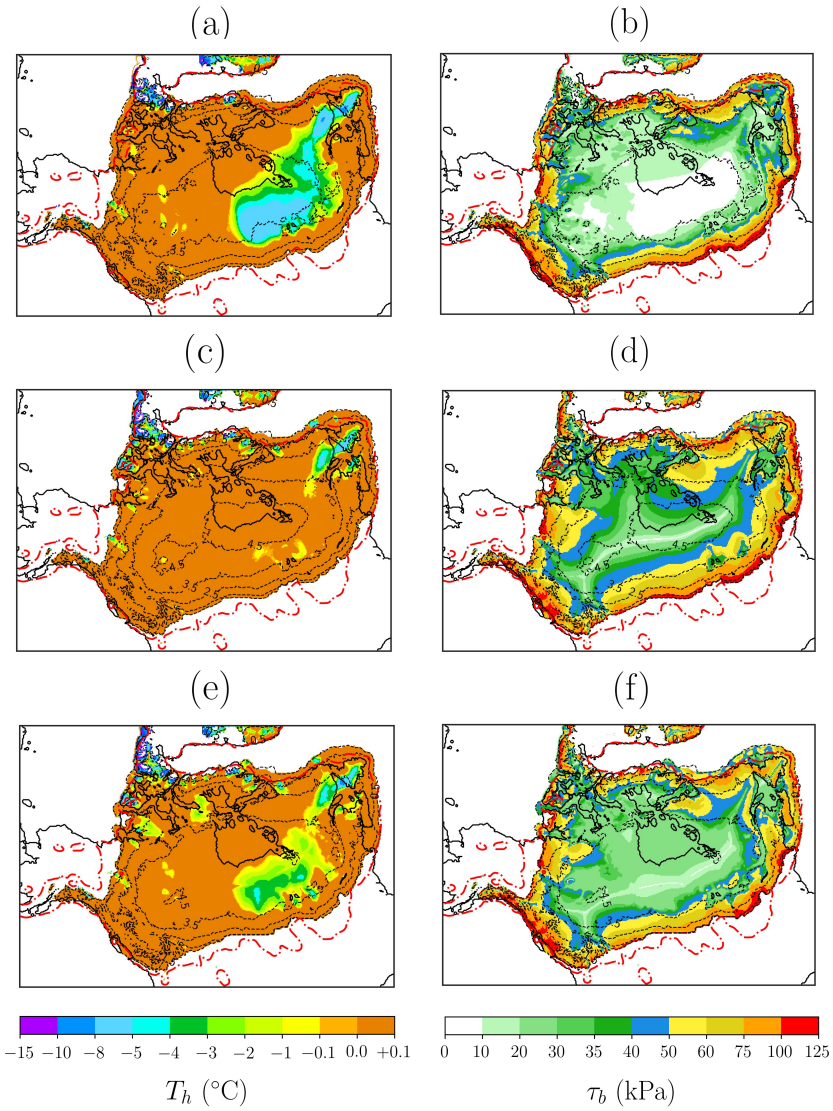

Fig. 5.3: Homologous ice-sheet base temperature (ºC) and shear stress τ_b (kPa) for the three friction laws: (a and b) linear, (b and e) purely plastic and (c and f) regularized-Coulomb. Red dashed line shows maximum reconstructed LIS extent (ICE-6G). Black dashed line shows ice thickness contours in kilometres.

deformation velocities close to the margin are the highest among the three laws herein considered as a result of an absent upper bound in the basal shear stress. Basal velocities near the dome of the LIS are also higher for a linear case given that $\tau_b(u_b)$ approaches zero more rapidly for $q = 1$ than for $q < 1$ (Eq. 3.9). Therefore, the ice thickness is the lowest as dictated by the continuity equation (consistent with Table 5.2). A subtle difference between the power law and the regularized-Coulomb case is visible on the surface elevation slope. In general, and particularly near the dome, the slope is slightly steeper in the power law case and the consequences are noticed in a higher deformation velocity (dashed blue line) in Fig. 5.6b than 5.6c.

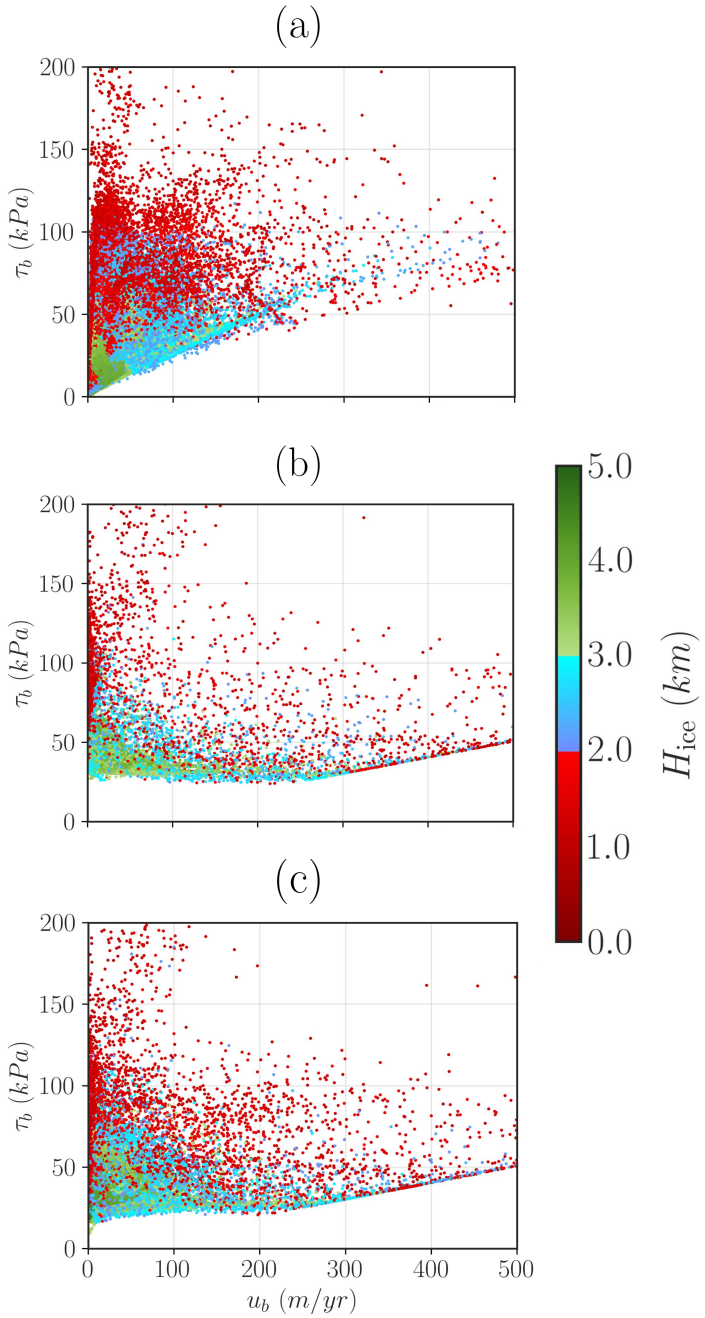

Fig. 5.4: Scatter plot of $\tau_b(u_b)$ phase space for three different basal friction laws: (a) linear, (b) purely plastic and (c) regularized-Coulomb. Every dot represents a pair (u_b, τ_b) evaluated in a single grid point.

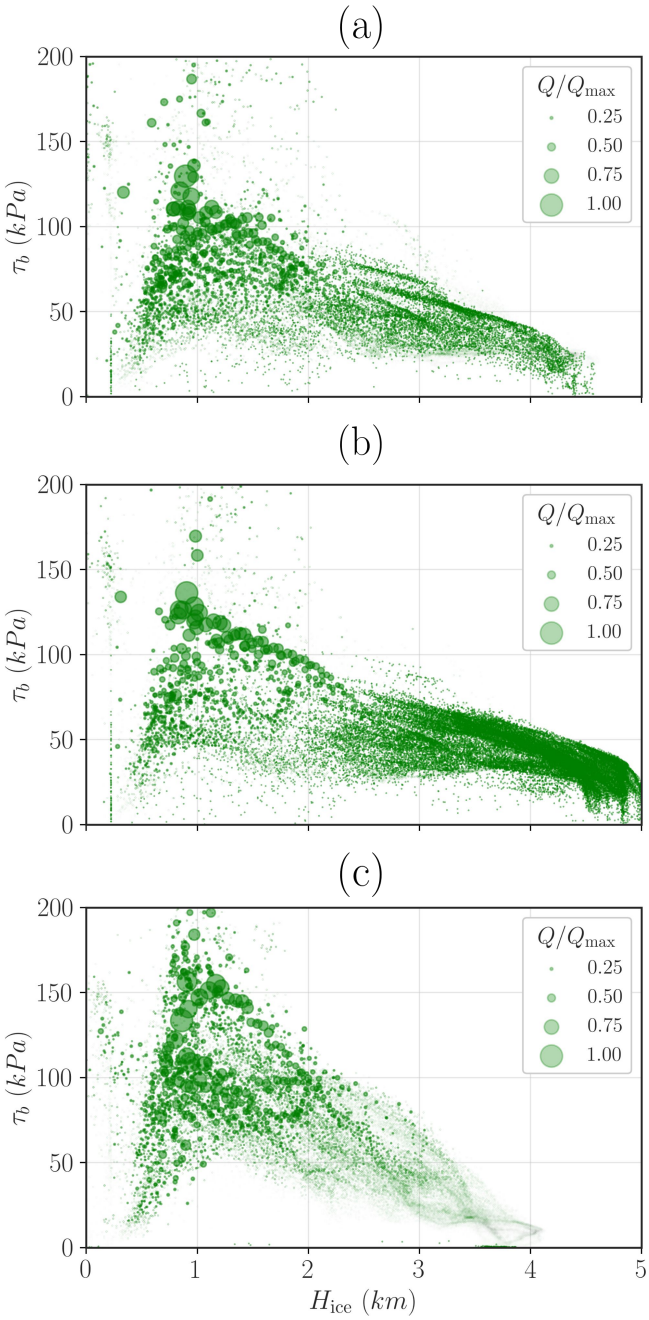

Fig. 5.5: Frictional heat distribution as a scatter plot of $\tau_b(H_{\text{ice}})$ for three different basal friction laws: (a) linear, (b) purely plastic and (c) regularized-Coulomb. Every dot represents a pair (H_{ice}, τ_b) evaluated in a single grid point. The marker size represents the normalised frictional heat Q/Q_{max}, where $Q = u_b\tau_b$ and Q_{max} is the maximum value of each simulation.

Table 5.2: Ice volume above flotation V, extent A, maximum ice thickness $H_{\max}$, spatially averaged basal temperature $\overline{T}_{\mathrm{b}}$ and sliding velocity $\overline{u}_{\mathrm{b}}$ for the three friction parametrizations under consideration. Standard deviation values σ are given between parentheses for averaged quantities.

Therm-coupled friction	Basal friction law	**V** (10^6 km^3)	**A** (10^6 km^2)	$H_{\max}$ (km)	$\overline{T}_{\mathrm{b}}(\sigma)$ ($^{\mathrm{o}}$C)	$\overline{u}_{\mathrm{b}}(\sigma)$ (m/yr)
No (overburden)	Linear	36.9	16.5	4.1	−1.0 (2.3)	33.8 (114.6)
	Purely plastic	39.5	19.5	5.0	−0.7 (1.7)	24.4 (137.2)
	Regularized-Coulomb	38.1	16.3	4.6	−0.8 (1.8)	28.4 (127.8)
Yes (water dependent)	Regularized-Coulomb	33.5	16.0	4.3	−0.7 (1.6)	27.7 (139.0)

[b]1.0

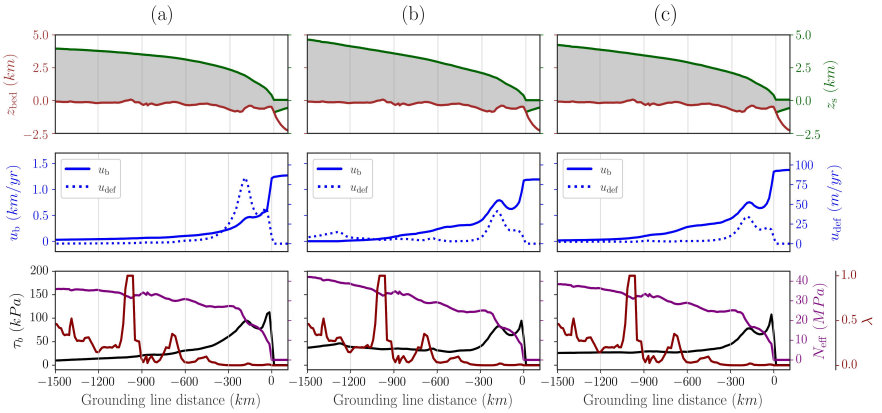

Fig. 5.6: Section along Hudson Strait ice stream (as noted in Fig. 5.2a) for purely mechanical basal frictions: linear, purely plastic and regularized-Coulomb. Green, LIS surface elevation; brown, bedrock height; blue, horizontal velocity (sliding and deformation contributions); purple, effective pressure and black, basal shear stress.

5.3.2 Thermomechanically coupled friction

Next, the effect of coupling basal friction to the thermal state of the base is investigated by comparing the simulated LIS under LGM conditions for the water-dependent parametrization with the purely mechanical friction formulation. A regularized Coulomb friction law is employed throughout this section. In terms of ice thickness, there is no clear distinction between a purely mechanical friction approach (Fig. 5.2c) and the thermomechanically coupled case (Fig. 5.8a) besides a minor decrease. More precisely, Table 5.2 shows slight differences in total ice volume and extent: the thermomechanically coupled simulations show a smaller extent and therefore a lower volume given that the ice thickness remains nearly identical. Nevertheless, such decrease brings our simulation closer to previous reconstructions (Fig. 5.7), but the ice extent remains in the upper limit compared to prior studies. This further suggests that, for our particular parameter choice, a thermomecanically-coupled fricton may be necessary to obtain a realistic LIS extent.

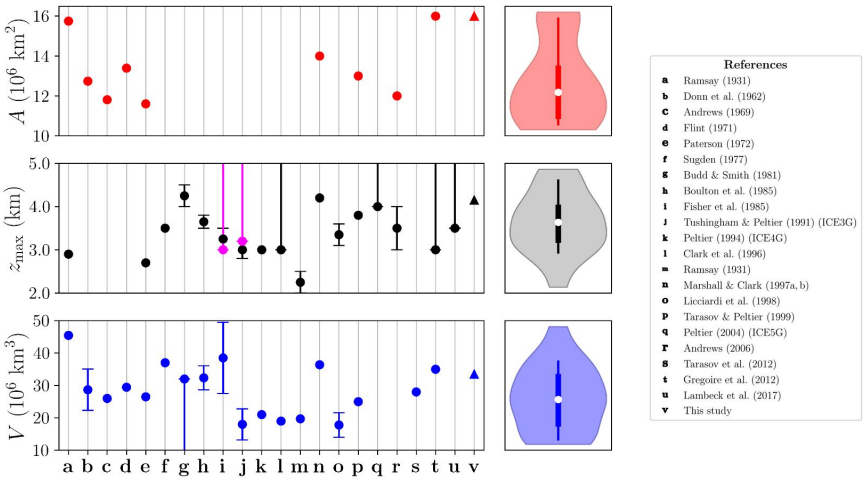

Fig. 5.7: Comparison of reconstructed LIS ice extent, maximum elevation and volume. Estimates from this study are given by triangle markers. Magenta dots show maximum ice-sheet elevation for the soft bed models.

It is illustrative to build a streaming mask to perform a qualitative comparison among parametrizations as well as previous inventories (e.g., Margold et al., 2015). Sliding regions are therefore defined as those points that satisfy the condition $u_b/u_{def} > 10$, thus ensuring that ice flow due to deformation is, at least, one order of magnitude lower than the sliding contribution. In terms of this streaming mask (Fig. 5.8a), this thesis generally simulate the most significant ice streams present in recent mapping inventories and comprehensive reviews of the LIS (e.g., Margold et al., 2014, 2015).

The thermomechanically coupled friction formulation entails fundamental changes in the LIS configuration and thermal state of the base. A direct inspection of Fig. 5.2c as compared to Fig. 5.8a further shows the implications in the simulated ice stream configuration and notable improvement is found in the Hudson Strait ice stream and tributary.

The probability density functions $P(u_b)$ and $P(T_b)$ (Fig. 5.9) further explore the differences among friction law formulations both for an overburden and a water-dependent effective pressure. For the linear law, the coldest ice base on average is found (see Table 5.2) as the tail of the distribution reaches leftmost values compared to a power or Coulomb formulation. Notably, these two last friction laws show minor differences in terms of $P(u_b)$ and $P(T_b)$,

showing physically equivalent reconstructions in terms of probability densities. On the contrary, when the basal friction is coupled with thermodynamics via Eq. 4.55, it is noted a shift towards higher velocities $P\left(u_{\mathrm{b}}\right)$ for low velocities (i.e., $u_{\mathrm{b}} < 250$ m/yr), thus implying a speed-up of the slower regions of the ice sheet. Consequently, the outflow of ice becomes larger and the equilibrium thickness is reduced compared to the Coulomb overburden scenario (Table 5.2).

When the basal friction is thermomechanically coupled (Table 5.2), the LIS extent is reduced and the maximum ice thickness is lower, leading to a smaller equilibrium volume (consistent with AIS mass sensitivity results by Dawson et al., 2022). This is explained through the decrease in basal friction. In this case, there is an additional degree of freedom that may yield a reduction in basal friction: the effective pressure. All temperate grid points undergo a reduction in their effective pressure (and consequently in the basal stress) by up to a 10% of their original value. As a result, the stress balance will yield higher velocities and a lower equilibrium thickness for a fixed set of boundary conditions. On the contrary, in the purely mechanical friction case, the value of c_b is determined solely by the bedrock elevation, which does not change significantly over the course of the experiment.

Nevertheless, the equilibrium volume, relevant for the sea level contribution, does not encapsulates all the relevant information about the LIS, especially for the Hudson subdomain. Notably, the ice volume in the Hudson subdomain (as defined by the black rectangle in Fig. 5.2a) reaches a constant equilibrium value both in the purely mechanical and thermomechanically coupled experiments. Likewise, the vertically averaged horizontal velocity also attains a constant value, yet slightly higher due to the water-dependent effective pressure for the aforementioned mechanism.

Global variables such as the total LIS volume are not the only ones that undergo changes when the basal friction is further coupled to thermodynamics. This result is captured by Fig. 5.10a. Unlike its counterpart in the purely mechanical case (Fig. 5.4a), an interesting behaviour of the non-monotonic minimum shear stress values in the low velocity regime ($u_b < 150$ m/yr) is found when the basal friction is coupled with thermodynamics. Nonetheless, all points taking part in this minimum shear stress region correspond to a fully drained till. Hence, explicit water changes do not explain the difference in behaviour. Presumably, it is argued that those points with lowest τ_b cannot

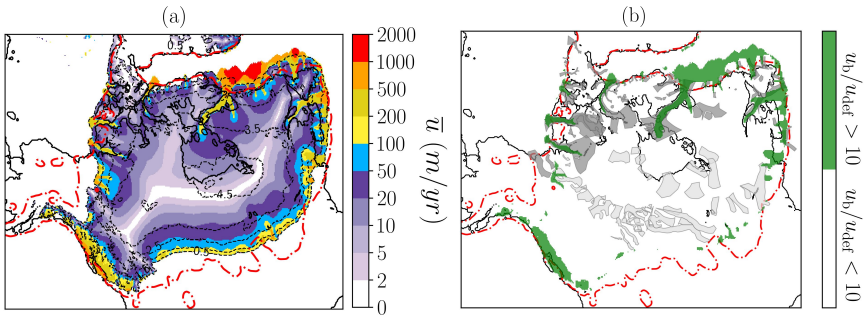

Fig. 5.8: Left panel, LIS depth-averaged horizontal velocity; right panel, spatial mask (green) depicting the two ice flow regimes overlaid with the ice-stream inventory of Margold et al. (2014) (polygons). Solid polygons correspond to land terminating (light grey) and marine terminating (dark grey) ice streams respectively. Streaming grid points meet the condition $u_{\mathrm{b}}/u_{\mathrm{def}} > 10$ so that the flow due to ice deformation represents, at highest, a contribution one order of magnitude below sliding. Both fields are shown for a water-dependent effective pressure. Red dashed line shows maximum reconstructed LIS extent (ICE-6G). Black dashed line shows ice thickness contours in kilometres of 1.0, 2.5, 3.0, 3.5, 4.0 and 4.5 km.

be reached given the new stress balance (i.e., the SSA equations) is changed if N_{eff} is considered. Since the SSA solution is non-local, the particular shape of $\tau_b(u_b)$ can be modified by a water-dependent effective pressure even for regions that are fully drained. This implicit effect would be a direct consequence of the non-local nature of the SSA solutions in regions where the water content remain constant.

It is also illustrative to compare the Coulomb friction law for both a purely mechanical friction and the thermomechanically coupled case from a frictional heat perspective (Fig. 5.5c and 5.10c, respectively). When the basal friction is coupled with the thermal state of the base via a the water layer thickness H_{w}, two main changes are noted. The shear stress values are generally reduced and the thicker regions of the LIS contribute more to frictional heat dissipation (larger region covered in green for $H > 3.0$ km).

It is clear from Fig. 5.10b that, for an effective pressure that depends on basal water thickness, sliding occurs when the till is saturated in water. This requires a sustained supply of heat (e.g., basal frictional heat, geothermal heat flow, etc.) to melt enough water so as to keep a saturated till, thus surpassing the drainage rate and eluding refreezing (due to heat diffusion-

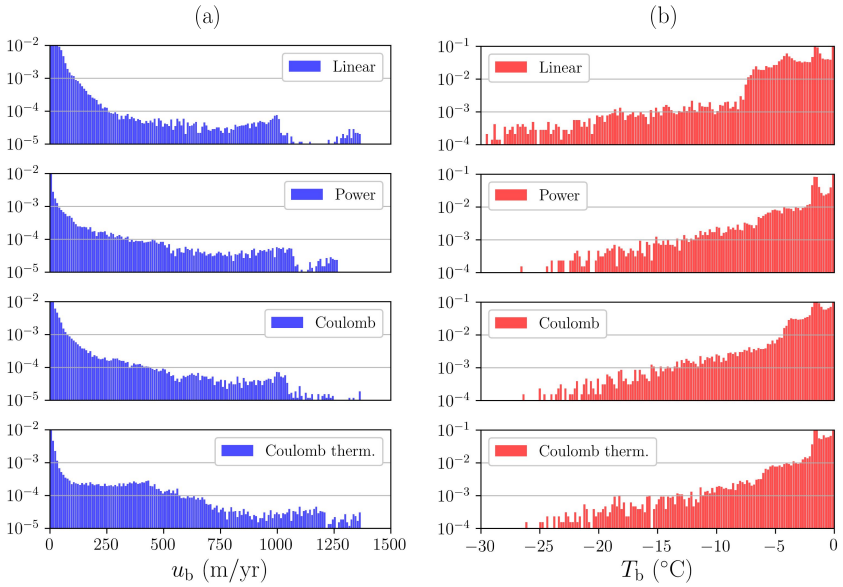

Fig. 5.9: Probability density functions (PDF) of (a) $\log_{10}P(u_b)$ and (b) $\log_{10}P(T_b)$. Each row represent a different friction formulation. From top to bottom: linear, power law, regularized-Coulomb and regularized-Coulomb with a water-dependent effective pressure formulation. Note the difference in y-axis limits.

advection). This is unlikely to occur in the central region of the ice sheet where neither low troughs nor high surface slopes are present, consequently yielding low driving stresses and basal frictional heat.

5.4 Discussion

In general, the ice sheets simulated herein are consistent with our knowledge of the LGM Laurentide ice-sheet state. Qualitatively, this can be seen by a comparison of Fig. 5.8b with previous reconstructions of LIS ice dynamics (e.g., Margold et al., 2015; Stokes et al., 2016). Notably, the main ice streams of the LIS (i.e., Amudsen Gulf, M'Clure Strait, Massey Sound, Gulf of Boothia, Lancaster Sound and Hudson Strait) are present in our simulation even in the absence of thermomechanical coupling (Fig. 5.2b and 5.2c).

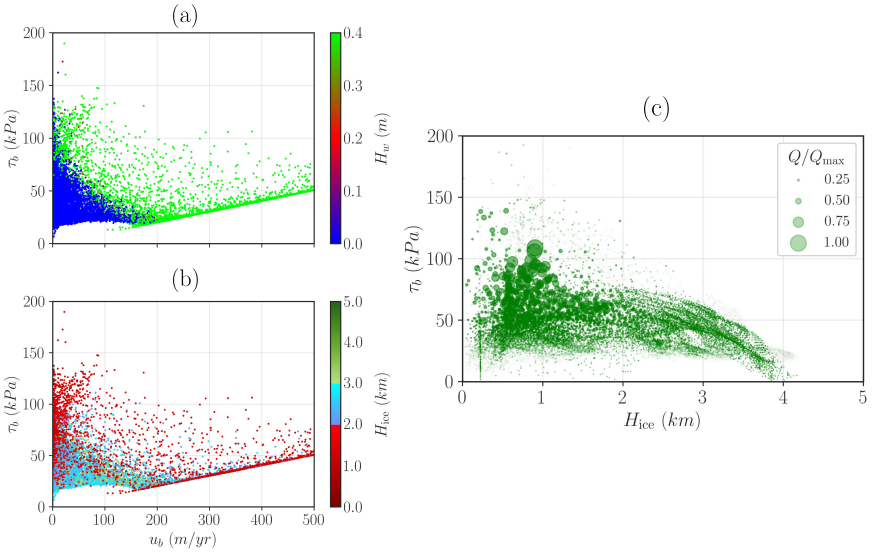

Fig. 5.10: Scatter plot of $\tau_b(u_b)$ phase space for the water-dependent effective pressure formulation and coloured according to (a) ice thickness and (b) basal water content. Every dot represents a pair (u_b, τ_b) evaluated in a single grid point. Panel (c) shows a scatter plot of $\tau_b(H_{\text{ice}})$ for the water-dependent effective pressure, where each dot represents a pair (H, τ_b) evaluated in a single grid point. The marker size depicts the normalised frictional heat Q/Q_{max}, where Q_{max} is the maximum frictional heat value.

However, both the configuration of ice streams and the total ice sheet volume are found to be strongly dependent on the basal friction formulation.

In particular, the linear basal friction law clearly yields significantly lower shear stress values compared to the other formulations (Fig. 5.2). Despite the fact that both ice extent and volume do not fall far from previous studies, relatively high velocities are found further inland in ice streams along the northern LIS and are not fully constrained to lower troughs (Fig. 5.2a). As a result, the ice sheet under this parametrization exhibits a minimum volume and a simple-domed ice sheet that resembles past reconstructions that ignore deformable beds (e.g., Denton, 1981). This can be understood as follows. The equilibrium thickness is in fact explicitly dependent on the horizontal velocity via the continuity equation, thus reaching a minimum value when the velocity is high for a fixed set of boundary conditions (i.e., the accumu-

lation rate). Hence, the maximum ice thickness yields its lowest value in this reconstruction.

These results could lead to the hypothesis that rapid ice-streaming spatially constrained to lower troughs requires a thermal coupling with the base. Nevertheless, the absence of a thermomechanical coupling solely exhibits a fully-developed and spatially constrained ice stream structure when a more realistic function for $\tau_b(u_b)$ is provided (i.e., a power-law or a regularized-Coulomb). Although the same ice extent appears to be reached independent of such a function, it closely matches the ICE-6G reconstruction. Thus, thermomechanical coupling is not necessary to simulate a fully-developed ice-stream network in the expected locations. In fact, a more realistic $\tau_b(u_b)$ is sufficient to find rapid streaming regions spatially constrained to low troughs as is the case for a purely plastic or a regularized-Coulomb parametrization. Significantly lower basal friction values are yielded by the former, yet the dynamic configuration of the ice sheet seems almost identical. Despite these similarities, from a purely thermodynamic perspective of the ice-sheet base, the choice of $\tau_b(u_b)$ is fundamental even when thermal coupling is not considered. This is presumably due to the insulator effect of a thicker ice sheet from the colder atmosphere (see maximum equilibrium thickness in Table 5.2).

Fundamental changes are noticed when the basal friction parametrization is coupled with the thermal state of the base (Fig. 5.9 and 5.10). Rapidly-flowing ice streams are present in expected locations, such as through Hudson Strait, Amundsen Gulf, M'Clure Strait, Lancaster Sound and Gulf of St Lawrence (Margold et al., 2015). Consequently, both the total volume and the equilibrium ice thickness are reduced. This result is in good agreement with the mass loss sensitivity in the AIS as a response of idealised basal thawing (Dawson et al., 2022). Overall, the simulated ice sheet closely matches the reconstructed ICE-6G extent, even though it is somewhat lower than for the overburden case. All friction laws herein presented yield a multi-domed ice sheet where two independent domes are found (western and eastern) irrespective of the thermomechanical coupling. The total ice volume, in terms of contribution above flotation, is 33.5×10^6 km^3 (Table 5.2). This value is larger than the estimate given by Sims et al. (2019) ($30.4 \pm 2.7 \times 10^6$ km^3), though close to Gregoire et al. (2012) (35×10^6 km^3). Furthermore, no large volume changes are found either in the entire LIS nor the Hudson region that would resemble binge-purge oscillations (MacAyeal, 1993a).

Not only does the Bueler and van Pelt (2015) effective pressure formulation couple ice dynamics with the thermomechanical state of the base, but also the amount of liquid water is considered to compute the effective pressure. Figure 5.4 shows a significant difference in terms of the horizontal velocity and the basal friction coefficient. As described above, the simulated ice sheet also appears to be a multi-domed configuration with two relative maxima that resemble the previous result (western and eastern domes). Even so, the ice-stream structure strongly differs from the purely mechanical friction approach. First, the ice streams are more restricted spatially, in the sense that they do not propagate as far inland. Second, even for non-streaming regions, τ_b values are generally higher for the water-dependent effective pressure formulation.

The fact that all our reconstructions share a multi-domed equilibrium configuration resembles the prevailing approach of LIS reconstructions that have accounted for lubricated basal conditions, in which the ice sheet over Hudson Bay was consequently thinner and less steeply sloped (e.g., Boulton et al., 1985; Fisher et al., 1985). Nonetheless, the surface elevation over Hudson Bay was substantially lower in those cases, with a maximum elevation above present sea level of 3.0-3.5 km, in contrast to our $\sim$ 4-5 km thickness. This comparison must be taken with caution since surface elevation and ice thickness do not represent the same magnitude. Yet, it is possible to have an approximate comparison among reconstructions by also looking at the volume differences. Boulton et al. (1985) spans a volume of 33-44 $\times$ 10^6 km^3, substantially larger than the 21.1-25.9 $\times 10^6$ km^3 range of Fisher et al. (1985) for the hard bed model in both cases (Fig. 5.7). Our particular volume values fall within Boulton et al.'s 1985 range. In terms of volume and ice extent, results from the water-dependent effective pressure formulation yield a slightly larger ice volume as a result of narrower and shorter ice streams that consequently advect less ice towards the margins. This dynamic distinction is significant for ice extent given that the reconstructions exhibits the lowest ice extent value (16.0×10^6 km^2).

Notably, the most realistic parametrization (a water-dependent effective pressure formulation) shows an interesting behaviour that deviates from the cases using the overburden pressure approach. For low velocities, the shape of $\tau_b(u_b)$ is almost identical to the overburden case. Nevertheless, for higher velocities ($u_b > 80$ m/yr), the phase space $\tau_b(u_b)$ differs from the purely me-

chanical reconstructions, where quite low basal stresses are yielded. Figures 5.10a and 5.10b then establish the distribution of ice thickness and basal water content throughout the ice sheet. In terms of the former (Fig. 5.10a), fast sliding occurs in grid points with a medium-size thickness (1.0-3.0 km), exhibiting a perfect correlation with water-saturated grid points (Fig. 5.10b).

In a somewhat more realistic approach to basal friction, the additional dependency on the effective pressure $\tau_b(u_b, N_{\text{eff}})$ must be considered, thus triggering rapid ice streaming in temperate regions. Nevertheless, the assumption that ice streaming occurs in all temperate grid points leads to an extremely low shear stress in the centre of the ice sheet (Fig. 5.4). For this reason, accounting for hydrological processes (e.g., the basal water content) appears to be fundamental to simulate Laurentide ice streams in accordance with geological reconstructions (Margold et al., 2015) and further yields ice-sheet volume and maximum elevation values closer to prior studies (Fig. 5.7). Besides, a water-dependent friction substantially considers the thermal state of the base, rather than just local dynamics. This implies a stress balance influenced by the geothermal heatflux as well as the frictional and deformation heat contributions.

Overall, the simulated ice streams are numerically well-behaved and spatially constrained to lower troughs. In general, horizontal velocities reach an equilibrium value once the ice sheet has stabilized. However, global LIS variables as the total ice volume are highly sensitive to both the choice of friction law and the thermal coupling at the base.

5.5 Conclusions

The LIS under LGM boundary conditions has been simulated considering three basal friction scenarios of varying dynamic complexity and their consequences on the LIS ice streams, configuration, extent and volume.

First, in the purely mechanical friction formulation, the force exerted by the weight of the ice column on a given grid point (overburden pressure) is solely considered. In this context, three different dependencies of the basal shear stress on the sliding velocity are investigated: linear, purely plastic and regularized-Coulomb. Friction was thus independent of the thermal state of the base. The LIS extent closely matches the reconstructed ICE-6G ice sheet,

yet the volume appears to be slightly larger. For the linear case, this is a consequence of the absence of an active ice-stream network spatially constrained to low troughs that advects ice from the centre of the ice sheet to the margins. The surface elevation reflects a simple-domed ice sheet (except for the regularized-Coulomb scenario) resembling past results where the LIS deformable bedrock was ignored. Remarkably, a fully-developed ice-stream network was simulated for a purely plastic and regularized-Coulomb formulation without any thermomechanical coupling requirements, yet the equilibrium ice volume appears to be slightly larger than previous reconstructions.

Hydrological processes were considered by coupling the basal friction to the thermal state of the base via the implementation of a water-dependent effective pressure formulation (Bueler and van Pelt, 2015). The simulated ice sheet also appears to be a multi-domed configuration with two relative maxima, yet the ice-stream structure strongly differs from the overburden approach for two reasons. First, the ice streams are spatially more restricted and second, the basal friction coefficient is generally higher for non-streaming regions. This approach yields the closest ice sheet volume to prior LIS reconstructions that also consider fast sliding in regions of a lubricated bed. These results support the hypothesis that hydrological processes are necessary to achieve physical realism in our simulations and to obtain realistic ice volume reconstructions similar to previous work.

Notably, ice volume above flotation reached a constant equilibrium value for the all cases under consideration. Precise values are highly sensitive to thermomechanical coupling of the basal friction. The overburden case seems to overestimate the LIS volume compared to previous reconstructions. Nevertheless, significantly lower values are simulated when the thermal state of the base is accounted for, yet the particular coupling parametrization does not exhibit significant changes regarding ice volume nor total ice sheet extent. A water-dependent formulation yield volume and ice extent values substantially closer to prior studies.

To conclude, the most sophisticated scenario in this work (a thermomechanically coupled regularized-Coulomb basal friction) appears to be the reconstruction closest to reality compared to previous ice stream inventories. Future experiments shall focus on a more realistic basal hydrology, where conservative non-local processes (as the horizontal advection) are also resolved.

Chapter 6
Could the Laurentide have exhibited internal oscillations?

A conclusive physical explanation underlying any oscillatory mechanism that causes the HEs is still under debate. More importantly, whether the cause is unique still remains as an open question (Roberts et al., 2016). Any theory that attempts to provide an answer must explain three key observations: a roughly 7-kyr periodicity (Hemming, 2004), the presence of IRD layers in sediment cores taken from the North Atlantic (formed on short timescales) and the spatial source of such debris as traced from geological evidence. In fact, such evidence narrowed the spatial uncertainty to Hudson Strait (e.g., Naafs et al., 2013) and the sediments are thought to be transported due to oceanic circulation, thus turning a periodic surge from Hudson Strait into a necessary condition.

There are several mechanisms proposed to provide an explanation for such periodic surges. The triggering mechanism can follow either (1) an ice-internal ("binge-purge") oscillation (MacAyeal, 1993a) or (2) an externally-driven behaviour (Moros et al., 2002; Hulbe et al., 2004; Alvarez-Solas et al., 2013; Bassis et al., 2017). Multiple studies support both hypothesis. For instance, MacAyeal (1993a), Marshall and Clarke (1997) and Payne (1995a) suggested that internal instabilities are self-sufficient mechanisms to trigger a periodic collapse of the LIS. On the other hand, Johnson and Lauritzen (1995) presents evidence for a discharging ice-dammed lake in Hudson Bay and (Hulbe, 1997; Hulbe et al., 2004) proposed a collapse of an ice shelf in Davis Strait a physical explanation of periodic surges.

This study focuses on the physics behind modelled ice thermomechanical instabilities and it is structured as follows. The following chapter is structured as follows. First, a physical description of the methods and the experimental

setup is presented, with particular stress over the the till hydrology (Section 6.1). Then the results are laid in Section 6.2, further divided into multiple subsections addressing the role of each physical component of the employed basal hydrology formulation. Reference simulations at equilibrium are first shown in Section 6.2.1, followed by a physical description of the oscillation Section 6.2.2. Next, the implications of three physical aspects are assessed: till compressibility 6.2.3, maximum thickness of the basal water layer 6.2.4 and the till drainage rate 6.2.5. All results are dicussed in Section 6.3. Lastly, the main conclusions of this work are summarized (Section 6.4).

6.1 Methods and experimental setup

The methods herein presented are identical to those described in Chapter 5 and thus omitted to avoid repetition. Nevertheless, a number of processes are further elaborated here for their relevance in this study.

Four main ensemble experiments were performed throughout this study accounting for each parameter tested: till compressibility C_t, maximum allowed basal water layer $H_{\mathrm{w,max}}$, minimum effective pressure δN and till rate d_r. The majority of simulations were performed with a horizontal grid resolution of $\Delta x = 32$ km. However, a numerical stability study was also performed in which the spatial resolution was consequently increased to $\Delta x = 20$, 16 km.

6.2 Results

6.2.1 Equilibrium states

First, results below describe our reference simulation (see Fig. 6.1), which employs the Bueler and van Pelt (2015) effective pressure parametrization and the following parameter values: $H_{\mathrm{w,max}} = 0.4$ m, $e_0/C_c = 37.9$ (overconsolidated till) and $d_r = 5$ mm/yr. The simulated ice sheet under constant LGM conditions is also shown in the companion paper (Moreno et al., this issue) and closely matches the reconstructed ICE-6G extension and major

ice streams are also present in expected locations, such as through Hudson Strait, Amudsen Gulf, M'Clure Strait, Lancaster Sound and Gulf of St Lawrence (Margold et al., 2015). In general, the ice sheet is consistent with our knowledge of the LGM Laurentide ice-sheet state, and is a suitable reference point for a study of the stability of the ice sheet. It must be stressed that, likewise Moreno et al, (this issue), there is no oscillatory forcing whatsoever throughout this work in any boundary field.

Notably, in this reference simulation, ice streaming over Hudson Strait does not exhibit a constant velocity equilibrium value. Rather, this region transitions between two modes of ice flow: rapid sliding over a saturated till and slow creeping ice over a fully drained till (Fig. 6.2). The switch mechanism between these two states as well as the physical conditions required for each mode are thoroughly described in Section 3.2 6.2.2. In this simulation, oscillatory behaviour is not found in any other LIS stream, where a constant equilibrium velocity is reached (Fig. 6.1). This illustrates that Yelmo yields two stationary solutions of different nature (i.e., oscillatory and non-oscillatory) depending on bedrock topography, till properties and the geometry of the ice sheet. Hence, it further manifests that ice streaming is not necessarily oscillatory in Yelmo, but likely depends on the boundary conditions and the state of the ice sheet.

6.2.2 Physics of the oscillation

The oscillatory behaviour exhibited by Yelmo is well behaved and stable. Along with the horizontal velocity, a number of variables share this oscillatory nature (Fig. 6.2), thus showing a clear correlation among them. To start with, it is evident that maximum velocities occur when the till is completely saturated ($s = 1$) whereas a fully drained till ($s = 0$) corresponds to minimum velocity values. The opposite relationship is found for the basal shear stress τ_b, in which the minimum value is found for saturated till. The link between ice flow and basal hydrology imposed by a water-dependent effective pressure formulation is thus straightforward in our results.

Let us now focus on a single event at one point in the upstream region of the Hudson Strait ice stream (Fig. 6.3). Three stages in terms of ice velocity can be distringuished: acceleration, stabilization and slowdown. First, the

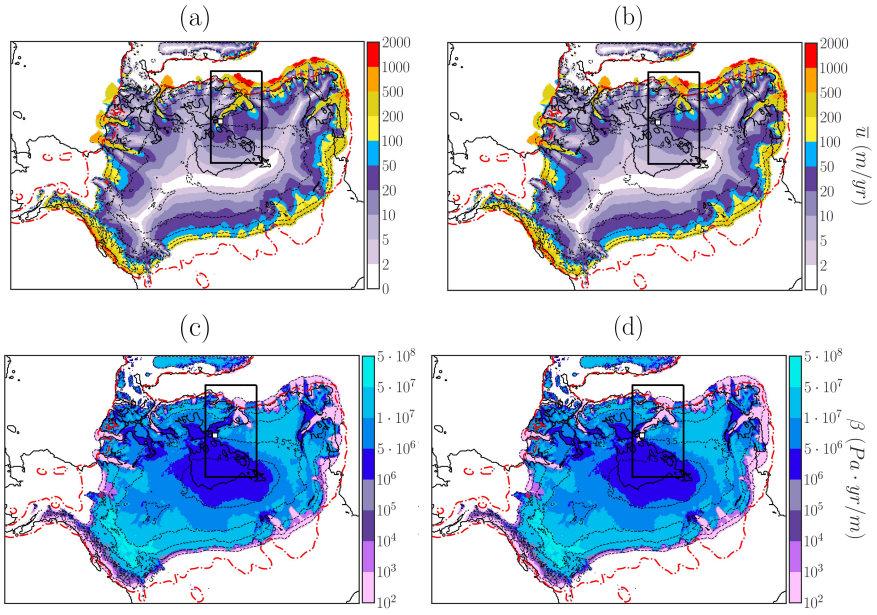

Fig. 6.1: LIS vertically integrated horizontal velocity and basal friction coefficient β (Pa·yr/m) for an oscillatory equilibrium state over Hudson Strait: left column, creeping mode; right column, rapid sliding. Red dashed line shows maximum reconstructed LIS extension (ICE-6G). Black dashed line shows ice thickness contours in km. The blue rectangle defines the Hudson Strait subdomain as referred to in the text. Time series and vertical profiles evaluated over a 9-grid-point square are centred in the white dot.

acceleration corresponds to a gradual increase in ice velocity and a consequent decrease in ice thickness due to advection. This gradual increase in ice velocity reaches an unstable equilibrium value ($u_b \approx 275$ m/yr) determined by the balance among β, the ice-surface gradient and the ice flux. Halfway into this stage ($u_b \approx 150$ m/yr), colder ice is advected from upstream faster than heat travels upwards vertically (following the advection-diffusion). As a result, both the temperature (Fig. 6.4) and ice thickness continue to decrease. The stabilization stage then begins by a reduction in ice acceleration and a slowly decreasing ice thickness. Eventually, during the slowdown, the till-water thickness diminishes (drainage) with a consequent increase in N. As a result, the sliding velocity is drastically reduced, thus returning to the value

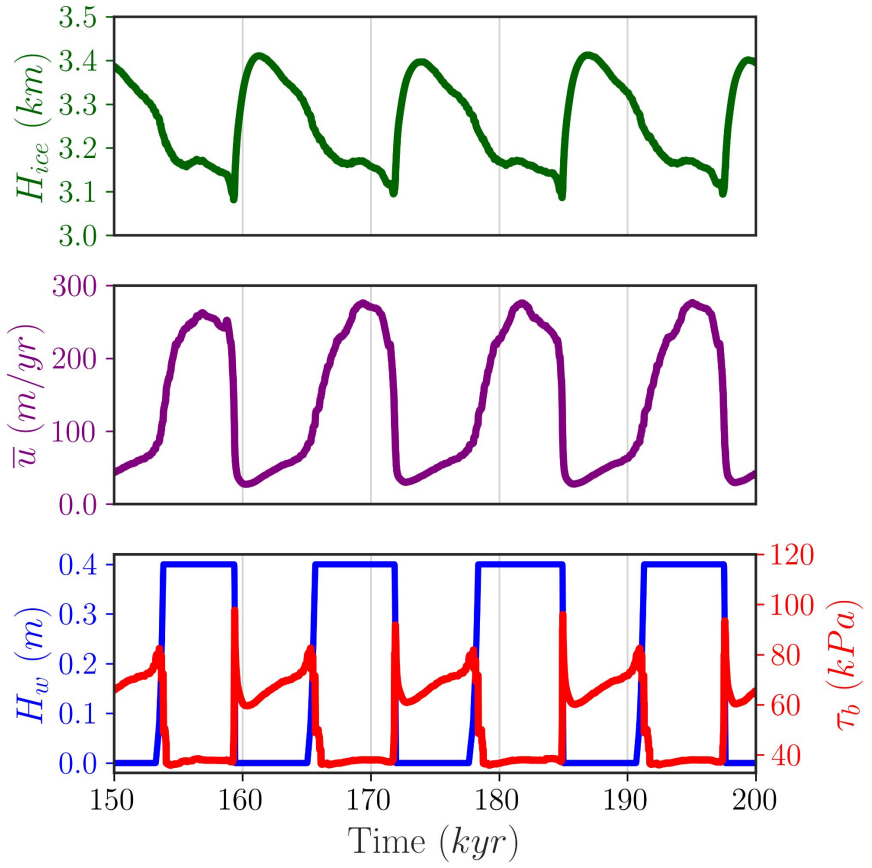

Fig. 6.2: From top to bottom: time evolution of ice thickness, vertically-averaged horizontal velocity, basal water content and shear stress. Each time series represents the mean value over a square formed by 9 grid points taken in Hudson Strait (see Fig. 6.1 for the exact location).

of the initial acceleration stage. This reduction in basal velocity takes the form of a "wave" that propagates downstream along Hudson Strait.

The rapid decrease in ice thickness during the slowdown stage may seem counterintuitive. Yet it can be understood in terms of ice advection given that the ice velocity follows a downstream "wave". In other words, the decrease in ice velocity starts over Hudson Bay and then propagates along Hudson strait. Therefore, for a given point in Hudson strait, the ice continues flowing

downstream while no ice is advected from Hudson bay (thus the decrease in ice thickness).

Meanwhile, the temperature at the base remains constant and at the pressure-melting point during the first two stages. Nevertheless, once the drainage of the basal water layer takes place, the temperature rapidly decreases below the pressure melting point as a consequence of the plummeting horizontal velocity values and the consequent reduction in basal frictional heating. This highlights the strong contribution of the $Q_b \sim u^2$ term on the total basal heat budget in advection-diffusion equation (unlike intermediate height vertical layers within the column, where horizontal advection and strain heat are relevant).

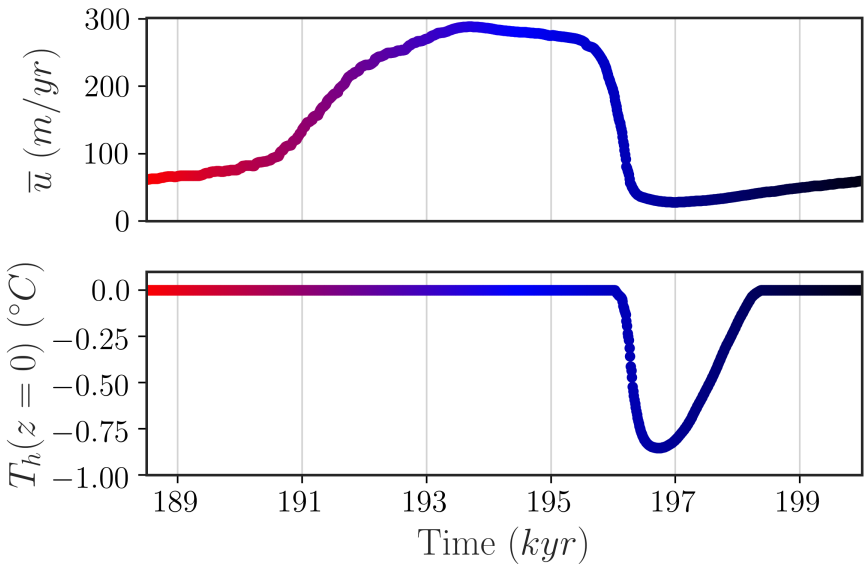

Fig. 6.3: Top, vertically-averaged horizontal velocity time series for a single event; bottom, homologous ice temperature at the base. Colours are a temporal label that evenly divides a single event in three parts: first, red; second, blue and red, end. The time series were obtained from the average values of the point in Hudson Strait shown in Fig. 6.1 and its 8 neighbours.

The oscillation can be also understood as a hysteresis process of the basal water content H_w as a function of the sliding velocity u_b (Fig. 6.5a). First, for a fully drained till (s = 0) there is a minimum velocity ($u_b \approx 100$ m/yr)

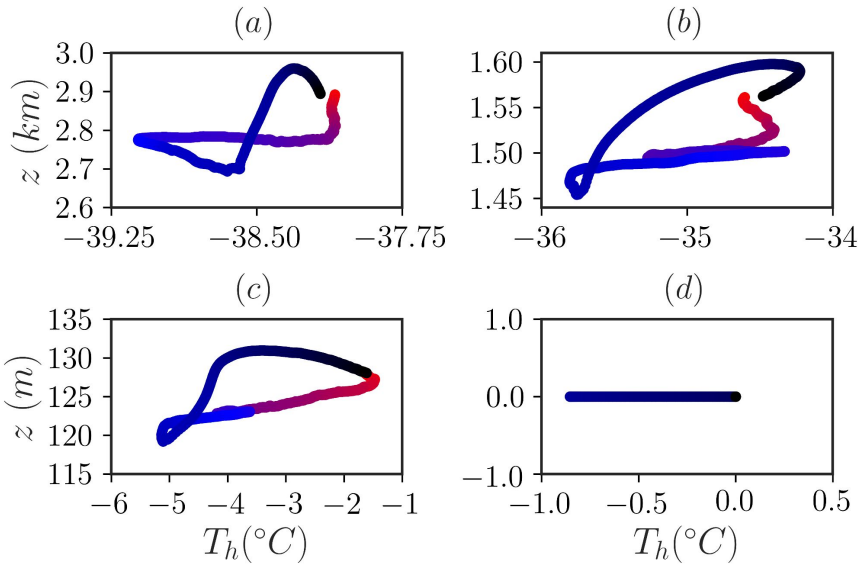

Fig. 6.4: Layer height versus homologous ice temperature T_h at four vertical layers within the ice sheet for an event given an overconsolidated till and $H_{\mathrm{w,max}} = 0.4$ m. (a) $1H_{ice}$ (i.e., the surface), (b) $0.9H_{ice}$, (c) $0.1H_{ice}$ and (d) base $0H_{ice}$. The values were obtained from the average values of the point in Hudson Strait shown in Fig. 6.1 and its 8 neighbours.

required to dissipate enough frictional heat so that melting surpasses d_r and the till becomes saturated. Nevertheless, smaller u_b values must be achieved in order to retrieve the initial drained condition. Strictly speaking, the till is not fully drained until $u_b < 75$ m/yr. It is then straightforward to see that a certain sliding velocity value within this range $u_b \in [75, 100]$ m/yr can be found in two different hydraulic regimes depending on the previous stage of the system. It is worth noting that this behaviour is imposed by the Bueler and van Pelt (2015) effective pressure formulation. The water-induced decrease in effective pressure maintains the ice streaming for sufficiently large periods of time before the till water is drained and the effective pressure is then restored to its maximum value.

Even so, the sliding velocity u_b does not appear to be the cause of an event but rather, the mechanism allowing for downstream propagation. Therefore, contributions of either the total heat budget Q (e.g., geothermal heat flux, strain heat, etc.) or the driving stress in the DIVA (i.e., ice surface gradient

∇h) must dictate the onset of the oscillation. This also highlights the relevance of d_r since it sets the threshold for switching between negative and positive values of $\partial H_{\mathrm{w}}/\partial t$.

For a gridpoint within the ice stream, a feedback exists between the sliding velocity and the basal water content (through the Q_b contribution, Fig. 6.5). It is clear that H_{w} starts to increase as the frictional heat contribution Q_b yields positive values of $\partial H_{\mathrm{w}}/\partial t$. As a result, sufficiently low values of u_b allow such a point to modify its saturation state (since the basal water is drained faster than melting supply), thus dictating the propagation of the oscillation along the stream. Nevertheless, it does not necessarily mean that u_b can be regarded as the cause of an event. Since the oscillation begins upstream, the reasons why the beginning of the stream starts to oscillate in the first place must be addressed and what determines whether such perturbation will be propagated or not.

Presumably, the driving stress at the beginning of the ice stream reaches a minimum value $|\nabla h|_{\min}$ during the stabilization stage since the ice is being advected at its maximum rate. Consequently, the ice velocity at the beginning of the stream may be reduced, thus triggering a decline in basal melting given that the leading term in Eq. 4.52 is the basal frictional heat Q_b. In terms of the local basal-water evolution (Eq. 4.52), the condition $d_r > Q/\rho_w L_i$ can be met, implying drainage of the water in the till. This is, in fact, a potential mechanism for the onset of the slowdown (drainage state in terms of basal hydrology) that allows the ice stream to fall in a cyclic behaviour. The importance of the till drainage rate for the existence of oscillatory behavior will be investigated in sensitivity experiments described in Section 3.5.

It should be noted that despite the relatively large spatial scale of the oscillations in the Hudson Strait ice stream, the impact in terms of ice volume is quite small (Fig. 6.6). Stable oscillations in ice volume in the Hudson Strait region amount to variability of $\pm 2.5\%$ of the total regional volume. Therefore, in terms of total Laurentide ice volume, the change in volume is almost imperceptible. This is in large part due to the fact that the ice-stream oscillations are well behaved and occur on a long enough timescale for the surrounding ice sheet to adjust. Furthermore, the width of the ice stream is relatively narrow, so despite its length of hundreds of kilometers, it is not effective at advecting large amounts of ice towards the margin.

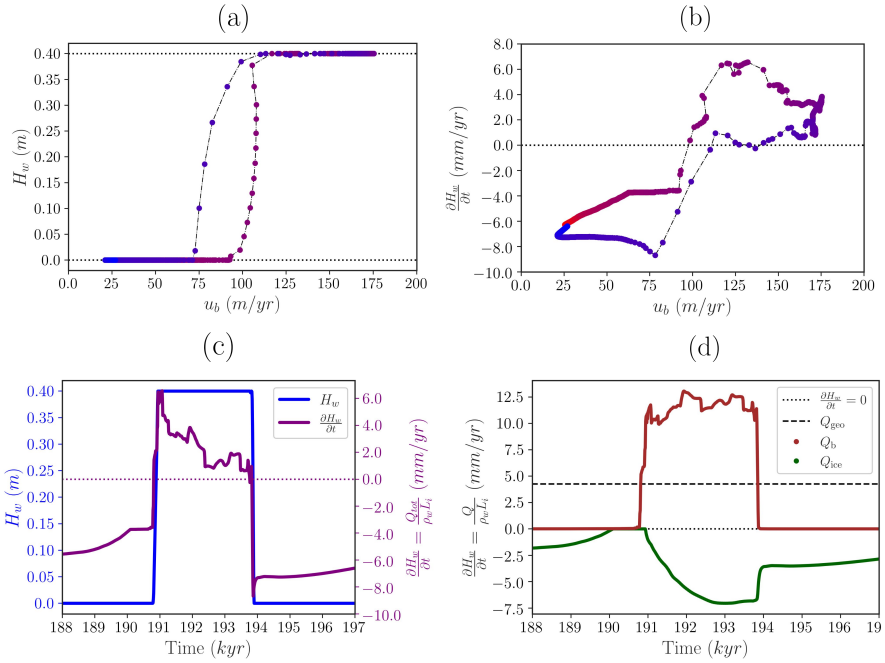

Fig. 6.5: (a) Basal water content as a function of sliding velocity. (b) Basal water time derivative as a function of the sliding velocity. (c) Basal water content and time derivative for total heat contribution. (d) Decomposition of the three basal heat contributions fluxes: geothermal Q_{geo}, frictional Q_{b} and vertical conductive Q_{ice}. All values are taken from a grid point over Hudson Bay during a single event. Colours in (a) and (b) consistent with Fig. 6.3 and 6.4.

6.2.3 Till compressibility

Here the LIS equilibrium configuration under LGM conditions is presented for different values of the aforementioned till compressibility coefficient C_t. Rather than a synthetic tuning of the dimensionless parameter e_0/C_t, following experimental results from geotechnical tests (Tulaczyk et al., 2000a). Namely, the cases under consideration include normally consolidated till (NCL), overconsolidation (URL) and sheared states (critical state line, CSL). However, CSL and NCL can be treated equally in terms of C_t since they exhibit the same compressibility in general (Clarke, 1987; Jones, 1994; Karig and Morgan, 1994).

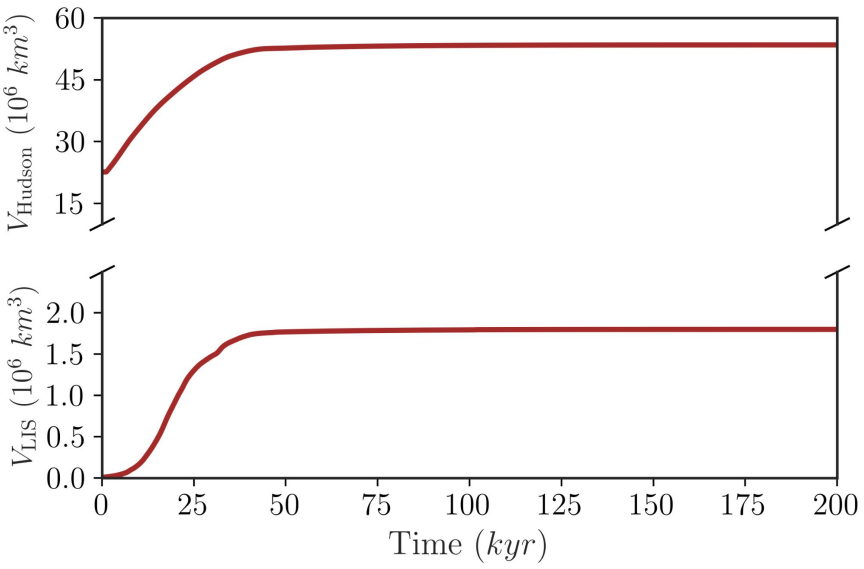

Fig. 6.6: Total ice sheet volume for the entire Laurentide Ice Sheet V_{LIS} and Hudson Strait region V_{Hudson} (as defined by the black box, Fig. 6.1) as a function of time. Shaded grey region represents the model spin-up.

For a given parameter choice, normally consolidated tills (Fig. 6.7a) do not yield oscillatory behaviour, in contrast to overconsolidated tills (Fig. 6.7b and 6.7c). In both cases, the simulated mean ice thickness is not affected by the consolidation state of the till. Small sudden increments in ice thickness are found for oscillatory cases (Fig. 6.7b and 6.7c), corresponding to minimum and maximum values of horizontal velocity and basal shear stress respectively. Even so, LIS volume changes are not relevant (Fig. 6.6) since the amplitude of H_{ice} oscillations is $3-4\%$ of the total thickness. The potential cause of this cyclic behaviour will be thoroughly studied in Section 4.

To study the oscillatory properties more generally, a Fast Fourier Transform analysis of the velocity time series is performed for a range of parameter choices. Namely, $e_0/C_t = 5,\ 10,\ 15,\ 20,\ 25,\ 30,\ 35,\ 39.5$ (ref. sim.) and 40.0; whereas three values of maximum water layer thickness were considered, $H_{\text{w,max}} = 0.10,\ 0.40$ and 0.80 m. Figure 6.3 shows these results in terms of the most significant oscillation period T. The oscillation period shows a strong dependence on $H_{\text{w,max}}$, and to some extent e_0/C_t. Notably,

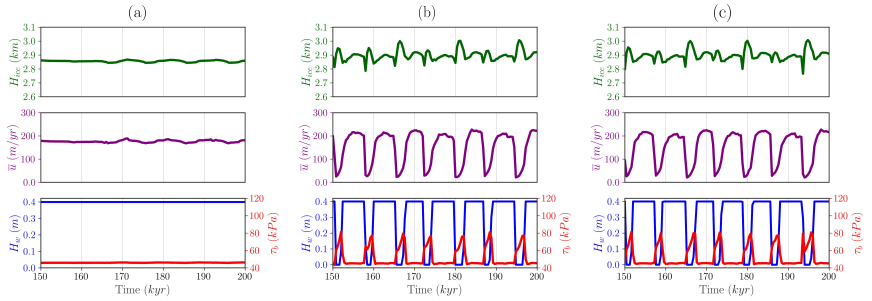

Fig. 6.7: Hudson Strait time series for steady-state LGM simulations using three different consolidation states: (a) CSL (consolidated till), (b) URL (preconsolidation at 568 kPa) and (c) URL (preconsolidation at 71 kPa). Parameter values of $H_{\mathrm{w,max}} = 0.4$ m and $\delta = 0.02$ were used in all experiments.

the period reduces with smaller values of $H_{\mathrm{w,max}}$, and with $H_{\mathrm{w,max}} = 0.1$ m, high frequency oscillations are found irrespective of e_0/C_t.

6.2.4 Maximum basal water layer

As seen above, the period of our simulated oscillations also exhibits a strong dependence on the maximum basal water layer $H_{\mathrm{w,max}}$ (Fig. 6.8). For all cases under consideration in this study, the period T increases as $H_{\mathrm{w,max}}$ is allowed to reach higher values. Notably, the more compressible the till is, the stronger this dependency is found to be. In addition, there exists an upper limit of $H_{\mathrm{w,max}}$ beyond which oscillations are damped. This limit is smaller for normally consolidated tills, thus narrowing the H_{w} range that yields stationary oscillations.

To study the impact of the minimum $N_{\mathrm{min}} = \delta P_0$, a smaller value $\delta = 0.013$ was considered for a given compressibility (overconsolidated URL, Fig. 4.7). A number of additional simulations were also conducted with $\delta < 0.013$ yielding extremely high velocity values as well as LIS extensions far from the ICE-6G reference. Remarkably, the calculated period converges to those values found for the default case $\delta = 0.020$ at low values of $H_{\mathrm{w,max}}$. However, the period for the $\delta = 0.013$ simulations remains smaller as $H_{\mathrm{w,max}}$ increases. Unlike the default δ case, with $\delta = 0.013$ all simulations considered yielded stationary oscillatory behaviour.

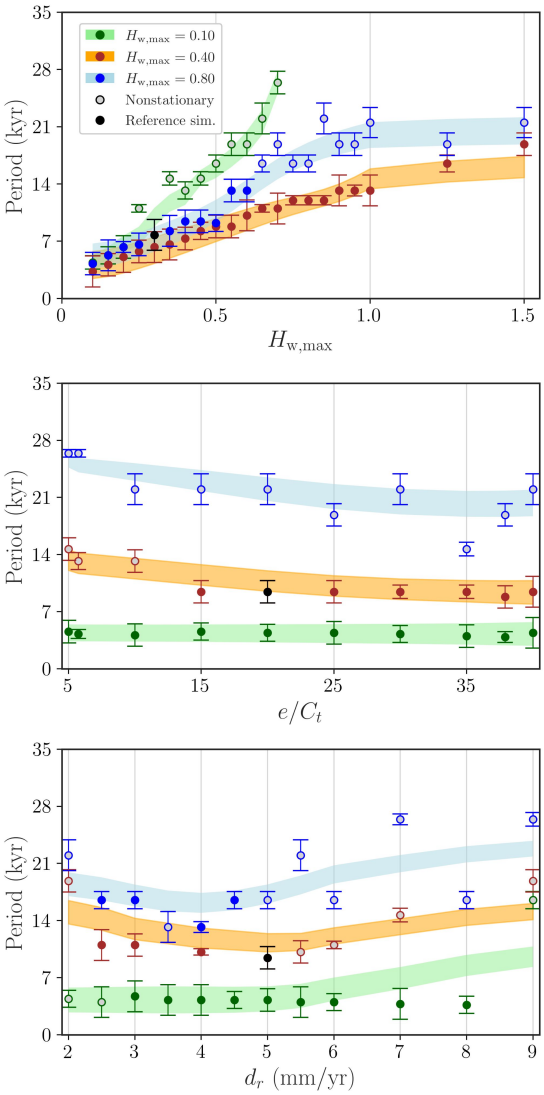

Fig. 6.8: Period of oscillation as a function of (a) $H_{w,max}$ (b) Till compressibility e_0/C_t and (c) Drainage rate d_r. Stationary oscillations (colour filled points) represent a constant amplitude in time; nonstationary (grey filled points), damped/small amplitude oscillations. Shading colours: running mean of $T \pm \Delta T$.

6.2.5 Till rate

The significant impact of the till drainage rate d_r is shown on the oscillation period as an additional degree of freedom besides $H_{\mathrm{w,max}}$. Figure 6.8c shows the periodicity dependence on d_r for three fixed values of $H_{\mathrm{w,max}}$. As can be seen, this oscillatory phenomenon over Hudson Strait appears to be particularly sensitive to d_r for high $H_{\mathrm{w,max}}$ values. Moreover, the d_r value range that yields oscillations becomes narrower as Hw,max increases. On the contrary, for $H_{\mathrm{w,max}} = 0.1$ m, the periodicity is independent of the exact d_r value even though oscillations were only found within the range $d_r \in [3.0, 8.0]$ mm/yr.

Unlike our previous results, the period T has a minimum value $T_{\mathrm{min}} \approx$ 10 kyr ($H_{\mathrm{w,max}} = 0.40$ m) within the considered d_r range (Fig. 7). This T_{min} value is reached at nearly $d_{r,min} \approx 5$ mm/yr and corresponds to a stationary oscillation. From a stability point of view, small perturbations in d_r do not imply large changes in ice flow periodicity since $\partial T/\partial d_r \approx 0$. Nevertheless, drainage values above dr,min yield damped oscillations with $2-4$ events before reaching a non-oscillatory equilibrium velocity value (Fig. 6.9b). On the contrary, nonstationary oscillations with $d_r < d_{r,min}$ show a slowly amplifying amplitude (Fig. 6.9s) that eventually reaches the same equilibrium values as for $d_{r,min}$. Even so, sufficiently small values of $H_{\mathrm{w,max}}$ exhibit no d_r dependency.

6.2.6 Model resolution

The oscillatory phenomena described throughout the previous sections are subject to potential numerical issues, so this work also chooses to explore the dependence of the oscillatory behavior on grid resolution. Namely, two ensembles with eleven different d_r values were launched for three different spatial resolutions $\Delta x = 32,\ 20$ and 16 km. Figure 6.10 summarizes our experiments for the highest and lowest resolution.

In general, these simulations lead to three main observations. First, the use of different resolutions gives rise to a slight shift in the d_r phase space that yields oscillations. Second, large amplitude oscillations exist for a broad range of till rate values regardless of the spatial resolution. Finally, the periodicity appears to be model-resolution independent.

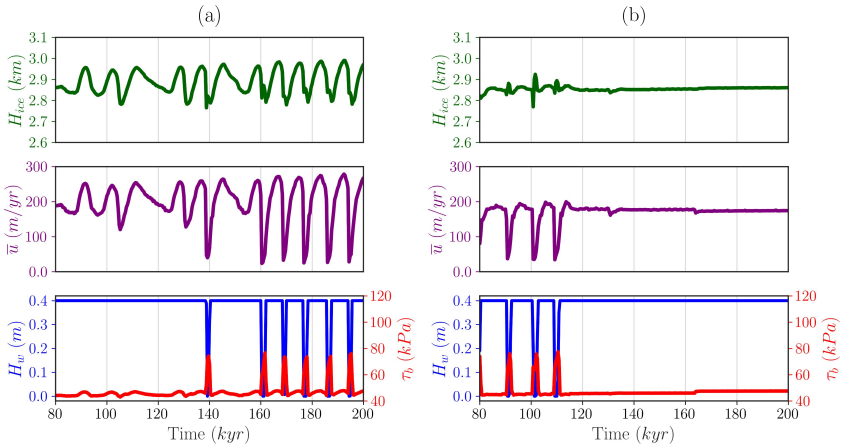

Fig. 6.9: Time series for ice thickness, velocity, shear stress and basal water content (overconsolidated till). Drainage (a) $d_r = 2.5$ mm/yr and (b) $d_r = 6.0$ mm/yr. Amplitude of oscillation is amplified until an equilibrium amplitude is reached (a). For higher drain rates (b), the oscillation is rapidly attenuated after a few events.

A minor shift in phase space exists between the 32 and 16 km spatial resolutions in terms of the till rate d_r. In other words, large amplitude oscillations require slightly higher values of d_r when Δx is reduced. This can be understood by considering the difference in area covered by a grid point of different resolution. The propagation of one event along the ice stream requires the bordering grid points to switch their motion state. In fact, the stream boundary must either change from slow flow (i.e., drained till $s = 0$) to a streaming state (i.e., saturated till $s = 1$) or vice versa. Since the spatial resolution determines the width of the curve enclosing the ice stream under consideration, it also indirectly determines the horizontal propagation speed of an event in every timestep.

Strictly speaking, certain differences are expected since the area enclosed by a single grid point is drastically reduced for higher resolutions. A doubling of the spatial resolution yields a reduction by a factor four of the area enclosed by a new grid point. For instance, the driving stress term ∇h includes spatial derivatives that can be perturbed when the spatial resolution is modified. Besides, a coarse spatial discretization can smooth the existence of local maxima/minima in both topography and ice thickness. This is of paramount

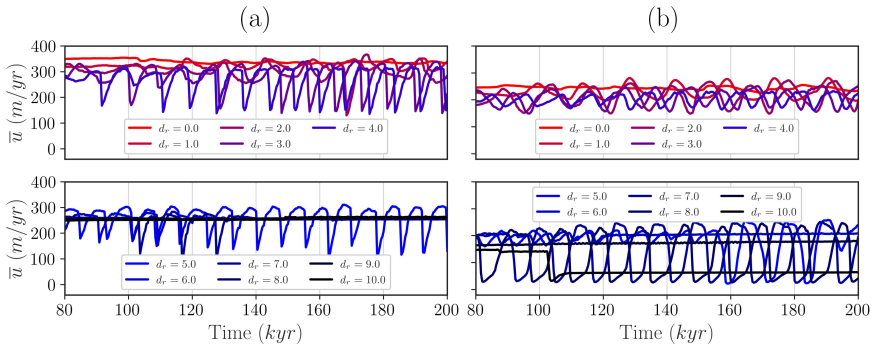

Fig. 6.10: Horizontal velocity time series for $\Delta x = 32$ km (left) and $\Delta x = 16$ km (right) spatial resolutions. Till drainage rate d_r given in mm/yr. Time series were obtained from the spatial average of the 9-point square around the point in Hudson Strait indicated in Fig. 6.1

importance when working with non-local dynamics solutions as is this case of the DIVA solver used here.

6.2.7 Sensitivity tests

Lastly, a sensitivity study was conducted to determine the range of parameters that yield oscillations. Our aim here is to determine whether the oscillatory solutions are a limited subset of the solutions for a particular parameter choice or a generalized behaviour. Herein, the two variables under consideration are δ and d_r. The till compressibility is set to $e_0/C_c = 39.5$, which is within an empirical range provided by the two consolidation states of the till (Tulaczyk et al., 2000a). Furthermore, $H_{\mathrm{w,max}}$ is set to 2.0 m following the value given in Bueler and van Pelt (2015).

Figure 6.11 shows the fraction of Hudson Strait in a rapid sliding regime as a function of time for two ensembles of sensitivity tests: δ and d_r. This is a notable piece of information since Eq. 4.55 establishes the shape of the curve $N(H_{\mathrm{w}})$ for a given δ. It is clear that δ (along with d_r) determines a H_{w} equilibrium value. In addition, oscillations are always present for sufficiently small values of δ, thus showing that oscillatory behaviour is not a small subset of the solutions using the higher-order DIVA solver, but a robust result over Hudson Strait. Nonetheless, rather small δ values ($< 1.3 \times 10^{-2}$)

are unrealistic and lead to extremely high velocity as well as ice extensions far from the ICE-6G reference. In contrast, d_r has both upper (not shown) and lower limits beyond which no oscillations are found (Fig. 6.11b).

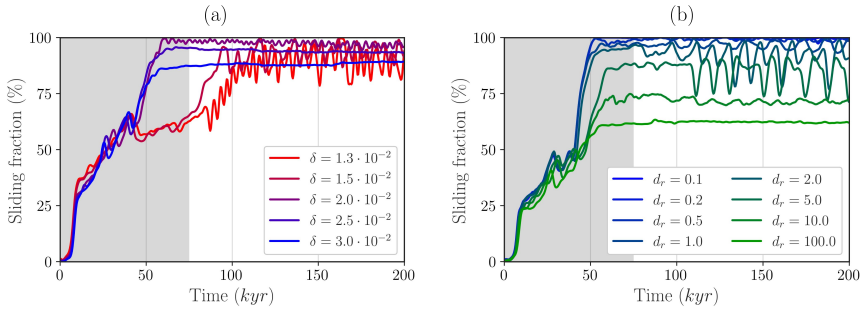

Fig. 6.11: Fraction of Hudson Strait in a rapid sliding regime for two ensembles of sensitivity tests: minimum effective pressure δ (left) and till rate d_r (mm/yr) (right). Robustness for a broad range of parameters. Shaded grey region represents the model spin-up.

6.3 Discussion

Our simulations of the LIS under LGM climatic conditions show good agreement with reconstructed characteristics such as the ice extent. While the ice sheet arrives at an equilibrium state in terms of size and thermodynamics, the ice stream located over Hudson Strait shows an oscillatory equilibrium under constant LGM boundary conditions. This result highlights the ability of a higher-order ice-dynamics model to internally oscillate given a hydraulic effective pressure formulation. It further shows notable agreement with Pattyn (1996), where cyclic behaviour relies on the condition of a sliding law that explicitly includes the effect of basal water. Nevertheless, this behaviour falls far from being a common feature of the rapid sliding over the LIS due to the absence of oscillations in the remaining ice streams. Moreover, this phenomenon appears to be a numerically robust result since it is found for a relatively wide range of parameter values and do not show a critical dependence on the model resolution. Even so, the period and amplitude of

oscillation are dependent on parameter choices, highlighting the importance of a fair description of the physical properties of the till.

Our results show that the choice of till consolidation state entails strong consequences for ice-stream oscillations. Particularly, for a fixed value of $H_{\mathrm{w,max}} = 0.4$ m, oscillations are only found for overconsolidated tills (Fig. 6.2). Given that fluctuations of water pressure are sufficient to induce overconsolidation in the till (Tulaczyk et al., 2000a), it is likely that an overconsolidated state best describes the till under the Laurentide ice sheet since the condition $N(t) < N_{\mathrm{max}}$ is easily met. This leads to the possibility of ice-stream oscillations, yet it has to be stressed that higher $H_{\mathrm{w,max}}$ values dampen the oscillatory behaviour. Furthermore, under an $H_{\mathrm{w,max}}$ approach, the basal water is not conserved in the model. Particularly, once the till reaches saturation $s = 1$, the basal melting contribution is no longer accounted for in this hydrology model.

The difference in behavior between normally consolidated and overconsolidated till can be explained by the shape of $N(H_{\mathrm{w}})$. For every value of the parameter C_t, there exists a curve $N(H_{\mathrm{w}})$, thus yielding a different effective pressure value for a given basal water content (recall Fig. 4.7). A normally consolidated till (e.g., CSL or NCL) presents a higher compressibility. As a result, N smoothly transitions from its maximum value P_0 to the minimum allowed δP_0 while the ice flow adjusts. On the contrary, overconsolidated tills show an abrupt decrease in N rather close to saturation. Thus, small perturbations of H_{w} imply large differences in N. In this way, the overconsolidated till can produce an abrupt reduction in effective pressure and a nonlinear response of the ice sheet that leads to oscillations.

Throughout this work, $H_{\mathrm{w,max}}$ has been imposed in our simulations as a parameter without further physical explanation. Nevertheless, it is worth noting that by assuming a certain mineral till thickness instead, a consistent value of $H_{\mathrm{w,max}}$ can be derived directly from the Bueler and van Pelt (2015) formulation without any additional approximation. This provides a reference value from physical arguments and experimental data that accounts for the particular properties of the LIS. From Eq. 4.54 and a mineral till thickness η defined as:

$$\eta = \frac{H_{\mathrm{w}}}{e}, \tag{6.1}$$

an expression for $H_{\mathrm{w,max}}$ as a function of η can be readily obtained:

$$H_{w.max} = \eta \left[e_0 - C_t \log \left(\frac{\delta P_0}{N_0} \right) \right], \tag{6.2}$$

Robel et al. (2013) used an effective till-layer thickness of $\eta = 2$ m based on estimates of total IRD volume (Hemming, 2004). Since overconsolidation conditions are easily met even for small fluctuations of basal water pressure (Eq. 4.58), an appropriate parameter values corresponding to an overconsolidated till shall be employed ($e_0 = 0.53$, $C_t = 0.014$), which yields $H_{\mathrm{w,max}} \approx 0.42$ m from Eq. 6.2. This provides a reference value from physical arguments and experimental data that accounts for the particular properties of the LIS. Remarkably, from Fig. 6.4 this estimation yields a $7 - 11$ kyr period of oscillation, consistent with periods found for IRD deposition in sediment cores (Hemming, 2004).

Furthermore, it is illustrative to compare our $H_{\mathrm{w,max}} \approx 0.42$ m value with that obtained from an inversion study performed in Greenland in which $H_{\mathrm{w,max}} \approx 0.10 - 0.36$ m (Koziol and Arnold, 2017). Both results are notably similar even though some differences were expected since they do not share the same domain. Yet the independent estimate lends confidence to the value estimated here, and demonstrates the importance of a realistic $H_{\mathrm{w,max}}$ value. Additionally, it should be considered that till saturation $H_{\mathrm{w}} = H_{\mathrm{w,max}}$ often signifies changes in morphology (e.g., Schoof, 2010). It is then important to note that such alterations are not explicitly modeled in our current simulations, thus leading to a non-mass-conserving hydrology.

In fact, a local evolution equation for basal water content H_{w} without horizontal advection (Eq. 4.52) assumes negligible horizontal basal water transport. This assumption can be understood in terms of the hydraulic diffusivity coefficient c_v since it readily captures water mobility in till pore spaces. Measurements have shown that such water significantly lacks mobility (Lingle and Brown, 1987a; Truffer et al., 2001), In fact, c_v has been estimated as 10^{-8} m^2/s for a clay-rich till (Ice Stream B, West Antarctica; Tulaczyk et al., 1998) and it is probably characteristic of all clay-rich tills (Iverson et al., 1995), given that samples studied by (Tulaczyk et al., 2000a) are 35% silt and 23% clay. Since both Hudson Bay and Hudson Strait are mostly silt sediments (Gowan et al., 2019), it seems reasonable to assume the rather low hydraulic diffusivity of $c_v = 10^{-8}$ m^2/s.

The ability of the till to rapidly reach saturation does not alone explain the presence of oscillations. The value of d_r (Eq. 4.52) is also fundamental considering that sufficiently large values of d_r are necessary to yield negative values of $\partial H_\mathrm{w}/\partial t$, thus allowing the till to deviate from the saturated state $s = 1$ imposed by basal ice melting due to frictional heat Q_b. Notably, even for the idealised scenario $d_r = 0$ (null till drainage rate), small amplitude oscillations of u_b always take place at the beginning of the stream (Hudson Bay). Therefore, d_r cannot be regarded as the cause of the oscillations. Rather, the balance between geothermal heat flow, strain heat and advection of ice provides a potential source of perturbations in H_w regardless of d_r (Fig. 6.12). However, this balance implies no changes in ice dynamics so long as d_r remains small compared to $Q/\rho_w L_i$ (i.e., the sign of $\partial H_\mathrm{w}/\partial t$ remains unchanged in Eq. 4.52). Yet when the till drainage becomes relevant, these small perturbations can be amplified in time. Namely, in terms of Eq. 4.52, d_r is non-negligible if $d_r > Q/\rho_w L_i$ and consequently $\partial H_\mathrm{w}/\partial t < 0$ for sufficiently long periods of time.

The source of perturbations in basal water (i.e., contributions of either the total heat budget Q or the driving stress) and consequently in N, holds true in general for low u_b values irrespective of d_r. This yields an explanation as to why small d_r values do not trigger large-amplitude oscillations (Fig. 6.9) given that the non-local dynamics solution propagates this perturbation downstream. The spatial propagation of the oscillation can be either attenuated (damped oscillation) or amplified to an equilibrium amplitude. This is determined by two factors: d_r and $N(H_\mathrm{w})$. Strictly speaking, only when small perturbations in Q are sufficiently large to yield a change in the sign of $\partial H_\mathrm{w}/\partial t$ (Eq. 4.52) so that a significant variation in $N(H_\mathrm{w})$ is induced, will the oscillation be amplified along the ice stream. That is, the ice flow will be perturbed due to a change in τ_b through a water-dependent effective pressure $N(H_\mathrm{w})$ (Fig. 6.12). Otherwise, Q perturbations might yield changes in $\partial H_\mathrm{w}/\partial t$ but these are negligible compared to d_r. Hence, the function $N(H_\mathrm{w})$ as well as the particular d_r value can be seen as a threshold on the amplification.

Furthermore, this behaviour entails a straightforward dependency on both C_t and $H_\mathrm{w,max}$. Since $\partial N/\partial H_\mathrm{w} \sim -e_0/(C_t H_\mathrm{w,max})$, the more compressible a till is, the larger the perturbation in H_w is necessary to induce a significant

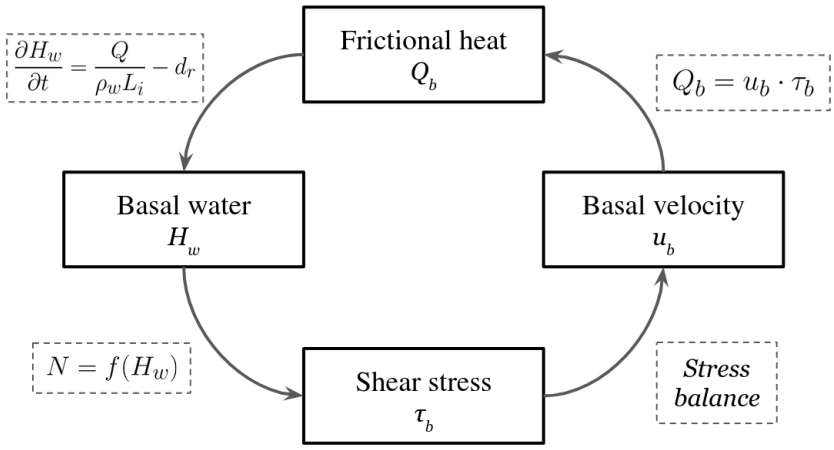

Fig. 6.12: A conceptual view of the main feedback triggering oscillatory behaviour for a water-dependent effective pressure formulation. Frictional heat perturbations may induce changes in the basal water content H_{w}, drastically modifying the effective pressure N. As a result, the basal velocity adjusts following the new force balance established by the DIVA solver (i.e., driving and shear stress).

change in N. The same reasoning can be applied in terms of $H_{\mathrm{w,max}}$ for all simulations.

The oscillatory behaviour is not restricted to a water-dependent N formulation so long as $\tau_b(u_b)$ is allowed to take sufficiently different τ_b values for a given sliding velocity u_b. With the choice $N = f(H_{\mathrm{w}})$, the basal water content spans a broad range of shear stress values τ_b for a fixed u_b. Nevertheless, a simpler approach was also tested in which the effective pressure follows a two-valued approach (simulations not shown in this work). Namely, the effective pressure is computed as the weighted average of two coefficients determining sliding over a frozen or temperate hard bed (see companion paper; Moreno et al., this issue). It is worth noting that even such a simple parametrization also rendered thermomechanical instabilities within the ice sheet, comparable to those shown here. The key feature of both approaches

is that the basal friction is a function of the thermodynamic state of the ice sheet and that a large difference in friction is imposed between a cold and a temperate base.

Regarding spatial discretization, plausible numerical issues pose a problem when the physical realism of the simulated phenomena must be addressed. This does not necessarily mean that the presence of oscillations in itself is a numerical artefact without a real physical counterpart but rather, that the metric or the triggering mechanism can be also altered by the numerical treatment of the ice sheet. In particular, additional simulations show that the spatial resolution can have a minor influence on the period and magnitude of oscillations (Fig. 6.10). For instance, the implications are straightforward if the spatial resolution is doubled. In terms of a water-dependent effective pressure formulation, when the ice stream propagates further inland during the onset of a single event, four grid points (rather than merely one) must simultaneously switch from a non-sliding regime $N = P_0$ to a sliding regime $N_{\min} = \delta P_0$, so that the same area is at a fast sliding mode for the current time step. This can be understood as the buttressing stability at the margins of the ice stream and provides a potential explanation for the slight increase in the d_r values required to yield large amplitude oscillations.

In contrast to other studies, the oscillatory behavior found in our simulations of the Laurentide ice sheet did not manifest large changes in ice volume (Fig. 6.6). This result is robust regardless of the particular physical parametrization of the till (C_t, $H_{\mathrm{w,max}}$ and δP_0). This interesting result represents a scenario in which thermomechanical instabilities take place within the ice sheet, yet the triggered oscillations do not resemble a binge-purge mechanism where large volume changes occur. Importantly, this outcome is model resolution independent.

Minor changes in ice volume are largely due to the extent at which the oscillatory mechanism operate. All points outside the region enclosed by the stream margin do not oscillate, thus leaving the LIS volume nearly unchanged. The area covered by this rapidly sliding region remains small (compared to the total LIS extension) as a consequence of the bedrock topography. More precisely, our experimental setup is elevation-dependent (Moreno et al., this issue; Eq. 9), naturally confining the ice streams to narrow lower troughs where rapid sliding is enhanced. Therefore, it seems plausible to conceive such mechanism operating on larger spatial scales with the consequent increase in

ice volume advection, though inevitably compromising the realism of the ice stream network.

The ice stream extension plays an essential role in this result. As shown in Section 3.1, large amplitude oscillations in both ice thickness and velocity are present along the Hudson Strait ice stream (Fig. 6.2). Yet the area covered by this rapidly sliding region remains small (compared to the total LIS extension) as a consequence of the bedrock topography. Strictly speaking, since the occurrence of sliding is favored at low bedrock elevations (Moreno et al., this issue; Eq. 9), the horizontal extension of such oscillations is consequently restricted to a narrow ice stream. Hence, all points outside the region enclosed by the stream do not oscillate, thus leaving the LIS volume nearly unchanged.

6.4 Conclusions

Chapter 6 has investigated the plausibility of physically-based oscillations of the LIS. The simulated ice sheet under constant LGM conditions closely matches the reconstructed ICE-6G extension, thus indicating a high level of realism of our experiment. After a thorough study of a friction parametrization dependent on the local basal water content and the physical properties of the till, this study has determined under which conditions such oscillations are plausible and their properties (period and amplitude).

First, a broad range of parameter values of C_t and $H_{\mathrm{w,max}}$ related to the till and basal hydrology yield oscillatory behaviour even though both the period and amplitude present strong parameter sensitivity. In fact, both the period and the amplitude exhibit an inverse relationship to C_t and $H_{\mathrm{w,max}}$. For sufficiently large values of either C_t or $H_{\mathrm{w,max}}$, the amplitude is reduced leading to damped (or even absent) oscillations.

Secondly, an overconsolidated parametrization of the till exhibits the best description of the subglacial water pressure irrespective of the ice-thickness evolution (assuming that, most of the time, $N(t) < N_{\mathrm{max}}$). A proper parameter choice entails consequences not only in the period and amplitude of the simulated oscillatory phenomenon, but also in the very presence of oscillations. Interestingly, an overconsolidated till is found to yield a period of the oscillation of the Hudson Strait ice stream on the order of $7 - 11$ kyr, which

is comparable to that of IRD deposition in sea sediment cores (MacAyeal, 1993a). In contrast, applying the normally consolidated till leads to much larger oscillation periods and yields a rather limited (perhaps unrealistic) oscillatory phase space.

Furthermore, a mineral effective thickness estimation of Hudson Strait from IRD volume data allows us to determine $H_{\mathrm{w,max}} \approx 0.42$ m for such a region. It is worth noting that $H_{\mathrm{w,max}}$ was solely estimated from the effective pressure parametrization without further approximation. Even so, this value triggers large amplitude oscillations with a period $T \approx 7 - 11$ kyr, thus in agreement with (MacAyeal, 1993a). The lower and upper bounds in our simulations correspond to overconsolidated and normally consolidated till respectively.

Lastly, it should be stressed that only minor LIS volume changes are found throughout this study as a consequence of the topographic driving of the ice stream. These results are robust independent of the horizontal grid resolution, which leads us to conclude that the oscillations do not arise from a numerical issue. This interesting result represents a scenario in which thermomechanical instabilities take place within the ice sheet under constant LGM boundary conditions, yet the triggered oscillations do not resemble a binge-purge mechanism where large volume changes occur.

In conclusion, thermomechanical instabilities yield Hudson Strait ice-stream oscillations featured by a period in agreement with observations. Moreover, the spatial distribution of this oscillatory behaviour closely matches the source of IRD as traced from geological evidence. Even so, the absence of significant LIS volume changes poses a question on whether internal ice discharges determined by the basal hydrology are sufficient to account for the IRD layers present in the North Atlantic sediments cores.

Chapter 7
Discussion

This thesis investigated internal ice-sheet instabilities as a potential physical explanation underlying any oscillatory mechanism that might cause the Heinrich Events. Understanding internal ice-sheet dynamics is not only relevant to expand our knowledge of past conditions, but it will also improve our insight of ice-sheet stability, essential for future predictions. Given the complexity of the problem and the number of key reconstructions that must be explained, the question remains open and a conclusive physical explanation underlying any oscillatory mechanism that causes the HEs is still under debate. For this reason, the problem was thus approached from a modelling perspective with increasing comprehensiveness: (1) theoretical advances from analytical work on the thermal description, (2) a purely modelling study by developing Nix ice-sheet model focusing on grounding-line migration under thermomechanical coupling and (3) three-dimensional modelling under realistic LGM conditions. The results described within this thesis address the four fundamental questions posed in Section 1.5.

Can we obtain a time-dependent analytical description of the ice-sheet temperature?

Analytical solutions were found for the 1D time-dependent advective-diffusive heat problem including additional terms due to strain heating and depth-integrated horizontal advection. A Robin-type top boundary condition considered potential non-equilibrium temperature states across the ice-air inter-

face. The solution is expressed in terms of confluent hypergeometric functions following a separation of variables approach. The study has been extended to a broader range of vertical velocities by using a general power-law dependence on depth, unlike prior studies limited to linear and quadratic velocity profiles. Lastly, a suite of benchmark experiments is presented to test numerical solvers. Four experiments of gradually increasing complexity capture the main physical processes for heat propagation. Analytical solutions are then compared to their numerical counterparts, upon discretisation over unevenly-spaced coordinate systems.

A time-dependent description of the ice-sheet temperatures is of particular interest given the difficulties to estimate the thermal state of an ice sheet at any given time. The lack of historic forcing fields pose an obstacle for ice sheets and glaciers to be "spun up" towards the present state, unlike other components of the climate system. A commonly used methodology consists of initialising models from observations, though limited to surface magnitudes such as elevation and velocity (Payne et al., 2004; Joughin et al., 2004, 2010; Favier et al., 2014; Seroussi et al., 2014). Traditional approaches rely on the so-called "snapshot" calibration, where observations are assumed to be instantaneous for ice velocity and geometry. This calibration might be problematic knowing that temporal consistency is required among datasets. Furthermore, data and model discretisations must also be consistent to avoid non-physical transients which persist for decades, which are critical in projections with comparable timescales.

Allowing ice-sheet models to adjust to potential inconsistencies does not resolve this problem as models would drift to a new state distinct from observations. Rather, a transient calibration has proven to outperform the "snapshot" counterpart given the better agreement with spatially and temporally resolved observations (Goldberg et al., 2015). Even so, the temperature-dependent rheology is relaxed towards a steady state, with a fixed velocity and geometry of the ice. This assumption of thermal equilibrium could be avoided by including the analytical description herein presented that accounts for the transient behaviour. The incorporation of internal temperature data (e.g., boreholes, thawed versus frozen extent of the ice-bed interface, radar attenuation, etc.) would then provide a convenient initial thermal state of our solutions without further computational costs. Moreover, these models (e.g., Joughin et al., 2004, 2010; Favier et al., 2014; Seroussi et al., 2014; Goldberg

et al., 2015) are initialised with temperature analytical solutions that neglect horizontal advection (Zotikov, 1986) and are not appropriate to describe temperatures at large velocity regimes. Solutions presented in this thesis include horizontal advection via a inhomogeneous term to obtain analytical results in ice streaming regions and are potentially convenient to improve intialisation avoiding transients.

Analytical solutions herein presented allow for a time-dependent description of the temperatures within the ice at any desired resolution, both spatial and temporal. Nevertheless, there are certain limitations that are necessary to keep the analytical tractability of the problem, some of which are now discussed. First, ice thermal diffusivity was assumed to be constant along the column, though more importantly, no phase changes within the ice were considered. This further implies that the pressure melting point is never reached. Unlike stationary studies such as Meyer et al. (2019), there is no account for an ice column fraction that is considered to be thawed. It is currently beyond the analytical tractability of the problem, as it would imply that the height at which the lower boundary condition is imposed should change over time. Therefore, one eigenvalue problem should be solved at each time.

Even so, there is room for partial improvement by including an explicit time dependency directly on the top boundary condition that further reflects changes in the climate. This possibility is subjected to the complexity of the forcing, as an extremely complex function given at the top boundary condition is unlikely to be solved analytically. Nonetheless, a linear increase of the atmospheric temperatures could be potentially considered to reflect the current warming scenarios.

How does the thermomechanical coupling affect the grounding line migration and the overall stability of an ice sheet?

This question has been addressed by developing the 2D ice-sheet model Nix, that simultaneously solves for the momentum balance equations, mass conservation and temperature evolution. Nix's velocity solver includes a hierarchy of Stokes approximations: Blatter-Pattyn, depth-integrated higher order,

shallow-shelf and shallow-ice. The grounding-line position is explicitly solved by a moving coordinate system that avoids further interpolations. The model can be easily forced with any external boundary conditions, including those of stochastic nature. Nix has been verified for standard test problems. Here results are shown for a number of benchmark tests from standard intercomparison projects and assess grounding-line migration with an overdeepened bed geometry. Thermomechanical coupling is further exploited by designing a suite of experiments where the forcing is a physical variable, unlike previously idealised forcing scenarios where ice temperatures are implicitly fixed via an ice rate factor. Namely, atmospheric temperatures and oceanic temperature anomalies were employed to assess model hysteresis behaviour with active thermodynamics.

One of the main limitations of this model is the current absence of buttressing. A priori, this is not critical as theoretically shown by MacAyeal and Barcilon (1988) and later underlined by Schoof (2007a), for that grounded ice dynamics is independent of the potential floating ice in a 2D geometry. Nevertheless, in a more realistic 3D geometry this no longer holds truth, given that ice shelves strongly influence the behaviour of grounded ice via buttressing to the inland stress balance. Even so, the importance of buttressing can be already captured in 2D models by parametrising this effect following e.g., Dupont and Alley (2005) and Jamieson et al. (2012). An implementation of such a parametrisation is straightforward in Nix and would most likely imply a further reduction in the width of the hysteresis loop herein presented. The reason to suspect so relies on the fact that buttressing provides additional stability, as shown in the stable grounding line example on a retrograde slope. Nonetheless, this parametric approach results in a prescribed buttressing at the grounding line and does not fully reflect a 3D geometry configuration.

All simulations performed with the Nix ice-sheet model are stable and reach an equilibrium constant value for the main physical variables. This is currently a result of the somewhat idealised basal friction formulation. A more sophisticated description would entail an additional coupling of the friction coefficients with the thermal state of base. There is a broad range of complexity to include this coupling (e.g., Flowers, 2015), from a synthetic reduction in friction coefficients to full hydrological models that employ 2D hydraulic potentials and further ensure water mass conservation. Ideally, Nix should be coupled to a basal hydrology module to explicitly account for the

potential mass-conserving water content. Nevertheless, it is expected for Nix to be capable of producing Heinrich-type free oscillations if boundary conditions are sufficiently favourable in the sense of Calov et al. (2010). Surface mass balance, ice surface temperatures and friction reduction due to thawing are presumably the controlling conditions for a potential oscillatory regime.

What are the implications of different basal friction formulations to simulate the LIS?

To tackle this question, the LIS has been simulated with the higher-order three-dimensional ice-sheet model Yelmo. Constant climatic LGM conditions define the boundary conditions of the system. To this end, atmospheric temperature and precipitation are climatologies obtained from the mean of the output of the 11 GCMs participating in PMIP3 as part of CMIP5 (Taylor et al., 2012). The geothermal heat flow is also a spatially-variable boundary condition in this thesis and it is acquired from Shapiro and Ritzwoller (2004). A number of scenarios with varying basal friction complexity were considered with a further assessment of their consequences in terms of ice extent, volume and ice-stream stability. Two sets of experiments were carried out. First, the effective pressure is assumed to solely depend on the overburden pressure exerted by the ice column. In this simple scenario (purely mechanical friction), three different basal friction laws are considered with different dependencies of the basal shear stress on the sliding velocity: linear, power law (purely plastic) and regularized-Coulomb parametrizations. Second, for the most comprehensive basal friction parametrization law (i.e., regularized-Coulomb), thermomechanical coupling of the sliding is allowed by introducing an additional dependency of the effective pressure on the thermal state of the base.

The strongest assumption on this study is the steady-state climatic condition that, even though reasonable, implies further simplifications. Moreover, the ice-sheet model must be equilibrated to such conditions to ensure that the geometry, extent and velocities are stable. In this thesis, such a steady-state was assessed by a two-phase linear regression approach (following Hinkley, 1969, 1971; Solow, 1987). Particularly, the ice volume above flotation time series was employed as the regressand to determine the length of the spin-

up and thus ensure an equilibrated state. Ideally, a most sophisticated LIS reconstruction under LGM conditions should be performed by simulating an entire glacial cycle, for that the thermal inertia of the system, the transient behaviour and the potential new sensitivity of the system would be then fully captured. Moreover, to study transient behaviour, consistent climatologies provided by each model should be considered independently. Despite the fact that transient simulations may have an impact given ice stream sensitivity, minor implications on the results of the present thesis are expected.

Another important aspect of the employed climatic forcing is the fact that the 11 PMIP3 simulations were averaged, thus removing the consistent climatology provided by a single model. Nevertheless, for this study, constant boundary conditions are desired rather than a time-dependent forcing. Thus, taking the average among climatologies provides a more robust boundary condition and smoothes potential peculiarities of each General Circulation Model. If we were to study transient behaviour, consistent climatologies provided by each model should be considered independently.

Another crucial element of the experimental setup is an inherently contained LIS previous reconstruction in the PMIP3 fields. Whilst ice extent is implicitly contained in our climatic forcing, the simulated LIS extension is still highly sensitive to the ice-sheet model parameter choice. In the end it is a question of surface mass balance, determined by the climatology and affected by the extent (and more notably the elevation) and dynamics, which are very much dependent on model parameters. For the same climatic forcing, an ice sheet that would largely differ from prior reconstructions could be obtained solely by employing a different parameter space. The interesting result is that the model was not tuned to match a certain volume/extent value, but rather to develop an ice stream network compatible with existing inventories. Moreover, in order to avoid any inertia of the model to evolve towards the inherent previous ice extent, a lapse rate factor correction of the temperature and precipitation PMIP3 forcing fields is further applied as a function of the local surface elevation.

Perhaps most importantly, there are potential inconsistencies taken into account in the validation step. This is the result of the larger interval of 29-17 kyr before present spanned by the LGM compared to the 21 kyr target. Furthermore, ice streams inventories likely cover an even larger period including pre-LGM remnants and deglacial ice streams. This caveat was al-

ready noted by (Margold et al., 2015), who stated that no inferences on the timing of ice stream operation are possible because very few of the mapped ice streams have any chronological control. However, it is clear that the mapped ice stream tracks represent a time-transgressive imprint of evolving ice stream trajectories, i.e. they cannot have all operated at once. Nonetheless, some broad spatial patterns appear and this time-transgressive ice stream map is exploited to compare our simulations. It must be stressed that potential timing inconsistencies are thus inevitable, though the time-transgressive inventory remains as an appropriate reference for the simulated ice streams.

Could the LIS have exhibited internal oscillations?

In an attempt to answer this question, this thesis carried out a comprehensive study on the potential ice stream activation when basal friction is thermo-mechanically coupled. To this end, a reference simulation is presented for a water-dependent effective pressure formulation that closely matches previous reconstructions. This experiment exhibits an oscillatory equilibrium state of the ice stream located along Hudson Strait whose period is consistent with hypothesised discharges from the LIS observed in ocean sediment cores. More precisely, the ice stream transitions between two modes of ice flow: rapid sliding over a saturated till and slow creeping ice over a fully drained till. In contrast, the remaining ice streams reach a constant equilibrium state. Furthermore, a number of sensitivity tests show that the oscillatory behaviour is found for a certain range of parameters. Yet the period and amplitude of the oscillations are highly dependent on the hydrology parametrization and the physical properties of the till. Notably, this phenomenon does not appear to be model-resolution dependent, thus discounting a numerical cause of the oscillatory behaviour. It must be stressed that only minor changes on the LIS and Hudson Bay ice volume are found throughout this study as a consequence of the ice stream temporal variability. Therefore, ice discharges herein shown may not be sufficient to account for the IRD layers present in the North Atlantic sediments cores, given that each Heinrich layer contains 100-350 km^3 of IRD and the concentration of the former in ice ranges 0.01-10% (Hemming, 2004).

One of the main limitations of this work concerns the current basal hydrology formulation in Yelmo. A local evolution for basal water content is considered, thus neglecting horizontal advection. This further implies that the liquid water stored in till pore spaces exhibits negligible mobility as a result of a low hydraulic conductivity of the till (Lingle and Brown, 1987b; Truffer et al., 2001). Ideally, simulations should be performed by a fully coupled hydrology module as in Bueler and van Pelt (2015) so that the basal water production is conserved. Although it is expected a priori that the effect of such a model would not necessarily imply a significant change in the ice streaming extent, the temporal variability could be perturbed. This would be the result of the complex interplay between the characteristic time scales at which ice streams and hydraulic potentials operate. Moreover, the surplus of basal water beyond till saturation could contribute to saturate nearby regions that were previously drained if an explicit advective model is considered, thus leading to a potential growth of the ice streaming area.

Lastly, the Glacial Isostatic Adjustment (GIA) treatment in this thesis is rather simple, through an Elastic-Lithosphere/Relaxing-Asthenosphere (Meur and Huybrechts, 1996) with a parametrised relaxation time of 3000 years. Even so, a more sophisticated GIA description would not necessarily imply changes in either equilibrium values of total ice volume or in ice stream activation. As noted by Bueler et al. (2007), the relaxation times vary from 0.5 to 10 kyr for load scales between 10^2-10^3 km, comparable to the ice stream extent and irrespective of the particular mass. Nevertheless, results show that the oscillatory regime herein presented entails minor changes in ice volume and therefore, even though the relaxation time might largely vary, the new equilibrated bedrock geometry will be nearly identical before and after the periodic surges. This further implies a small impact on more sophisticated GIA descriptions such as Elastic-Lithosphere/Viscous-Asthenosphere (Lingle and Clark, 1985), the laterally-variable LV-ELRA (Coulon et al., 2021) or the self-gravitating visco-elastic Earth models (i.e., 1D GIA models Mitrovica and Milne, 2003; Kendall et al., 2005; Spada and Melini, 2019).

Yelmo model limitations

The two last studies presented here (Chapters 5 and 6) share some model limitations that should be acknowledged. First, the Yelmo model computes ice velocities by adding the SIA solution (shearing regime) to the DIVA solution (depth-integrated sliding regime). In order to ensure continuity at the grounding line it is necessary to consider the SSA/DIVA solution, as the SIA is a local solution of the ice geometry and does not take into account membrane stresses that drive the flow of floating ice shelves. The accurate representation of the grounding-line position is a necessary condition for the evolution of marine ice sheets and is especially relevant for simulating its reversibility (e.g., Pattyn et al. 2012, 2013).

At the marine boundaries, high spatial resolution is required for representing precise grounding-line motions (below 1 km resolution). Because such a resolution for the continental-scale domains is computationally prohibitive, the most sophisticated models use adaptive meshes (e.g., Gladstone et al., 2010; Larour et al., 2012; Hoffman et al., 2018). In addition, even with a sub-grid parameterisation, coarse resolution models do not fully capture grounding-line migrations correctly (Seroussi et al., 2014; Gladstone et al., 2017). The most accurate ice-sheet models at continental-scale that have studied future scenarios at a spatial resolution of around 10 km. However, high-resolution simulations also require high-resolution input fields, such as bedrock characteristics. Nonetheless, even the most modern maps have low resolution in certain zones (Morlighem et al., 2019). The results in this thesis have resolutions of 16 by 16 km in Chapter 5 and 6. An additional resolution-dependent study performed in Section 6.10 shows that the ice stream activation appears to be a persistent behaviour at $\Delta x = 16$, 20 and 32 km. Although it is expected that the main conclusions of these works would remain unchanged, higher resolutions could lead to some differences in local patterns and a potentially shifted parameter space in which the oscillatory regime is found.

In Chapters 5 and 6, the process of surface melt in Yelmo is determined using the PDD model (number of positive degree-days), which was first introduced by an empirical relation which states that the melt rate is proportional to the surface-air temperature excess above 0^{o}C (e.g., Braithwaite and Olesen, 1989; Hock, 2003). Braithwaite (1995) laid the physical bases of

such relation as well as other temperature-based melt-index methods. Reeh (1991) proposed a form that is widely employed in ice-sheet models based on the work of Braithwaite (1985) that suggested that the PDD could be calculated from the normal probability distribution around the long-term monthly mean temperatures. Namely, the PDD model assesses the number of days with temperatures favourable for ice melting, derived from a normal statistical distribution centred around a mean value. Widely used in the Antarctic domain, this method proves effective due to the minimal ablation observed at these latitudes, as noted by (Winkelmann et al., 2011; Pollard and DeConto, 2012b; Pattyn, 2017). For regions where surface melt has a major influence, such as Greenland, there are more sophisticated methods, such as the ITM (Robinson et al., 2012).

Evaluating ice-shelf stability can be crucial for potential periodic ice streaming events (e.g., MacAyeal et al., 2003; Hulbe et al., 2004; Alvarez-Solas et al., 2013). In this context, surface melt has a strong influence on driving ice-shelf collapse, as evidenced by the Larsen B and C collapses. Furthermore, surface melt over ice shelves enhances the hydrofracturing of crevasses (Scambos et al., 2000; MacAyeal et al., 2003; van den Broeke, 2005; McGrath et al., 2012; Bevan et al., 2017) and also induces "hydrostatic rebound" when meltwater lakes drain (MacAyeal and Sergienko, 2013). This can ultimately lead to the MICI mechanism, where grounded ice cliffs may rapidly collapse after ice shelf breakup (DeConto and Pollard, 2016). Nonetheless, how such processes are implemented in ice-sheet models, through calving laws and supralakes formation, remains one of the biggest challenges in the glaciological community (Yu et al., 2019; Pattyn and Morlighem, 2020). As shown in Sun et al. (2020), the removal of ice shelves has a strong influence on the AIS, though larger uncertainties rise when assessing the ice shelf stability as a potential trigger of periodic ice streaming events.

Chapter 8
Conclusions

In this thesis, the potential physically-based oscillations of the Laurentide Ice Sheet were investigated from three different perspectives: a theoretical approach from analytical advances in the associated heat problem, an idealised modelling work by the development of Nix ice sheet model and realistic 3D simulations of the LIS under LGM climatic conditions. The ultimate mechanism behind the oscillatory behaviour that could explain the HEs remains unclear and it has implications not only in the understanding of the former largest ice mass, but also in the present picture of ice dynamics in a rapidly warming climate. This thesis takes a step forward to understand the time-dependent behaviour of ice temperatures, the implications of thermomechanical coupling in ice dynamics and grounding line stability and the role played by different friction complexities when simulating the LIS during the LGM.

Described in Chapter 2, the first study investigated the time-dependent nature of ice temperatures along the vertical dimension. Specifically, this work analytically solves the 1D time-dependent advective-diffusive heat problem including additional terms due to strain heating and depth-integrated horizontal advection. A Robin-type top boundary condition considers potential non-equilibrium temperature states across the ice-air interface. The solution is expressed in terms of confluent hypergeometric functions following a separation of variables approach. Non-dimensionalisation reduces the parameter space to four numbers that fully determine the shape of the solution at equilibrium: surface insulation, effective geothermal heat flow, the Peclét number and the Brinkman number. The initial temperature distribution ex-

ponentially converges to the stationary solution. Transient decay timescales are only dependent on the Peclét number and the surface insulation, so that higher advection rates and lower insulating values imply shorter equilibration timescales, respectively. On the contrary, equilibrium temperature profiles are mostly independent of the surface insulation parameter. The study is further extended to a broader range of vertical velocities by using a general power-law dependency on depth, unlike prior studies limited to linear and quadratic velocity profiles. Lastly, Chapter 2 presents a suite of benchmark experiments to test numerical solvers. Four experiments of gradually increasing complexity capture the main physical processes for heat propagation. Analytical solutions are then compared to their numerical counterparts, upon discretisation over unevenly-spaced coordinate systems. A symmetric scheme for the advective term and a three-point asymmetric scheme for the basal boundary condition are found to be the best match our analytical solutions. A further convergence study shows that $n \geq 15$ vertical points are sufficient to accurately reproduce the temperature profile. The solutions presented herein are general and fully applicable to any problem with an equivalent set of boundary conditions and any given initial temperature distribution.

The second piece of work in this thesis, described in Chapter 3, aimed to develop the ice-sheet model Nix v1.0: a 2D thermomechanical model written in C/C++ that simultaneously solves for the momentum balance equations, mass conservation and temperature evolution. Nix's velocity solver includes a hierarchy of Stokes approximations: Blatter-Pattyn, depth-integrated higher order, shallow-shelf and shallow-ice. The grounding-line position is explicitly solved by a moving coordinate system that avoids further interpolations. The model can be easily forced with any external boundary conditions, including those of stochastic nature. Nix has been verified for standard test problems and here results are shown for a number of benchmark tests from standard intercomparison projects and assess grounding-line migration with an overdeepened bed geometry. Lastly, the thermomechanical coupling is further exploited by designing a suite of experiments where the forcing is a physical variable, unlike previously idealised forcing scenarios where ice temperatures are implicitly fixed via an ice rate factor. Namely, atmospheric temperatures and oceanic temperature anomalies are employed to assess model hysteresis behaviour with active thermodynamics. Results show that hysteresis in

an overdeepened bed geometry is similar for atmospheric and oceanic forcings. It is additionally found that not only the particular sub-shelf melting parametrisation determines the temperature anomaly at which the ice sheet retreats, but also the particular value of calibrated heat exchange velocities. Notably, the classical hysteresis loop is narrowed for both forcing scenarios (i.e., atmospheric and oceanic) if the ice sheet is thermomechanically active as a results of the internal feedback among ice temperature, stress balance and viscosity. In summary, Nix combines rapid computational capabilities with a Blatter-Pattyn stress balance fully coupled to a thermomechanical solver, not only validating against established benchmarks but also offering a powerful tool for advancing our insight on ice dynamics and grounding line stability.

The third work, described in Chapter 5 investigated the repercussions of different basal friction formulations when simulating the LIS during the LGM and their explicit implications in ice extent, volume and ice-stream representation. Uncertainties underlying its modelling have led to notable differences in fundamental features such as its maximum elevation, extent and total volume. As a result, the uncertainty in ice dynamics and thus in ice extent, volume and ice-stream stability remains large. A higher-order three-dimensional ice-sheet model is herein used to simulate the LIS under LGM boundary conditions for a number of basal friction formulations of varying complexity. Their consequences on the Laurentide ice streams, configuration, extent and volume were explicitly quantified. Total volume and ice extent generally reach a constant equilibrium value that falls close to prior LIS reconstructions. Simulations exhibit high sensitivity to the dependency of the basal shear stress on the sliding velocity. In particular, a regularized-Coulomb friction formulation appears to be the best choice in terms of ice volume and ice-stream realism. Pronounced differences are found when the basal friction stress is thermomechanically coupled: the base remains colder and the LIS volume is lower than in the purely mechanical friction scenario counterpart. Thermomechanical coupling is fundamental for producing rapid ice streaming, yet it leads to a similar ice distribution overall.

Described in Chapter 6, the fourth work of this thesis addressed the potential ice stream oscillations triggered by thermomechanical instabilities. Special attention is paid to the mechanism of ice stream activation as a re-

sult of the potentially variable basal water content. To this end, a reference simulation is presented for a water-dependent effective pressure formulation that closely matches previous LIS reconstructions. This experiment exhibits an oscillatory equilibrium state of the ice stream located along Hudson Strait whose period is consistent with hypothesized discharges from the LIS observed in ocean sediment cores. More precisely, the ice stream transitions between two modes of ice flow: rapid sliding over a saturated till and slow creeping ice over a fully drained till. Furthermore, a number of sensitivitiy tests show that the oscillatory behaviour is found for a certain range of parameters. Yet the period and amplitude of the oscillation are highly dependent on the hydrology parametrization and the physical properties of the till. Notably, this phenomenon does not appear to be model-resolution dependent, thus discounting a numerical cause of the oscillatory behaviour. It must be stressed that only minor changes on the LIS and Hudson Bay ice volume are found throughout this study as a consequence of the ice stream temporal variability. Therefore, ice discharges herein shown may not be sufficient to account for the IRD layers present in the North Atlantic sediments cores.

To conclude, the thermal behaviour of the ice is a fundamental block to understand both the past and future of large ice masses. Yet it is poorly understood. The inherent coupling with other key elements such as glacial hydrology and ice dynamics shapes the complexity of this problem. Basal friction appears to be a crucial component, of which little is known particularly in past ice-sheet reconstructions with evidence of periodic ice stream activation. This work demonstrates the unveiled potential of a time-dependent analytical description of the ice temperatures. Low dimensional models, though far from an exhaustive description of reality, present themselves as an extremely convenient tool to understand the basic physical mechanisms that are otherwise hidden by the complexity of highly sophisticated models. By means of a balanced combination of novel theoretical advances and modelling efforts, this thesis has cast light upon the thermal activation of ice streaming behaviour in the LIS and the overall stability marine of terminating glaciers.

Appendix A

Appendix A

A.1 Separation of variables and full solution

It is herein briefly outline the separation of variables technique before elaborating on the solutions of our general problem. Consider the following initial/boundary problem on an interval $\mathcal{L} \subset \mathbb{R}$,

$$\begin{cases} \mu_\tau = \mu_{\xi\xi} - w\mu_\xi, & \xi \in \tilde{\mathcal{L}},\ \tau > 0, \\ \mu = \mu_0, & \xi \in \tilde{\mathcal{L}},\ \tau = 0, \\ \mu_\xi = 0, & \xi = 0,\ \tau > 0, \\ \beta\mu_\xi + \mu = 0, & \xi = 1,\ \tau > 0, \end{cases} \tag{A.1}$$

This technique looks for a solution of the form:

$$\mu(\xi, \tau) = X(\xi)T(\tau), \tag{A.2}$$

where the functions Y and T are to be determined. Assuming that there exists a solution of A.5 and plugging the function $\mu = XT$ into the heat equation, it follows:

$$\frac{T_\tau}{T} = \frac{X_{\xi\xi}}{X} - w\frac{X_\xi}{X} = -\lambda, \tag{A.3}$$

for some constant λ. Thus, the solution $\mu(\xi, \tau) = X(\xi)T(\tau)$ of the heat equation must satisfy these equations. In order for a function of the form $\mu(\xi, \tau) = X(\xi)T(\tau)$ to be a solution of the heat equation on the interval $\mathcal{I} \subset \mathbb{R}$, $T(\tau)$ must be a solution of the ODE $T_\tau = -\kappa\lambda T$. Direct integration leads to:

$$T(\tau) = Ae^{-\kappa\lambda\tau}, \tag{A.4}$$

for an arbitrary constant A.

Additionally, in order for $\mu(\xi, \tau)$ to satisfy the boundary conditions, I arrive to a second-order linear ordinary differential equation:

$$\begin{cases} X_{\xi\xi}(\xi) - w(\xi)X_{\xi}(\xi) + \lambda X(\xi) = 0, & \xi \in \tilde{\mathcal{L}}, \\ X_{\xi} = 0, & \xi = 0, \\ \beta X_{\xi} + X = 0, & \xi = 1, \end{cases} \tag{A.5}$$

It is necessary to provide the particular shape of the the function $w(\xi)$. First, I will employ the linear profile $w(\xi) = w_0\xi$ so that the differential equation now reads $X_{\xi\xi}(\xi) - w_0\xi X_{\xi}(\xi) + \lambda X(\xi) = 0$. This equation can be easily identified with the well-known confluent hypergeometric differential equation (e.g., Abramowitz and Stegun, 1965; Evans, 2010) defined as:

$$\xi X_{\xi\xi} + (\delta - \xi)X_{\xi} - \alpha X = 0, \tag{A.6}$$

Simply by defining $\alpha = -\lambda/(2w_0)$, $\delta = 1/2$ and $\zeta = w_0\xi^2/2$, I can write our solution in terms of the two independent Kummer and Tricomi functions:

$$X(\xi) = C_1\Phi(\alpha, \delta, \zeta) + C_2\Psi(\alpha, \delta, \zeta) \tag{A.7}$$

where C_1 and C_2 are constants to be determined from the boundary conditions. At the base, the solution must be finite, so I set $C_2 = 0$ given that Tricomi function $\Psi(\alpha, \delta, \zeta)$ diverges at the origin. The second boundary condition (i.e., at $\xi = 1$) allows us to determine the eigenvalues λ_n of the problem as I look for all values of α_n that satisfy:

$$\beta\Phi_{\xi}(\alpha_n, \delta, \zeta) + \Phi(\alpha_n, \delta, \zeta) = 0, \text{ at } \xi = 1, \tag{A.8}$$

and then I compute the eigenvalues $\lambda_n = -2w_0\alpha_n$. This is in fact a trascendental equation with no algebraic representation and therefore, the values of α_n are numerically determined.

Thus, for each eigenfunction X_n with corresponding eigenvalue λ_n, I have a solution T_n such that:

$$\mu_n(\xi, \tau) = X_n(\xi)T_n(\tau), \tag{A.9}$$

is a solution of the heat equation on our interval $\mathcal{I}$ which satisfies the BC. Moreover, given that the problem A.5 is linear, any finite linear combination of a sequence of solutions $\{\mu_n\}$ is also a solution. In fact, it can be shown that an infinite series of the form:

$$\mu(\xi,\tau) \equiv \sum_{n=0}^{\infty} \mu_n(\xi,\tau), \tag{A.10}$$

will also be a solution of the heat equation on the interval $\mathcal{I}$ that satisfies our BC, under proper convergence assumptions of this series. The discussion of this issue is beyond the scope of this work.

I can then express the transitory solution as:

$$\theta(\xi,\tau) = \sum_{n=0}^{\infty} A_n \Phi\left(\alpha_n;\delta;\zeta\right) e^{-\lambda_n \tau} \tag{A.11}$$

where the coefficients A_n are given by the initial condition.

Since the confluent hypergeometric functions are orthogonal, the normalized eigenfunctions form an orthonormal basis under the $\varrho(\xi)$-Iighted inner product in the Hilbert space L^2, thus allowing to write the coefficients A_n as:

$$A_n = \frac{1}{||\Phi_n||^2} \int_0^1 \left(\theta(\xi,0) - \vartheta(\xi)\right) \varrho(\xi) \Phi\left(\alpha_n;\delta;\zeta\right) d\xi. \tag{A.12}$$

where $\theta(\xi,0)$ is the initial temperature distribution, $\varrho(\xi) = e^{-w_0\xi^2/2}$ and $||\Phi_n||^2$ is defined by the inner product:

$$||\Phi_n||^2 = \langle \Phi_n, \Phi_n \rangle = \int_0^1 \Phi\left(\alpha_n;\delta;\zeta\right) \varrho(\xi) \Phi\left(\alpha_n;\delta;\zeta\right) d\xi. \tag{A.13}$$

A.2 Stationary solution

For the stationary regime, I do not need to apply separation of variables for that the problem reduces to a second-order ordinary differential equation in only one independent variable ξ:

$$\begin{cases} \Omega = \vartheta_{\xi\xi} - w\vartheta_{\xi}, & \xi \in \mathcal{L}, \\ \vartheta_{\xi} = \gamma, & \xi = 0, \\ \beta\vartheta_{\xi} + \vartheta = 1, & \xi = 1, \end{cases} \tag{B.1}$$

Even though I have increased the complexity of the problem with a refined top boundary condition and non-homogeneous term Ω, the solution can still be found analytically:

$$\vartheta(\xi) = \Omega\frac{\xi^2}{2}\ {}_2F_2\left(1, 1; \frac{3}{2}, 2; -\zeta\right) + A\ \mathrm{erf}\left[a\xi\right] + B \tag{B.2}$$

where ${}_2F_2(a_1, a_2; b_1, b_2, x)$ is the generalised hypergeometric function, $\zeta = (a\xi)^2$, $a = (w_0/2)^{1/2}$, $A = -\gamma\left(\pi/(4a)\right)^{1/2}$ and $B = 1 - A\left(2a\pi^{-1}\beta e^{-a^2} + \mathrm{erf}\left[a\right]\right) - \Omega\left((\beta + 1/2)\ {}_2F_2(1, 1; 3/2, 2, a^2) + \beta a^2\ {}_2F_2(2, 2; 5/2, 3, a^2)/3\right)$ is a constant given by the top boundary condition. Note that hypergeometric function can be easily differentiated following e.g., Eq. 15.2.1 in Abramowitz and Stegun (1965).

A.3 General power-law velocity profiles

In this section, I also assume thermal equilibrium, thus reducing again the problem to a second-order ordinary differential equation in only one independent variable ξ:

$$\begin{cases} 0 = \vartheta_{\xi\xi} - w\vartheta_{\xi}, & \xi \in \mathcal{L}, \\ \vartheta_{\xi} = \gamma, & \xi = 0, \\ \beta\vartheta_{\xi} + \vartheta = 1, & \xi = 1, \end{cases} \tag{C.1}$$

where I have set $\Omega = 0$ to ensure analytical tractability for a general power-law velocity profiles. This solution is consequently limited to regions where Pe, $\gamma \gg \Lambda$, Br.

Unlike the general stationary solution shown in Eq. B.2, I allow for a general power-law vertical velocity profile of the form $w(\xi) = w_0\xi^m$. The solution can be then expressed as:

$$\vartheta^-(\xi) = \frac{p\gamma}{(pw_0)^p}\ \Gamma\left(p, pw_0\xi^{m+1}\right) + C \tag{C.2}$$

where $p = (m+1)^{-1}$, $C = 1 - [2\beta\,(pw_0)^p\,e^{-pw_0} + \Gamma(p, w_0 p)]\,p\gamma/\,(pw_0)^p$ is a constant given by the top boundary condition and $\Gamma(\cdot,\cdot)$ is the upper incomplete gamma function defined as:

$$\Gamma\,(a,x) = \int_x^\infty e^{-t} t^{a-1} dt \tag{C.3}$$

Additionally, the solution can be also expressed in terms of Kummer confluent hypergeometric function Φ given the relation (Abramowitz and Stegun, 1965, Eqs. 6.5.3 and 6.5.12):

$$\Gamma\,(a,x) = \Gamma(a) - a^{-1} x^a e^{-x} \Phi(1, 1+a; x) \tag{C.4}$$

Hence, the stationary solution is equivalent to $\sim \Phi\left(1, p+1; pw_0\xi^{m+1}\right)$.

A.4 Discretisation schemes

Our finite differences discretisation considers unevenly-spaced grids, commonly used in the glaciological community where higher resolutions are desired near the base whilst minimising the required number of points to reduce computational costs. It is thus built a new coordinate system ζ considering two types of nonuniform grid spacing: polynomial and exponential. Given that our original variable $\xi \in [0,1]$, these relations can be expressed as:

$$\zeta = \xi^n \tag{D.1}$$

where n is the spacing order, and:

$$\zeta = \frac{e^{s\xi} - 1}{e^s - 1} \tag{D.2}$$

where s is the spacing factor for the exponential grid. In this study, I have employed $n = 2$ and $s = 2$.

Numerical schemes necessary to account for non-homogeneous grids ζ are now presented. The distance between two adjacent points is defined as $h_i = \zeta_{i+1} - \zeta_i$. The five-point symmetric second-order derivative then reads:

$$\begin{aligned}\theta_{\xi\xi}(\xi_i) \simeq & \frac{-2h_i(2h_{i+1}+h_{i+2})+2h_{i+1}(2h_{i+1}+h_{i+2})}{h_{i-1}(h_{i-1}+h_i)(h_{i-1}+h_i+h_{i+1})H_i}\theta_{i-2} \\ & + \frac{2(2h_{i-1}+h_i)(2h_{i+1}+h_{i+2})-2h_{i+1}(h_{i+1}+h_{i+2})}{h_{i-1}h_i(h_{i-1}+h_{i+1})(h_i+h_{i+1}+h_{i+2})}\theta_{i-1} \\ & + \frac{2h_i(h_{i-1}+h_i)-2(h_{i-1}+2h_i)(2h_{i+1}+h_{i+2})+2h_{i+1}(h_{i+1}+h_{i+2})}{(h_{i-1}+h_{i+1})h_ih_{i+1}(h_{i+1}+h_{i+2})}\theta_i \\ & + \frac{2(2h_{i-1}+2h_i)(h_{i+1}+h_{i+2})-2h_i(h_{i-1}+h_i)}{(h_{i-1}+h_i+h_{i+1})(h_i+h_{i+1})h_{i+1}h_{i+2}}\theta_{i+1} \\ & + \frac{2(h_{i-1}+h_i)h_i-2(2h_{i-1}+h_i)h_{i+1}}{H_i(h_i+h_{i+1}+h_{i+2})(h_{i+1}+h_{i+2})h_{i+2}}\theta_{i+2}\end{aligned} \tag{D.3}$$

where $H_i = h_{i-2}+h_{i-1}+h_i+h_{i+1}+h_{i+2}$. This result is consistent with Singh and Bhadauria (2009).

Appendix B

Appendix B

B.1 Discretization schemes

A thorough description of the discretization schemes of Nix model is herein elaborated, where the ordinary notation $q(\sigma_i, \zeta_j, \tau_n) \equiv q^n_{i,j}$ is followed.

The position in the spatial coordinates is then given by $\sigma_i = i\Delta\sigma_{i+1/2}$ and $\zeta_j = j\Delta\zeta_{j+1/2}$ and $\tau_n = n\Delta\tau$. The fractional index implies that the point $(i + 1/2, j)$ lies between (i, j) and $(i + 1, j)$ and analogously for the vertical index j. Note that Nix allows for a nonuniform spatial grid where the spacing between two consecutive points follows a desired distribution (polynomial or exponential). This yields high resolutions near the grounding line whilst minimising the total number of grid points. The horizontal index $i \in \mathcal{W}_r = \{0, 1, 2, ..., r\}$ where r is the number of points in which the horizontal axis is divided. Likewise, the vertical index follows $j \in \mathcal{W}_p = \{0, 1, 2, ..., p\}$ where p is the number of vertical layers.

B.2 Blatter-Pattyn stress balance discretization.

The discretization is straightforward for an Arakawa-C grid. The position of the grounding line $L(t)$ is located on the velocity grid (following Vieli and Payne, 2005). Thus, if the horizontal axis is divided in r points, the ice thickness grid ranges $i = 0, 1, ..., r - 1$, whereas the velocity grid (staggered) indexes read $i = 1/2,\ 3/2, ..., r - 1/2$.

The Blatter-Pattyn stress balance can be written as:

$$\frac{2}{L^2 \Delta\sigma_{i+1/2}}\left[\eta_{i+1,j}\frac{u_{i+3/2,j}-u_{i+1/2,j}}{\Delta\sigma_{i+3/2}+\Delta\sigma_{i+1/2}}-\eta_{i,j}\frac{u_{i+1/2,j}-u_{i-1/2,j}}{\Delta\sigma_{i+1/2}+\Delta\sigma_{i-1/2}}\right]+$$
$$\frac{1}{2\left(H_i\right)^2 \Delta\zeta_{j+1/2}}\left[\eta_{i,j+1}\frac{u_{i,j+3/2}-u_{i,j+1/2}}{\Delta\zeta_{j+3/2}+\Delta\zeta_{j+1/2}}-\eta_{i,j}\frac{u_{i,j+1/2}-u_{i,j-1/2}}{\Delta\zeta_{j+1/2}+\Delta\zeta_{j-1/2}}\right]=\rho g\frac{h_{i+1}-h_i}{L\Delta\sigma_{i+1/2}}, \tag{B.1}$$

This is a linear system of $6 \times r \times p$ unknowns that can be solved applying standard linear algebraic solvers. For each timestep, a matrix of coefficients with dimension $(rp) \times (rp)$ is built:

$$\underset{(rp)\times(rp)}{\mathrm{A}} * \underset{(rp)\times(1)}{\mathrm{u}} = \underset{(rp)\times(1)}{\mathrm{F}} \tag{B.2}$$

Since our discretization stencil includes 6 points: $(i+3/2, j)$, $(i+1/2, j)$, $(i-1/2, j+1)$, $(i, j+3/2)$, $(i, j+1/2)$ and $(i, j-1/2)$, a sparse matrix that allows for optimised inversion is obtained. For $r = 500$ and $p = 25$, only a 0.048% of the coefficient matrix are nonzero entries:

$$\begin{pmatrix} & & & & & & & & & & \\ & & & & & & & & & & \\ & & & & & & & & & & \\ & & & & & & & & & & \\ \alpha_{i-2M,j} & \cdots & \alpha_{i-M,j} & \cdots & \alpha_{i,j-1/2} & \alpha_{i,j+1/2} & \cdots & \alpha_{i+M,j} & \cdots & \alpha_{i+2M,j} \\ & & & & & & & & & & \\ & & & & & & & & & & \\ & & & & & & & & & & \\ & & & & & & & & & & \end{pmatrix} \begin{pmatrix} u_{i-3/2,j} \\ \vdots \\ u_{i-1/2,j} \\ \vdots \\ u_{i,j-1/2} \\ u_{i,j+1/2} \\ \vdots \\ u_{i+1/2,j} \\ \vdots \\ u_{i+3/2,j} \end{pmatrix} = \begin{pmatrix} F_{i-3/2,j} \\ \vdots \\ F_{i-1/2,j} \\ \vdots \\ F_{i,j-1/2} \\ F_{i,j+1/2} \\ \vdots \\ F_{i+1/2,j} \\ \vdots \\ F_{i+3/2,j} \end{pmatrix} \tag{B.3}$$

B.3 DIVA/SSA stress balance discretization.

The discretization is straightforward for a staggered grid. The position of the grounding line $L(t)$ is located on the staggered grid (following Vieli and Payne, 2005). Thus, if the domain is divided in n points, the ice thickness

grid ranges $i = 0, 1, ..., r-1$, whereas the velocity grid (staggered) indexes read $i = 1/2,\ 3/2, ..., r-1/2$.

The SSA stress balance can be then written as (note that the factor 2 difference in Eq. B.15, Vieli and Payne, 2005 since their viscosity definition is not preceded by 1/2 is cancelled by the average between two consecutive grid lengths $\Delta\sigma$ necessary to compute the velocity gradients):

$$\frac{2}{L^2\Delta\sigma_{i+1/2}}\left[\eta_{i+1}H_{i+1}\frac{u_{i+3/2,j}-u_{i+1/2,j}}{\Delta\sigma_{i+3/2}+\Delta\sigma_{i+1/2}}-\eta_i H_i\frac{u_{i+1/2,j}-u_{i-1/2,j}}{\Delta\sigma_{i+1/2}+\Delta\sigma_{i-1/2}}\right] -\beta^2_{i+1/2}u_{i+1/2}=\rho g\frac{H_{i+1}+H_i}{2}\frac{h_{i+1}-h_i}{L\Delta\sigma_{i+1/2}}, \tag{B.4}$$

where the friction coefficient β^2 reads:

$$\beta_{i+1/2}=Cu^{m-1}_{i+1/2}, \tag{B.5}$$

so that $\tau_b = \beta^2 u$.

Assuming our domain is divided in n points, the corresponding tridiagonal matrix is built at every time step as (where the super-index are dropped to lighten the notation):

$$\begin{pmatrix} B_0 & C_0 & & & \\ A_1 & B_1 & C_1 & & \\ & A_2 & B_2 & \ddots & \\ & & \ddots & \ddots & C_{r-2} \\ & & & A_{r-1} & B_{r-1} \end{pmatrix} \begin{pmatrix} u_{1/2} \\ u_{3/2} \\ \vdots \\ u_{r-3/2} \\ u_{r-1/2} \end{pmatrix} = \begin{pmatrix} F_0 \\ F_1 \\ \vdots \\ F_{r-2} \\ F_{r-1} \end{pmatrix} \tag{B.6}$$

where $A_0 = C_{n-1} = 0$ by definition.

The non-zero entries of the matrix and the inhomogeneous term read:

$$\begin{aligned} A_i &= \gamma_i\eta_i H_i \\ B_i &= -\gamma_i\left(\eta_{i+1}H_{i+1}+\eta_i H_i\right)-\beta_i^2 \\ C_i &= \gamma_i\eta_{i+1}H_{i+1} \\ F_i &= \rho g\frac{H_{i+1}+H_i}{2}\frac{h_{i+1}-h_i}{L\Delta\sigma_{i+1/2}} \end{aligned} \tag{B.7}$$

where $\gamma_i = 2/(L\Delta\sigma_{i+1/2})^2$.

For the edge of the matrix (i.e., $i = n - 1$), the following values are used:

$$\begin{aligned} A_{r-1} &= \eta_{r-1} H_{r-1} \\ B_{r-1} &= -\gamma_{r-1} \left(\eta_{r-1} H_{r-1}\right) - \beta_{n-1}^2 \\ C_{r-1} &= 0 \\ F_{r-1} &= \rho g H_{r-1} \frac{h_{r-1} - h_{r-2}}{L \Delta\sigma_{r-3/2}} \end{aligned} \tag{B.8}$$

For the boundary values, it is set (note that, in the staggered grid, $u_{1/2}$ is the very first velocity value of the domain):

$$\begin{aligned} u_{1/2} &= -u_{3/2}, \\ u_{r-1/2} &= u_{r-3/2} + \frac{L \Delta\sigma_{r-3/2}}{8\eta_{r-1}} \left(\rho g H_{r-1}^2 - \rho_w g D^2\right) \end{aligned} \tag{B.9}$$

where D is the bedrock depth below sea level, the first equality yields from symmetry arguments at the ice divide ($i = 1$) and the second implies that the ice momentum is equated by the hydrostatic pressure of the water.

B.4 Advection discretization

For the advection equation an implicit scheme is chosen for numerical stability:

$$\frac{H_i^{n+1} - H_i^n}{\Delta\tau^n} = \sigma_i \frac{\dot{L}^n}{L^n} \frac{H_{i+1}^{n+1} - H_{i-1}^{n+1}}{\left(\Delta\sigma_{i+1/2} + \Delta\sigma_{i-1/2}\right)} - \frac{2\left(q_{i+1/2}^{n+1} - q_{i-1/2}^{n+1}\right)}{L^n \left(\Delta\sigma_{i+1/2} + \Delta\sigma_{i-1/2}\right)} + S_i^n, \tag{B.10}$$

where the ice flux is defined as:

$$q_{i+1/2} = u_{i+1/2} \frac{H_{i+1} + H_i}{2} \tag{B.11}$$

However, at the grounding line the ice flux reads:

$$q_{r-1/2} = u_{r-1/2} H_{r-1} \tag{B.12}$$

The advection equation can be rewritten as:

$$A_i H_{i-1}^{n+1} + B_i H_i^{n+1} + C_i H_{i+1}^{n+1} = F_i \tag{B.13}$$

so that the corresponding matrix is also tridiagonal:

$$\begin{aligned} A_i &= \gamma_i^n \left(\sigma_i \dot{L} - u_{i-1} \right) \\ B_i &= 1 + \gamma_i^n \left(u_i - u_{i-1} \right) \\ C_i &= \gamma_i^n \left(-\sigma_i \dot{L} + u_i \right) \\ F_i &= H_i^n + \Delta\tau^n S_i^n \end{aligned} \tag{B.14}$$

where $\gamma_i^n = \Delta\tau^n / 2 \left(\Delta\sigma_{i+1/2} + \Delta\sigma_{i-1/2} \right) L^n$.

As the ice divide is located at $i = 1$ (note that the first element corresponds to $i = 0$), the boundary condition then reads:

$$H_0^n = H_2^n, \tag{B.15}$$

since $\sigma = 1$ is a symmetry axis.

B.5 Grounding line scheme

The terminus position L (i.e., the grounding line) is not fixed in time. Direct discretization of Eq. 3.18 in terms of σ-coordinates leads to:

$$\dot{L}^n \equiv \frac{dL}{d\tau} = \frac{-L^n \Delta\sigma_{r-1/2} S_{r-1}^n + 2 \left(q_{r-1/2}^n - q_{r-3/2}^n \right) / \left(\Delta\sigma_{r-1/2} + \Delta\sigma_{r-3/2} \right)}{H_{r-1}^n - H_{r-2}^n + \varrho \left(b_{r-1}^n - b_{r-2}^n \right)}, \tag{B.16}$$

B.6 Thermodynamics discretization scheme

Unlike previous discretizations, the temperature field $\theta(\sigma, \zeta, \tau)$ has an additional dependency on the vertical coordinate ζ that brings a higher degree of complexity (Eq. 3.24).

The energy balance (Eq. 3.28) is discretized using an upwind scheme with a forward Euler step and a centred difference for the spatial derivatives. The lengthy expression reads:

$$\rho c \left[\frac{\theta_{i,j}^{n+1} - \theta_{i,j}^{n}}{\Delta\tau^{n}} - \sigma_i \frac{\dot{L}^{n}}{L^{n}} \frac{\theta_{i+1,j}^{n} - \theta_{i-1,j}^{n}}{\Delta\sigma_{i+1/2} + \Delta\sigma_{i-1/2}} + \right.$$
$$\left. - \frac{\zeta_{i,j}}{H_i^{n}} \frac{H_i^{n+1} - H_i^{n-1}}{2\Delta\tau^{n}} \frac{\theta_{i,j+1}^{n} - \theta_{i,j-1}^{n}}{\Delta\zeta_{i,j+1/2} + \Delta\zeta_{i,j-1/2}} \right] = \frac{k}{\left(H_i^{n}\right)^2} \frac{\theta_{i,j+1}^{n} - 2\theta_{i,j}^{n} + \theta_{i,j-1}^{n}}{\left(\Delta\zeta_{i,j+1/2} + \Delta\zeta_{i,j-1/2}\right)^2} +$$
$$-\rho c \frac{u_i^{n}}{L^{n}} \left[\frac{\theta_{i+1,j}^{n} - \theta_{i-1,j}^{n}}{\Delta\sigma_{i+1/2} + \Delta\sigma_{i-1/2}} - \left(\frac{b_{i+1} - b_{i-1}}{\Delta\sigma_{i+1/2} + \Delta\sigma_{i-1/2}} + \zeta_{i,j} \frac{H_{i+1}^{n} - H_{i-1}^{n}}{\Delta\sigma_{i+1/2} + \Delta\sigma_{i-1/2}} \right) \right.$$
$$\left. \frac{\theta_{i,j+1}^{n} - \theta_{i,j-1}^{n}}{H_i^{n}\left(\Delta\zeta_{i,j+1/2} + \Delta\zeta_{i,j-1/2}\right)} + \Phi_i^{n} \right. \tag{B.17}$$

B.7 Adaptive time stepping

An adaptive timestepping approach is adopted to enhance the computational performance of the flowline model. Unlike the proportional-integral (PI) methods, the fact that Picard's iteration already computes a metric to determine convergence is further exploited. Thus, without additional calculations, the new timestep can evolve within a range set by the user $[\Delta t_{\min}, \Delta t_{\max}]$ with a quadratic dependency on the error:

$$\Delta\tilde{t} = \left(1 - \left(\frac{\min\left[\varepsilon(t), \phi_{\text{pic}}\right]}{\phi_{\text{pic}}} \right)^2 \right) \left(\Delta t_{\max} - \Delta t_{\min}\right) + \Delta t_{\min}, \tag{B.18}$$

where ϕ_{pic} is the tolerance on Picard's iteration and $\varepsilon(t)$ is the error on the current iteration defined as $\varepsilon^i = ||u^i - u^{i-1}||$ (De Schmedt et al., 2010). If the solution has not converged in the given timestep (i.e., $\varepsilon > \phi_{\text{pic}}$), Eq. B.18 ensures that the timestep is set to the minimum value.

Then, certain relaxation is applied to provide stability and avoid spurious oscillations:

$$\Delta t = \alpha \Delta t + (1 - \alpha)\Delta\tilde{t}, \tag{B.19}$$

where $\alpha = 0.7$. Lastly, the timestep is ensured not to exceed the CFL condition:

$$\Delta t = \min\left[\Delta t, \Delta t_{\text{CFL}}\right] \tag{B.20}$$

B.8 Stochastic boundary conditions

Internal climatic variability arises from chaotic fluctuation and its he effect over a real ice sheet mostly comes from the atmosphere and the ocean. The latter two interact with an ice sheet via the surface mass balance and the frontal melting/calving at the grounding line. Two random time series are created so that they fulfil three conditions: (1) random nature, (2) correlated with each other and (3) have a prescribed persistence.

A Fourier transform method to create such a series following Christian et al. (2022) is now described. Nevertheless, the methods herein presented is completely general and can generate random time series of any variables provided that the system is described by a first-order autoregressive process.

Starting with the power spectrum of an AR-1 process as a function of the frequency:

$$P(\nu) = \frac{P_0}{1 + r^2 - 2r\cos(2\pi\nu\Delta t)} \tag{B.21}$$

where P_0 scales the total variance (here the value $P_0 = 1$ is employed), r is the autocorrelation coefficient at a lag Δt.

The persistence time τ_{AR1} (i.e., decorrelation time) then reads:

$$\tau_{\mathrm{AR1}} = \frac{\Delta t}{1 - r} \tag{B.22}$$

a random complex spectrum can be simply obtained from a random phase rotation and then, applying the inverse Fourier transform:

$$P(t) = \mathcal{F}^{-1}\left[P(\nu)e^{i\phi}\right] \tag{B.23}$$

where $\phi \in [0, 2\pi]$.

B.9 Convergence and computational speed

It is hard to give a one-to-one comparison since other models that solve for the higher-order momentum balance coupled with a thermomechanical solver are full 3D solvers (partially providing Nix novelty). To give an estimation, MALI ice-sheet model (Hoffman et al., 2018) control simulations averaged 5.26 sim-

ulated years per wall-clock hour. On the contrary, MISMIP experiments run with Nix reach $\sim 10^5$ simulated years per wall-clock hour on average. Thus, there is a 5-order magnitude difference in terms of computational time.

Figure B.1 shows the the grounding line deviation $\varepsilon = L_{\text{Nix}} - L_{\text{Schoof}}$ from the semi-analytical result of Schoof (2007a). The same panel additional illustrates the computational speed dependency to the total number of grid points. Note the small changes for $\Delta x < 1.0$ km given the SSA solver.

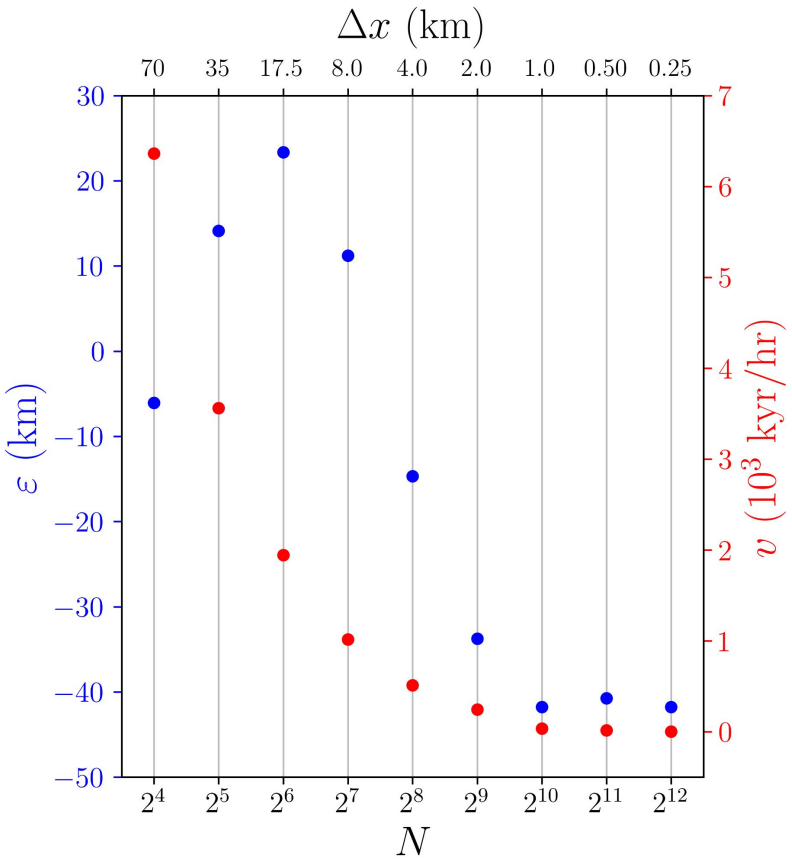

Fig. B.1: Nix convergence study and computational speed as function of the grid resolution. SSA solver comparison against semi-analytical result of Schoof (2007a) $\varepsilon = L_{\text{Nix}} - L_{\text{Schoof}}$.

Appendix C

Appendix C

C.1 The two-phase regression model

The two-phase linear regression model was studied by Hinkley (1969, 1971) and later also applied by Solow (1987). For our purpose, the underlying idea is to determine the *changepoint* in a given time series $y(t)$ to estimate the necessary length of the equilibration time in our simulations. Conceptually, the two-phase regression model assumes that there are two different behaviours in our data and these are captured by two independent linear functions (Eq. C.1). In the present study, these behaviours correspond to the transitory and stationary nature of the solutions respectively. The *changepoint* is thus defined as the abscissa of intersection that minimizes the residual sum of squares. Mathematically, this model can be written as:

$$y_i = \begin{cases} \alpha + \beta t_i, & i = 1, ..., r, \\ \gamma + \mu t_i, & i = r+1, ..., n, \end{cases} \tag{C.1}$$

where the abscissa of the intersection of these two regression lines reads:

$$t_c = \frac{\alpha - \gamma}{\mu - \beta} \tag{C.2}$$

and it is referred to as the changepoint.

Following Solow (1987), for our *changepoint* definition, continuity of the underlying time series must be ensured by imposing t_c to lie in the interval $\mathfrak{I} \in (t_r, t_{r+1})$. Otherwise, the two-phase regression will include a discontinuity at t_c.

The approach thus aims at finding the estimate t_c. Since no closed form expression of t_c is possible, the model given by C.1 is usually rewritten as:

$$y_i = \alpha + \beta t_i + \lambda \Omega_i(c) t_{i-c} + \varepsilon_i \tag{C.3}$$

where ε_i is the error term, $\lambda = \mu - \beta$ and $\Omega_i(c)$ is given by:

$$\Omega_i(c) = \begin{cases} 0, & \text{if } \ i \leq c, \\ 1, & \text{if } \ i > c. \end{cases} \tag{C.4}$$

Fixing a value of c, the modified model C.3 becomes a standard linear regression with two regressor variables: t_i and t_{i-c}. Our problem is now reduced to finding t_c so that its value minimizes the residual sum of squares (Fig. C.1). For large datasets, Hinkley (1971) provides with a description of an efficient algorithm, though this study simply applies a direct grid search given the dimensions of our time series.

Particularly, the ice volume above sea level is used as the regressand and performed the calculations aforementioned described. The vertical dashed line in Fig. 5.1 represent the abscissa of the changepoint t_c. Solow (1987) determines such value by minimizing the residual sum of squares RSS, though these results are additionally compared to those given by maximizing the determination coefficient R^2 (Fig. C.1). The values yielded by each method coincides.

[b]0.8

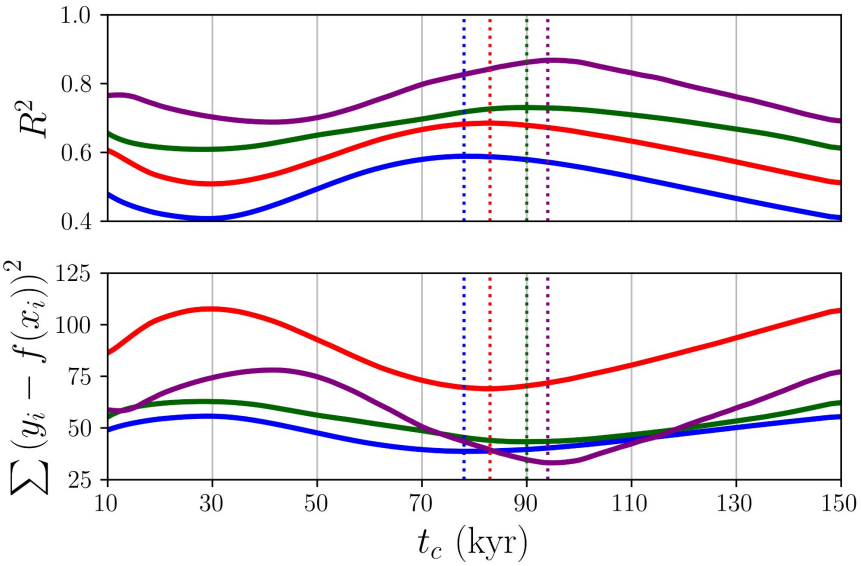

Fig. C.1: Determination coefficient R^2 (top panel) and residual sum of squares RSS (bottom panel) as a function of the fixed *changepoint* value taken. For each t_c value, a standard linear regression (Eq. C.3) with two regressor variables is performed using the volume above sea level as a regressand. The vertical dashed lines correspond to the maximum and minimum values of R^2 and RSS respectively.

List of publications and conference contributions related to this thesis

Scientific publications as first author

- **Moreno-Parada, D.,** Alvarez-Solas, J., Blasco, J., Montoya, M., and Robinson, A.: Simulating the Laurentide Ice Sheet of the Last Glacial Maximum, *The Cryosphere*, **17**, 121-133, DOI 10.5194/tc-17-2139-2023., https://doi.org/10.5194/tc-17-2139-2023

- **Moreno-Parada, D.,** Robinson, A., Montoya, M., and Alvarez-Solas, J.: Description and validation of the ice sheet model Nix v1.0, *EGUsphere* [preprint], https://doi.org/10.5194/egusphere-2023-2690,2023.

- **Moreno, D.,** Robinson, A., Montoya, M., and Alvarez-Solas, J.: On the periodicity of free oscillations for a finite ice column, *The Cryosphere Discuss.* [preprint], 2022, DOI 10.5194/tc-2022-97 https://doi.org/10.5194/tc-2022-97.

Contribution in other scientific publications

- Blasco, J., Tabone, I., **Moreno-Parada, D.,** Robinson, A., Alvarez-Solas, J., Pattyn, F., and Montoya, M.: Antarctic Tipping points triggered by the mid-Pliocene warm climate, Clim. Past, 20, 1919–1938, https://doi.org/10.5194/cp-20-1919-2024, 2024.

Oral contributions - Conferences

- **Moreno-Parada, D.,** Robinson, A., Montoya, M., and Alvarez-Solas, J.: Description and validation of the ice sheet model Nix v1.0, EGU General Assembly 2024, Vienna, Austria, 14–19 Apr 2024, EGU24-13290, https://doi.org/10.5194/egusphere-egu24-13290, 2024.

- **Moreno-Parada, D.,** Swierczek-Jereczek, J., Montoya, M., Alvarez-Solas, J., and Robinson, A.: Transition indicators on a flowline ice sheet model, EGU General Assembly 2023, Vienna, Austria, 24–28 Apr 2023, EGU23-14486, https://doi.org/10.5194/egusphere-egu23-14486, 2023.

- **Moreno-Parada, D.,** Montoya, M., and Robinson, A., and Alvarez-Solas, J.: Periodicity of free oscillations for a finite ice column, International Glaciological Society, Ice on a Sustainable Society Bilbao, Spain, 5-10 June 2022. https://www.igsoc.org/wp-content/uploads/2022/06/procabstracts_77.html#A3758, 2022.

- **Moreno, D.,** Alvarez-Solas, J., Robinson, A., Blasco, J., Tabone, I., Swierczek-Jereczek, J., Perez-Montero, S., Juarez, A. and Montoya, M.: Could the Laurentide have exhibited internal oscillations? Polar CSIC, 11-13 May 2022.

- **Moreno, D.,** Alvarez-Solas, J., Montoya, M., Blasco, J., and Robinson, A.: Could the Laurentide Ice Sheet have exhibited internal oscillations?, EGU General Assembly 2022, Vienna, Austria, 23–27 May 2022, EGU22-3080, https://doi.org/10.5194/egusphere-egu22-3080, 2022.

- **Moreno, D.,** Alvarez-Solas, J., Robinson, A., Blasco, J., Tabone, I., and Montoya, M.: Physically-based oscillations of the Laurentide Ice Sheet under glacial conditions, EGU General Assembly 2021, online, 19–30 Apr 2021, EGU21-10208, https://doi.org/10.5194/egusphere-egu21-10208, 2021.

- **Moreno, D.,** Alvarez-Solas, J., Robinson, A., Blasco, J., Tabone, I., and Montoya, M.: Physically-based oscillations of the Laurentide Ice Sheet un-

der glacial conditions, TiPES project, Oct 2020.

- Montoya, M., Alvarez-Solas, J., Banderas, R., Blasco, J., Juarez, A., **Moreno, D.,** Perez, S., Robinson, A., Segalla, D. and Tabone, I.: Ocean-ice interactions: from the past to the future. VI Expanding Ocean Frontiers conference (EOF 2021), Barcelona (Spain), 5th - 7th July 2021.

Poster contributions - Conferences and Schools

- **Moreno-Parada, D.,** Swierczek-Jereczek, J., Montoya, M., Alvarez-Solas, J., and Robinson, A.: Transition indicators on a flowline ice sheet model, EGU General Assembly 2023, Vienna, Austria, 24–28 Apr 2023, EGU23-14486, https://doi.org/10.5194/egusphere-egu23-14486

Other oral and poster contributions

- **Moreno-Parada, D.,** García-Pereira, F., Montoya, M., Alvarez-Solas, J., and Robinson, A.: Heat propagation in the cryosphere. *Oral contribution*, Jornadas Investigación de la UCM, Madrid (Spain), March 2023.

- **Moreno-Parada, D.,** Montoya, M., Robinson, A. and Alvarez-Solas, J.: A thermomechanically coupled flowline model. *Poster contribution*, PhDay Físicas 2022, Madrid (Spain), October 2022.

- **Moreno-Parada, D.,** Montoya, M., Alvarez-Solas, J., and Robinson, A.: Can ice sheets interanlly oscillate? *Poster contribution*, PhDay Físicas 2021, Madrid (Spain), October 2021.

References

Abramowitz, M. and I. Stegun, 1965: *Handbook of Mathematical Functions: With Formulas, Graphs, and Mathematical Tables*. Applied mathematics series, Dover Publications.
URL https://books.google.es/books?id=MtU8uP7XMvoC

Al-Niami, A. and K. Rushton, 1977: Analysis of flow against dispersion in porous media. *Journal of Hydrology*, **33**, 87–97, doi:10.1016/0022-1694(77)90100-7.

Albrecht, T., R. Winkelmann, and A. Levermann, 2020: Glacial-cycle simulations of the antarctic ice sheet with the parallel ice sheet model (PISM) – part 2: Parameter ensemble analysis. *The Cryosphere*, **14**, 633–656, doi:10.5194/tc-14-633-2020.

Alley, R. B., D. D. Blankenship, C. R. Bentley, and S. T. Rooney, 1986: Deformation of till beneath ice stream b, west antarctica. *Nature*, **322**, 57–59, doi:10.1038/322057a0.

Alley, R. B., P. U. Clark, P. Huybrechts, and I. Joughin, 1999: The deglaciation of the northern hemisphere: a global perspective. *Ann. Rev. Earth and Plan. Sci.*, **27**, 149–182, doi: 10.1146/annurev.earth.27.1.149.

Alvarez-Solas, J., S. Charbit, C. Ritz, D. Paillard, G. Ramstein, and C. Dumas, 2010: Links between ocean temperature and iceberg discharge during Heinrich events. *Nature Geoscience*, **3**, 122–126.

Alvarez-Solas, J., M. Montoya, C. Ritz, G. Ramstein, S. Charbit, C. Dumas, K. Nisancioglu, T. Dokken, and A. Ganopolski, 2011: Heinrich event 1: an example of dynamical ice-sheet reaction to oceanic changes. *Climate of the Past*, **7**, 1297–1306, doi:10.5194/cp-7-1297-2011.

Alvarez-Solas, J., A. Robinson, M. Montoya, and C. Ritz, 2013: Iceberg discharges of the last glacial period driven by oceanic circulation changes. *Proceedings of the National Academy of Sciences*, **110**, 16350–16354, doi:10.1073/pnas.1306622110.

Arakawa, A. and V. R. Lamb, 1977: Computational design of the basic dynamical processes of the UCLA general circulation model. *Methods in Computational Physics: Advances in Research and Applications*, Elsevier, 173–265.

Aral, M. M. and B. Liao, 1996: Analytical solutions for two-dimensional transport equation with time-dependent dispersion coefficients. *Journal of Hydrologic Engineering*, **1**, 20–32.

Arthern, R. J., R. C. A. Hindmarsh, and C. R. Williams, 2015: Flow speed within the antarctic ice sheet and its controls inferred from satellite observations. *Journal of Geophysical Research: Earth Surface*, **120**, 1171–1188, doi:10.1002/2014jf003239.

Arthern, R. J. and C. R. Williams, 2017: The sensitivity of west antarctica to the submarine melting feedback. *Geophysical Research Letters*, **44**, 2352–2359, doi:10.1002/2017gl072514.

Asay-Davis, X. S., N. C. Jourdain, and Y. Nakayama, 2017: Developments in simulating and parameterizing interactions between the southern ocean and the antarctic ice sheet. *Current Climate Change Reports*, **3**, 316–329, doi:10.1007/s40641-017-0071-0.

Aschwanden, A., G. Aalgeirsdóttir, and C. Khroulev, 2013: Hindcasting to measure ice sheet model sensitivity to initial states. *The Cryosphere*, **7**, 1083–1093, doi:10.5194/tc-7-1083-2013.

Bamber, J. L., D. G. Vaughan, and I. Joughin, 2000: Widespread complex flow in the interior of the antarctic ice sheet. *Science*, **287**, 1248–1250, doi:10.1126/science.287.5456.1248.

Banks, R. B. and I. Ali, 1964: Dispersion and adsorption in porous media flow. *J. Hydraul. Div., Am. Soc. Civ. Eng.; (United States)*, **90:HY5**. URL https://www.osti.gov/biblio/6949390

Barker, S., J. Chen, X. Gong, L. Jonkers, G. Knorr, and D. Thornalley, 2015: Icebergs not the trigger for north atlantic cold events. *Nature*, **520**, 333–336, doi:10.1038/nature14330.

Bartholomaus, T. C., R. S. Anderson, and S. P. Anderson, 2011: Growth and collapse of the distributed subglacial hydrologic system of kennicott

glacier, alaska, USA, and its effects on basal motion. *Journal of Glaciology*, **57**, 985–1002, doi:10.3189/002214311798843269.

Bassis, J. N., S. V. Petersen, and L. M. Cathles, 2017: Heinrich events triggered by ocean forcing and modulated by isostatic adjustment. *Nature*, **542**, 332–334, doi:10.1038/nature21069.

Bear, J., 1975: Dynamics of fluids in porous media. *Soil Science*, **120**, 162–163.

Bevan, S. L., A. Luckman, B. Hubbard, B. Kulessa, D. Ashmore, P. Kuipers Munneke, M. O'Leary, A. Booth, H. Sevestre, and D. McGrath, 2017: Centuries of intense surface melt on larsen c ice shelf. *The Cryosphere*, **11**, 2743–2753, doi:10.5194/tc-11-2743-2017.

Blake, E., 1992: The deforming bed beneath a surge-type glacier; measurement of mechanical and electrical properties, phd thesis. *University of British Columbia*.

Blankenship, D. D., C. R. Bentley, S. T. Rooney, and R. B. Alley, 1986: Seismic measurements reveal a saturated porous layer beneath an active antarctic ice stream. *Nature*, **322**, 54–57, doi:10.1038/322054a0.

Blasco, J., J. Alvarez-Solas, A. Robinson, and M. Montoya, 2021: Exploring the impact of atmospheric forcing and basal drag on the antarctic ice sheet under last glacial maximum conditions. *The Cryosphere*, **15**, 215–231, doi:10.5194/tc-15-215-2021.

Blatter, H., 1995: Velocity and stress fields in grounded glaciers: a simple algorithm for including deviatoric stress gradients. *Journal of Glaciology*, **41**, 333–344, doi:10.3189/s002214300001621x.

Bougamont, M., P. Christoffersen, and S. Tulaczyk, 2003: Response of subglacial sediments to basal freeze-on 1. theory and comparison to observations from beneath the west antarctic ice sheet. *Journal of Geophysical Research: Solid Earth*, **108**, doi:10.1029/2002jb001935.

Bougamont, M. and S. Tulaczyk, 2003: Glacial erosion beneath ice streams and ice-stream tributaries: constraints on temporal and spatial distribution of erosion from numerical simulations of a west antarctic ice stream. *Boreas*, **32**, 178–190, doi:10.1111/j.1502-3885.2003.tb01436.x.

Boulton, G. and M. Hagdorn, 2006: Glaciology of the british isles ice sheet during the last glacial cycle: form, flow, streams and lobes. *Quaternary Science Reviews*, **25**, 3359–3390, doi:10.1016/j.quascirev.2006.10.013.

Boulton, G. S., G. D. Smith, A. S. Jones, and J. Newsome, 1985: Glacial geology and glaciology of the last mid-latitude ice sheets. *Journal of the Geological Society*, **142**, 447–474, doi:10.1144/gsjgs.142.3.0447.

Braithwaite, R., 1985: Calculation of degree-days for glacier-climate research. *Zeitschrift für Gletscherkunde und Glazialgeologie*, **20/1984**, 1–8.

Braithwaite, R. and O. Olesen, 1989: *Calculation of glacier ablation from air temperature, West Greenland*, Kluwer Academic Publishers, Netherlands. J. oerlemans edition, 219–233.

Braithwaite, R. J., 1995: Positive degree-day factors for ablation on the greenland ice sheet studied by energy-balance modelling. *Journal of Glaciology*, **41**, 153–160, doi:10.3189/s0022143000017846.

Brocq, A. L., A. Payne, M. Siegert, and R. Alley, 2009: A subglacial water-flow model for west antarctica. *Journal of Glaciology*, **55**, 879–888, doi:10.3189/002214309790152564.

Brown, S. A., M. Folk, G. Goucher, R. Rew, and P. F. Dubois, 1993: Software for portable scientific data management. *Computers in Physics*, **7**, 304–308, doi:10.1063/1.4823180.

Bueler, E. and J. Brown, 2009: Shallow shelf approximation as a 'sliding law'in a thermomechanically coupled ice sheet model. *J. Geophys. Res*, **114**, F03008.

Bueler, E., C. S. Lingle, and J. Brown, 2007: Fast computation of a viscoelastic deformable earth model for ice-sheet simulations. *Annals of Glaciology*, **46**, 97–105, doi:10.3189/172756407782871567.

Bueler, E. and W. van Pelt, 2015: Mass-conserving subglacial hydrology in the parallel ice sheet model version 0.6. *Geoscientific Model Development*, **8**, 1613–1635, doi:10.5194/gmd-8-1613-2015.

Calonne, N., F. Flin, S. Morin, B. Lesaffre, S. Rolland du Roscoat, and C. Geindreau, 2011: Numerical and experimental investigations of the effective thermal conductivity of snow. *Geophysical Research Letters*, **38**, L23501, doi:10.1029/2011GL049234.

Calonne, N., L. Milliancourt, A. Burr, A. Philip, C. L. Martin, F. Flin, and C. Geindreau, 2019: Thermal conductivity of snow, firn, and porous ice from 3-d image-based computations. *Geophysical Research Letters*, **46**, 13079–13089, doi:10.1029/2019gl085228.

Calov, R., A. Ganopolski, V. Petoukhov, M. Claussen, and R. Greve, 2002: Large-scale instabilities of the Laurentide ice sheet simulated in a fully

coupled climate-system model. *Geophysical Research Letters*, **29**, 69–1.

Calov, R., R. Greve, A. Abe-Ouchi, E. Bueler, P. Huybrechts, J. V. Johnson, F. Pattyn, D. Pollard, C. Ritz, F. Saito, and L. Tarasov, 2010: Results from the ice-sheet model intercomparison project–heinrich event intercomparison (ISMIP HEINO). *Journal of Glaciology*, **56**, 371–383, doi:10.3189/002214310792447789.

Carslaw, H. S. and J. C. Jaeger, 1988: *Conduction of heat in solids*. Clarendon Press, Oxford.

Christian, J. E., A. A. Robel, and G. Catania, 2022: A probabilistic framework for quantifying the role of anthropogenic climate change in marine-terminating glacier retreats. *The Cryosphere*, **16**, 2725–2743, doi:10.5194/tc-16-2725-2022.

Chugunov, V. A. and A. V. Wilchinsky, 1996: Modelling of a marine glacier and ice-sheet-ice-shelf transition zone based on asymptotic analysis. *Annals of Glaciology*, **23**, 59–67, doi:10.3189/s0260305500013264.

Clark, J. A., 1980: The reconstruction of the laurentide ice sheet of north america from sea level data: Method and preliminary results. *Journal of Geophysical Research: Solid Earth*, **85**, 4307–4323, doi:10.1029/jb085ib08p04307.

Clarke, G. K. C., 1987: Subglacial till: A physical framework for its properties and processes. *Journal of Geophysical Research*, **92**, 9023, doi:10.1029/jb092ib09p09023.

Clarke, G. K. C., U. Nitsan, and W. S. B. Paterson, 1977: Strain heating and creep instability in glaciers and ice sheets. *Reviews of Geophysics*, **15**, 235, doi:10.1029/rg015i002p00235.

Colleoni, F., S. Masina, A. Cherchi, A. Navarra, C. Ritz, V. Peyaud, and B. Otto-Bliesner, 2014: Modeling northern hemisphere ice-sheet distribution during mis 5 and mis 7 glacial inceptions. *Climate of the Past*, **10**, 269–291, doi:10.5194/cp-10-269-2014.

Cornford, S. L., D. F. Martin, D. T. Graves, D. F. Ranken, A. M. Le Brocq, R. M. Gladstone, A. J. Payne, E. G. Ng, and W. H. Lipscomb, 2013: Adaptive mesh, finite volume modeling of marine ice sheets. *Journal of Computational Physics*, **232**, 529–549, doi:10.1016/j.jcp.2012.08.037.

Coulon, V., K. Bulthuis, P. L. Whitehouse, S. Sun, K. Haubner, L. Zipf, and F. Pattyn, 2021: Contrasting response of west and east antarctic ice

sheets to glacial isostatic adjustment. *Journal of Geophysical Research: Earth Surface*, **126**, doi:10.1029/2020jf006003.

Cuffey, K. M. and W. S. B. Paterson, 2010: *The Physics of Glaciers*. Elsevier Science Techn.
URL https://www.ebook.de/de/product/15174996/kurt_m_cuffey_w_s_b_paterson_the_physics_of_glaciers.html

Dahl-Jensen, D., 1989: Steady thermomechanical flow along two-dimensional flow lines in large grounded ice sheets. *Journal of Geophysical Research: Solid Earth*, **94**, 10355–10362, doi:10.1029/jb094ib08p10355.

Dansgaard, W. and S. J. Johnsen, 1969: A flow model and a time scale for the ice core from camp century, greenland. *Journal of Glaciology*, **8**, 215–223, doi:10.3189/s0022143000031208.

Dawson, E. J., D. M. Schroeder, W. Chu, E. Mantelli, and H. Seroussi, 2022: Ice mass loss sensitivity to the antarctic ice sheet basal thermal state. *Nature Communications*, **13**, doi:10.1038/s41467-022-32632-2.

de Fleurian, B., M. Morlighem, H. Seroussi, E. Rignot, M. R. van den Broeke, P. K. Munneke, J. Mouginot, P. C. J. P. Smeets, and A. J. Tedstone, 2016: A modeling study of the effect of runoff variability on the effective pressure beneath russell glacier, west greenland. *Journal of Geophysical Research: Earth Surface*, **121**, 1834–1848, doi:10.1002/2016jf003842.

Debnath, L. and D. Bhatta, 2014: *Integral Transforms and Their Applications, Third Edition*. Taylor & Francis.
URL https://books.google.es/books?id=tGpYBQAAQBAJ

DeConto, R. M. and D. Pollard, 2016: Contribution of antarctica to past and future sea-level rise. *Nature*, **531**, 591–597, doi:10.1038/nature17145.

Dee, D. P., S. M. Uppala, A. J. Simmons, P. Berrisford, P. Poli, S. Kobayashi, U. Andrae, M. A. Balmaseda, G. Balsamo, P. Bauer, P. Bechtold, A. C. M. Beljaars, L. van de Berg, J. Bidlot, N. Bormann, C. Delsol, R. Dragani, M. Fuentes, A. J. Geer, L. Haimberger, S. B. Healy, H. Hersbach, E. V. Hólm, L. Isaksen, P. Kållberg, M. Köhler, M. Matricardi, A. P. McNally, B. M. Monge-Sanz, J.-J. Morcrette, B.-K. Park, C. Peubey, P. de Rosnay, C. Tavolato, J.-N. Thépaut, and F. Vitart, 2011: The ERA-interim reanalysis: configuration and performance of the data assimilation system. *Quarterly Journal of the Royal Meteorological Society*, **137**, 553–597, doi:10.1002/qj.828.

Denton, a. H. T., G.H., 1981: The last great ice sheets, 484.

Donat-Magnin, M., N. C. Jourdain, P. Spence, J. Le Sommer, H. Gallée, and G. Durand, 2017: Ice-shelf melt response to changing winds and glacier dynamics in the amundsen sea sector, antarctica. *Journal of Geophysical Research: Oceans*, **122**, 10206–10224, doi:10.1002/2017jc013059.

Dukowicz, J. K., S. F. Price, and W. H. Lipscomb, 2010: Consistent approximations and boundary conditions for ice-sheet dynamics from a principle of least action. *Journal of Glaciology*, **56**, 480–496, doi:10.3189/002214310792447851.

Dupont, T. K. and R. B. Alley, 2005: Assessment of the importance of ice-shelf buttressing to ice-sheet flow. *Geophysical Research Letters*, **32**, doi:10.1029/2004gl022024.

Dyke, A., J. Andrews, P. Clark, J. England, G. Miller, J. Shaw, and J. Veillette, 2002: The laurentide and innuitian ice sheets during the last glacial maximum. *Quaternary Science Reviews*, **21**, 9–31, doi:10.1016/s0277-3791(01)00095-6.

Dyke, A. S., A. Moore, and L. Robertson, 2003: *Deglaciation of North America*.

Engelhardt, H., N. Humphrey, B. Kamb, and M. Fahnestock, 1990: Physical conditions at the base of a fast moving antarctic ice stream. *Science*, **248**, 57–59, doi:10.1126/science.248.4951.57.

Evans, L., 2010: *Partial Differential Equations*. Graduate studies in mathematics, American Mathematical Society.
URL https://books.google.es/books?id=Xnu0o_EJrCQC

Favier, L., G. Durand, S. L. Cornford, G. H. Gudmundsson, O. Gagliardini, F. Gillet-Chaulet, T. Zwinger, A. J. Payne, and A. M. Le Brocq, 2014: Retreat of pine island glacier controlled by marine ice-sheet instability. *Nature Climate Change*, **4**, 117–121, doi:10.1038/nclimate2094.

Favier, L., N. C. Jourdain, A. Jenkins, N. Merino, G. Durand, O. Gagliardini, F. Gillet-Chaulet, and P. Mathiot, 2019: Assessment of sub-shelf melting parameterisations using the ocean–ice-sheet coupled model NEMO(v3.6)–elmer/ice(v8.3). *Geoscientific Model Development*, **12**, 2255–2283, doi:10.5194/gmd-12-2255-2019.

Feldmann, J. and A. Levermann, 2017: From cyclic ice streaming to heinrich-like events: the grow-and-surge instability in the parallel ice sheet model. *The Cryosphere*, **11**, 1913–1932, doi:10.5194/tc-11-1913-2017.

Fisher, D. A., N. Reeh, and K. Langley, 1985: Objective reconstructions of the late wisconsinan laurentide ice sheet and the significance of deformable beds. *Géographie physique et Quaternaire*, **39**, 229–238, doi:10.7202/032605ar.

Flowers, G. E., 2015: Modelling water flow under glaciers and ice sheets. *Proceedings of the Royal Society A: Mathematical, Physical and Engineering Sciences*, **471**, 20140907, doi:10.1098/rspa.2014.0907.

Flowers, G. E. and G. K. C. Clarke, 2002: A multicomponent coupled model of glacier hydrology 1. theory and synthetic examples. *Journal of Geophysical Research: Solid Earth*, **107**, ECV 9–1–ECV 9–17, doi:10.1029/2001jb001122.

Fowler, A. C., 1992: Modelling ice sheet dynamics. *Geophysical amp; Astrophysical Fluid Dynamics*, **63**, 29–65, doi:10.1080/03091929208228277.

Gagliardini, O. and T. Zwinger, 2008: The ismip-hom benchmark experiments performed using the finite-element code elmer. *The Cryosphere*, **2**, 67–76, doi:10.5194/tc-2-67-2008.

Gladstone, R. M., V. Lee, A. Vieli, and A. J. Payne, 2010: Grounding line migration in an adaptive mesh ice sheet model. *Journal of Geophysical Research: Earth Surface*, **115**, doi:10.1029/2009jf001615.

Gladstone, R. M., R. C. Warner, B. K. Galton-Fenzi, O. Gagliardini, T. Zwinger, and R. Greve, 2017: Marine ice sheet model performance depends on basal sliding physics and sub-shelf melting. *The Cryosphere*, **11**, 319–329, doi:10.5194/tc-11-319-2017.

Glen, J. W., 1955: The creep of polycrystalline ice. *Proceedings of the Royal Society of London. Series A. Mathematical and Physical Sciences*, **228**, 519–538, doi:10.1098/rspa.1955.0066.

Glovinetto, M. B. and H. J. Zwally, 2000: Spatial distribution of net surface accumulation on the antarctic ice sheet. *Annals of Glaciology*, **31**, 171–178, doi:10.3189/172756400781820200.

Goldberg, D. N., 2011: A variationally derived, depth-integrated approximation to a higher-order glaciological flow model. *Journal of Glaciology*, **57**, 157–170, doi:10.3189/002214311795306763.

Goldberg, D. N., P. Heimbach, I. Joughin, and B. Smith, 2015: Committed retreat of smith, pope, and kohler glaciers over the next 30 years inferred by transient model calibration. *The Cryosphere*, **9**, 2429–2446, doi:10.5194/tc-9-2429-2015.

Gomez, N., J. X. Mitrovica, P. Huybers, and P. U. Clark, 2010: Sea level as a stabilizing factor for marine-ice-sheet grounding lines. *Nature Geoscience*, **3**, 850–853, doi:10.1038/ngeo1012.

Gomez, N., D. Pollard, J. X. Mitrovica, P. Huybers, and P. U. Clark, 2012: Evolution of a coupled marine ice sheet–sea level model. *Journal of Geophysical Research: Earth Surface*, **117**, doi:10.1029/2011jf002128.

Gowan, E. J., L. Niu, G. Knorr, and G. Lohmann, 2019: Geology datasets in north america, greenland and surrounding areas for use with ice sheet models. *Earth System Science Data*, **11**, 375–391, doi:10.5194/essd-11-375-2019.

Gowan, E. J., X. Zhang, S. Khosravi, A. Rovere, P. Stocchi, A. L. C. Hughes, R. Gyllencreutz, J. Mangerud, J.-I. Svendsen, and G. Lohmann, 2021: A new global ice sheet reconstruction for the past 80 000 years. *Nature Communications*, **12**, doi:10.1038/s41467-021-21469-w.

Gregoire, L. J., A. J. Payne, and P. J. Valdes, 2012: Deglacial rapid sea level rises caused by ice-sheet saddle collapses. *Nature*, **487**, 219–222, doi:10.1038/nature11257.

Greve, R. and H. Blatter, 2009: *Dynamics of Ice Sheets and Glaciers*. Springer Berlin Heidelberg.

Grosfeld, K., R. Gerdes, and J. Determann, 1997: Thermohaline circulation and interaction between ice shelf cavities and the adjacent open ocean. *Journal of Geophysical Research: Oceans*, **102**, 15595–15610, doi:10.1029/97jc00891.

Gudmundsson, G. H., J. Krug, G. Durand, L. Favier, and O. Gagliardini, 2012: The stability of grounding lines on retrograde slopes. *The Cryosphere*, **6**, 1497–1505, doi:10.5194/tc-6-1497-2012.

Guennebauda, G., B. Jacob, et al., 2010: Eigen v3. http://eigen.tuxfamily.org.

Guvanasen, V. and R. E. Volker, 1983: Experimental investigations of unconfined aquifer pollution from recharge basins. *Water Resources Research*, **19**, 707–717, doi:10.1029/wr019i003p00707.

Harleman, D. R. F. and R. R. Rumer, 1963: Longitudinal and lateral dispersion in an isotropic porous medium. *Journal of Fluid Mechanics*, **16**, 385–394, doi:10.1017/S0022112063000847.

Haseloff, M. and O. V. Sergienko, 2018: The effect of buttressing on grounding line dynamics. *Journal of Glaciology*, **64**, 417–431, doi:10.1017/jog.2018.30.

Heinrich, H., 1988: Origin and consequences of cyclic ice rafting in the northeast Atlantic Ocean during the past 130,000 years. *Quaternary Research*, **29**, 142–152.

Hemming, S. R., 2004: Heinrich events: Massive late Pleistocene detritus layers of the North Atlantic and their global climate imprint. *Rev. Geophys*, **42**, RG1005.

Hewitt, I., 2013: Seasonal changes in ice sheet motion due to melt water lubrication. *Earth and Planetary Science Letters*, **371-372**, 16–25, doi:10.1016/j.epsl.2013.04.022.

Hindmarsh, R. C., 2006: The role of membrane-like stresses in determining the stability and sensitivity of the antarctic ice sheets: back pressure and grounding line motion. *Philosophical Transactions of the Royal Society A: Mathematical, Physical and Engineering Sciences*, **364**, 1733–1767, doi:10.1098/rsta.2006.1797.

Hindmarsh, R. C. and E. le Meur, 2001: Dynamical processes involved in the retreat of marine ice sheets. *Journal of Glaciology*, **47**, 271–282, doi:10.3189/172756501781832269.

Hindmarsh, R. C. A., 1993a: Qualitative dynamics of marine ice sheets. URL https://api.semanticscholar.org/CorpusID:126410372

— 1993b: Qualitative dynamics of marine ice sheets. *Ice in the Climate System*, Springer Berlin Heidelberg, 67–99.

— 1996: Stability of ice rises and uncoupled marine ice sheets. *Annals of Glaciology*, **23**, 105–115, doi:10.3189/s0260305500013318.

Hinkley, D. V., 1969: Inference about the intersection in two-phase regression. *Biometrika*, **56**, 495–504, doi:10.1093/biomet/56.3.495.

— 1971: Inference in two-phase regression. *Journal of the American Statistical Association*, **66**, 736–743, doi:10.1080/01621459.1971.10482337.

Hock, R., 2003: Temperature index melt modelling in mountain areas. *Journal of Hydrology*, **282**, 104–115, doi:10.1016/s0022-1694(03)00257-9.

Hoffman, M. and S. Price, 2014: Feedbacks between coupled subglacial hydrology and glacier dynamics. *Journal of Geophysical Research: Earth Surface*, **119**, 414–436, doi:10.1002/2013jf002943.

Hoffman, M. J., M. Perego, S. F. Price, W. H. Lipscomb, T. Zhang, D. Jacobsen, I. Tezaur, A. G. Salinger, R. Tuminaro, and L. Bertagna, 2018: Mpas-albany land ice (mali): a variable-resolution ice sheet model for earth

system modeling using voronoi grids. *Geoscientific Model Development*, **11**, 3747–3780, doi:10.5194/gmd-11-3747-2018.

Holland, P. R., A. Jenkins, and D. M. Holland, 2008: The response of ice shelf basal melting to variations in ocean temperature. *Journal of Climate*, **21**, 2558–2572, doi:10.1175/2007jcli1909.1.

Hooke, R. L., 2005: *Principles of Glacier Mechanics*. Cambridge University Press.

Hooke, R. L., B. Hanson, N. R. Iverson, P. Jansson, and U. H. Fischer, 1997: Rheology of till beneath storglaciären, sweden. *Journal of Glaciology*, **43**, 172–179, doi:10.3189/s0022143000002938.

Hughes, T., G. H. Denton, B. G. Anderson, D. H. Schilling, J. L. Fastook, and C. Lingle, 1980: The last great ice sheets: A global view. *in The Last Great Ice Sheets*.

Hulbe, C., D. MacAyeal, G. Denton, J. Kleman, and T. Lowell, 2004: Catastrophic ice shelf breakup as the source of Heinrich event icebergs. *Paleoceanography*, **19**.

Hulbe, C. L., 1997: An ice shelf mechanism for heinrich layer production. *Paleoceanography*, **12**, 711–717, doi:10.1029/97pa02014.

Hutter, K., 1983: *Theoretical glaciology: material science of ice and the mechanics of glaciers and ice sheets*. Springer.

Huybrechts, P. and T. Payne, 1996: The eismint benchmarks for testing ice-sheet models. *Annals of Glaciology*, **23**, 1–12, doi:10.3189/S0260305500013197.

Iverson, N. R., B. Hanson, R. L. Hooke, and P. Jansson, 1995: Flow mechanism of glaciers on soft beds. *Science*, **267**, 80–81, doi:10.1126/science.267.5194.80.

Jamieson, S. S. R., A. Vieli, S. J. Livingstone, C. Cofaigh, C. Stokes, C.-D. Hillenbrand, and J. A. Dowdeswell, 2012: Ice-stream stability on a reverse bed slope. *Nature Geoscience*, **5**, 799–802, doi:10.1038/ngeo1600.

Jenkins, A., D. Shoosmith, P. Dutrieux, S. Jacobs, T. W. Kim, S. H. Lee, H. K. Ha, and S. Stammerjohn, 2018: West antarctic ice sheet retreat in the amundsen sea driven by decadal oceanic variability. *Nature Geoscience*, **11**, 733–738, doi:10.1038/s41561-018-0207-4.

Jenssen, D., 1977: A three-dimensional polar ice-sheet model. *Journal of Glaciology*, **18**, 373–389, doi:10.3189/s0022143000021067.

Johnson, R. and S.-E. Lauritzen, 1995: Hudson bay-hudson strait jökulhlaups and heinrich events: a hypothesis. *Palaeogeography, Palaeoclimatology, Palaeoecology*, **117**, 123–137, doi:https://doi.org/10.1016/0031-0182(94)00120-W.
URL https://www.sciencedirect.com/science/article/pii/003101829400120W

Jones, M., 1994: Mechanical principles of sediment deformation. *The Geological Deformation of Sediments*, Springer Netherlands, 37–71.

Joughin, I., 2015: Measures greenland ice sheet velocity map from insar data, version 2.

Joughin, I., D. R. MacAyeal, and S. Tulaczyk, 2004: Basal shear stress of the ross ice streams from control method inversions. *Journal of Geophysical Research: Solid Earth*, **109**, n/a–n/a, doi:10.1029/2003jb002960.

Joughin, I., B. E. Smith, and D. M. Holland, 2010: Sensitivity of 21st century sea level to ocean-induced thinning of pine island glacier, antarctica. *Geophysical Research Letters*, **37**, doi:10.1029/2010gl044819.

Joughin, I., B. E. Smith, and B. Medley, 2014: Marine ice sheet collapse potentially under way for the thwaites glacier basin, west antarctica. *Science*, **344**, 735–738, doi:10.1126/science.1249055.

Joughin, I., B. E. Smith, and C. G. Schoof, 2019: Regularized coulomb friction laws for ice sheet sliding: Application to pine island glacier, antarctica. *Geophysical Research Letters*, **46**, 4764–4771, doi:10.1029/2019gl082526.

Joughin, I., S. Tulaczyk, R. Bindschadler, and S. F. Price, 2002: Changes in west antarctic ice stream velocities: Observation and analysis. *Journal of Geophysical Research: Solid Earth*, **107**, EPM 3–1–EPM 3–22, doi:10.1029/2001jb001029.

Karig, D. and J. Morgan, 1994: Tectonic deformation: stress paths and strain histories. *The Geological Deformation of Sediments*, Springer Netherlands, 167–204.

Kendall, R. A., J. X. Mitrovica, and G. A. Milne, 2005: On post-glacial sea level - ii. numerical formulation and comparative results on spherically symmetric models. *Geophysical Journal International*, **161**, 679–706, doi:10.1111/j.1365-246x.2005.02553.x.

Kirchner, N., K. Hutter, M. Jakobsson, and R. Gyllencreutz, 2011: Capabilities and limitations of numerical ice sheet models: a discussion for

earth-scientists and modelers. *Quaternary Science Reviews*, **30**, 3691–3704, doi:10.1016/j.quascirev.2011.09.012.

Kleman, J., C. Hättestrand, I. Borgström, and A. Stroeven, 1997: Fennoscandian palaeoglaciology reconstructed using a glacial geological inversion model. *Journal of Glaciology*, **43**, 283–299, doi:10.1017/s0022143000003233.

Koziol, C. P. and N. Arnold, 2017: Incorporating modelled subglacial hydrology into inversions for basal drag. *The Cryosphere*, **11**, 2783–2797, doi:10.5194/tc-11-2783-2017.

Kummer, E., 1836: Über die hypergeometrische reihe ... . *Journal für die reine und angewandte Mathematik*, **15**, 39–83.
URL http://eudml.org/doc/146951

Lai, S.-H. and J. Jurinak, 1971: Numerical approximation of cation exchange in miscible displacement through soil columns. *Soil Science Society of America Journal*, **35**, 894–899.

Larour, E., H. Seroussi, M. Morlighem, and E. Rignot, 2012: Continental scale, high order, high spatial resolution, ice sheet modeling using the ice sheet system model (issm). *Journal of Geophysical Research: Earth Surface*, **117**, doi:10.1029/2011jf002140.

Lawley, C. J. M., P. Giddy, L. Katz, N. Chu, A. Francis, J. Carvajal, M. Pinheiro, K. Tirona, A. Dettman, H. Chen, and F. Aucoin, 2024: *Canada geological map compilation*.

Le clec'h, S., A. Quiquet, S. Charbit, C. Dumas, M. Kageyama, and C. Ritz, 2019: A rapidly converging initialisation method to simulate the present-day greenland ice sheet using the grisli ice sheet model (version 1.3). *Geoscientific Model Development*, **12**, 2481–2499, doi:10.5194/gmd-12-2481-2019.

Leguy, G. R., X. S. Asay-Davis, and W. H. Lipscomb, 2014: Parameterization of basal friction near grounding lines in a one-dimensional ice sheet model. *The Cryosphere*, **8**, 1239–1259, doi:10.5194/tc-8-1239-2014.

Lie, S. and G. Scheffers, 1893: *Vorlesungen über continuierliche Gruppen mit geometrischen und anderen Anwendungen / Sophus Lie bearbeitet und herausgegeben von Georg Scheffers.*. B.G. Teubner,.

Lingle, C. S. and T. J. Brown, 1987a: A subglacial aquifer bed model and water pressure dependent basal sliding relationship for a west antarctic ice

stream. *Dynamics of the West Antarctic Ice Sheet*, Springer Netherlands, 249–285.

— 1987b: A subglacial aquifer bed model andwater pressure-dependent basal sliding relationship for a westantarctic ice stream, in: Dynamics of the west antarctic icesheet. *edited by: der Veen, C. J. V. and Oerlemans, J., D. Rei-del, Dodrecht, the Netherlands,*.

Lingle, C. S. and J. A. Clark, 1985: A numerical model of interactions between a marine ice sheet and the solid earth: Application to a west antarctic ice stream. *Journal of Geophysical Research: Oceans*, **90**, 1100–1114, doi:10.1029/jc090ic01p01100.

Lipscomb, W. H., S. F. Price, M. J. Hoffman, G. R. Leguy, A. R. Bennett, S. L. Bradley, K. J. Evans, J. G. Fyke, J. H. Kennedy, M. Perego, D. M. Ranken, W. J. Sacks, A. G. Salinger, L. J. Vargo, and P. H. Worley, 2019: Description and evaluation of the community ice sheet model (CISM) v2.1. *Geoscientific Model Development*, **12**, 387–424, doi:10.5194/gmd-12-387-2019.

Lliboutry, L., 1963: Regime thennique et deformation de la base des calottes polaires. *Annales de Geophysique*, volume 19, 149–50.

Ma, Y., O. Gagliardini, C. Ritz, F. Gillet-Chaulet, G. Durand, and M. Montagnat, 2010: Enhancement factors for grounded ice and ice shelves inferred from an anisotropic ice-flow model. *Journal of Glaciology*, **56**, 805–812, doi:10.3189/002214310794457209.

MacAyeal, D., 1989: Large-scale ice flow over a viscous basal sediment- Theory and application to ice stream B, Antarctica. *Journal of Geophysical Research*, **94**, 4071–4087.

MacAyeal, D. R., 1993a: Binge/purge oscillations of the Laurentide ice sheet as a cause of the North Atlantic's Heinrich events. *Paleoceanography*, **8**, 775–784.

— 1993b: A low-order model of the Heinrich event cycle. *Paleoceanography*, **8**, 767–773.

MacAyeal, D. R. and V. Barcilon, 1988: Ice-shelf response to ice-stream discharge fluctuations: I. unconfined ice tongues. *Journal of Glaciology*, **34**, 121–127, doi:10.3189/s002214300000914x.

MacAyeal, D. R., R. A. Bindschadler, and T. A. Scambos, 1995: Basal friction of ice stream e, west antarctica. *Journal of Glaciology*, **41**, 247–262, doi:10.3189/s0022143000016154.

MacAyeal, D. R., T. A. Scambos, C. L. Hulbe, and M. A. Fahnestock, 2003: Catastrophic ice-shelf break-up by an ice-shelf-fragment-capsize mechanism. *Journal of Glaciology*, **49**, 22–36, doi:10.3189/172756503781830863.

MacAyeal, D. R. and O. V. Sergienko, 2013: The flexural dynamics of melting ice shelves. *Annals of Glaciology*, **54**, 1–10, doi:10.3189/2013aog63a256.

Mahaffy, M. W., 1976: A three-dimensional numerical model of ice sheets: Tests on the barnes ice cap, northwest territories. *Journal of Geophysical Research*, **81**, 1059–1066, doi:10.1029/jc081i006p01059.

Marcott, S., P. Clark, L. Padman, G. Klinkhammer, S. Springer, Z. Liu, B. Otto-Bliesner, A. Carlson, A. Ungerer, J. Padman, et al., 2011: Ice-shelf collapse from subsurface warming as a trigger for heinrich events. *Proceedings of the National Academy of Sciences*, **108**, 13415–13419.

Margold, M., C. R. Stokes, and C. D. Clark, 2015: Ice streams in the laurentide ice sheet: Identification, characteristics and comparison to modern ice sheets. *Earth-Science Reviews*, **143**, 117–146, doi:10.1016/j.earscirev.2015.01.011.

Margold, M., C. R. Stokes, C. D. Clark, and J. Kleman, 2014: Ice streams in the laurentide ice sheet: a new mapping inventory. *Journal of Maps*, **11**, 380–395, doi:10.1080/17445647.2014.912036.

Marino, M. A., 1974: Distribution of contaminants in porous media flow. *Water Resources Research*, **10**, 1013–1018, doi:10.1029/wr010i005p01013.

Maris, M. N. A., S. R. M. Ligtenberg, M. Crucifix, B. de Boer, and J. Oerlemans, 2014: Modelling the evolution of the antarctic ice sheet since the last interglacial. doi:10.5194/tcd-8-85-2014.

Marshall, S. and G. Clarke, 1997: A continuum mixture model of ice stream thermomechanics in the laurentide ice sheet 2. application to the hudson strait ice stream. *Journal of Geophysical Research*, **102**, 20615–20.

Marshall, S. J., G. K. C. Clarke, A. S. Dyke, and D. A. Fisher, 1996a: Geologic and topographic controls on fast flow in the laurentide and cordilleran ice sheets. *Journal of Geophysical Research: Solid Earth*, **101**, 17827–17839, doi:10.1029/96jb01180.

Marshall, T. J., J. W. Holmes, and C. W. Rose, 1996b: *Soil Physics*. Cambridge University Press.

Martin, M. A., R. Winkelmann, M. Haseloff, T. Albrecht, E. Bueler, C. Khroulev, and A. Levermann, 2011: The potsdam parallel ice sheet

model (PISM-PIK) – part 2: Dynamic equilibrium simulation of the antarctic ice sheet. *The Cryosphere*, **5**, 727–740, doi:10.5194/tc-5-727-2011.

McGrath, D., K. Steffen, H. Rajaram, T. Scambos, W. Abdalati, and E. Rignot, 2012: Basal crevasses on the larsen c ice shelf, antarctica: Implications for meltwater ponding and hydrofracture. *Geophysical Research Letters*, **39**, doi:10.1029/2012gl052413.

McLachlan, N., 2014: *Laplace Transforms and Their Applications to Differential Equations*. Dover Books on Mathematics, Dover Publications.
URL https://books.google.es/books?id=TDFeBAAAQBAJ

Medley, B., T. A. Neumann, H. J. Zwally, B. E. Smith, and C. M. Stevens, 2022: Simulations of firn processes over the greenland and antarctic ice sheets: 1980–2021. *The Cryosphere*, **16**, 3971–4011, doi:10.5194/tc-16-3971-2022.

Merks, R., A. Hoekstra, and P. Sloot, 2002: The moment propagation method for advection–diffusion in the lattice boltzmann method: Validation and péclet number limits. *Journal of Computational Physics*, **183**, 563–576, doi:10.1006/jcph.2002.7209.

Meur, E. L. and P. Huybrechts, 1996: A comparison of different ways of dealing with isostasy: examples from modelling the antarctic ice sheet during the last glacial cycle. *Annals of Glaciology*, **23**, 309–317, doi:10.3189/s0260305500013586.

Meyer, C. and B. Minchew, 2018: Temperate ice in the shear margins of the antarctic ice sheet: Controlling processes and preliminary locations. *Earth and Planetary Science Letters*, **498**, 17–26, doi:10.1016/j.epsl.2018.06.028.

Meyer, C. R., A. A. Robel, and A. W. Rempel, 2019: Frozen fringe explains sediment freeze-on during heinrich events. *Earth and Planetary Science Letters*, **524**, 115725, doi:10.1016/j.epsl.2019.115725.

Minchew, B. M., C. R. Meyer, A. A. Robel, G. H. Gudmundsson, and M. Simons, 2018: Processes controlling the downstream evolution of ice rheology in glacier shear margins: case study on rutford ice stream, west antarctica. *Journal of Glaciology*, **64**, 583–594, doi:10.1017/jog.2018.47.

Mitrovica, J. X. and G. A. Milne, 2003: On post-glacial sea level: I. general theory. *Geophysical Journal International*, **154**, 253–267, doi:10.1046/j.1365-246x.2003.01942.x.

Moreno-Parada, D., J. Alvarez-Solas, J. Blasco, M. Montoya, and A. Robinson, 2023a: Simulating the laurentide ice sheet of the last glacial maximum.

The Cryosphere, **17**, 2139–2156, doi:10.5194/tc-17-2139-2023.

Moreno-Parada, D., A. Robinson, M. Montoya, and J. Alvarez-Solas, 2022: On the periodicity of free oscillations for a finite ice column. doi:10.5194/tc-2022-97.

— 2023b: Nix ice sheet model v1.0.0. doi:10.5281/ZENODO.10228874.

Morlighem, M., E. Rignot, T. Binder, D. Blankenship, R. Drews, G. Eagles, O. Eisen, F. Ferraccioli, R. Forsberg, P. Fretwell, V. Goel, J. S. Greenbaum, H. Gudmundsson, J. Guo, V. Helm, C. Hofstede, I. Howat, A. Humbert, W. Jokat, N. B. Karlsson, W. S. Lee, K. Matsuoka, R. Millan, J. Mouginot, J. Paden, F. Pattyn, J. Roberts, S. Rosier, A. Ruppel, H. Seroussi, E. C. Smith, D. Steinhage, B. Sun, M. R. v. d. Broeke, T. D. v. Ommen, M. v. Wessem, and D. A. Young, 2019: Deep glacial troughs and stabilizing ridges unveiled beneath the margins of the antarctic ice sheet. *Nature Geoscience*, **13**, 132–137, doi:10.1038/s41561-019-0510-8.

Morlighem, M., E. Rignot, H. Seroussi, E. Larour, H. Ben Dhia, and D. Aubry, 2010: Spatial patterns of basal drag inferred using control methods from a full-stokes and simpler models for pine island glacier, west antarctica. *Geophysical Research Letters*, **37**, doi:10.1029/2010gl043853.

— 2011: A mass conservation approach for mapping glacier ice thickness. *Geophysical Research Letters*, **38**, n/a–n/a, doi:10.1029/2011gl048659.

Morlighem, M., H. Seroussi, E. Larour, and E. Rignot, 2013: Inversion of basal friction in antarctica using exact and incomplete adjoints of a higher-order model. *Journal of Geophysical Research: Earth Surface*, **118**, 1746–1753, doi:10.1002/jgrf.20125.

Moros, M., A. Kuijpers, I. Snowball, S. Lassen, D. Bäckström, F. Gingele, and J. McManus, 2002: Were glacial iceberg surges in the north atlantic triggered by climatic warming? *Marine Geology*, **192**, 393–417, doi:https://doi.org/10.1016/S0025-3227(02)00592-3.
URL https://www.sciencedirect.com/science/article/pii/S0025322702005923

Naafs, B., J. Hefter, and R. Stein, 2013: Millennial-scale ice rafting events and hudson strait heinrich(-like) events during the late pliocene and pleistocene: a review. *Quaternary Science Reviews*, **80**, 1–28, doi:10.1016/j.quascirev.2013.08.014.

Nickolls, J., I. Buck, M. Garland, and K. Skadron, 2008: Scalable parallel programming with cuda: Is cuda the parallel programming model

that application developers have been waiting for? *Queue*, **6**, 40–53, doi:10.1145/1365490.1365500.

Nowicki, S. and D. Wingham, 2008: Conditions for a steady ice sheet–ice shelf junction. *Earth and Planetary Science Letters*, **265**, 246–255, doi:10.1016/j.epsl.2007.10.018.

Noël, B., J. T. M. Lenaerts, W. H. Lipscomb, K. Thayer-Calder, and M. R. van den Broeke, 2022: Peak refreezing in the greenland firn layer under future warming scenarios. *Nature Communications*, **13**, doi:10.1038/s41467-022-34524-x.

Ogata, A., 1970: Theory of dispersion in a granular medium.

Ogata, A. and R. B. Banks, 1961: A solution of the differential equation of longitudinal dispersion in porous media.

Ottesen, D., J. Dowdeswell, and L. Rise, 2005: Submarine landforms and the reconstruction of fast-flowing ice streams within a large quaternary ice sheet: The 2500-km-long norwegian-svalbard margin (57°–80°n). *Geological Society of America Bulletin*, **117**, 1033, doi:10.1130/b25577.1.

Paterson, W. S. B., 1972: Laurentide ice sheet: Estimated volumes during late wisconsin. *Reviews of Geophysics*, **10**, 885, doi:10.1029/rg010i004p00885.

Pattyn, F., 1996: Numerical modelling of a fast-flowing outlet glacier: experiments with different basal conditions. *Annals of Glaciology*, **23**, 237–246, doi:10.3189/s0260305500013495.

— 2003: A new three-dimensional higher-order thermomechanical ice sheet model: Basic sensitivity, ice stream development, and ice flow across subglacial lakes. *Journal of Geophysical Research*, **108**, doi:10.1029/2002jb002329.

— 2017: Sea-level response to melting of antarctic ice shelves on multi-centennial timescales with the fast elementary thermomechanical ice sheet model (f.etish v1.0). *The Cryosphere*, **11**, 1851–1878, doi:10.5194/tc-11-1851-2017.

Pattyn, F., A. Huyghe, S. D. Brabander, and B. D. Smedt, 2006: Role of transition zones in marine ice sheet dynamics. *Journal of Geophysical Research*, **111**, doi:10.1029/2005jf000394.

Pattyn, F. and M. Morlighem, 2020: The uncertain future of the antarctic ice sheet. *Science*, **367**, 1331–1335, doi:10.1126/science.aaz5487.

Pattyn, F., L. Perichon, G. Durand, L. Favier, O. Gagliardini, R. C. Hindmarsh, T. Zwinger, T. Albrecht, S. Cornford, D. Docquier, J. J. Fürst,

D. Goldberg, G. H. Gudmundsson, A. Humbert, M. Hütten, P. Huybrechts, G. Jouvet, T. Kleiner, E. Larour, D. Martin, M. Morlighem, A. J. Payne, D. Pollard, M. Rückamp, O. Rybak, H. Seroussi, M. Thoma, and N. Wilkens, 2013: Grounding-line migration in plan-view marine ice-sheet models: results of the ice2sea mismip3d intercomparison. *Journal of Glaciology*, **59**, 410–422, doi:10.3189/2013jog12j129.

Pattyn, F., C. Schoof, L. Perichon, R. C. A. Hindmarsh, E. Bueler, B. de Fleurian, G. Durand, O. Gagliardini, R. Gladstone, D. Goldberg, G. H. Gudmundsson, P. Huybrechts, V. Lee, F. M. Nick, A. J. Payne, D. Pollard, O. Rybak, F. Saito, and A. Vieli, 2012: Results of the marine ice sheet model intercomparison project, MISMIP. *The Cryosphere*, **6**, 573–588, doi:10.5194/tc-6-573-2012.

Payne, A., 1995a: Limit cycles in the basal thermal regime of ice sheets. *JOURNAL OF GEOPHYSICAL RESEARCH-ALL SERIES-*, **100**, 4249–4249.

Payne, A., A. Vieli, A. Shepherd, D. Wingham, and E. Rignot, 2004: Recent dramatic thinning of largest west-antarctic ice stream triggered by oceans. *Geophysical research letters.*, **31**, L23401.

Payne, A. J., 1995b: Limit cycles in the basal thermal regime of ice sheets. *Journal of Geophysical Research: Solid Earth*, **100**, 4249–4263, doi:10.1029/94jb02778.

Pelt, W. J. V. and J. Oerlemans, 2012: Numerical simulations of cyclic behaviour in the parallel ice sheet model (PISM). *Journal of Glaciology*, **58**, 347–360, doi:10.3189/2012jog11j217.

Peltier, W., 2004: Global glacial isostasy and the surface of the ice-age Earth-The ICE-5 G(VM 2) model and GRACE. *Ann. Rev. Earth and Plan. Sci.*, **32**, 111–149.

Peltier, W. R., 1994: Ice age paleotopography. *Science*, **265**, 195–201, doi:10.1126/science.265.5169.195.

Perego, M., S. Price, and G. Stadler, 2014: Optimal initial conditions for coupling ice sheet models to earth system models. *Journal of Geophysical Research: Earth Surface*, **119**, 1894–1917, doi:10.1002/2014jf003181.

Perol, T. and J. R. Rice, 2011: Control of the width of west antarctic ice streams by internal melting in the ice sheet near the margins. *AGU Fall Meeting Abstracts*, volume 2011, C11B–0677.

— 2015: Shear heating and weakening of the margins of west antarctic ice streams. *Geophysical Research Letters*, **42**, 3406–3413, doi:10.1002/2015gl063638.

Peyaud, V., C. Ritz, and G. Krinner, 2007: Modelling the early weichselian eurasian ice sheets: role of ice shelves and influence of ice-dammed lakes. *Climate of the Past*, **3**, 375–386, doi:10.5194/cp-3-375-2007.

Pollard, D. and R. M. DeConto, 2012a: Description of a hybrid ice sheet-shelf model, and application to antarctica. *Geoscientific Model Development*, **5**, 1273–1295, doi:10.5194/gmd-5-1273-2012.

— 2012b: A simple inverse method for the distribution of basal sliding coefficients under ice sheets, applied to antarctica. *The Cryosphere Discussions*, **6**, 1405–1444, doi:10.5194/tcd-6-1405-2012.
URL http://www.the-cryosphere-discuss.net/6/1405/2012/

Pralong, M. R. and H. G. Gudmundsson, 2011: Bayesian estimation of basal conditions on rutford ice stream, west antarctica, from surface data. *Journal of Glaciology*, **57**, 315–324, doi:10.3189/002214311796406004.

Quiquet, A., C. Dumas, C. Ritz, V. Peyaud, and D. M. Roche, 2018: The GRISLI ice sheet model (version 2.0): calibration and validation for multi-millennial changes of the antarctic ice sheet. *Geoscientific Model Development*, **11**, 5003–5025, doi:10.5194/gmd-11-5003-2018.

Ramsay, W., 1931: Changes of sea-level resulting from the increase and decrease of glaciation. *Fennia, Geographical Society of Finland*, **52**, 1–62.

Raymond, C. F., 1983: Deformation in the vicinity of ice divides. *Journal of Glaciology*, **29**, 357–373, doi:10.3189/S0022143000030288.

Reeh, N., 1991: Parameterization of melt rate and surface temperature in the greenland ice sheet. *Polarforschung*, **59**, 113–128.

Rew, R. and G. Davis, 1990: Netcdf: an interface for scientific data access. *IEEE Computer Graphics and Applications*, **10**, 76–82, doi:10.1109/38.56302.

Rezvanbehbahani, S., C. J. van der Veen, and L. A. Stearns, 2019: An improved analytical solution for the temperature profile of ice sheets. *Journal of Geophysical Research: Earth Surface*, **124**, 271–286, doi:10.1029/2018jf004774.

Robel, A. A., E. DeGiuli, C. Schoof, and E. Tziperman, 2013: Dynamics of ice stream temporal variability: Modes, scales, and hysteresis. *Journal of Geophysical Research: Earth Surface*, **118**, 925–936, doi:10.1002/jgrf.20072.

Robel, A. A., C. Schoof, and E. Tziperman, 2014: Rapid grounding line migration induced by internal ice stream variability. *Journal of Geophysical Research: Earth Surface*, **119**, 2430–2447, doi:10.1002/2014jf003251.

Robel, A. A., H. Seroussi, and G. H. Roe, 2019: Marine ice sheet instability amplifies and skews uncertainty in projections of future sea-level rise. *Proceedings of the National Academy of Sciences*, **116**, 14887–14892, doi:10.1073/pnas.1904822116.

Roberts, W. H. G., A. J. Payne, and P. J. Valdes, 2016: The role of basal hydrology in the surging of the laurentide ice sheet. *Climate of the Past*, **12**, 1601–1617, doi:10.5194/cp-12-1601-2016.
URL https://cp.copernicus.org/articles/12/1601/2016/

Roberts, W. H. G., P. J. Valdes, and A. J. Payne, 2014: Topography's crucial role in heinrich events. *Proceedings of the National Academy of Sciences*, **111**, 16688–16693, doi:10.1073/pnas.1414882111.

Robin, G. d. Q., 1955: Ice movement and temperature distribution in glaciers and ice sheets. *Journal of Glaciology*, **2**, 523–532, doi:10.3189/002214355793702028.

Robinson, A., J. Alvarez-Solas, M. Montoya, H. Goelzer, R. Greve, and C. Ritz, 2020: Description and validation of the ice-sheet model yelmo (version 1.0). *Geoscientific Model Development*, **13**, 2805–2823, doi:10.5194/gmd-13-2805-2020.

Robinson, A., R. Calov, and A. Ganopolski, 2010: An efficient regional energy-moisture balance model for simulation of the greenland ice sheet response to climate change. *The Cryosphere*, **4**, 129–144, doi:10.5194/tc-4-129-2010.

— 2012: Multistability and critical thresholds of the greenland ice sheet. *Nature Climate Change*, **2**, 429–432, doi:10.1038/nclimate1449.

Robinson, A., D. Goldberg, and W. H. Lipscomb, 2022: A comparison of the stability and performance of depth-integrated ice-dynamics solvers. *The Cryosphere*, **16**, 689–709, doi:10.5194/tc-16-689-2022.

Scambos, T. A., C. Hulbe, M. Fahnestock, and J. Bohlander, 2000: The link between climate warming and break-up of ice shelves in the antarctic peninsula. *Journal of Glaciology*, **46**, 516–530, doi:10.3189/172756500781833043.

Schaffer, J., R. Timmermann, J. E. Arndt, S. S. Kristensen, C. Mayer, M. Morlighem, and D. Steinhage, 2016: A global, high-resolution data set

of ice sheet topography, cavity geometry, and ocean bathymetry. *Earth System Science Data*, **8**, 543–557, doi:10.5194/essd-8-543-2016.

Schoof, C., 2005: The effect of cavitation on glacier sliding. *Proceedings of the Royal Society A: Mathematical, Physical and Engineering Sciences*, **461**, 609–627, doi:10.1098/rspa.2004.1350.

— 2006a: A variational approach to ice stream flow. *Journal of Fluid Mechanics*, **556**, 227, doi:10.1017/s0022112006009591.

— 2006b: Variational methods for glacier flow over plastic till. *Journal of Fluid Mechanics*, **555**, 299, doi:10.1017/s0022112006009104.

— 2007a: Ice sheet grounding line dynamics: Steady states, stability, and hysteresis. *J. Geophys. Res*, **112**.

— 2007b: Marine ice-sheet dynamics. part 1. the case of rapid sliding. *Journal of Fluid Mechanics*, **573**, 27–55, doi:10.1017/s0022112006003570.

— 2010: Ice-sheet acceleration driven by melt supply variability. *Nature*, **468**, 803–806, doi:10.1038/nature09618.

— 2011: Marine ice sheet dynamics. part 2. a stokes flow contact problem. *Journal of Fluid Mechanics*, **679**, 122–155, doi:10.1017/jfm.2011.129.

Schoof, C. and R. C. A. Hindmarsh, 2010: Thin-film flows with wall slip: An asymptotic analysis of higher order glacier flow models. *The Quarterly Journal of Mechanics and Applied Mathematics*, **63**, 73–114, doi:10.1093/qjmam/hbp025.

Schubert, G. and D. A. Yuen, 1982: Initiation of ice ages by creep instability and surging of the east antarctic ice sheet. *Nature*, **296**, 127–130, doi:10.1038/296127a0.

Scott, R. F., 1963: *Principles of Soil Mechanics*. Addison-Wesley Educational Publishers Inc.

Selvadurai, A. P. S., 2004: On the advective-diffusive transport in porous media in the presence of time-dependent velocities. *Geophysical Research Letters*, **31**, doi:10.1029/2004gl019646.

Sergienko, O. V., D. N. Goldberg, and C. M. Little, 2013: Alternative ice shelf equilibria determined by ocean environment. *Journal of Geophysical Research: Earth Surface*, **118**, 970–981, doi:10.1002/jgrf.20054.

Seroussi, H., M. Morlighem, E. Larour, E. Rignot, and A. Khazendar, 2014: Hydrostatic grounding line parameterization in ice sheet models. *The Cryosphere*, **8**, 2075–2087, doi:10.5194/tc-8-2075-2014.

Shapiro, N. M. and M. H. Ritzwoller, 2004: Inferring surface heat flux distributions guided by a global seismic model: particular application to antarctica. *Earth and Planetary Science Letters*, **223**, 213–224, doi:10.1016/j.epsl.2004.04.011.

Shepherd, A. and D. Wingham, 2007: Recent sea-level contributions of the antarctic and greenland ice sheets. *Science*, **315**, 1529–1532, doi:10.1126/science.1136776.

Siegert, M. J., 2009: *Binge-Purge Cycles of Ice Sheet Dynamics*, Springer Netherlands. 94–96.

Singh, A. K. and B. Bhadauria, 2009: Finite difference formulae for unequal sub-intervals using lagrange's interpolation formula. *Journal of Math. Analysis*, **3**, 815–827.

Solow, A. R., 1987: Testing for climate change: An application of the two-phase regression model. *Journal of Climate and Applied Meteorology*, **26**, 1401–1405, doi:10.1175/1520-0450(1987)026¡1401:tfccaa¿2.0.co;2.

Spada, G. and D. Melini, 2019: Selenamp;lt;supamp;gt;4amp;lt;/supamp;gt; (selen version 4.0): a fortran program for solving the gravitationally and topographically self-consistent sea-level equation in glacial isostatic adjustment modeling. *Geoscientific Model Development*, **12**, 5055–5075, doi:10.5194/gmd-12-5055-2019.

Spikes, V. B., G. S. Hamilton, S. A. Arcone, S. Kaspari, and P. A. Mayewski, 2004: Variability in accumulation rates from gpr profiling on the west antarctic plateau. *Annals of Glaciology*, **39**, 238–244, doi:10.3189/172756404781814393.

Stearns, L. A. and C. J. van der Veen, 2018: Friction at the bed does not control fast glacier flow. *Science*, **361**, 273–277, doi:10.1126/science.aat2217.

Stevens, C. M., V. Verjans, J. M. D. Lundin, E. C. Kahle, A. N. Horlings, B. I. Horlings, and E. D. Waddington, 2020: The community firn model (CFM) v1.0. *Geoscientific Model Development*, **13**, 4355–4377, doi:10.5194/gmd-13-4355-2020.

Stokes, C., 2017: Deglaciation of the laurentide ice sheet from the last glacial maximum. *Cuadernos de Investigación Geográfica*, **43**, 377, doi:10.18172/cig.3237.

Stokes, C. R. and C. D. Clark, 1999: Geomorphological criteria for identifying pleistocene ice streams. *Annals of Glaciology*, **28**, 67–74, doi:10.3189/172756499781821625.

Stokes, C. R., M. Margold, C. D. Clark, and L. Tarasov, 2016: Ice stream activity scaled to ice sheet volume during laurentide ice sheet deglaciation. *Nature*, **530**, 322–326, doi:10.1038/nature16947.

Stokes, C. R. and L. Tarasov, 2010: Ice streaming in the laurentide ice sheet: A first comparison between data-calibrated numerical model output and geological evidence. *Geophysical Research Letters*, **37**, n/a–n/a, doi:10.1029/2009gl040990.

Sturm, M., J. Holmgren, M. König, and K. Morris, 1997: The thermal conductivity of seasonal snow. *Journal of Glaciology*, **43**, 26–41, doi:10.3189/s0022143000002781.

Sturm, M., D. K. Perovich, and J. Holmgren, 2002: Thermal conductivity and heat transfer through the snow on the ice of the beaufort sea. *Journal of Geophysical Research: Oceans*, **107**, doi:10.1029/2000jc000409.

Suckale, J., J. D. Platt, T. Perol, and J. R. Rice, 2014: Deformation-induced melting in the margins of the west antarctic ice streams. *Journal of Geophysical Research: Earth Surface*, **119**, 1004–1025, doi:10.1002/2013jf003008.

Sugden, D. E., 1977: Glacial geomorphology. *Progress in Physical Geography: Earth and Environment*, **1**, 312–318, doi:10.1177/030913337700100205.

Sun, S., F. Pattyn, E. G. Simon, T. Albrecht, S. Cornford, R. Calov, C. Dumas, F. Gillet-Chaulet, H. Goelzer, N. R. Golledge, R. Greve, M. J. Hoffman, A. Humbert, E. Kazmierczak, T. Kleiner, G. R. Leguy, W. H. Lipscomb, D. Martin, M. Morlighem, S. Nowicki, D. Pollard, S. Price, A. Quiquet, H. Seroussi, T. Schlemm, J. Sutter, R. S. W. van de Wal, R. Winkelmann, and T. Zhang, 2020: Antarctic ice sheet response to sudden and sustained ice-shelf collapse (abumip). *Journal of Glaciology*, **66**, 891–904, doi:10.1017/jog.2020.67.

Tabone, I., A. Robinson, J. Alvarez-Solas, and M. Montoya, 2019: Impact of millennial-scale oceanic variability on the greenland ice-sheet evolution throughout the last glacial period. *Climate of the Past*, **15**, 593–609, doi:10.5194/cp-15-593-2019.

Tarasov, L., A. S. Dyke, R. M. Neal, and W. Peltier, 2012: A data-calibrated distribution of deglacial chronologies for the north american ice complex from glaciological modeling. *Earth and Planetary Science Letters*, **315-316**, 30–40, doi:10.1016/j.epsl.2011.09.010.

Tarasov, L. and W. Peltier, 2004: A geophysically constrained large ensemble analysis of the deglacial history of the north american ice-sheet complex. *Quaternary Science Reviews*, **23**, 359–388, doi:10.1016/j.quascirev.2003.08.004.

Taylor, K. E., R. J. Stouffer, and G. A. Meehl, 2012: An overview of CMIP5 and the experiment design. *Bulletin of the American Meteorological Society*, **93**, 485–498, doi:10.1175/bams-d-11-00094.1.

Teschl, G., 2012: *Ordinary Differential Equations and Dynamical Systems*. Graduate studies in mathematics, American Mathematical Society. URL https://books.google.es/books?id=FZ0CAQAAQBAJ

Thomas, R. H., 1979: Ice shelves: A review. *Journal of Glaciology*, **24**, 273–286, doi:10.3189/s0022143000014799.

Thomas, R. H. and C. R. Bentley, 1978: A model for holocene retreat of the west antarctic ice sheet. *Quaternary Research*, **10**, 150–170, doi:10.1016/0033-5894(78)90098-4.

Truffer, M., K. A. Echelmeyer, and W. D. Harrison, 2001: Implications of till deformation on glacier dynamics. *Journal of Glaciology*, **47**, 123–134, doi:10.3189/172756501781832449.

Truffer, M. and M. Fahnestock, 2007: Rethinking ice sheet time scales. *Science*, **315**, 1508–1510, doi:10.1126/science.1140469.

Tulaczyk, S., 1999: Ice sliding over weak, fine-grained tills: Dependence of ice-till interactions on till granulometry. *Glacial Processes Past and Present*, Geological Society of America.

Tulaczyk, S., B. Kamb, R. P. Scherer, and H. F. Engelhardt, 1998: Sedimentary processes at the base of a west antarctic ice stream constraints from textural and compositional properties of subglacial debris. *Journal of Sedimentary Research*, **68**, 487–496, doi:10.2110/jsr.68.487.

Tulaczyk, S., W. B. Kamb, and H. F. Engelhardt, 2000a: Basal mechanics of ice stream b, west antarctica: 1. till mechanics. *Journal of Geophysical Research: Solid Earth*, **105**, 463–481, doi:10.1029/1999jb900329.

— 2000b: Basal mechanics of ice stream b, west antarctica: 2. undrained plastic bed model. *Journal of Geophysical Research: Solid Earth*, **105**, 483–494, doi:10.1029/1999jb900328.

U.S. Geological Survey (USGS), t. B. A. S. B., the National Aeronautics, and S. A. (NASA), 2008: Landsat image mosaic of antarctica.

https://lima.usgs.gov/.
URL https://lima.usgs.gov/

van den Broeke, M., 2005: Strong surface melting preceded collapse of antarctic peninsula ice shelf. *Geophysical Research Letters*, **32**, doi:10.1029/2005gl023247.

van der Wel, N., P. Christoffersen, and M. Bougamont, 2013: The influence of subglacial hydrology on the flow of kamb ice stream, west antarctica. *Journal of Geophysical Research: Earth Surface*, **118**, 97–110, doi:10.1029/2012jf002570.

van Kreveld, S. A., M. Sarnthein, H. Erlenkeuser, P. M. Grootes, S. J. A. Jung, U. Pflaumann, and A. H. L. Voelker, 2000: Foraminifera, sedimentological parameters and sea surface temperature and salinity calculated on core $so82_5 - 2$.

van Wessem, J. M., W. J. van de Berg, B. P. Y. Noël, E. van Meijgaard, C. Amory, G. Birnbaum, C. L. Jakobs, K. Krüger, J. T. M. Lenaerts, S. Lhermitte, S. R. M. Ligtenberg, B. Medley, C. H. Reijmer, K. van Tricht, L. D. Trusel, L. H. van Ulft, B. Wouters, J. Wuite, and M. R. van den Broeke, 2018: Modelling the climate and surface mass balance of polar ice sheets using racmo2 – part 2: Antarctica (1979–2016). *The Cryosphere*, **12**, 1479–1498, doi:10.5194/tc-12-1479-2018.

Vaughan, D. G. and R. Arthern, 2007: Why is it hard to predict the future of ice sheets? *Science*, **315**, 1503–1504, doi:10.1126/science.1141111.

Veen, C. V. D. and I. Whillans, 1989: Force budget: I. theory and numerical methods. *Journal of Glaciology*, **35**, 53–60, doi:10.3189/002214389793701581.

Vieli, A. and A. J. Payne, 2005: Assessing the ability of numerical ice sheet models to simulate grounding line migration. *Journal of Geophysical Research*, **110**, doi:10.1029/2004jf000202.

Weertman, J., 1957: On the sliding of glaciers. *Journal of Glaciology*, **3**, 33–38, doi:10.3189/s0022143000024709.

— 1974: Stability of the junction of an ice sheet and an ice shelf. *Journal of Glaciology*, **13**, 3–11, doi:10.3189/s0022143000023327.

Werder, M. A., I. J. Hewitt, C. G. Schoof, and G. E. Flowers, 2013: Modeling channelized and distributed subglacial drainage in two dimensions. *Journal of Geophysical Research: Earth Surface*, **118**, 2140–2158, doi:10.1002/jgrf.20146.

Whillans, I. M. and C. J. van der Veen, 1997: The role of lateral drag in the dynamics of ice stream b, antarctica. *Journal of Glaciology*, **43**, 231–237, doi:10.3189/s0022143000003178.

Whitehouse, P. L., 2018: Glacial isostatic adjustment modelling: historical perspectives, recent advances, and future directions. *Earth Surface Dynamics*, **6**, 401–429, doi:10.5194/esurf-6-401-2018.

Whitehouse, P. L., N. Gomez, M. A. King, and D. A. Wiens, 2019: Solid earth change and the evolution of the antarctic ice sheet. *Nature Communications*, **10**, doi:10.1038/s41467-018-08068-y.

Winkelmann, R., M. A. Martin, M. Haseloff, T. Albrecht, E. Bueler, C. Khroulev, and A. Levermann, 2011: The potsdam parallel ice sheet model (pism-pik) – part 1: Model description. *The Cryosphere*, **5**, 715–726, doi:10.5194/tc-5-715-2011.

Winsborrow, M., C. Clark, and C. Stokes, 2004: Ice streams of the Laurentide ice sheet. *Géographie Physique et Quaternaire*, **58**, 269.

Wood, D. M., 1991: *Soil Behaviour and Critical State Soil Mechanics*. Cambridge University Press.

Yu, H., E. Rignot, H. Seroussi, M. Morlighem, and Y. Choi, 2019: Impact of iceberg calving on the retreat of thwaites glacier, west antarctica over the next century with different calving laws and ocean thermal forcing. *Geophysical Research Letters*, **46**, 14539–14547, doi:10.1029/2019gl084066.

Ziemen, F. A., M.-L. Kapsch, M. Klockmann, and U. Mikolajewicz, 2019: Heinrich events show two-stage climate response in transient glacial simulations. *Climate of the Past*, **15**, 153–168, doi:10.5194/cp-15-153-2019.

Zoet, L. K. and N. R. Iverson, 2020: A slip law for glaciers on deformable beds. *Science*, **368**, 76–78, doi:10.1126/science.aaz1183.

Zotikov, I. A., 1986: The thermophysics of glaciers.
URL https://www.osti.gov/biblio/5967995